Numerical Methods for Neutron Transport Calculations of Nuclear Reactors

POLITECNICO DI TORINO

SCUOLA DI DOTTORATO

Doctoral course in Energetics - Cycle XXVI

PhD Thesis

Numerical Methods for Neutron Transport Calculations of Nuclear Reactors

Andrea Barbarino

Advisors	Course Director
Prof. Sandra Dulla	Prof. Roberto Zanino
Prof. Piero Ravetto	

May 2014

a Grazia, Marta, Fabio, Roberto

à les séctions PEPDDF et PEPDVF d'AREVA NP

"...there ain't no journey what don't change you some."
— David Mitchell, *Cloud Atlas*

Contents

Introduction

Nuclear reactor design and safety analysis require an accurate assessment of the power distribution inside the core region and in the surrounding structures. The high level of definition is imposed by the heterogeneity of the materials constituting the fuel assemblies with respect to their neutron transport properties; the characteristic length-scale of power variations inside the calculation domain may vary locally, introducing gradients that are to be correctly taken into consideration. When a fine characterization of the nuclear power is not viable, extremely expensive provisions have to be taken into account at the design phase as well as during operation; in case of commercial reactors, this results in substantial reductions of the profitability of the system. Moreover the national safety authorities impose to the enterprises and research centers a continuous revision of their simulation tools in order to minimize their uncertainties, task that can be achieved mainly by the improvement of the models and, secondly, of the numerical schemes.

Anyway, especially in the industrial framework, the quest for continuous modeling enhancements is in conflict with practicability issues.

The distribution of the power induced by fission may be described in terms of a single equation, the linear Boltzmann equation for neutrons, whose structure does not allow a direct numerical solution even with today's computational resources and after decades of advances in numerical schemes. Several approximations have been produced by reactor physicists so far, but nowadays they still receive a meager welcome among nuclear professionals because of their complexity compared to simpler but more robust techniques. Time consumption is still the first criterion for industry when evaluating an analysis method, trivially because order millions of full-core flux assessments have to be performed for each commercial nuclear reactor for its design phase, licensing and operation surveillance.

The objective of this thesis, which in clearly inspired by an industrial framework, is to try and narrow the gap between theoretical neutron modeling and application; of course, this ambitious plan is only partly accomplished here, but the aim is to introduce a set of research topics which might be further developed in the future.

Even if the extent of the present work is to study innovative numerical methods in neutron transport, for a more realistic research approach the same limitations as the industrial framework are taken into account.

First, even if modern and fast computers are available to the scientific community through the research centers, only limited computational resources were available to the author, mimicking the actual conditions of the industrial world where the number of core-hours per user are limited by the large amount of assessments to be performed simultaneously. Moreover, as for all budget-constrained developments, an ideal applicability target in the short-medium future is envisaged.

To respect these restrictions and accomplish the initial task, simple and practical solu-

tions have been preferred for this thesis, both for the modeling aspect and for the implementation. The extensive use of second-order transport is due to these limits. Of course, since *there is no free lunch*, the use this kind of approximation leads to results which do not show the robustness of a consistent numerical scheme applied directly on the exact model; these deviations are isolated and discussed.

This thesis is divided into three main chapters, preceded by a general overview. This structure reflects the three main topics which were chosen for this research project.

Chapter 1 provides an introduction to some key topics which are needed to understand the rest of the work. This part is intended to make the thesis self-consistent, so the author recommends reading it to those which are not accustomed with high-order discretization methods for differential equations and second-order transport approximations. Section 1.1 gathers basically all the models used in the chapters that follow, trying to derive them, avoiding much of the details, from the transport equation for neutrons in order to underline their consistency or inconsistency when this is the case. Section 1.2 is devoted to the introduction of the basics of the Spectral Element Method (SEM), which is the object of Chapter 2. Leaving the analytical aspects to the works cited in the references, a simple example of SEM implementation is given and commented step-by-step. These two sections should also help the reader in familiarizing with the notation.

Chapter 2 develops the SEM approach and its use in conjunction with transport approximations. As it is documented in the specialized numerical analysis handbooks and in the MSc thesis of the author [Barbarino, 2010], the method has an excellent convergence rate which outperforms most classical schemes, but it has also some important drawbacks which sometimes seem to discourage its use for linear transport problems applied to non-trivial benchmarks. In order to elaborate the methodology of the specific problems encountered in reactor physics, three aspects are addressed looking for improvements. The first topic analyzed is related to the convergence order, whose value is less straightforward to define a priori by means of functional analysis than other numerical schemes. The adjective "spectral" refers in fact to the maximum order claimed, exponential with respect to the average size of the mesh. A comprehensive set of convergence tests is carried out in section 2.1, applying SEM to a few transport models and with the aid of manufactured solutions, thus isolating the numerical effects from the deviations which are due only to modeling approximations. Section 2.2 relaxes the hypothesis of grid conformity, replacing the classical Galerkin variational formulation with the Discontinuous Galerkin theory, characterized by a more flexible treatment of the mesh interfaces; this scheme allows local grid refinement and opens the way, in perspective, to mesh adaption. Finally, section 2.3 presents a simple and sufficiently flexible technique to deform the boundaries of each mesh, in order to adapt the grid to curved geometries. In this way, the advantages of SEM can be applied to a vast class of common problems like lattice calculations. Moreover, thanks to a change of the basis functions used in SEM, it is possible to obtain elements with three sides (straight or deformed), that are a typical war horse of the Finite Element approach.

Chapter 3 is essentially devoted to the most "industrial" part of the thesis, developed entirely during the stay of the author in the AREVA NP headquarters in Paris. In AREVA, and in all other nuclear engineering enterprises, neutron diffusion is still the preferred neu-

tronic model for full-core studies. Better approximations are reserved for library preparation, fuel studies and code validation, none of these being typically too much time or budget-constrained. Today needs start to require a certain level of improvement also in full-core analyses, trying to fitly model localized dis-homogeneities and reduce the penalizing engineering margins which are taken as provisions. On the other hand, a change in the model does not mean only an effort to write a new code, but has huge follow-ups due to the validation processes required by the authorities. Second-order transport may support the foreseen methodology update because it can be implemented re-using diffusion routines as the computational engine. The A_N method, a second-order approximation of the transport equation, has been introduced in some studies, and its effect is discussed. Moreover, some effort has been reserved to the introduction of linear anisotropy in the model.

The last topic is addressed in chapter 4, dealing with ray effects; they are a known issue of the discrete ordinate approach (S_N methods) which is responsible for a reduction in the accuracy of the solution, especially in penetration problems with low scattering, like several shielding calculations performed for operator safety concerns. Ray effects are here characterized from a formal point of view in both static and time dependent situations. Then, quantitative indicators are defined to help with the interpretation of the S_N results. Based on these studies, some mitigation measures are proposed and their efficacy is discussed.

Some of the topics are to be regarded as first approaches in reactor physics. The extent of the PhD work does not allow a complete treatment of all aspects, which would require a complete implementation and a long validation phase on a suitable benchmark base, lasting years. The scope is to explore these rather innovative fields and suggest interesting research topic to the scientific community.

This thesis is complemented by several tenth of hundreds of lines of codes, gathered in a few demonstrative packages implementing the theoretical developments presented. For the SEM part no "professional" dedicated libraries are available for the moment: three different solvers have been created basically from scratch by the author. The first is a one-dimensional code able to cope with multi-slab problems in an arbitrary number of energy groups, for both critical and source-driven configurations. For a direct comparison of SEM with other classical algorithms, also P_N and S_N solvers are available within the same environment. Envisaging a didactic purpose, this code has been equipped with a MATLAB® GUI interface for launching and post-processing. Nonetheless, this solver may be promptly used for instance for reflector homogenization. The Discontinuous Galerkin approach has been implemented in a transport solver for non-conformal Cartesian grids (i.e. grids composed by rectangles) able to cope with multi-group second-order transport in source and critical mode. This code is written in Fortran 95, and is configured to run together with Gnuplot to provide a graphical output. Advanced features like convergence acceleration are available for critical calculations. Problems on deformed non-conformal grids are handled with another solver, customized for specific domains. The realization of a general purpose solver would have required too much time and would have largely passed the coding skills of the author. The package is capable to solve source problems (extension to critical ones is nonetheless simple) applying second-order transport.

The developments on the industrial core analysis are in form of modifications to existing code packages belonging to the AREVA production suite. Without disclosing sensible

pieces of information about the software architecture, these codes are written in Fortran interfaced with customized scripting languages; their structure is extremely complex and results from many decades of continuous optimization driven by the specific activities performed. The actions on these codes have touched only the static neutronic solvers, eventually modifying some cascades of classes to allow more cross sections to be passed from the external libraries to the inner solvers. For the 1D cases and the part on anisotropy, separated routines were developed in Fortran and SCILAB® frameworks.

The part on ray effect is pretty theoretical and the coding part has little relevance: just a few hundreds lines of straightforward listings helped studying the different discretizations by means of standard numerical tools.

Three articles have been published so far as a result of this work; they are reported in the bibliography under the names of Barbarino et al. [2013c], Barbarino et al. [2014] and Dulla et al. [2014]. In addition, a book chapter has been written and is available as Barbarino et al. [2013b]. One more article concerning SEM is in preparation. Several proceedings, namely Barbarino et al. [2011, 2012] and Barbarino and Tomatis [2013a,b], gather some additional material presented during the international conferences attended. Finally, a few AREVA technical reports have been produced, but they are not available to the public.

1 Background concepts

This chapter is an introduction to the two main mathematical tools that provide the background of this thesis: second order transport approximations and the Spectral Element method (SEM). The chapter is intended to make the reading of this thesis self-sustaining, defining the notation and establishing concepts which will be used in all the following chapters.

Section 1.1 introduces the Boltzmann neutron transport equation and its approximations. The aim is certainly not to provide a theory manual for neutronic specialists, but to contextualize correctly the second order transport models, which are used throughout the text; according to the author, the best way to accomplish this task is to draw the path of successive hypotheses and simplifications from the integro-differential neutron transport equation, and proceed in a deductive way. Of course, this process is done without lingering on the details; the interested reader is strongly advised to consult the reference literature (for instance the books by Meghreblian and Holmes [1960], Lewis and Miller [1993] or Hébert [2009]), which present the topic from a rigorous point of view.

Section 1.2 makes an overview of the basic concepts of the Spectral Element Method (SEM) for elliptic problems, a numerical technique for the discretization of spatial transport operators. The combined use of SEM and transport approximations has already been covered partly in the master thesis of the author [Barbarino, 2010]; only the basic concepts are here recalled, reduced to a few pages and directly applied to the solution of a simple elliptic problem, in order to see the methodology in action. Nonetheless, notation is introduced as well as some operators which are used in chapter 2, where the methodology is extended; for this reason the reading of this section is quite compulsory for non specialists. This chapter does not contain all the theoretical developments which explain the subtleties of the method; this is due both to the scope of the thesis – to provide a practical background for SEM implementation in neutron transport – and the complexity of the topic, which requires a deep knowledge of functional analysis. The interested reader should refer to Canuto et al. [2006, 2007] for an exhaustive presentation of the topic and to Deville et al. [2002] for a more direct approach, mainly intended for engineers.

1.1 Transport

The starting point for all transport formulations and approximations is the Boltzmann transport equation. This extremely general model can be adapted according to the type of particle considered: for neutrons in matter one can suppose that no forces are acting on them (no charge) and scattering is just the result of physical collisions in the background

medium. In the next section all the simplifying hypotheses are introduced, in order to delineate correctly the descriptive limitations of the derived models, long before the accuracy loss introduced by the numerical scheme chosen for the solution.

1.1.1 The Boltzmann equation for neutrons

All the present work is an effort to address the problem of solving a single equation, the Boltzmann transport equation for neutrons. This model is the reference for the study of the neutron distribution in phase space in presence of nuclear reactions. The derivation of this equation is not introduced here (any transport textbook, like Prinja and Larsen [2010], cover this topic); the equation is:

$$\frac{1}{\mathrm{v}(E)}\frac{\partial\Phi(\boldsymbol{r},E,\boldsymbol{\Omega},t)}{\partial t}+\boldsymbol{\Omega}\cdot\nabla\phi(\boldsymbol{r},E,\boldsymbol{\Omega},t)+\Sigma(\boldsymbol{r},E,t)\,\phi(\boldsymbol{r},E,\boldsymbol{\Omega},t)= \\ =\int \mathrm{d}E'\oint \mathrm{d}\boldsymbol{\Omega}'\Sigma_{\mathrm{s}}(\boldsymbol{r},E',t)\,\phi(\boldsymbol{r},E',\boldsymbol{\Omega}',t)\,f_{\mathrm{s}}(\boldsymbol{r},E'\to E,\boldsymbol{\Omega}'\cdot\boldsymbol{\Omega})+S(\boldsymbol{r},E,\boldsymbol{\Omega},t)\,. \quad (1.1)$$

The notation is standard; the unknown function is the angular flux ϕ, which represents the density of neutrons traveled paths in a certain region of the phase space at time t. The independent variables defining the phase space are the position $\boldsymbol{r}$, the total energy E (or alternately the speed v) and the direction assumed by the flight of the particles $\boldsymbol{\Omega}$. The material in which the neutrons are being transported is defined by means of a set of probabilities of interaction per unit path between the atoms of the matter and particles streaming sufficiently close; for the moment they are the total cross section Σ (any interaction) and the scattering cross section Σ_{s}; the latter is responsible for the streaming of neutrons across regions of the phase space according to the scattering kernel f_{s}. An external source S can inject or remove particles in any point of the phase space.

For practical purposes, the scalar flux, whose definition is

$$\Phi(\boldsymbol{r},E,t)=\oint\phi(\boldsymbol{r},E,\boldsymbol{\Omega},t)\,\mathrm{d}\boldsymbol{\Omega}, \quad (1.2)$$

is handier than the angular flux, being linked to the thermal power that can be extracted from the medium.

Equation (1.1) has both a differential and an integral connotation (belongs to the class of the integro-differential models), and so special numerical techniques were developed. Typically they tend to eliminate one of the two features, as it will be clear later.

In case of fissionable material, if a particle undergoes fission (with probability per unit length Σ_{f} it may emit a certain number of neutrons in a different point of the phase space. This number follows a statistical distribution having ν as expected value. As in scattering, all contributions from the other points of the phase space have to be considered. A simplification comes from the observation that fission always produces an isotropic emission of

particles. So, the Boltzmann equation for a multiplicative medium is:

$$\frac{1}{\mathrm{v}(E)}\frac{\partial\phi(\boldsymbol{r},E,\boldsymbol{\Omega},t)}{\partial t}+\boldsymbol{\Omega}\cdot\nabla\phi(\boldsymbol{r},E,\boldsymbol{\Omega},t)+\Sigma(\boldsymbol{r},E,t)\,\phi(\boldsymbol{r},E,\boldsymbol{\Omega},t)= \\ =\int \mathrm{d}E'\oint \mathrm{d}\boldsymbol{\Omega}'\Sigma_{\mathrm{s}}\left(\boldsymbol{r},E',t\right)\phi\left(\boldsymbol{r},E',\boldsymbol{\Omega}',t\right)f_{\mathrm{s}}\left(\boldsymbol{r},E'\to E,\boldsymbol{\Omega}'\cdot\boldsymbol{\Omega}\right)+ \\ \frac{\chi(\boldsymbol{r},E)}{4\pi}\int_0^\infty \mathrm{d}E'\oint \mathrm{d}\boldsymbol{\Omega}'\nu\Sigma_f(\boldsymbol{r},E')\phi(\boldsymbol{r},\boldsymbol{\Omega}',E',t)+S(\boldsymbol{r},E,t)\,. \quad (1.3)$$

Finally, in steady state and in the absence of external sources, the balance between absorption and multiplication may damp the overall neutron population, keep it constant or make it diverge. Introducing the multiplication factor k, the eigenvalue of the system, one has

$$\frac{1}{\mathrm{v}(E)}\frac{\partial\phi(\boldsymbol{r},E,\boldsymbol{\Omega},t)}{\partial t}+\boldsymbol{\Omega}\cdot\nabla\phi(\boldsymbol{r},E,\boldsymbol{\Omega},t)+\Sigma(\boldsymbol{r},E,t)\,\phi(\boldsymbol{r},E,\boldsymbol{\Omega},t)= \\ =\int \mathrm{d}E'\oint \mathrm{d}\boldsymbol{\Omega}'\Sigma_{\mathrm{s}}\left(\boldsymbol{r},E',t\right)\phi\left(\boldsymbol{r},E',\boldsymbol{\Omega}',t\right)f_{\mathrm{s}}\left(\boldsymbol{r},E'\to E,\boldsymbol{\Omega}'\cdot\boldsymbol{\Omega}\right)+ \\ \frac{1}{k}\frac{\chi(\boldsymbol{r},E)}{4\pi}\int_0^\infty \mathrm{d}E'\oint \mathrm{d}\boldsymbol{\Omega}'\nu\Sigma_f(\boldsymbol{r},E')\phi(\boldsymbol{r},\boldsymbol{\Omega}',E',t). \quad (1.4)$$

Boundary and interface conditions

Let the equation be defined on a finite region of space $\boldsymbol{r}\in V$. There are five basic boundary conditions that may be imposed to the transport equation [Hébert, 2010]:

Albedo The known outgoing flux is related to the incoming flux by the following Robin type condition

$$\phi(\boldsymbol{r}_{\mathrm{s}},E,\boldsymbol{\Omega})=\beta\phi(\boldsymbol{r}_{\mathrm{s}},E,\boldsymbol{\Omega}')\quad \boldsymbol{\Omega}\cdot\boldsymbol{n}_{\mathrm{s}}<0, \quad (1.5)$$

where $\boldsymbol{n}_s$ is the outbound normal to the surface of V at the boundary point $\boldsymbol{r}_s$. if $\beta=0$, any outgoing particle will not re-enter, modeling the behavior at a vacuum convex (non re-entrant) boundary. If $\beta=1$, the particle is reflected; specular reflection satisfies the additional constraints $\boldsymbol{\Omega}\cdot\boldsymbol{n}_s=-\boldsymbol{\Omega}'\cdot\boldsymbol{n}_s$ and $(\boldsymbol{\Omega}\times\boldsymbol{\Omega})\cdot\boldsymbol{n}_s=0$. Void and reflective boundary conditions are almost the only boundary conditions used in reactor analysis.

White It is a particular case of albedo condition where all particles bounce at the boundary and are re-emitted inward with an isotropic angular distribution.

$$\phi(\boldsymbol{r}_s,E,\boldsymbol{\Omega})=\frac{\beta}{\pi}\int_{\boldsymbol{\Omega}\cdot\boldsymbol{n}_s>0}\mathrm{d}^2\boldsymbol{\Omega}'\left[\boldsymbol{\Omega}'\cdot\boldsymbol{n}_s\right]\phi(\boldsymbol{r}_s,E,\boldsymbol{\Omega}'),\quad \boldsymbol{\Omega}\cdot\boldsymbol{n}_s<0. \quad (1.6)$$

Periodic The particle coming to one boundary is translated to a parallel boundary, emulating a periodic lattice. If $\Delta\boldsymbol{r}$ is the lattice pitch, one has

$$\phi(\boldsymbol{r}_s,E,\boldsymbol{\Omega})=\phi(\boldsymbol{r}_s+\Delta\boldsymbol{r},E,\boldsymbol{\Omega}). \quad (1.7)$$

Zero flux No particles are present of the boundary of V, i.e.

$$\phi(\boldsymbol{r}_s, E, \boldsymbol{\Omega}) = 0. \tag{1.8}$$

This condition is not physical, but quite used in the diffusive approximation.

Inside V, the angular flux is continuous along $\boldsymbol{\Omega}$ except if the source density contains a Dirac delta contribution in space.

The energy discretization

The energy variable E is often discretized [Hébert, 2010], and the energy range is divided into energy groups. All the distributions of interest are reformulated as averages over the extension of each energy group:

$$\phi_g(\boldsymbol{r}, \boldsymbol{\Omega}, t) = \int_{E_{g-1}}^{E_g} \phi(\boldsymbol{r}, E, \boldsymbol{\Omega}, t)\, \mathrm{d}E, \tag{1.9a}$$

$$\Phi_g(\boldsymbol{r}, t) = \int_{E_{g-1}}^{E_g} \phi(\boldsymbol{r}, E, t)\, \mathrm{d}E, \tag{1.9b}$$

$$S_g(\boldsymbol{r}, \boldsymbol{\Omega}, t) = \int_{E_{g-1}}^{E_g} S(\boldsymbol{r}, E, \boldsymbol{\Omega}, t)\, \mathrm{d}E, \tag{1.9c}$$

where E_{g-1} and E_g identify the limits of the energy group g. The definition of the multigroup cross sections introduce a non linearity in their definition, since they require the knowledge of the scalar flux in order to conserve the reaction rate during the discretization.

Given a certain set of condensed multigroup cross sections, the transport equation is often solved in each energy range, where particles are then supposed to move with a single energy. This simplifies the treatment, and do not interfere with the analytical nature of the other integro-differential operators; for this reason quite often the numerical techniques are presented applied over one-energy models only, as done in this thesis, with no limitations on the generality of the approaches used.

Other techniques are available; for instance the migration mode method [Tomatis, 2010] projects the energy dependence on a polynomial approximation space.

The equation in one and two-flat dimensions

Throughout the thesis some simplified models are developed, which may consider only a subset of the spatial and angular scalar variables.

The one-dimensional version of the transport approximation is used to model the behavior of neutrons in slabs of material, where only a dimension is relevant. To obtain it, it it sufficient to remember that in Cartesian coordinates the angular direction $\boldsymbol{\Omega}$ is typically written as

$$\boldsymbol{\Omega} = \mu \boldsymbol{e}_x + \cos\varphi\sqrt{1-\mu^2}\,\boldsymbol{e}_y + \sin\varphi\sqrt{1-\mu^2}\,\boldsymbol{e}_z, \tag{1.10}$$

where μ is the cosine of the latitude θ and φ is the longitude. Integrating the angular flux on φ one simply obtains:

$$\frac{1}{v}\frac{\partial\phi(x,\mu,E,t)}{\partial t}+\mu\frac{\partial\phi(x,\mu,E,t)}{\partial x}+\Sigma(x,E,t)\phi(x,\mu,E,t)= \int \mathrm{d}E'\int_{-1}^{+1}\mathrm{d}\mu\Sigma_s(x,\mu,E',t)f_s(x,\mu\mu',E'\rightarrow E)+S(x,\mu,E,t), \quad (1.11)$$

where the generic source may be also a fission term. For many simplified calculations, like those in chapter 2, scattering is assumed isotropic with perfectly elastic collisions. In addition to a monochromatic source, the equation reduces to

$$\frac{1}{v}\frac{\partial\phi(x,\mu,t)}{\partial t}+\mu\frac{\partial\phi(x,\mu,t)}{\partial x}+\Sigma(x,t)\phi(x,\mu,t)=\frac{\Sigma_s(x,t)}{2}\int_{-1}^{+1}\mathrm{d}\mu'\phi(x,\mu',t)+S(x,\mu,t). \quad (1.12)$$

The equation in two dimensions is trivially found with a similar procedure. Indeed, in the chapter dedicated to ray effect (chapter 4) a *flat*[1] 2D model is used to simplify some developments:

$$\cos\theta\frac{\partial\phi}{\partial x}+\cos\varphi\frac{\partial\phi}{\partial y}+\Sigma\phi=\frac{\Sigma_s}{2}\Phi+S, \quad (1.13)$$

where all dependencies are omitted. This formula models a steady-state population of neutrons which may only move in two directions in space, with always zero component in the third one (z in this case). This is a different framework compared to a 2D model: this equation is not the projection of the transport equation on plane, but is endowed with a different physics, which anyway is a sufficiently representative trade-off between reality and simple analytical treatment.

1.1.2 The integral form of the transport equation

An alternative form of the neutron transport equation (1.1) can be obtained by a spatial integration along the characteristic line of motion of neutrons, for both steady-state and time-dependent situations [Prinja and Larsen, 2010; Barbarino et al., 2013b].

Using (1.1), the spatial dependency can be reformulated including the line along which particles are moving:

$$\frac{1}{v}\frac{\partial\phi(\boldsymbol{r},E,\boldsymbol{\Omega},t)}{\partial t}-\frac{\partial\phi(\boldsymbol{r}-s\boldsymbol{\Omega},E,\boldsymbol{\Omega})}{\partial s}+\Sigma(\boldsymbol{r}-s\boldsymbol{\Omega},E,t)\phi(\boldsymbol{r}-s\boldsymbol{\Omega},E,\boldsymbol{\Omega},t)=Q(\boldsymbol{r}-s\boldsymbol{\Omega}), \quad (1.14)$$

where s is the coordinate on the system of reference of the trajectory and Q gathers the scattering term and the fixed and/or fission source. Equation (1.14) is also called characteristic form of the transport equation. The streaming term $\nabla\cdot(\boldsymbol{\Omega}\phi)=\boldsymbol{\Omega}\cdot\nabla\phi$ has become a simple directional derivative in this reference. The Laplace transform is applied on t in

[1] To be considered an absolutely informal notation, suggested by the *satirical novella* "Flatland" by Abbott [1884]. The characters of the book populate a fictional world where one Cartesian direction is forbidden.

order to get rid, for the time being, of the time derivative, and the the integration on s is performed. One obtains:

$$\phi^{\star}\left(\boldsymbol{r},E,\boldsymbol{\Omega},p\right)=\phi^{\star}\left(\boldsymbol{r}-s\boldsymbol{\Omega},E,\boldsymbol{\Omega},p\right)\exp\left[-\int_0^s\Sigma\left(\boldsymbol{r}-s'\boldsymbol{\Omega},E\right)\mathrm{d}s'\right]\exp\left(-\frac{p}{v}s\right)$$
$$+\int_0^s Q\left(\boldsymbol{r}-s\boldsymbol{\Omega},p\right)\exp\left[-\int_0^s\Sigma\left(\boldsymbol{r}-s''\boldsymbol{\Omega},E\right)\mathrm{d}s''\right]\exp\left(-\frac{p}{v}s'\right)\mathrm{d}s'. \quad (1.15)$$

Then, the inverse Laplace transform is carried out and, extending the s coordinate up to the non re-entrant boundary $s_B(\boldsymbol{r},\boldsymbol{\Omega})$ of the domain, and waiting for the system to diffuse all the initial distribution of particles, one obtains

$$\phi\left(\boldsymbol{r},E,\boldsymbol{\Omega},t\right)=\int_0^{s_B(\boldsymbol{r},\boldsymbol{\Omega})}Q\left(\boldsymbol{r}-s'\boldsymbol{\Omega},E,\boldsymbol{\Omega},t-\frac{s'}{v}\right)\exp\left[-\int_0^{s'}\mathrm{d}s''\Sigma\left(\boldsymbol{r}-s''\boldsymbol{\Omega},E\right)\right]\mathrm{d}s'. \quad (1.16)$$

Physically, the term

$$\exp\left[-\int_0^{s'}\mathrm{d}s''\Sigma\left(\boldsymbol{r}-s''\boldsymbol{\Omega},E\right)\right] \quad (1.17)$$

has the meaning of the probability that the particles moving between $\boldsymbol{r}-s'\boldsymbol{\Omega}$ and $\boldsymbol{r}$ undergoes a collision. The integral is also called optical path length, the distance measured in terms of the local mean free path. Then, it is intuitive to see that equation (1.16) collects, by integration along the points on the segment connecting $\boldsymbol{r}$ to the boundary and lying on $\boldsymbol{\Omega}$, the contributions to the flux by all neutrons emitted or scattered in direction $\boldsymbol{\Omega}$ that are capable to reach $\boldsymbol{r}$ without undergoing collision.

In the particular case where all sources can be considered isotropic, i.e. $Q(\boldsymbol{r},E,\boldsymbol{\Omega},t)=Q(\boldsymbol{r},E,t)/4\pi$, the equation can be integrated over all directions, thus leading to an integral expression for the scalar flux Φ, called Peierls equation [Duderstadt and Martin, 1979]:

$$\Phi\left(\boldsymbol{r},E,t\right)=\frac{1}{4\pi}\int Q\left(\boldsymbol{r}',E,t-\frac{\left|\boldsymbol{r}-\boldsymbol{r}'\right|}{v(E)}\right)\frac{\exp\left[-\int_0^{|r-r'|}\mathrm{d}s'\Sigma\left(\boldsymbol{r}-\frac{\boldsymbol{r}-\boldsymbol{r}'}{|\boldsymbol{r}-\boldsymbol{r}'|}s',E\right)\right]}{\left(\boldsymbol{r}-\boldsymbol{r}'\right)^2}\mathrm{d}\boldsymbol{r}', \quad (1.18)$$

that in steady-state becomes:

$$\Phi\left(\boldsymbol{r},E\right)=\frac{1}{4\pi}\int Q\left(\boldsymbol{r}',E\right)\frac{\exp\left[-\int_0^{|r-r'|}\mathrm{d}s'\Sigma\left(\boldsymbol{r}-\frac{\boldsymbol{r}-\boldsymbol{r}'}{|\boldsymbol{r}-\boldsymbol{r}'|}s',E\right)\right]}{\left(\boldsymbol{r}-\boldsymbol{r}'\right)^2}\mathrm{d}\boldsymbol{r}'. \quad (1.19)$$

This model will be used later as starting point to obtain a differential model, the A_N model, that will be used through the thesis. Nonetheless, it is the basis for many efficient transport solvers used nowadays for lattice calculations.

1.1.3 Quick overview of some angular treatment methodologies

Several deterministic methods are available to treat the angular dependence of the neutron transport equation. The most known are the spherical harmonics method, the discrete ordinates method, the collision probability method and the method of characteristics

[Hébert, 2010]. Some of them address the integro-differential form, others the integral one. A huge literature is available on each of these algorithms; here, the fist two are very briefly reviewed since they are used in the following.

The spherical harmonics method The spherical harmonics method, or P_N method, addressed the integro-differential form in equation (1.1), by representing the angular flux as a truncated series expansion in terms of spherical harmonics [Abramowitz and Stegun, 1972]. The use of weighted residual techniques allows then to get a finite set of differential equations which can be solved with standard techniques.

The derivation of the method can be found for instance in Hébert [2006]. For what follows, it is worth just introducing the 1D slab formulation. One starts from the 1D transport equation (1.12) and expands the flux as:

$$\phi(x,\mu) = \sum_{\ell=0}^{N} \frac{2\ell+1}{2} \phi_\ell(x) P_\ell(\mu), \tag{1.20}$$

where P_ℓ is the ℓ-th order Legendre polynomial and ϕ_ℓ are the moments of the angular flux

$$\phi_\ell(x) = \int_{-1}^{+1} P_\ell(\mu)\phi(x,\mu)\,\mathrm{d}\mu.$$

The moments $\{\phi_\ell\}$ with $\ell = 0,\ldots,N$ become the new unknowns to be determined. Also the source can be expanded in moments, $\{S_\ell\}$. Then, one substitutes these expansions into (1.12) and applies the weighted residual technique multiplying by $P_m(\mu)$ and integrating in $[-1,+1]$. After some algebraic elaborations one obtains

$$\frac{\ell}{2\ell+1}\frac{\mathrm{d}\phi_{\ell-1}(x)}{\mathrm{d}x} + \frac{\ell+1}{2\ell+1}\frac{\mathrm{d}\phi_{\ell+1}(x)}{\mathrm{d}x} + \Sigma(x)\phi_\ell(x) = \Sigma_s(x) f_\ell \Phi(x) + S_\ell(x). \tag{1.21}$$

Albedo boundary conditions can be imposed, in the approximation used by Marshak. It can be written as

$$\big(1+\beta\big)\phi_\ell(x_\pm) \pm (1-\beta)\sum_{m=0}^{N-1} M_{\ell,m}\phi_m(x_\pm) = 0, \tag{1.22}$$

where $x_\pm$ is the left or right boundary, ℓ is odd and $1 \le \ell \le N$, m is even and the elements of the **M** matrix are

$$M_{\ell,m} = (2m+1)\int_0^1 P_\ell(\mu)P_m(\mu). \tag{1.23}$$

The discrete ordinate method The disrcrete ordinates method, or S_N method, solves the transport equation along the directions identified by a finite set of values $\mathbf{\Omega}_n$ (or equivalently by a set of director cosines), always in even number.

According to the type of geometry, the director cosines are chosen so as to integrate polynomials with maximum accuracy [Hébert, 2010]. In 1D slab geometry, they are trivially identified by the nodes of the Gauss Legendre quadrature formula [Abramowitz and Stegun, 1972]. The 1D S_N transport equation is then

$$\mu_n \frac{\mathrm{d}\phi_n(x)}{\mathrm{d}x} + \Sigma(x)\phi_n(x) = \frac{\Sigma_s}{2}\sum_{m=1}^{2N} w_m\phi_m(x) + S_n(x), \tag{1.24}$$

where $\{\mu_n\}$ and $\{w_n\}$ are the nodes and weights of the chosen quadrature formula, $\phi_n(x) = \phi(x,\mu_n)$ and $S_n(x) = S(x,\mu_n)$.

Void boundary conditions are usually imposed by Mark formalism, requiring that all ϕ_n whose director cosine is inbound at a certain boundary point to vanish. Reflection is imposed by equating the ϕ_n with opposed director cosines.

1.1.4 Second-order transport

The use of second-order methods, also called even-parity methods, for the solution of neutron transport problems has increased in the last two decades [Lewis, 2010]. The eye-catching differences stand in the second-order streaming operator, opposed to the first order which is observed in (1.3), and in the fact that the angle is solved in half of the domain. First and second-order transport approximations may be cast in differential form, but the nature of the equations obtained and the solution methods for large engineering problems are contrasting.

From an historical point of view, diffusion theory is the first second-order transport approximation to be used, and general even parity transport and the variational framework are well-known at least since 1961 with the work by Vladimirov [1961]. However, computers used in early computational transport did not have sufficient memory to cope with large differential problems, and other methods, especially those able to "march" in space without too much memory footprint, were largely preferred. With the advance of computer performances in the 1990s, second-order transport started to be applied on larger problems, and now it is a tool for specific engineering tasks.

In this very short section the general second-order transport equation is introduced. Then, the P_N and S_N methods presented in section 1.1.3 are applied in the 1D case, leading to two equivalent formulations (but they may differ according to the numerical method used for the space discretization) which will be object of chapter 2. The SP_N model is also presented, which cannot be directly linked to the second-order transport equation, but is by far the election second-order model for more than one dimension. Finally, the A_N model is introduced, following a peculiar derivation from the integral transport equation (1.19) and suggesting its equivalence to SP_N.

General second-order neutron transport equation

Consider the steady-state, one-energy, transport equation in the isotropic medium (for simplicity), namely equation (1.4); then, all neutrons have the same energy $E = \text{const.}$. In this framework only the zeroth-order moment of scattering is non vanishing, leading to:

$$\boldsymbol{\Omega}\cdot\nabla\phi(\boldsymbol{r},\boldsymbol{\Omega}) + \Sigma(\boldsymbol{r})\phi(\boldsymbol{r},\boldsymbol{\Omega}) = \frac{\Sigma_s(\boldsymbol{r})}{4\pi}\int \phi(\boldsymbol{r},\boldsymbol{\Omega}')\,\mathrm{d}\boldsymbol{\Omega}' + S(\boldsymbol{r}). \tag{1.25}$$

Defining the even and odd components of the angular flux [Lewis, 2010] respectively as:

$$\begin{aligned}\phi^+(\boldsymbol{r},\boldsymbol{\Omega}) &= \frac{1}{2}\left[\phi(\boldsymbol{r},\boldsymbol{\Omega}) + \phi(\boldsymbol{r},-\boldsymbol{\Omega})\right],\\ \phi^-(\boldsymbol{r},\boldsymbol{\Omega}) &= \frac{1}{2}\left[\phi(\boldsymbol{r},\boldsymbol{\Omega}) - \phi(\boldsymbol{r},-\boldsymbol{\Omega})\right],\end{aligned} \tag{1.26}$$

one may write (1.25) for $\mathbf{\Omega}$ and $-\mathbf{\Omega}$; adding and subtracting the two versions one obtains a set of first-order equations in ϕ^+, ϕ^- and the scalar flux Φ. Finally, eliminating ϕ^- one obtains the even-parity transport equation:

$$-\mathbf{\Omega}\cdot\nabla\frac{1}{\Sigma(\boldsymbol{r})}\mathbf{\Omega}\nabla\phi^+(\boldsymbol{r},\mathbf{\Omega})+\Sigma(\boldsymbol{r})\phi^+(\boldsymbol{r},\mathbf{\Omega})=\frac{\Sigma_s(\boldsymbol{r})}{4\pi}\Phi(\boldsymbol{r})+S(\boldsymbol{r}), \tag{1.27}$$

where the scalar flux Φ is formulated as dependent on the even parity flux

$$\Phi(\boldsymbol{r})=\int\phi^+(\boldsymbol{r},\mathbf{\Omega})\,\mathrm{d}\mathbf{\Omega}. \tag{1.28}$$

Eliminating ϕ^- in place of ϕ^- brings the odd-parity equation, where the neutron current appear.

Since it is extensively used in chapter 2, it is worth introducing and elaborating the 1D version of the equation. From (1.27) one obtains

$$-\mu^2\frac{\partial}{\partial x}\Big(\frac{1}{\Sigma_{\mathrm{t}}(x)}\frac{\partial\phi^+(x,\mu)}{\partial x}\Big)+\Sigma(x)\,\phi^+(x,\mu)=\frac{\Sigma_{\mathrm{s}}(x)}{2}\,\Phi(x)+Q(x,\mu), \tag{1.29}$$

where the scalar flux may be simplified to

$$\Phi(x)=\int_{-1}^{+1}\phi^+(x,\mu)\,\mathrm{d}\mu=2\int_0^{+1}\phi^+(x,\mu)\,\mathrm{d}\mu, \tag{1.30}$$

because of the parity required to ϕ^+. Moreover, if the even and odd-parity sources are defined similarly to (1.26), the source term may be decomposed as follows

$$Q(x,\mu)=S^+(x,\mu)-\frac{\mu}{\Sigma(x)}\frac{\partial S^-}{\partial x}(x,\mu). \tag{1.31}$$

The equation must be supplied with proper boundary conditions, which must be formulated to include the even parity flux. For a 1D problem with $x\in[a,b]$, void boundary conditions on the angular flux are

$$\phi(a,\mu)=0,\quad\forall\,\mu\in[0,1];\qquad\qquad\psi(b,\mu)=0,\quad\forall\,\mu\in[-1,0]. \tag{1.32}$$

Assuming that no emission from the external source is taking place on the boundary, i.e. $S(a,\mu)=S(b,\mu)=0$, one can write (1.29), impose (1.32) and elaborate using the definitions of ϕ^+ and ϕ^-, obtaining the following Robin type boundary conditions:

$$\begin{aligned}\mu\frac{\partial\phi^+}{\partial x}(a,\mu)-\Sigma(a)\,\phi^+(a,\mu)=0,&\qquad\forall\,\mu\in[0,1],\\ \mu\frac{\partial\psi^+}{\partial x}(b,\mu)+\Sigma(b)\,\psi^+(b,\mu)=0,&\qquad\forall\,\mu\in[-1,0].\end{aligned} \tag{1.33}$$

For the reflective boundary conditions, one has simply to put to zero the derivatives of ϕ^+ at the boundaries.

Even-parity S_N and P_N formalisms

The discrete ordinate model A discrete ordinate model can be derived easily from the second-order transport equation (1.29) with boundary conditions given by (1.32), assuming piece-wise constant cross sections. For brevity, it is useful to set the following definitions:

$$\varphi_\ell(x) := \psi^+(x,\mu_\ell) \qquad \text{and} \qquad Q_\ell(x) := Q(x,\mu_\ell). \tag{1.34}$$

Assuming a domain with homogeneous material properties, and choosing a set of N symmetric angular directions $\{\mu_\ell\}_{\ell=1}^N$, one can write (1.29) for each direction $\mu_\ell > 0$, obtaining the following system of coupled differential equations:

$$-\frac{\mu_\ell^2}{\Sigma_t}\frac{\mathrm{d}^2\varphi_\ell(x)}{\mathrm{d}x^2} + \Sigma_t\varphi_\ell(x) = \frac{\Sigma_s}{2}\phi(x) + Q_\ell(x), \qquad \ell = 1,\ldots,N/2. \tag{1.35}$$

Recalling (1.32), at the boundary points a and b one can write:

$$\begin{aligned} \mu_\ell\frac{\mathrm{d}\varphi_\ell}{\mathrm{d}x}(a) - \Sigma_t(a)\varphi_\ell(a) &= 0, \\ \mu_\ell\frac{\mathrm{d}\varphi_\ell}{\mathrm{d}x}(b) + \Sigma_t(b)\varphi_\ell(b) &= 0, \qquad \ell = 1,\ldots,N/2. \end{aligned} \tag{1.36}$$

Interface conditions need also to be imposed at points x_∂ between two different homogeneous sub-domains:

$$\begin{aligned} \varphi_\ell(x_\partial^-) &= \varphi_\ell(x_\partial^+) \\ \frac{1}{\Sigma_t(x_\partial^-)}\frac{\mathrm{d}\varphi_\ell(x_\partial^-)}{\mathrm{d}x} &= \frac{1}{\Sigma_t(x_\partial^+)}\frac{\mathrm{d}\varphi_\ell(x_\partial^+)}{\mathrm{d}x}, \qquad \ell = 1,\ldots,N/2. \end{aligned} \tag{1.37}$$

If the directions are chosen as the nodes of a suitable quadrature formula, the scalar flux can be written as:

$$\phi(x) = 2\sum_{\ell=1}^{N/2} w_\ell\varphi_\ell(x), \tag{1.38}$$

where $\{w_\ell\}_{\ell=1}^N$ is the set of quadrature weights. Note that, for the even parity approach, one needs to use only half of the nodes and weights of a quadrature set to evaluate the total flux, since $\psi^+(x,\mu) = \psi^+(x,-\mu)$.

Using a compact matrix notation, the set of $N/2$ ordinary differential equations given in (1.35) and the two boundary conditions given in (1.36) become for each homogeneous subdomain:

$$-\frac{1}{\Sigma_t}\mathbf{D}\frac{\mathrm{d}^2\boldsymbol{\varphi}}{\mathrm{d}x^2} + \Sigma_t\boldsymbol{\varphi}(x) = \Sigma_s\mathbf{W}\boldsymbol{\varphi}(x) + \boldsymbol{Q}(x), \tag{1.39}$$

and

$$\mathbf{D}^{1/2}\frac{\mathrm{d}\boldsymbol{\varphi}}{\mathrm{d}x}(a) - \Sigma_t(a)\boldsymbol{\varphi}(a) = \mathbf{0}, \mathbf{D}^{1/2}\frac{\mathrm{d}\boldsymbol{\varphi}}{\mathrm{d}x}(b) + \Sigma_t(b)\boldsymbol{\varphi}(b) \quad = \mathbf{0}, \tag{1.40}$$

with $\boldsymbol{\varphi}(x) := \{\varphi_1(x),\ldots,\varphi_{N/2}\}^T$ and $\boldsymbol{Q}(x) := \{Q_1(x),\ldots,Q_{N/2}(x)\}^T$. The $(N/2)\times(N/2)$ diagonal matrix $\mathbf{D}$ has the non-zero elements equal to μ_ℓ^2, while $\mathbf{W}$ contains $N/2$ identical rows with one Gaussian quadrature weight w_ℓ per column. Matrix $\mathbf{D}^{1/2}$ is clearly diagonal with non-zero elements equal to μ_ℓ.

The even-parity spherical harmonics approach The angular treatment can be dealt with adopting the spherical harmonics approach, that amounts to an expansion in terms of Legendre polynomials in plane geometry, thus leading to a set of coupled equations for the even moments of the flux. The angular even parity flux and source are expanded as:

$$\phi^+(x,\mu) = \sum_{\ell=0}^{\infty} \frac{4\ell+1}{2} \phi_{2\ell}(\mu), \tag{1.41}$$

$$\begin{aligned} S^+(x,\mu) &= \sum_{\ell=0}^{\infty} \frac{4\ell+1}{2} S_{2\ell}(x) P_{2\ell}(\mu), \\ S^-(x,\mu) &= \sum_{\ell=0}^{\infty} \frac{4\ell+3}{2} S_{2\ell+1}(x) P_{2\ell+1}(\mu). \end{aligned} \tag{1.42}$$

It can be easily noticed that the zeroth-order moment of the angular flux ϕ_0 coincides with the scalar flux Φ defined by (1.30). Inserting (1.41) and (1.42) into (1.29) and (1.31) and using the Legendre polynomial orthogonality property and the three term recurrence relationship [Abramowitz and Stegun, 1972], an infinite set of coupled second-order differential equations is obtained. An approximation scheme follows after truncation at, say, $\ell = N$, setting $\mathrm{d}^2\phi_{2N+2}/\,\mathrm{d}x^2 = 0$. This leads to the P_{2N+1} approximation to the transport equation. In compact matrix notation, for a homogeneous region one has:

$$-\frac{1}{\Sigma}\mathbf{D}\frac{\mathrm{d}^2\boldsymbol{\phi}}{\mathrm{d}x^2} + \Sigma\mathbf{I}_c\boldsymbol{\phi}(x) = \boldsymbol{Q}(x), \tag{1.43}$$

where $\mathbf{D}$ is an unsymmetrical tri-diagonal matrix and $\mathbf{I}_c$ is the identity matrix where the first element is changed to $(1-\Sigma_s/\Sigma)$; the two vectors $\boldsymbol{\phi}(x)$ and $\boldsymbol{Q}(x)$ gather all the unknown moments of the flux and the known moments of the source, respectively:

$$\boldsymbol{\phi}(x) = \left(\phi_0(x), \phi_2(x), \ldots, \phi_{2N}(x)\right)^T, \qquad \boldsymbol{Q}(x) := \left(Q_0(x), Q_2(x), \ldots, Q_{2N}(x)\right)^T. \tag{1.44}$$

The vacuum boundary conditions (1.5) cannot be fulfilled exactly and one must extend the classical conditions of Mark or Marshak type, developed for the first-order transport formulation. Using the formulation by Mark, for instance, at the left boundary of the domain, one imposes

$$\mu_n \frac{\partial\psi^+}{\partial x}(a,\mu_n) - \Sigma_t\psi^+(a,\mu_n) = 0, \qquad n = 1,2,\ldots,N+1, \tag{1.45}$$

with

$$P_{2N+1}(\mu_n) = 0, \qquad \mu_n > 0. \tag{1.46}$$

The simplified spherical harmonics method (SP_N)

The SP_N method is an annular discretization which is based on an incomplete basis of orthogonal functions, with the advantage of bringing a system of differential equations with diffusive structure and a limited number of unknowns, that can be solved in 2D and 3D

situations where the "parent" (in a very broad sense) method P_N cannot be used basically for memory reasons [Hébert, 2010; Lewis, 2010].

The derivation is due to Gelbard [1960] in a quite heuristic form, later consolidated by several authors (for instance Pomraning [1993] and Larsen et al. [1996]). Basically, Gelbard took the 1D P_N equation (1.21) and replaced the total derivatives with a divergence for the even equations and a gradient for the odd ones, obtaining:

$$\begin{cases} \dfrac{2n+1}{4n+1}\nabla\cdot\phi_{2n+1}+\dfrac{2n}{4n+1}\nabla\cdot\phi_{2n-1}+\Sigma_{\mathrm{tr},2n}\phi_{2n}=\dfrac{1}{k}\nu\Sigma_f f_0\delta_{n0}, \\ \dfrac{2n+2}{4n+3}\nabla\phi_{2n+2}+\dfrac{2n+1}{4n+3}\nabla\phi_{2n}+\Sigma_{\mathrm{tr},2n+1}\phi_{2n+1}=0, \end{cases} \tag{1.47}$$

where $\Sigma_{\mathrm{tr},n}=\Sigma_\mathrm{t}-\Sigma_{\mathrm{s},n}$ is called n-th order transport cross section.

Even though this derivation starts from the spherical harmonics method, there is no formal link between P_N and SP_N. A few remarks should be done in the use of the SP_N method for transport calculations [Hébert, 2010]:

- SP_1, the lowest order approximation, is equivalent to P_1 in all dimensions; moreover, if scattering is isotropic, it is equivalent to diffusion.
- In 1D, the SP_N, P_N and S_{N+1} methods are equivalent
- SP_N uses an incomplete basis to expand the angular flux. This means that the numerical results generally do not converge to the real transport solutions. Anyway, there is a good quantity of literature supporting the improvement of accuracy with higher orders N, at least for the configurations where transport effect are not paramount.

The A_N approximation

By substitution in (1.47) of the odd moments ϕ_{2n+1} and ϕ_{2n-1} in the even equations, one obtains a general second-order form:

$$\left[-\nabla^2\begin{pmatrix} v_0 & w_0 & 0 & \cdots & 0 \\ u_2 & v_2 & w_2 & \cdots & 0 \\ \vdots & \vdots & \vdots & \vdots & \vdots \\ 0 & \cdots & u_{N-3} & v_{N-3} & w_{N-3} \\ 0 & \cdots & 0 & u_{N-1} & v_{N-1} \end{pmatrix}+\mathrm{diag}\begin{pmatrix} \Sigma_{\mathrm{tr},0} \\ \Sigma_{\mathrm{tr},2} \\ \cdots \\ \Sigma_{\mathrm{tr},N-3} \\ \Sigma_{\mathrm{tr},N-1} \end{pmatrix}\right]\begin{pmatrix} \phi_0 \\ \phi_2 \\ \vdots \\ \phi_{N-3} \\ \phi_{N-1} \end{pmatrix}=\frac{1}{k}\begin{pmatrix} \nu\Sigma_f\phi_0 \\ 0 \\ \vdots \\ 0 \\ 0 \end{pmatrix}, \tag{1.48a}$$

where

$$\begin{aligned} u_m &= \frac{1}{\Sigma_{\mathrm{tr},m-1}}\frac{m(m-1)}{(2m+1)(2m-1)}, \\ v_m &= \frac{1}{\Sigma_{\mathrm{tr},m-1}}\frac{m^2}{(2m+1)(2m-1)}+\frac{1}{\Sigma_{\mathrm{tr},m+1}}\frac{(m+1)^2}{(2m+1)(2m+3)}, \\ w_m &= \frac{1}{\Sigma_{\mathrm{tr},m+1}}\frac{(m+1)(m+2)}{(2m+1)(2m+3)}, \end{aligned} \tag{1.48b}$$

for $m = 0, 2, \ldots, N-1$.

Moreover, to the extent of this section, isotropic scattering will be considered, i.e. $\Sigma_{\mathrm{tr},n} = \Sigma$, for $n > 0$ (trivially $\Sigma_{\mathrm{tr},0} = \Sigma - \Sigma_\mathrm{s}$). In this case, system (1.48) can be simplified as

$$-\frac{1}{\Sigma}\nabla^2\left(\mathbf{A}\boldsymbol{\phi}\right) + \Sigma\boldsymbol{\phi} = \boldsymbol{q}, \tag{1.49}$$

where matrix $\mathbf{A}$ contains only the numerical coefficients (1.48b), the transport cross sections being gathered outside since they are all equal to Σ; the source $\boldsymbol{q}$ contains both isotropic scattering and fission (or possibly a fixed source), i.e. $\boldsymbol{q} = \Sigma_\mathrm{s}\phi_0 + (1/k)\nu\Sigma_\mathrm{f}$.

Matrix $\mathbf{A}$ has some interesting properties which are demonstrated in Ciolini et al. [2002]: first, its N eigenvalues are real, distinct and correspond to the first N zeros μ_α, $\alpha = 1, \ldots, N$ of the Legendre Polynomial of order $2N$, all elevated to the second power. Moreover, its eignvectors can be easily written by taking the set of even Legendre polynomials from order 0 to $2N-2$: the components of each eigenvector are the values of the polynomials in one of the aforementioned zeros, i.e.

$$\boldsymbol{\psi}_\alpha = \left(P_0(\mu_\alpha), P_2(\mu_\alpha), \ldots, P_{2N-2}(\mu_\alpha)\right)^T, \quad \alpha = 1, 2, \ldots, N. \tag{1.50}$$

The presence of the tridiagonal second-order operator $\nabla^2\mathbf{A}\cdot$, and thus of the coupling of the equations through the differential term, is a limiting feature from the implementation point of view because it requires a specific solver. It is possible to diagonalize this operator and shift the coupling to the linear terms, obtaining a set of diffusion-like equations, with just one ∇^2 operator for each line.

The procedure is quite straightforward. First, matrix $\mathbf{A}$ is decomposed according to the definition of diagonal matrix:

$$\mathbf{A} = \mathbf{G}\mathbf{D}\mathbf{G}^T, \tag{1.51}$$

where $\mathbf{G}$ is a square matrix whose columns are the eigenvectors $\boldsymbol{\psi}_\alpha$ of $\mathbf{A}$, while $\mathbf{D}$ is a diagonal matrix containing the eigenvalues, i.e. $\mathbf{D} = \mathrm{diag}(\mu_1^2, \mu_2^2, \ldots, \mu_N^2)$. Second, the flux is projected on the basis formed by the eigenvectors

$$\boldsymbol{\phi} = \mathbf{G}\boldsymbol{\varphi}, \tag{1.52}$$

where vector $\boldsymbol{\varphi}(\boldsymbol{r})$ contains the pseudo-fluxes, a set of N scalar functions

$$\boldsymbol{\varphi} = \left(\varphi_1, \varphi_2, \ldots, \varphi_N\right)^T, \tag{1.53}$$

and constitutes the new unknowns of the problem. In particular, the scalar flux $\Phi(\boldsymbol{r}) = \phi_0(\boldsymbol{r})$, usually the only component of practical interest, may be expressed as

$$\Phi(\boldsymbol{r}) = \sum_{\alpha=1}^{N} w_\alpha \varphi(\boldsymbol{r}), \tag{1.54}$$

where w_α are the first components of each eigenvector (the first row of $\mathbf{G}$).

Equations (1.51) and (1.52) are then substituted into (1.49), which is then left and right multiplied by $\mathbf{G}^{-1}$. Imposing a specific normalization to $\mathbf{G}$ which causes the first row of $\mathbf{G}$ to be filled with ones, one obtains

$$-\frac{\mu_\alpha^2}{\Sigma}\nabla^2\varphi_\alpha(\boldsymbol{r})+\Sigma\varphi_\alpha(\boldsymbol{r})=\Sigma_s\sum_{\beta=1}^{N}w_\beta\varphi_\beta(\boldsymbol{r})+q(\boldsymbol{r}),\quad(\alpha=1,2,\ldots,N)\,, \tag{1.55}$$

where w_β are now equal to the weights of the Gauss-Legendre formula of order $2N$, having as nodes the same μ_α appearing in front of the differential operator. System (1.55) is called the A_N approximation [Coppa and Ravetto, 1982].

The evaluation of ϕ_1 leads to the computation of the current. By inserting the A_N solution into (1.47) one has

$$\boldsymbol{J}(\boldsymbol{r})=-\frac{1}{\Sigma}\sum_{\alpha=1}^{N}w_\alpha\mu_\alpha^2\nabla\varphi_\alpha. \tag{1.56}$$

It is interesting to note that this relation may be obtained by the weighted sums of the pseudo-currents, the quantities obtained in direct analogy to the diffusion currents according to Fick's law

$$\boldsymbol{J}(\boldsymbol{r})=\sum_{\alpha=1}^{N}w_\alpha\boldsymbol{j}_\alpha(\boldsymbol{r})=\sum_{\alpha=1}^{N}w_\alpha\left(-\frac{\mu_\alpha^2}{\Sigma}\nabla\varphi(\boldsymbol{r})\right). \tag{1.57}$$

In the form (1.55) the model is amenable only to homogeneous domains. In the cited references it is shown that the suitable interface conditions to be enforced at $\boldsymbol{r}_{ij}$ where two homogeneous regions $\Omega^{(i)}$ and $\Omega^{(j)}$ meet are:

$$\varphi_\alpha^{(i)}\left(\boldsymbol{r}_{ij}\right)=\varphi_\alpha^{(j)}\left(\boldsymbol{r}_{ij}\right). \tag{1.58}$$

On the outer boundary $\boldsymbol{r}_\partial$, one can use a reflective condition for each pseudo-flux (Neumann type)

$$\frac{\mathrm{d}\varphi_\alpha}{\mathrm{d}\boldsymbol{n}}\left(\boldsymbol{r}_\partial\right)=0, \tag{1.59}$$

or the vacuum Mark boundary condition

$$-\frac{\mathrm{d}\varphi_\alpha}{\mathrm{d}\boldsymbol{n}}\left(\boldsymbol{r}_\partial\right)=\frac{\Sigma}{\mu_\alpha}\varphi_\alpha\left(\boldsymbol{r}_\partial\right). \tag{1.60}$$

Each condition involves only a single pseudo-group.

For multigroup calculations, there is a set like (1.55) for each group. For G groups, the A_N model is

$$\frac{\mu_\alpha^2}{\Sigma_g}\nabla^2\varphi_{\alpha,g}(\boldsymbol{r})-\Sigma_g\varphi_{\alpha,g}(\boldsymbol{r})+\sum_{g'=1}^{G}\left(\Sigma_{\mathrm{s},0,g'}+\chi_g\frac{1}{k}\nu\Sigma_{\mathrm{f},g'}\right)\sum_{\beta=1}^{N}w_\beta\varphi_{\beta,g'}\left(\boldsymbol{r}\right)=0, \tag{1.61}$$

for $g=1,\ldots,G$ and $\alpha=1,\ldots,N$. Interface and boundary equations are modified accordingly, still being a set of coupling relations involving only a condition on a single pseudo-flux of each group.

The A_N formalism is just a projection of the SP_N transport approximation on a different basis, and models the transport phenomena in the same way (under the conditions of isotropy of scattering)[2]. The added value is that it is formally equivalent to a set of multigroup diffusion equations (including boundary and interface conditions), and thus in principles any multigroup solver should be able to cope with these calculations without any major modification. Chapter 3 deals with the industrial implementation of this model.

Derivation from integral transport The A_N approximation may also derive directly from the neutron transport equation recast in integral form, under some simplifying conditions. This derivation helps unveiling some of the meaning of each A_N pseudo-flux φ_α; moreover, it provides a consistency proof for the validity of the SP_N model, which was questioned at its appearance because of its heuristic derivation by Gelbard [1960].

The integral transport equation (1.18) can be simplified in case of homogeneous medium and isotropic scattering simply as

$$\Phi(\mathbf{r}) = \frac{e^{-\Sigma|\boldsymbol{r}-\boldsymbol{r}'|}}{4\pi|\boldsymbol{r}-\boldsymbol{r}'|^2}\left[\Sigma_s\Phi(\boldsymbol{r}') + \frac{1}{k}\nu\Sigma_f\Phi(\boldsymbol{r}')\right]\mathrm{d}\boldsymbol{r}'. \tag{1.62}$$

The kernel of this integral may be considered as the result of the following integration

$$\frac{e^{-s\Sigma}}{4\pi s^2} = \frac{1}{4\pi s}\int_0^1 \Sigma e^{-s\Sigma/\mu}\frac{\mathrm{d}\mu}{\mu^2}, \tag{1.63}$$

and thus it may be approximated by a Gauss-Legendre quadrature formula of degree N (having weights w and nodes μ) on $[0,1]$, as follows

$$\frac{e^{-s\Sigma}}{4\pi s^2} \approx \sum_{\alpha=1}^{N} w_\alpha \frac{\Sigma e^{-s\Sigma/\mu_\alpha}}{4\pi s\mu_\alpha^2}. \tag{1.64}$$

It should be noted that the terms in the summation have the formal structure of kernels of the diffusion equation in integral form [Coppa et al., 2011]. By substitution one has

$$\begin{aligned}\Phi(\mathbf{r}) = \sum_{\alpha=1}^{N} w_\alpha \int_{\mathscr{D}} \frac{e^{-\Sigma|\boldsymbol{r}-\boldsymbol{r}'|/\mu_\alpha}}{4\pi|\boldsymbol{r}-\boldsymbol{r}'|\mu_\alpha^2}\left[\Sigma_s\Phi(\boldsymbol{r}') + \frac{1}{k}\nu\Sigma_f\Phi(\boldsymbol{r}')\right]\mathrm{d}\boldsymbol{r}' \\ = \sum_{\alpha=1}^{N} w_\alpha\varphi_\alpha(\boldsymbol{r}).\end{aligned} \tag{1.65}$$

Given the following identity, demonstrated in Coppa and Ravetto [1982]:

$$\left(\nabla_{\mathbf{r}}^2 - a^2\right)\frac{e^{-a|\boldsymbol{r}-\boldsymbol{r}'|}}{|\boldsymbol{r}-\boldsymbol{r}'|} + 4\pi\delta\left(\boldsymbol{r}-\boldsymbol{r}'\right) = 0, \tag{1.66}$$

[2] As SP_N in isotropic conditions, at lowest order the A_N formulation is equivalent to diffusion. In fact the Gauss-Legendre formula of order $2N = 2$ has two nodes at $\pm 1/\sqrt{3}$, with unitary weights. The only equation of the A_1 model is then

$$-\frac{1}{3\Sigma}\nabla^2\varphi_1(\boldsymbol{r}) + (\Sigma - \Sigma_s)\varphi_1(\boldsymbol{r}) = S(\boldsymbol{r}),$$

where $\phi_1 = \Phi$ for (1.54), and the diffusion coefficient is defined as $D = 1/(3\Sigma)$.

one gets back to the differential A_N operator.

The derivations helps highlighting the fact that the neutron flux is approximated by a superposition of N fictitious neutron population following a diffusive behavior, with adjusted parameters.

Anisotrpic A_N

In order to obtain a more general form of equation (1.55), a step backwards in the derivation is necessary. Starting from (1.48), it is now supposed that scattering is linearly anisotropic, i.e. $\Sigma_{\mathrm{tr},n} = \Sigma$, starting from $n = 2$, while $\Sigma_{\mathrm{tr},0}$ and $\Sigma_{\mathrm{tr},1}$ have non-zero values. Using then the same procedure outlined in the previous sections, one obtains [Coppa and Ravetto, 1982]

$$\frac{\mu_\alpha^2}{\Sigma}\nabla^2\varphi_\alpha - \Sigma\varphi_\alpha + \left(\Sigma_{s,0} + \frac{1}{k}\nu\Sigma_f\right)\Phi - 3\Sigma_{s,1}\frac{\mu_\alpha^2}{\Sigma}\nabla\cdot\boldsymbol{J} = 0, \tag{1.67}$$

where $\Sigma_{\mathrm{s},1} = \Sigma - \Sigma_{\mathrm{tr},1}$ is the first moment of scattering and the current $\boldsymbol{J}$ is defined after (1.48) as:

$$\boldsymbol{J} = -\sum_{\alpha=1}^{N} w_\alpha \frac{\mu_\alpha^2}{\Sigma_{\mathrm{tr},1}}\nabla\varphi_\alpha. \tag{1.68}$$

The multigroup version of (1.67) is

$$\frac{\mu_\alpha^2}{\Sigma_{t,g}}\nabla^2\varphi_{\alpha,g} - \Sigma_g\varphi_{\alpha,g} + \sum_{g'=1}^{G}\left[\Sigma_{s,0,g'\to g} + \frac{1}{k}\chi_g\,\nu\Sigma_{f,g'}\right]\Phi_{g'} - 3\Sigma_{s,1,g}\frac{\mu_\alpha^2}{\Sigma_{t,g}}\nabla\cdot\boldsymbol{J}_g = 0, \tag{1.69}$$

the current being simply

$$\boldsymbol{J}_g = -\sum_{\alpha=1}^{N} w_\alpha \frac{\mu_\alpha^2}{\Sigma_{\mathrm{tr},g}}\nabla\varphi_{\alpha,g}. \tag{1.70}$$

Some methods were studied for the solution of this model, and some results were produced. This activity is part of the PhD program and is introduced in chapter 3, together with the implementation of the isotropic A_N formulation in core simulators.

1.2 The Spectral Element method

Simulation of reactor physics requires the solution of the multi-group Boltzmann equation in complicated geometries. Approximate models, such as classic P_N and S_N or A_N methods, reduce the problem to a system of coupled partial differential equations in the space variables. Depending on the approximation, the equations are first or second-order. Afterwards, the problem is handled by a space discretization scheme. Several approaches have been developed in the past for the space discretization of the problem, and have been implemented in reactor codes [Lewis and Miller, 1993]. The spectral element method (SEM) is a new space discretization scheme in this context, deserving careful attention.

Like the Finite Element Method (FEM), SEM is a variational technique ideally suited for second-order problems and it is highly accurate when applied to fairly regular problems

[Deville et al., 2002]. The error reduction as a function of the number of degrees of freedom in the most favorable cases shows exponential behaviour which is much better than the polynomial error reduction characterizing the use of low-order methods such as finite differences (FD) or Lagrangian FEM. The one dimensional SEM discretization technique is quite simple: the problem domain is partitioned into fairly large sub-domains, and into each sub-domain one introduces Lagrange interpolation polynomials of degree k on a convenient (*i.e* Gauss-Lobatto) grid with $(K+1)$ nodes including the end points to ensure continuity, as it will be explained in section 1.2.1. Using the nodal values and the associated interpolation polynomials one builds a trial function that is introduced into the weak formulation of the problem. All quadratures involved in this process (namely the inner products of the basis functions or of their derivatives) are performed on the Gaussian grid. The resulting algebraic system is solved using one of the common iterative techniques (like preconditioned GMRES [Saad and Schultz, 1986; Deville et al., 1987]) to deal with side-effects such as the large number of unknowns or ill-conditioning of the associated linear system. An interesting and convenient aspect of the method lies in the fact that multi-dimensional problems are systematically handled in quadrangular geometry (even deformed ones as shown later on), with the help of tensor products. Finally, refinement of the computation comes either by increasing the number of sub-domains (reminding the h-version of FEM) or by increasing the degree of the Gaussian grid (reminding the p-version of FEM).

This section is an introduction to the method of the spectral elements for transport applications. Most of the material comes from the MSc thesis of the author, defended in November 2010 at the Politecnico di Torino [Barbarino, 2010]; other sources are reference books and articles. The developments on this subject carried out during the PhD program are addressed in chapter 2, but it is mandatory to become familiar with the following few concepts in order to read it profitably.

1.2.1 Some generalities of the method

Spectral Element Methods (SEM) are one of the families of numerical methods obtained from the application of the Galerkin variational procedure. The first formalization of SEM is dated back to 1984, in the article by Patera [1984]. They have a tight relation with finite element discretization (FEM), including features of both p and h-versions.

The connection with the h-version of the finite element method stands in the use of a Lagrangian interpolation basis; it should be noted that all basis functions have essentially local support, restricted to the element's domain. The SEM shares with the p-version, instead, the predilection for high order polynomials on a fixed (and often quite coarse) grid.

The specific feature of SEM is the synergy between orthogonal polynomials and Gaussian quadrature. The orthogonality of typical basis functions of FEM is mainly due to the fact that local superimposition is avoided, while in the SEM this property is induced both by their topological nature (no trans-element extension) and analytical form.

From the first attempts to consolidate this method, two main variants have been proposed, based respectively on Chebyshev and Legendre polynomials. In both cases these polynomials are used to write a set of Lagrangian interpolants on a special grid, generated according to the nodes of the Gauss-Lobatto-Legendre (GLL) quadrature formula. Cheby-

shev polynomials were introduced first, because of the possibility to exploit fast transform techniques; moreover, the quadratures needed to evaluate the basic operators (*stiffness* and *mass* matrices) have also analytical form. Even if the results showed the expected exponential behavior of the error for smooth problems, the implementation was not straightforward and was abandoned if favor of the Legendre version.

***A priori* error estimates and advantage over FEM** A complete treatment of the basics of the SEM method is definitely out of the scope of this thesis; excellent references for a complete overview of the mathematical justification of the method and its performances are the books by Canuto et al. [2006, 2007] and Quarteroni [2009]. A simplified approach, intended for implementation, is presented by Deville et al. [2002] and Karniadakis and Sherwin [2005].

In what follows a simple comparison between SEM and FEM is introduced, based on the *a priori* error estimates that are obtained with some notions of functional analysis.

As known, all the numerical methods based on the Galerkin procedure do not address directly the given differential problem, but transform it into a variational problem whose solution is in general weaker, meaning that the regularity requirements are relaxed compared to those requested by the original form.

Consider a simple elliptic problem on the domain Ω. If $u \in H^{r+1}(\Omega)$ is the exact solution of the associated variational problem (where H denotes a Sobolev space) and u_h is the approximated solution obtained using FEM of order r and mesh average size h, one can affirm that

$$\|u - u_h\|_{H^1(\Omega)} \leq C h^r \, |u|_{H^{r+1}(\Omega)} \, . \tag{1.71}$$

Thus, the error can be reduced by decreasing h, *i.e.* refining the grid, or increasing r, using elements with higher order, always if u has a sufficient regularity. In any case, the error is reduced by the parameters of the method only.

Indeed, if SEM is used with elements of order N and size h, it is true that

$$\|u - u_h\|_{H^1(\Omega)} \leq C_r \, h^{\min(N,r)} N^{-r} \|u\|_{H^{r+1}(\Omega)} . \tag{1.72}$$

It is clear that the regularity of the solution, represented by the order r of the Sobolev space to which u belongs, acts directly on the magnitude on the error: besides the possibility to reduce the mesh size h and increase the order N, a more regular solution will make SEM converge faster.

In case the solution is analytical (i.e. with infinite regularity), the order of convergence becomes exponential; in the more common case of finite regularity, SEM is able to reach anyway the maximum convergence speed allowed by the regularity of the exact u. Furthermore, similar estimates are given when numerical integration is used to evaluate the variational operators, that is the most common approach for both SEM and FEM.

Similar considerations can be made for other types of differential problems, but the associated estimates are not introduced here. Of course, these performances are paid in terms of limitations on the geometry flexibility (this is one of the topics developed in Chapter 2), the high number of elements in the algebraic matrix and its bad conditioning, which reduce the effectiveness of sparse matrix solvers.

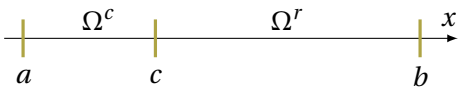

Figure 1.1: The 1D domain which is used in section 1.2.2.

1.2.2 Application of the method to 1D elliptic equations

What follows is the implementation of the SEM method for the solution of the diffusion equation. This introduction, which proceeds step-by-step sacrificing formal elegance for clarity, is required to non-experts to handle correctly the SEM operators and understand all the developments contained in the next chapter, which focuses on the advances covered during the PhD activity. Much of this work reflects the first implementation by Mund [2011b], who firstly ported the methodology to second-order equations in neutron transport (even-parity P_N).

Weak form Be the one-energy one-dimensional diffusion equation:

$$\begin{cases} -D(x)\dfrac{\mathrm{d}^2\Phi(x)}{\mathrm{d}x^2} + \Sigma(x)\Phi(x) = f(x) & x \in [a,b] \\ \dfrac{\mathrm{d}\Phi}{\mathrm{d}x} = 0 & x = a,b, \end{cases} \tag{1.73}$$

where the notation is standard. The model is source-driven, but the extension to the case of eigenvalue problems is straightforward, and does not affect the SEM operators nor the convergence properties with respect to the spatial discretization.

This problem is solved in a simple cell problem, where different material properties characterize regions $\Omega^c := x \in [a,c]$ and $\Omega^r := x \in [c,b]$, represented in Figure 1.1. Reflective boundary conditions are imposed at both boundaries: like in FEM, the homogeneous Neumann condition is natural at all contours, and this simplifies the developments. *Figure 1.1*

In order to apply a variational procedure, (1.73) is tested in the distributional sense against a set of functions, called test functions $\{\theta(x)\}$, belonging to a suitable functional space in which the solution will be represented. A classical choice is the Sobolev space $\mathbb{V} = H^1$, where functions are square integrable together with their derivatives at least on the domain of the problem.

The problem obtained is called weak form of (1.73):

$$\int_0^b \mathrm{d}x \left[\left(D(x)\frac{\mathrm{d}\phi}{\mathrm{d}x} \right) \cdot \frac{\mathrm{d}\theta}{\mathrm{d}x} + \sigma_t\left(\phi(x)\right) \cdot \theta(x) \right] = \int_0^b \mathrm{d}x \left[s(x)\theta(x) \right]. \tag{1.74}$$

The solution of this problem is the only ϕ which satisfies (1.74) for any choice of $\theta \in H^1(a,b)$. The integration by parts responsible for the first term in (1.74) brings also a second term containing the derivative evaluated in $x = a,b$, which is used to impose Neumann and Robin type boundary conditions; in this case they vanish because a zero derivative condition is required by the problem at both extremes.

Figure 1.2: The reference element $\widetilde{\Omega}$ in 1 dimension, with the internal positioned according to the GLL formula with K=6.

Choice of the approximation space and integration Sobolev space $\mathbb{V} = H^1(a,b)$ is infinitely dimensional. A finite Γ-dimensional approximation space $\mathbb{V}_\Gamma$ is used instead, described by a set of finite basis functions $\{\widetilde{\theta}_\gamma(x)\}$, i.e.

$$\mathbb{V}_\Gamma := \text{span}\{\theta_\gamma, \gamma \in [1,\Gamma]\}. \tag{1.75}$$

This also implies that the unknown of the discretized problem is no more the continuous function $\Phi(x)$, but the coefficients of its approximate representation on $\mathbb{V}_\Gamma$, i.e. the $\{\Phi_k\}$ terms in

$$\Phi(x) \approx \sum_{\gamma=1}^{\Gamma} \Phi_\gamma \theta_\gamma(x), \tag{1.76}$$

where Φ_γ terms are the coefficients to be determined.

Galerkin theory, a classical argument in all numerical methods textbook, states the conditions for the stability and consistency of the approximation [Quarteroni, 2009]. The testing procedure is now the same, but it produces a finite set of equations which, normally by means of numerical integration (Galerkin with Numerical Integration method, GNI) is of algebraic type. Notably, the conditioning number of this set depends on the basis functions used and on the dimensionality of the approximation space, which become the distinctive feature of each single Galerkin type method.

For standardization and an easier implementation, the actual domain chosen for the approximation space is not, to begin, the physical domain, but a reference domain. The
Figure 1.2 typical choice for SEM methods in 1D is $\widetilde{\Omega} := s \in [-1,+1]$ (Figure 1.2).

In this way a set of reference matrix operators are produced, which are then adapted with suitable coordinate transformations to the physical domain, reducing the number of computations in general multi-mesh configurations. In $\widetilde{\Omega}$ the dependence of the parameters on the spatial coordinate is typically assumed smooth, in order to use classical quadrature formulas; this may not be the case for the entire physical domain (in this problem, for instance, in $x = a$ all parameters have a sharp discontinuity). For this reason, the physical domain is partitioned into subdomains Ω^E (sometimes called improperly elements), and continuity relations are imposed to some basis functions (the boundary adapted ones) in order to join the solution in a consistent way. In order to be mathematically consistent, the basis functions ascribable to each element cannot be undefined out of it: they are then extended with null value throughout the domain (they have local support on the element itself, and on an adjacent one if they are boundary adapted).

The basis functions on the reference domain are $K+1$ Lagrange interpolation polynomi-
Figure 1.3 als (Figure 1.3)

$$\chi_k(\xi) = -\frac{1}{K(K+1)}\frac{1}{L_K(\xi_k)}\frac{(1-\xi^2)L_K(\xi)}{(\xi-\xi_k)} \qquad \chi_k(\xi) \in \mathbb{P}_K(\mathscr{D}_x^I). \tag{1.77}$$

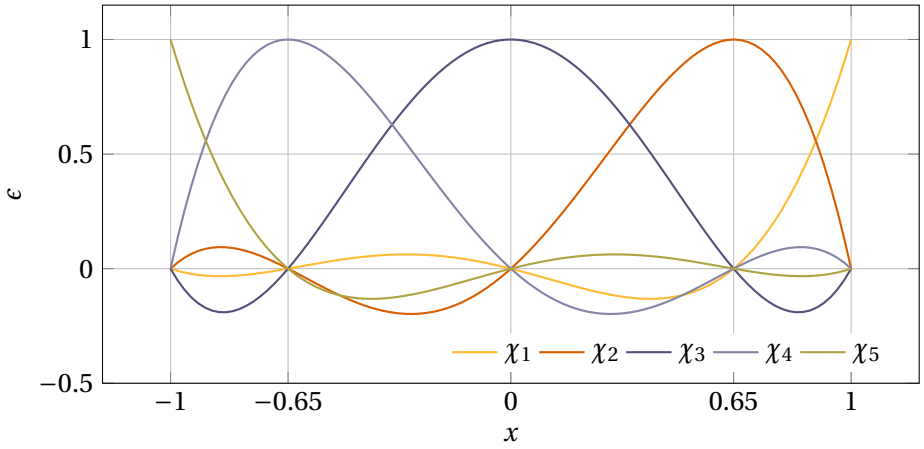

Figure 1.3: Lobatto basis in 1D, for $K = 4$.

where $K \in \mathbb{N}^+$ is the common order of all basis functions; thus, also the solution will be polynomial of the same order, i.e. it is assumed that the unknown can be represented by

$$\Phi(x) \approx \sum_{k=1}^{K+1} \Phi_k \chi_k(x). \tag{1.78}$$

Abscissas $\xi_k, k \in [1, K+1]$ are the nodes of the Gauss-Lobatto-Legendre (GLL) quadrature formula, a Gaussian formula defined on $[-1,+1]$: the extremes are included in the set, limiting the accuracy to order $2K-1$. Nodes are tabulated or easily obtained solving

$$\left(1-\xi_k^2\right) P'_N(\xi) = 0 \qquad 1 \le k \le K+1. \tag{1.79a}$$

The associated weights are

$$\rho_k = \frac{2}{K(K+1)} \frac{1}{P_K^2(\xi_k)} \qquad 1 \le k \le K+1. \tag{1.79b}$$

The same basis functions are then used also as test functions $\{\theta\} = \{\chi_k\}$.

Looking at the definition (1.77), each basis function is worth exactly 1 at the corresponding ξ_k, and 0 in all the others. So, the unknown coefficients Φ_k are nothing but the values of the interpolated solution at the nodes of the GLL grid. Moreover, using the GLL formula, is immediate to verify numerically that

$$\int_{-1}^{+1} \chi_k \, \mathrm{d}s = \rho_k, \tag{1.80a}$$

$$\int_{-1}^{+1} \chi_k \chi_\ell \, \mathrm{d}s \approx \rho_k \delta_{k\ell}, \tag{1.80b}$$

$$\int_{-1}^{+1} f(s) \chi_k \, \mathrm{d}s = \rho_k f(\xi_k). \tag{1.80c}$$

The derivatives of (1.77) are available analytically for the set of ξ_k nodes, and are gathered in the derivation matrix $\mathbf{D}$, whose elements are:

$$\mathrm{D}_{ij} = \left.\frac{\mathrm{d}\chi_j}{\mathrm{d}s}\right|_{s=\xi_i} = \begin{cases} \dfrac{P_K(\xi_i)}{P_K(\xi_j)}\dfrac{1}{\xi_i-\xi_j}, & i \neq j, \\ -\dfrac{(K+1)K}{4}, & i=j=1, \\ \dfrac{(K+1)K}{4}, & i=j=K+1, \\ 0, & \text{otherwise.} \end{cases} \tag{1.81}$$

It is worth noting that an easy way to evaluate the derivative in any point of the reference domain consists in interpolating the nodal values of the derivative using the same basis of interpolation polynomials $\{\chi_k\}$, as follows[3]:

$$\frac{\mathrm{d}\xi_\ell}{\mathrm{d}s} = \sum_{k=1}^{K+1} D_{k\ell}\chi_k(s). \tag{1.82}$$

This feature is not used in this chapter, but will be useful to assemble the operators using the Discontinuous Galerkin formalism (chapter 2).

At this point, the weak form is tested against all basis functions, expanding the unknowns as in (1.78) and using the GLL formula as needed. After some algebra (for a step-by-step derivation see Barbarino [2010]; Deville et al. [2002]; Mund [2011b]) if cross sections are constant on each element[4] one obtains the following set of algebraic equations:

$$\left(D\widetilde{\mathbf{K}} + \Sigma\widetilde{\mathbf{M}}\right)\boldsymbol{\Phi} = \widetilde{\mathbf{M}}\boldsymbol{f}, \tag{1.83}$$

where

$$\widetilde{\mathbf{K}} = \left\{\tilde{\mathrm{K}}_{kl} = \int_{-1}^{+1} \mathrm{d}s \frac{\mathrm{d}\chi_k}{\mathrm{d}s}\frac{\mathrm{d}\chi_l}{\mathrm{d}s}\right\} = \mathrm{diag}(\boldsymbol{\rho})\mathbf{D}\mathbf{D}^T, \tag{1.84a}$$

$$\widetilde{\mathbf{M}} = \left\{\tilde{\mathrm{M}}_{kl} = \int_{-1}^{+1} \mathrm{d}s\chi_k\chi_l\right\} = \mathrm{diag}(\boldsymbol{\rho}). \tag{1.84b}$$

which are called *reference stiffness matrix* and *reference mass matrix* respectively.

Using a coordinate transformation from the reference domain to a generic physical element $\Omega^e := x \in [x_{\mathrm{inf}}, x_{\mathrm{sup}}]$,

$$x(s) = x^e_{\mathrm{inf}}\frac{1-s}{2} + x^e_{\mathrm{sup}}\frac{1+s}{2}, \tag{1.85}$$

[3] It is also an exact representation, because the polynomial order of the derivative is $K-1$, and so no approximation error is introduced if a K order basis is used.

[4] Non-constant cross sections can be easily inserted in this type of schemes, provided they are sufficiently smooth to be represented by an interpolation with the same set of basis functions $\{\chi_k\}$ used for the flux. The approximation

$$\Sigma(x) \approx \sum_{k=1}^{K+1} \Sigma_k\chi_k(x),$$

is then inserted into the weak form, and integrals are carried out numerically as usual. It is possible to write the SEM operators for this case explicitly still using the reference matrices $\widetilde{\mathbf{K}}$ and $\widetilde{\mathbf{M}}$, with little effort.

and the Jacobian is

$$J^e = \frac{x^e_{\text{sup}} - x^e_{\text{inf}}}{2} = \frac{h^e}{2}. \tag{1.86}$$

Thus, if the weak form had been tested on the physical element, the algebraic system to be solved would have been

$$\left(D\mathbf{K}^e + \Sigma\mathbf{M}^e\right)\mathbf{\Phi} = \mathbf{M}^e\boldsymbol{f}, \tag{1.87}$$

where

$$\mathbf{K}^e = \frac{1}{J^e}\widetilde{\mathbf{K}}, \tag{1.88a}$$

$$\mathbf{M}^e = J^e\widetilde{\mathbf{M}}. \tag{1.88b}$$

In order to attach more elements, one writes a set of equations for each of them, and then imposes suitable interface conditions. Within the Continuous Galerkin (CG) framework, the continuity of the unknowns is imposed, i.e.:

$$\Phi^{e-1}_{K+1} = \Phi^e_1. \tag{1.89}$$

This results in a partial superposition of the single-element matrices while assembling the final algebraic system, and for this the technique is often referred to as direct stiffness summation.

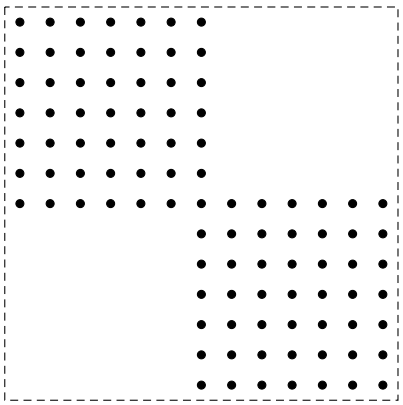

Figure 1.4: Assembled matrix for a domain with 2 elements, each with the same polynomial.

1.2.3 Application of the method to 2D elliptic equations

The procedure outlined in the previous section is now adapted to cope with 2 spatial dimensions. Extension to 3 dimensions is straightforward analytically, but heavier from an implementation point of view for numerical reasons.

Again, for simplicity, the problem solved is of diffusive type, with reflection on all sides:

$$\begin{cases} -D(x,y)\nabla^2\Phi(x,y) + \Sigma(x)\Phi(x,y) = f(x,y) & \text{on } \Omega \\ \nabla\Phi\cdot\boldsymbol{n} = 0 & \text{on } \partial\Omega, \end{cases} \tag{1.90}$$

where $\boldsymbol{n}$ is the outward normal versor to the boundary $\partial\Omega$.

Some hints on the construction of multidimensional SEM operators are given in the following, using some concepts already defined for the 1D case; for a complete derivation one may refer to Barbarino [2010].

Domain The domain Ω is meshed with E non-overlapping volumes Ω^e (quadrilaterals in two dimensions), such that

$$\Omega = \bigcup_{e=1}^{E} \Omega^e. \tag{1.91}$$

On the external boundary $\partial\Omega$ one assumes the existence of a set of non-overlapping surfaces $\Gamma_i^{(D)}$, $i = 1,\dots,N_D$, on which a Dirichlet boundary condition applies. Non-overlapping surfaces $\Gamma_j^{(N)}$, $j = 1,\dots,N_N$ exist also where Neumann (or Robin) boundary conditions apply. Of course, the union of all these surfaces covers the whole external boundary, as:

$$\partial\Omega = \left(\bigcup_{i=1}^{N_D} \Gamma_i^{(D)}\right) \cup \left(\bigcup_{j=1}^{N_N} \Gamma_j^{(N)}\right). \tag{1.92}$$

The reasons for the decomposition are two: as in the 1D case, one looks for regions where parameters vary smoothly with the spatial coordinate and, in addition, one tries not to deform too much the grid, especially trying to adapt to skewed boundaries. For this first (classical) approach, the domain is decomposed into rectangular domains only, in a fully structured mesh. Chapter 2 will introduce more flexibility in the design of the grid.

Weak form The integration of the laplacian is handled with the Green's theorem, giving rise to a volume integral and a surface integral, which is used to impose Neumann and Robin boundary conditions.

Reference domain the reference domain is the square $[-1,+1]^2$. It is the tensor product of two 1D reference segments.

Approximation space The basis functions of the approximation space are all separable in each variable, being products of 1D basis:

$$\theta_n = \chi_k \chi_p \quad k,p \in [1,K+1]. \tag{1.93}$$

so, it is clear that on the reference domain a grid on internal nodes is created, and it is the result of the tensor product of a GLL grid on the s coordinate and a grid on the t coordinate (Figure 1.5).

Figure 1.5

For convenience during the operator assembly, basis functions, nodes and nodal values have two numbering systems: one (using k and p in this example) with two indices which refer to the original 1D grids, and one with just a single index (n) which follows a lexicographical convention, i.e. $n = (k-1)*(K+1)+p$. This constructions preserves the fact that θ_n functions are still Lagrangian interpolators built on the two dimensional grid of internal nodes, and properties (1.80) are maintained.

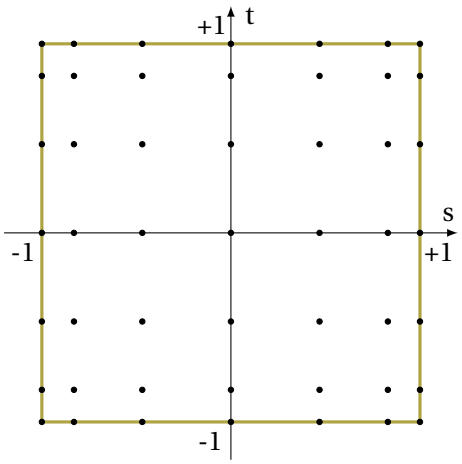

Figure 1.5: The reference element Ω in 2 dimensions, with the internal nodes formed by the tensor product of the GLL grids on s and t (K=6).

As before, for simplicity the problem is first set on a single rectangular domain, and then joined through the direct stiffness summation procedure. For a single element with constant input parameters D and Σ, the Galerkin procedure brings the following operators

$$(D\mathbf{K} + \Sigma\mathbf{M})\,\boldsymbol{\Phi} = \mathbf{M}\boldsymbol{f}\,, \tag{1.94}$$

where, considering again the definitions (1.84):

$$\mathbf{K}^e = \frac{L_y^e}{L_x^e}\left(\widetilde{\mathbf{M}}\otimes\widetilde{\mathbf{K}}\right) + \frac{L_x^e}{L_y^e}\left(\widetilde{\mathbf{K}}\otimes\widetilde{\mathbf{M}}\right), \tag{1.95a}$$

$$\mathbf{M}^e = \frac{L_x^e L_y^e}{4}\left(\widetilde{\mathbf{M}}\otimes\widetilde{\mathbf{M}}\right), \tag{1.95b}$$

$$\boldsymbol{\Phi} = \left\{\Phi_n = \Phi_{k,p}\right\} \quad \boldsymbol{f} = \left\{f_n = f_{k,p}\right\}, \tag{1.95c}$$

and the tensor product operation $\otimes$ between matrices is defined as

$$\mathbf{A}\otimes\mathbf{B} = \begin{pmatrix} a_{11}\mathbf{B} & a_{12}\mathbf{B} & \cdots & a_{1\ell}\mathbf{B} \\ a_{21}\mathbf{B} & a_{22}\mathbf{B} & \cdots & a_{2\ell}\mathbf{B} \\ \vdots & \vdots & & \vdots \\ a_{k1}\mathbf{B} & a_{k2}\mathbf{B} & \cdots & a_{k\ell}\mathbf{B} \end{pmatrix}. \tag{1.96}$$

If solved as it is, reflection boundary conditions are used on all 4 sides, because they are natural in this approach. Continuity of the unknowns across different elements is enforced, but different strategies are now possible; here the Continuous Galerkin (CG) approach is introduced. The CG scheme assumes that the solution is represented by the same number of basis on each element, and imposes that a strong continuity of the interpolation of the

solution across adjacent edges. In turn, this means that all edges have the same number of degrees of freedom and that they are all superimposed (for the GLL grid and the structured grid): the corresponding nodal values are imposed equal.

The working principle is the same as in 1D, but of course implementation is slightly more complex. Details are available in Barbarino [2010] and Deville et al. [2002].

In the end, the result can be written as a single set of equations comprising all elements and all unknown coefficients.

The extension of the equation building process to three space dimensions is straightforward. For instance, the elemental stiffness matrix (1.95a) of a subdomain with edge lengths L_x^e, L_y^e and L_z^e writes

$$\mathbf{K}^e = \frac{L_y^e L_z^e}{L_x^e}(\mathbf{M}\otimes\mathbf{M}\otimes\mathbf{K}) + \frac{L_x^e L_z^e}{L_y^e}(\mathbf{M}\otimes\mathbf{K}\otimes\mathbf{M}) + \frac{L_x^e L_y^e}{L_z^e}(\mathbf{K}\otimes\mathbf{M}\otimes\mathbf{M}). \tag{1.97}$$

Chapter 2 introduce a new paradigm in the treatment of interfaces, which allows unstructured grids, different orders of interpolation across elements and edge deformations.

1.2.4 Application to the A_N set

The diffusive problem seen in the previous two sections is used to assemble a scheme able to solve the A_N set, since it is formed by a set of equations which are of elliptic type.

Application of the spectral element discretization requires every equation of the A_N problem (1.55) to be cast in variational formulation. Using for each of the N unknowns the same approximation space used in the previous example on the diffusion model, one gets:

$$\int_{\mathscr{D}} \frac{\mu_\alpha^2}{\Sigma(\boldsymbol{r})}\nabla\varphi_\alpha(\boldsymbol{r})\cdot\nabla\theta(\boldsymbol{r})\,\mathrm{d}\boldsymbol{r} - \int_{\partial\mathscr{D}} \frac{\mu_\alpha^2}{\Sigma(\boldsymbol{r})}\theta(\boldsymbol{r})\frac{\partial\varphi_\alpha}{\partial\boldsymbol{n}}\,\mathrm{d}s + \int_{\mathscr{D}} \Sigma(\boldsymbol{r})\varphi_\alpha(\boldsymbol{r})\theta(\boldsymbol{r})\,\mathrm{d}\boldsymbol{r} - \sum_{\beta=1}^{N} w_\beta \int_{\mathscr{D}} \Sigma_s(\boldsymbol{r})\varphi_\beta(\boldsymbol{r})\theta(\boldsymbol{r})\,\mathrm{d}\boldsymbol{r} = \int_{\mathscr{D}} S(\boldsymbol{r})\theta(\boldsymbol{r})\,\mathrm{d}\boldsymbol{r}. \tag{1.98}$$

With these notations, one may write the variational formulation of the problem in the following expanded form:

$$\begin{cases} \displaystyle\sum_{e=1}^{E}\left(\int_{\mathscr{D}_e} \frac{\mu_\alpha^2}{\Sigma(\boldsymbol{r})}\nabla\varphi_\alpha(\boldsymbol{r})\cdot\nabla\theta(\boldsymbol{r})\,\mathrm{d}\boldsymbol{r} + \int_{\mathscr{D}_e} \Sigma(\boldsymbol{r})\varphi_\alpha(\boldsymbol{r})\theta(\boldsymbol{r})\,\mathrm{d}\boldsymbol{r}\right) \\ \qquad - \displaystyle\sum_{e=1}^{E}\sum_{\beta=1}^{N} w_\beta \int_{\mathscr{D}_e} \Sigma_s(\boldsymbol{r})\varphi_\beta(\boldsymbol{r})\theta(\boldsymbol{r})\,\mathrm{d}\boldsymbol{r} - \sum_{i=1}^{N_D}\int_{\Gamma_i^{(D)}} \frac{\mu_\alpha^2}{\Sigma(\boldsymbol{r})}\theta(\boldsymbol{r})\frac{\partial\varphi_\alpha}{\partial\boldsymbol{n}}\,\mathrm{d}s \\ \qquad\qquad - \displaystyle\sum_{j=1}^{N_N}\int_{\Gamma_j^{(N)}} \frac{\mu_\alpha^2}{\Sigma(\boldsymbol{r})}\theta(\boldsymbol{r})\frac{\partial\varphi_\alpha}{\partial\boldsymbol{n}}\,\mathrm{d}s = \sum_{e=1}^{E}\int_{\mathscr{D}_e} S(\boldsymbol{r})\theta(\boldsymbol{r})\,\mathrm{d}\boldsymbol{r} \\ \varphi_\alpha = g_i^{(D)}(s) \qquad \text{on} \quad \Gamma_i^{(D)} \qquad i = 1,\dots,N_D \\ \dfrac{\partial\varphi_\alpha}{\partial\boldsymbol{n}} = g_j^{(N)}(s) \qquad \text{on} \quad \Gamma_j^{(N)} \qquad j = 1,\dots,N_N. \end{cases} \tag{1.99}$$

A full algebraic problem could be assembled, trying to solve at once for all nodal values of all pseudo-fluxes; the resulting matrix would have an extremely sparse pattern, requiring a specific solver. Another path is pursued here: a SEM matrix is assembled considering as unknowns only the coefficients related to the pseudo-flux appearing in the streaming and collisional terms; the others contribute to the right hand side. A block Gauss-Seidel scheme is then used: pseudo-fluxes are initialized, then each discretized A_N equation is solved and the updated coefficents are used to update all right hand sides, till convergence. This algorithm is widely used when dealing with multigroup models, and exploits the analogy between A_N and multigroup diffusion.

2 Application of the Spectral Element Method to second order neutron transport

In this chapter, the Spectral Element Method (SEM) approach for neutron transport problems is developed.

Section 1.2 of the introductory chapter makes a first overview of the early developments by Mund [2011b], with additional contributions by the author [Barbarino, 2010]. Further methodological developments took place during this PhD activity, in order to better understand the behavior of the scheme and allow more flexibility in the types of problems it is able to cope with.

Section 2.1 deals with some assessments of fundamental type aimed at testing the convergence properties of the scheme; the method of the manufactured solutions allows isolating and evaluating the error introduced by the discretization of the spatial operators.

As discussed in section 1.2, the original version of SEM requires a conformal grid (i.e. a grid with no hanging nodes) and the same interpolation base on each mesh; these features greatly simplify the implementation and open the way to efficient solution algorithms [Deville et al., 2002], but such a scheme does not let the user perform a local refinement. For this reason section 2.2 introduced the Discontinuous Galerkin (DG) framework, thanks to which it is possible to create Cartesian grids where the number of degrees of freedom can vary from an element to another, and the conformity constraint is relaxed, too.

Finally, section 2.3 adds the possibility to deform the grid using a simple technique called transfinite interpolation to limit the numerical evaluations in this phase in favor of a highly accurate analytic node placement.

The combination of the tools in sections 1.2, 2.2 and 2.3 should be enough to cope, in perspective, with a wide class of involved reactor configurations.

The complement to each section should be a comment on the coding of the features of the method, since most is constituted by original work. No SEM dedicated libraries have been used because they are not available at the moment. All the code details could not fit a single chapter, nor are indicated for a PhD dissertation, but its worth remembering that code engineering has a paramount importance for this kind of applications. Some configurations were analyzed with such tools, and a selected set of results are present at the end of each part. Their aim is mainly to benchmark the method on literature examples in order to highlight its advantages compared to other classical approaches.

2.1 Convergence studies

In this section, the numerical performance of the SEM method is investigated in detail. In order to carry out an accurate monitoring of the behavior of the error up to levels close to numerical round-off, it is necessary to have an exact reference solution. Exact benchmarks are available either through fully analytical solutions [Ganapol, 2008] or through a manufactured solution process [Warsa et al., 2010]. Manufactured solutions can be easily obtained for source-injected neutron transport problems, by tailoring the external neutron source and the boundary conditions to a prearranged analytical neutron distribution in a given system. In what follows, manufactured and analytical solutions are derived and the performance of SEM is assessed by direct comparisons and error studies.

Even if the interest in the SEM approach lies mainly on multidimensional configurations, the convergence studies in this section are focused on simpler 1D cases, in order to compare the results with the ones obtained by applying other standard approximations such as spherical harmonics (section 2.1.2) and discrete ordinate (section 2.1.1) formulations. This allows a more consistent evaluation of the error, eliminating differences associated to the angular treatment adopted and focusing on the spatial discretization schemes only.

2.1.1 Spectral elements applied to the discrete ordinate equations

The discrete ordinates even-parity formulation of the transport equation (section 1.1.4) is used as a first approach with SEM, followed by the spherical harmonics expansion. Basically, any second-order, 1-dimensional transport model could be adopted with the same result. This section is devoted to the first scheme. Anyway, the possibility to have both P_N and S_N formalism solved with the same numerical technique helps also demonstrating numerically their equivalence, which is proven formally.

The SEM approach can be applied along the same line established previously. Let $\boldsymbol{\theta}(x) \in (H^1(a,b))^{N/2}$ denote any suitable $N/2$-dimensional test vector defined on the domain $\mathscr{D}_x = x \in [a,b]$. We take the inner product of (1.39) by $\boldsymbol{\theta}(x)$ which, after integration by parts and application of the boundary conditions, (1.36), yields:

$$\int_a^b \mathrm{d}x \left[\frac{1}{\Sigma_\mathrm{t}(x)} \left(\mathbf{Y} \frac{\mathrm{d}\boldsymbol{\varphi}}{\mathrm{d}x} \right) \cdot \frac{\mathrm{d}\boldsymbol{\theta}}{\mathrm{d}x} + \Sigma_\mathrm{t}(x) \boldsymbol{\varphi}(x) \cdot \boldsymbol{\theta}(x) \right] + \mathbf{D}^{1/2} \boldsymbol{\varphi}(a) \cdot \boldsymbol{\theta}(a) + \mathbf{D}^{1/2} \boldsymbol{\varphi}(b) \cdot \boldsymbol{\theta}(b) = \\ = \int_a^b \mathrm{d}x \left[\Sigma_\mathrm{s}(x) (\mathbf{W} \boldsymbol{\varphi}(x)) \cdot \boldsymbol{\theta}(x) + \boldsymbol{Q}(x) \cdot \boldsymbol{\theta}(x) \right]. \quad (2.1)$$

Then, the spatial domain $\mathscr{D}_x$ is partitioned into E adjacent elements $\mathscr{D}_x^e$ $(e = 1, \ldots, E)$ and inside each element a GLL quadrature grid is imposed with its associated Lagrange interpolation polynomials of degree $(K+1)$. By this process a $(EK+1)$-dimensional subspace of $H^1(a,b)$ is built, say $\mathbb{V}_{EK+1}$. For each element e, the even parity unknown fluxes can be written as:

$$\varphi_\ell^e(x) = \sum_{k=1}^{K} \varphi_\ell^e(x_k^e) \chi_k^e(x), \qquad \ell = 1, \ldots, N/2, \quad e = 1, \ldots, E, \quad (2.2)$$

where $\chi_k^e(x)$ belongs to the set of GLL Lagrangian interpolation polynomials mapped from the reference domain onto the element e.

The approximation scheme looks for the unique vector $\boldsymbol{\varphi}(x) \in (V_{EK+1})^{N/2}$ such that (2.1) holds for any vector $\boldsymbol{\theta}(x) \in (\mathbb{V}_{EK+1})^{N/2}$. Thus, $\boldsymbol{\varphi}(x)$ and $\boldsymbol{\theta}(x)$ are taken according to the same approximation shape and share the same basis functions, in line with Galerkin-type schemes. Introducing the stiffness and mass matrices $\mathbf{K}$ and $\mathbf{M}$ as calculated in section 1.2, one can easily show that the linear system induced by the spectral element Galerkin approximation of (1.39) with element constant cross sections writes:

$$\mathbf{L}\boldsymbol{\Phi} := (\mathbf{Y} \otimes \mathbf{K} + \mathbf{I} \otimes \mathbf{M} - c\mathbf{W} \otimes \mathbf{M})\,\boldsymbol{\Phi} = \mathbf{M}\boldsymbol{q}. \tag{2.3}$$

Here, the $(EK+1)N/2$ unknown quantities appearing in the expansions of (2.2) have been assembled into vector $\boldsymbol{\Phi}$ respecting the order of the indices. The matrix tensor product $\mathbf{Y} \otimes \mathbf{K}$ has a block diagonal structure, explicitly:

$$\mathbf{Y} \otimes \mathbf{K} = \begin{pmatrix} \mu_1^2\mathbf{K} & & & \\ & \mu_2^2\mathbf{K} & & \\ & & \ddots & \\ & & & \mu_{N/2}^2\mathbf{K} \end{pmatrix}. \tag{2.4}$$

The elements responsible for the scattering terms are tensor-multiplied with the mass matrix and their product,$\mathbf{W} \otimes \mathbf{M}$, can be written as:

$$\mathbf{W} \otimes \mathbf{M} = \begin{pmatrix} w_1\mathbf{M} & w_2\mathbf{M} & \dots & w_{N/2}\mathbf{M} \\ w_1\mathbf{M} & w_2\mathbf{M} & \dots & w_{N/2}\mathbf{M} \\ \vdots & \vdots & \vdots & \vdots \\ w_1\mathbf{M} & w_2\mathbf{M} & \dots & w_{N/2}\mathbf{M} \end{pmatrix}. \tag{2.5}$$

Matrix $\mathbf{M}$ shows a diagonal structure. This fact leads to have a rather sparse structure for matrix $\mathbf{L}$, ans this feature is conserved for the P_N formulation which will be addressed shortly.

2.1.2 The even-parity SEM-P_N formulation

Second-order 1D P_N has already been derived and analyzed in chapter 1 at section 1.1.4. The derivation is similar to that for S_N, then it will quickly introduced.

The weak formulation of the problem looks for the unique vector $\phi(x) \in \left(H^1(a,b)\right)^{N+1}$ such that $\forall \boldsymbol{\theta}(x) \in \left(H^1(a,b)\right)^{N+1}$ one has:

$$\int_a^b \mathrm{d}x \left[\frac{1}{\Sigma_\mathrm{t}} \left(\mathbf{D} \frac{\mathrm{d}\phi}{\mathrm{d}x} \right) \cdot \frac{\mathrm{d}\boldsymbol{\theta}}{\mathrm{d}x} + \Sigma_\mathrm{t} \left(\mathbf{I}_c \phi(x) \right) \cdot \boldsymbol{\theta}(x) \right] - \frac{1}{\Sigma_\mathrm{t}} \left(\mathbf{D} \frac{\mathrm{d}\phi}{\mathrm{d}x} \right) \cdot \boldsymbol{\theta} \Big|_{x=a}^{x=b} = \int_a^b \mathrm{d}x \boldsymbol{Q}(x) \cdot \boldsymbol{\theta}(x). \tag{2.6}$$

Then, the problem is solved in the finite dimensional subspace $\mathbb{V}_{EK+1}$, having the same dimension of the S_N case (the solution will be defined in terms of polynomials of the same order, but only for the spatial part). As it is customary in Galerkin-type approximations, the same Lagrangian polynomials will be used for test and trial functions.

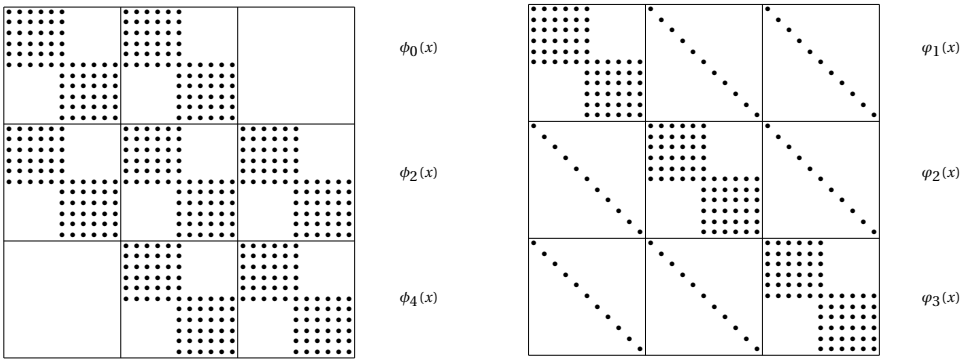

(a) P_5 formulation. (b) S_6 formulation.

Figure 2.1: Comparison of the structure of matrix $\mathbf{L}$ for P_5 and S_6 formulations; the integration domain is split into two elements, and in each element the GLL basis functions is of degree 5. The terms ϕ_n denote the angular moments of the flux.

After all quadratures, still using the $\mathbf{K}$ and $\mathbf{M}$ building blocks, the linear system induced by the spectral element Galerkin approximation of (1.43) tuns out to be:

$$\mathbf{L}\boldsymbol{\varphi} := \left(\mathbf{D} \otimes \overline{\mathbf{K}} + \mathbf{I}_c \otimes \overline{\mathbf{M}}\right) \boldsymbol{\varphi} = \mathbf{M}\boldsymbol{q}. \tag{2.7}$$

Also in the P_N case matrix $\mathbf{L}$ is sparse due to the diagonality of $\mathbf{M}$ (valid for both the reference domain and for each single element). However, since the scattering term involves all discrete ordinates, the bandwidth of $\mathbf{L}$ is in the S_N case relatively larger than in the P_N case. Figure 2.1 displays the algebraic structure of the matrices resulting from the spectral element formulation with the same discretization parameters for the equivalent P_5 and S_6 models [Bell and Glasstone, 1970], except for the boundary conditions.

Figure 2.1

2.1.3 Results

The spectral element results are compared to selected manufactured solutions, appropriate to isolate the convergence error from the approximation error of the model [Barbarino et al., 2014]. In these comparisons the exact solution of each transport approximation is thus known, allowing to appreciate the numerical features of the scheme in a clear way. Comparisons with other schemes [Lewis and Miller, 1993], namely diamond difference discrete ordinates (DD) and finite difference spherical harmonics (FD), can help in evaluating the advantages in the use of spectral elements. Furthermore, also some physically significant configurations are considered, and results are compared to available analytic solutions.

In order to quantify the discrepancy between the reference solution for the angular flux $\psi(x,\mu)$ and the total flux $\Phi(x)$ (be it determined through manufactured or analytical solution) against a numerical calculation that yields the solution for $\hat{\Phi}$ and $\hat{\psi}$ only at the given spatial grid nodes x_i, four different error definitions are introduced:

$$\delta(x_i) = \text{abs}\left[\Phi(x_i) - \hat{\Phi}(x_i)\right], \tag{2.8a}$$

$$\varepsilon(x_i) = \frac{\text{abs}\left[\Phi(x_i) - \hat{\Phi}(x_i)\right]}{\Phi(x_i)}, \tag{2.8b}$$

$$\Xi = \sqrt{\frac{\sum_i \left(\Phi(x_i) - \hat{\Phi}(x_i)\right)^2}{\sum_i \left[\Phi(x_i)\right]^2}}, \tag{2.8c}$$

$$\xi(\mu) = \sqrt{\frac{\sum_i \left(\psi(x_i,\mu) - \hat{\psi}(x_i,\mu)\right)^2}{\sum_i \left[\psi(x_i,\mu)\right]^2}}. \tag{2.8d}$$

Beside the classical absolute and relative errors δ and ε, the discrete L_2 norms Ξ and ξ are also used, as indicators of the performances of a method on a global rather than a pointwise scale [Deville et al., 2002].

Benchmarks using manufactured solutions

Exact solutions can be manufactured by determining the source that produces a given angular flux. This can be easily done by direct substitution into the transport equation if the flux is assumed to be given by an analytic expression [Warsa et al., 2010]. Such manufactured solutions constitute useful references to test the performance of numerical methods by direct comparisons. It is worth noticing that, given a manufactured solution to the transport problem, the associated source may turn out to be not physically meaningful (i.e., it may take negative values over the phase domain). Therefore, these exercises may only be regarded as useful tools to verify and assess the algorithm being studied.

In the following, for all cases presented and unless specified, the number of secondary neutrons per collision c is assumed to be 0.5.

The first manufactured solution adopted in the present work is the following:

$$\psi_1(x,\mu) = f(x)\,g(\mu) = \left(1-x^2\right)^2\left(1+3\mu^2\right), \tag{2.9}$$

over the spatially homogeneous domain $x \in [-1,1]$, $\mu \in [-1,1]$ characterized by a unitary cross section. By direct substitution into the one dimensional transport equation in the form (1.12), one can easily find out the source to be assumed in order to produce such a solution is:

$$S_1(x,\mu) = -4x\left(1-x^2\right)\mu + \Sigma(1-c)\left(1-x^2\right)^2. \tag{2.10}$$

The angular flux is factorized into a space and an angular polynomial factors (see Figure 2.2, where the source is also represented graphically). As far as the space part is concerned, *Figure 2.2*

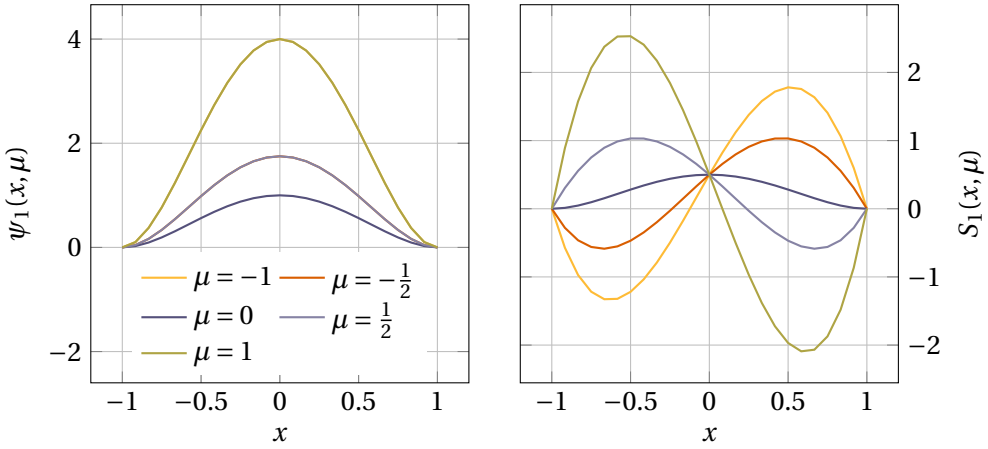

(a) Angular flux (b) Source

Figure 2.2: Left: the manufactured solution $\psi_1(x,\mu)$ for some values of the direction μ ($\mu = \pm 1$ and $\mu = \pm\frac{1}{2}$ are indistinguishable). Right: the source term $S_1(x,\mu)$ of (1.12) which reproduces $\psi_1(x,\mu)$.

the function ψ_1 is expected to be an easy benchmark for every scheme based on spatial polynomial interpolation (like SEM), since it is represented exactly also in the approximation space. For the angular part, a polynomial nature assures that the number of angular moments necessary for its representation is limited. One can then foresee that for certain schemes the error should drop close to round-off, thus allowing a further check for implementation mistakes.

It is easy to verify that the boundary conditions can be set indifferently to homogeneous Dirichlet ($\varphi_\ell(x = \pm 1) = 0, \forall \ell$) or to homogeneous Neumann ($\mathrm{d}\varphi_\ell / \mathrm{d}x(x = \pm 1) = 0, \forall \ell$). For practical purposes, homogeneous Neumann boundary conditions are preferred since they turn out to be simpler then in the Dirichlet case for the assembly of the operators, as explained in the previous sections. In the Dirichlet case, indeed, one has to prune the matrices by two rows and two columns.

Calculations are performed using both P_N and S_N methods (up to P_7 and S_8). For each scheme and each approximation, L_2-type errors are calculated for grids with an increasing number κ of nodes (equally spaced for the S_N DD scheme, and aligned to the GLL quadrature grid for S_N SEM), which can be assumed as a measure of the computational burden associated to the scheme. For SEM schemes, one can easily retrieve the order κ of the Lagrange polynomials used, since $K = \kappa - 1$ for one dimensional domains. Results for the angular flux at $\mu = 0.5$ are reported in Table 2.1. For the discrete ordinate approach an interpolation procedure is needed to reconstruct the solution at the required direction. Details on the angular flux reconstruction are given in Barbarino et al. [2014].

Table 2.1

As expected, the SEM S_N results are all at double precision round-off level even at the lowest order S_2, since this manufactured solution is polynomial as the SEM interpolating functions. Slight increases in the values observed throughout Table 2.1 are only due to error

Table 2.1: Errors ξ for different numerical schemes, as compared to the manufactured solution ψ_1. The direction of neutrons is fixed to $\mu = 0.5$.

	SEM		DD	FD	SEM		DD	FD
κ	S_2	P_1	S_2	P_1	S_4	P_3	S_4	P_3
5	5.006E-16	2.226E-01	7.799E-02	1.970E+00	9.011E-16	1.022E-15	7.905E-02	1.814E+00
7	5.120E-16	2.213E-01	4.160E-02	1.153E+00	5.895E-16	6.003E-16	4.217E-02	1.052E+00
9	2.096E-15	2.205E-01	2.561E-02	7.403E-01	1.855E-15	2.697E-15	2.596E-02	6.758E-01
11	2.483E-15	2.200E-01	1.729E-02	5.314E-01	5.286E-16	2.301E-15	1.753E-02	4.868E-01
13	4.804E-15	2.197E-01	1.244E-02	4.202E-01	1.933E-15	1.064E-14	1.262E-02	3.871E-01
15	2.350E-15	2.194E-01	9.373e-03	3.591E-01	1.994E-15	3.257E-15	9.506E-03	3.331E-01
21	3.079E-15	2.190E-01	4.804E-03	2.942E-01	8.397E-15	3.518E-15	4.872E-03	2.773E-01

	SEM		DD	FD	SEM		DD	FD
κ	S_6	P_5	S_6	P_5	S_8	P_7	S_8	P_7
5	8.638E-16	1.238E-15	7.913E-02	1.814E+00	3.267E-16	4.288E-16	7.914E-02	1.819E+00
7	6.907E-16	1.193E-15	4.222E-02	1.053E+00	7.702E-16	5.590E-16	4.223E-02	1.060E+00
9	3.932E-16	3.778E-15	2.600E-02	6.764E-01	4.800E-16	3.234E-15	2.600E-02	6.833E-01
11	2.252E-15	3.740E-15	1.756E-02	4.871E-01	7.291E-16	2.374E-15	1.756E-02	4.939E-01
13	1.039E-15	4.347E-15	1.263E-02	3.872E-01	2.677E-15	5.613E-15	1.264E-02	3.940E-01
15	1.736E-15	5.545E-15	9.519E-03	3.329E-01	3.089E-15	3.304E-15	9.520E-03	3.399E-01
21	4.817E-15	7.246E-15	4.879E-03	2.766E-01	5.162E-15	7.060E-15	4.880E-03	2.839E-01

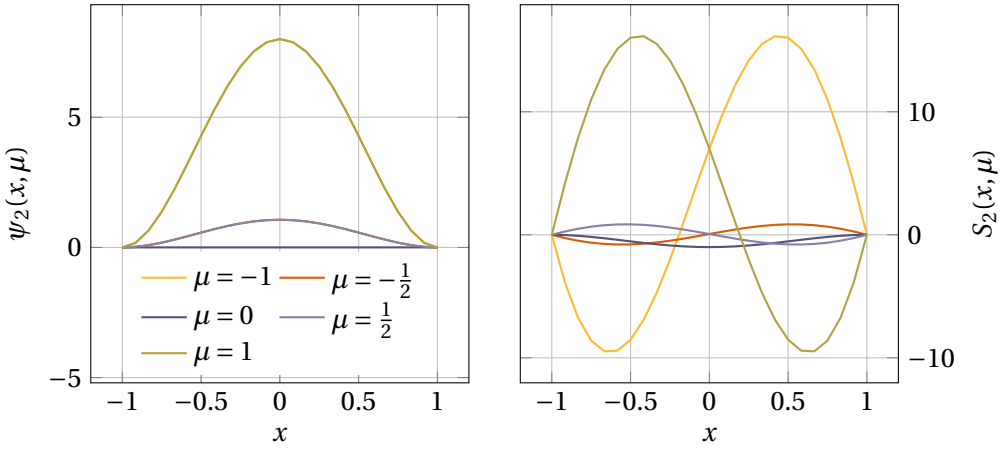

(a) Angular flux.

(b) Source.

Figure 2.3: Left: the manufactured solution $\psi_2(x,\mu)$ for some values of the direction μ ($\mu = \pm 1$ and $\mu = \pm\frac{1}{2}$ are indistinguishable). Right: the source term $S_2(x,\mu)$ of (1.12) which reproduces $\psi_2(x,\mu)$.

accumulation. The P_1 model fails to correctly represent the solution because, obviously, the quadratic angular part cannot be resolved by truncating the angular expansion to the first order. Table 2.1 clearly shows that SEM schemes outperform DD, which in turn has a much better performance when compared to FD on the same grid.

Figure 2.3

The second manufactured solution adopted is still factorized but no more polynomial in space, having the following form (see also Figure 2.3):

$$\psi_2(x,\mu) = f(x)\,g(\mu) = \left(1-x^2\right)^2 \exp\left(-0.2x^2\right)\left(3\mu^2+5\mu^4\right), \tag{2.11}$$

over the spatially homogeneous domain $x \in [-1,1]$, $\mu \in [-1,1]$ characterized by a unitary cross section. The corresponding source is the following:

$$S_2(x,\mu) = \exp\left(\frac{x^2}{5}\right)\left(1-x^2\right)\times \left\{\frac{2}{5}x\mu\left(3\mu^2+5\mu^4\right)\left(x^2-11\right)+\left(1-x^2\right)\left[\Sigma\left(3\mu^2+5\mu^4\right)-2c\Sigma\right]\right\}. \tag{2.12}$$

Both factors defining the flux belong to C^∞, hence one expects to obtain more accurate spatial results by increasing the number of the basis polynomials used. All ξ errors are shown in Table 2.2.

Table 2.2

In this case, the S_2-P_1 models cannot handle the quartic behavior with respect to the angular variable. Results can be improved only by increasing the order of the angular approximation; for sufficiently high-order angular models, by increasing the order of the spatial approximation (up to 21 grid points), SEM results can again be pushed to round-off levels for both P_N and S_N. On the other hand, standard discretization schemes show a much slower convergence rate (second-order for DD, first-order for FD).

Table 2.2: Errors ξ for different numerical schemes, as compared to the manufactured solution ψ_2. The direction is $\mu = 0.5$.

	SEM		DD	FD	SEM		DD	FD
κ	S_2	P_1	S_2	P_1	S_4	P_3	S_4	P_3
5	3.487E-01	5.145E-01	3.396E-01	5.713E-00	3.553E-02	8.013E-02	8.632E-02	3.986E+00
7	3.422E-01	5.443E-01	3.367E-01	3.303E-00	7.453E-04	5.321E-02	4.479E-02	2.157E+00
9	3.420E-01	5.425E-01	3.362E-01	2.286E-00	1.127E-05	5.285E-02	2.273E-02	1.284E+00
11	3.420E-01	5.416E-01	3.361E-01	1.861E-00	1.330E-07	5.265E-02	1.830E-02	8.456E-01
13	3.419E-01	5.405E-01	3.361E-01	1.672E-00	1.279E-09	5.251E-02	1.313E-02	6.052E-01
15	3.419E-01	5.399E-01	3.361E-01	1.580E-00	1.037E-11	5.241E-02	9.870E-03	4.650E-01
21	3.418E-01	5.389E-01	3.362E-01	1.489E-00	1.452E-14	5.221E-02	5.043E-03	2.980E-01

	SEM		DD	FD	SEM		DD	FD
κ	S_6	P_5	S_6	P_5	S_8	P_7	S_8	P_7
5	3.656E-02	3.656E-02	8.802E-02	2.702E+00	3.697E-02	3.697E-02	8.891E-02	2.862E+00
7	7.631E-04	7.631E-04	4.571E-02	1.391E+00	7.738E-04	7.738E-04	4.616E-02	1.471E+00
9	1.146E-05	1.146E-05	2.783E-02	7.824E-01	1.160E-05	1.160E-05	2.810E-02	8.221E-01
11	1.345E-07	1.345E-07	1.870E-02	4.968E-01	1.358E-07	1.358E-07	1.887E-02	5.134E-01
13	1.290E-09	1.290E-09	1.340E-02	3.619E-01	1.299E-09	1.299E-09	1.353E-02	3.640E-01
15	1.044E-11	1.044E-11	1.008E-02	3.048E-01	1.049E-11	1.050E-11	1.017E-02	2.978E-01
21	7.370E-15	9.654E-15	5.150E-03	2.886E-01	7.303E-15	9.764E-15	5.199E-03	2.754E-01

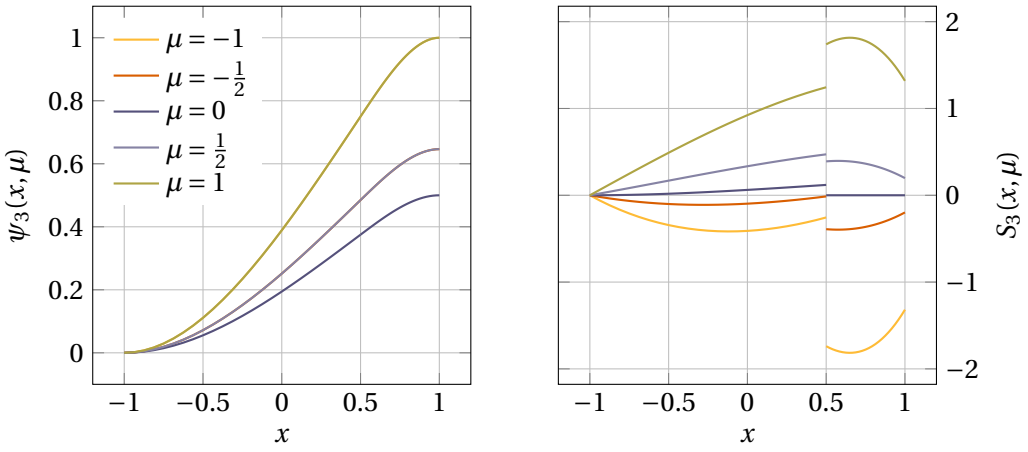

(a) Angular flux. (b) Source.

Figure 2.4: Left: the manufactured solution $\psi_3(x,\mu)$ for some values of the direction μ ($\mu = \pm 1$ and $\mu = \pm\frac{1}{2}$ are indistinguishable). Right: the source term $S_3(x,\mu)$ of (1.12) which reproduces $\psi_3(x,\mu)$.

The last manufactured solution considered belongs only to C^2 as far as its space behavior is concerned, and to C^∞, although not polynomial, with respect to the angular variable. However, in a spatial sub-domain the space function is assumed to be polynomial. This feature of the spatial dependence is an expedient adopted to assess the behavior of the solver when dealing with a non-Taylor-expandable function, which is a particularly severe test case for any quadrature rule based upon polynomial interpolation. Moreover, the domain is composed by a single element, simulating a case when the mesh is not sufficiently accurate to isolate regions with high smoothness.

Even if the physical significance of this function is questionable, it is worth noting that it lies on the solution space of the original transport model (the even parity model requires also the continuity of the second derivative of the solution) and, as such, it is definitely a valid neutron transport solution. Its analytical form is:

$$\psi_3(x,\mu) = \left[2 - \cos\left(\frac{\pi\mu}{2}\right)\right]\left[\left(-\frac{1}{18}x^3 + \frac{1}{12}x^2 + \frac{1}{3}x + \frac{7}{36}\right)\theta\left(\frac{1}{2} - x\right) + \left(-\frac{1}{2}x^3 + \frac{3}{4}x^2 + \frac{1}{4}\right)\theta\left(x - \frac{1}{2}\right)\right] \tag{2.13}$$

over the spatially homogeneous domain $x \in [-1,1]$, $\mu \in [-1,1]$ characterized by a unitary cross section, as usual; symbol θ stands for the Heaviside step function. The space and angular factors are shown in Figure 2.4, where also the source given by the following analytical formula is drawn as:

Figure 2.4

$$S_3(x,\mu) = S_3^L(x,\mu)\,\theta\left(\frac{1}{2} - x\right) + S_3^R(x,\mu)\,\theta\left(x - \frac{1}{2}\right), \tag{2.14}$$

Table 2.3: Errors ξ for the case of the manufactured solution ψ_3: only SEM results are reported. The direction is $\mu = 0.5$.

κ	S_2	S_4	S_6	S_8	S_{10}	S_{12}	S_{14}
6	8.189E-2	2.335E-3	3.234E-3	3.237E-3	3.235E-3	3.234E-3	3.234E-3
11	8.453E-2	2.138E-3	5.887E-4	5.769E-4	5.755E-4	5.748E-4	5.743E-4
16	8.386E-2	1.657E-3	1.276E-4	1.338E-4	1.335E-4	1.333E-4	1.337E-4
21	8.379E-2	1.688E-3	3.965E-5	4.502E-5	4.499E-5	4.494E-5	4.490E-5
31	8.371E-2	1.700E-3	1.230E-5	1.496E-5	1.499E-5	1.498E-5	1.497E-5
41	8.367E-2	1.713E-3	2.070E-5	8.207E-6	8.147E-6	8.143E-6	8.141E-6
51	8.363E-2	1.704E-3	1.236E-5	2.347E-6	2.384E-6	2.383E-6	2.382E-6
76	8.359E-2	1.704E-3	1.304E-5	8.019E-7	8.508E-7	8.507E-7	8.505E-7
101	8.357E-2	1.704E-3	1.409E-5	5.626E-7	5.050E-7	5.047E-7	5.045E-7

where

$$S_3^L(x,\mu) = \mu\left[\frac{x}{6}(1-x)+\frac{1}{3}\right]\left[2-\cos\left(\frac{\pi\mu}{2}\right)\right]+\left(\frac{7}{36}+\frac{x}{3}+\frac{x^2}{12}-\frac{x^3}{18}\right)\times \left\{\Sigma\left[2-\cos\left(\frac{\pi\mu}{2}\right)\right]-2\Sigma_s\left(1-\frac{1}{\pi}\right)\right\},$$

and

$$S_3^R(x,\mu) = \mu\left[\frac{3}{6}x(1-x)\right]\left[2-\cos\left(\frac{\pi\mu}{2}\right)\right]+\left(\frac{1}{4}+\frac{3}{4}x^2-\frac{x^3}{2}\right)\times \left\{\Sigma\left[2-\cos\left(\frac{\pi\mu}{2}\right)\right]-2\Sigma_s\left(1-\frac{1}{\pi}\right)\right\}.$$

Results obtained with SEM are presented in table 2.3 only for S_N calculations, since the numerical equivalence with the P_N scheme has already been established in the previous examples. The spatial convergence rate is dropping to about order three. It is again very interesting to compare the results with the two classical approaches, as can be seen in table 2.4, for the S_8 model. The convergence rate for the SEM is now quite close to the one observed with diamond differences (the finite difference scheme soon reaches saturation), but the absolute value of the error stands two orders of magnitude below. The point-wise spatial error is reported in 2.5; as expected, it decreases with an increasing order of the SEM scheme and it maintains about the same magnitude throughout the domain, even though some difficulties seem to appear close to the boundaries.

Table 2.3 *Table 2.4* *Figure 2.5*

One-dimensional analytical periodic problem

The domain is constituted by an infinite homogeneous material in planar symmetry, injected by a spatially periodic step function source. The period is assumed to be 7.5 m.f.p. and the source is isotropic, constant and unitary over a thickness of 2.5 m.f.p. This physical

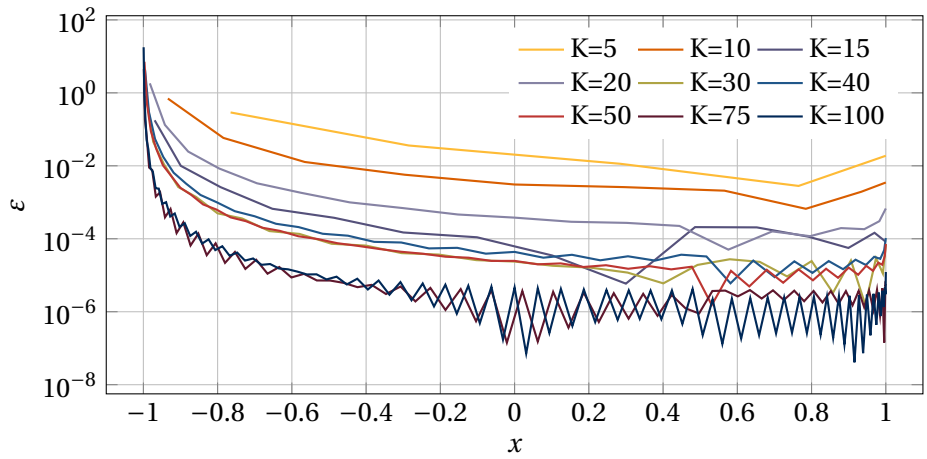

(a) Relative error ε.

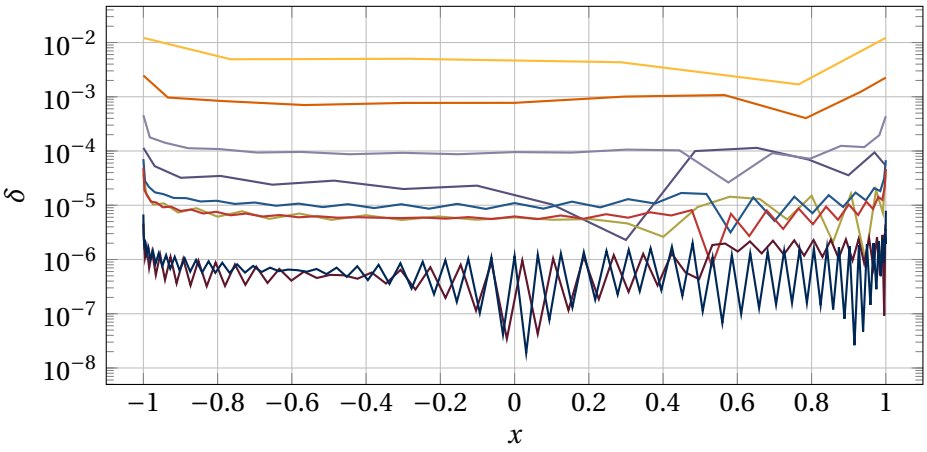

(b) Absolute error δ.

Figure 2.5: Spatial distribution of the relative and absolute errors on the scalar flux using SEM for the case of the manufactured solution ψ_3.

Table 2.4: Errors ξ for the SEM scheme, using the manufactured solution ψ_3: comparison with the classical schemes DD and FD. The direction is $\mu = 0.5$.

κ	S_8	S_8 DD	P_7 FD
6	3.237E-3	3.265E-1	1.832E-1
11	5.769E-4	3.820E-3	1.157E-1
16	1.338E-4	1.858E-3	1.189E-1
21	4.502E-5	1.096E-3	1.218E-1
31	1.496E-5	4.924E-4	1.258E-1
41	8.207E-6	2.860E-4	1.281E-1
51	2.347E-6	1.827E-4	1.295E-1
76	8.019E-7	8.271E-5	1.313E-1
101	5.626E-7	4.696E-5	1.323E-1

configuration recalls the well-known cell problem in reactor physics [Silva et al., 2013]. The analysis is carried out for different values of the number of secondaries per collision c.

The results presented are obtained by the SEM-P_N solver applied to the P_1, P_3, P_5 and P_7 models. As far as the reference calculations are concerned, two approaches are used. For P_1 and P_3, the fully analytic solutions to the equivalent A_1 and A_2 models have been determined in a preceding work by Barbarino [2010] and thus the results can be compared to the exact solution allowing to accurately evaluate the convergence rate of the numerical scheme. In order to check the results against the true transport solution, use is made of the exact transport Green function in the plane infinite medium [Case et al., 1953; Case and Zweifel, 1967], injected by an isotropic source spatially distributed as a periodic step function. Of course, one has to truncate the number of the step-function source contributions to be taken into account. However, the convergence rate of the procedure may be estimated by evaluating the role of the first neglected term.

Tables 2.5, 2.6 and 2.7 show the convergence in terms of the error Ξ for different values of the parameter c and for different polynomial orders for the SEM P_N solver. Comparisons between the SEM solution and the transport one are characterized by the error Ξ_{TR}; errors with respect to the analytic solution of the P_N model are indicated by Ξ_{AN}, in order to isolate the impact of the spatial discretization alone.

Table 2.5 *Table 2.6* *Table 2.7*

In all cases, except for the lowest orders which are considerably affected by the space approximation, Ξ errors are basically constant for increasing κ, for all values of c. The slight increase in the numerical values for some cases is due to the accumulation of numerical errors in the computation. This saturation in the resolution capabilities of the scheme is to be ascribed to the simplified transport model adopted; in fact, refining the angular detail considered by the formulation (thus increasing N), the asymptotic value of Ξ_{TR} decreases. As a further confirmation, Ξ_{AN} decreases very rapidly with increasing polynomial order, assuring that the SEM scheme adds only a negligible contribution to the error Ξ_{TR}. As theoretically expected, the reduction of the parameter c causes a subsequent reduction of the convergence speed for Ξ_{TR}, for the dominance of transport effects. Therefore, the results for the highly scattering cell reported in Table 2.7 are the closest to the real transport solu-

Table 2.5: Error Ξ for the periodic source problem using the P_N model; the number of secondaries per collision is $c = 0.1$.

	P_1		P_3		P_5	P_7
κ	Ξ_{TR}	Ξ_{AN}	Ξ_{TR}	Ξ_{AN}	Ξ_{TR}	Ξ_{TR}
5	3.205E-02	4.240E-03	1.522E-02	1.145E-02	1.617E-02	1.769E-02
7	3.886E-02	1.603E-04	1.469E-02	9.685E-04	7.851E-03	5.768E-03
9	4.111E-02	5.123E-06	1.737E-02	7.278E-05	9.597E-03	6.045E-03
11	4.173E-02	1.241E-07	1.845E-02	4.692E-06	1.085E-02	7.153E-03
13	4.197E-02	1.940E-08	1.883E-02	2.412E-07	1.140E-02	7.798E-03
15	4.209E-02	1.610E-08	1.899E-02	9.958E-09	1.163E-02	8.097E-03
21	4.225E-02	6.751E-09	1.914E-02	2.197E-13	1.182E-02	8.340E-03

Table 2.6: Error Ξ for the periodic source problem using the P_N model ($c = 0.5$).

	P_1		P_3		P_5	P_7
κ	Ξ_{TR}	Ξ_{AN}	Ξ_{TR}	Ξ_{AN}	Ξ_{TR}	Ξ_{TR}
5	2.783E-02	1.650E-03	9.819E-03	5.822E-03	9.309E-03	1.031E-02
7	3.216E-02	3.866E-05	1.079E-02	3.815E-04	5.301E-03	3.533E-03
9	3.323E-02	7.063E-07	1.240E-02	2.318E-05	6.512E-03	3.970E-03
11	3.354E-02	9.550E-09	1.295E-02	1.154E-06	7.234E-03	4.649E-03
13	3.367E-02	1.458E-10	1.314E-02	4.506E-08	7.525E-03	5.011E-03
15	3.375E-02	6.633E-11	1.322E-02	1.402E-09	7.642E-03	5.171E-03
21	3.386E-02	7.841E-11	1.331E-02	3.757E-14	7.742E-03	5.301E-03

tion. Not surprisingly, the same influence is found also when analyzing the fully numerical error Ξ_{AN}, indicating that, at least for this case, c has an effect also on the conditioning of the numerical scheme.

Figure 2.6 *Figure 2.7* The behavior of the spatial error is reported in 2.6 and 2.7, for $c = 0.1$ and $c = 0.9$ and the approximations P_1 and P_3. In the source-less region (5 m.f.p. thick, on the left in the graphs) the level of discrepancy is higher, with respect to the region where the source is located. Moreover, the spatial error distribution is not affected by the amount of scattering of neutrons.

2.1.4 Remarks on converge studies

This section has addressed the convergence properties of the Spectral Element Method applied to some standard transport models. In particular, the spherical harmonics and discrete ordinate formulations have been considered.

In all the cases examined, SEM applied to transport models confirms the high convergence rates which are postulated by the fundamental analysis with minor interactions with the type of transport problem, namely the amount of scattering in the medium. Lower

Table 2.7: Error Ξ for the periodic source problem using the P_N model ($c = 0.9$).

	P_1		P_3		P_5	P_7
κ	Ξ_{TR}	Ξ_{AN}	Ξ_{TR}	Ξ_{AN}	Ξ_{TR}	Ξ_{TR}
5	1.833E-02	7.340E-05	3.036E-03	9.100E-04	2.077E-03	2.319E-03
7	1.903E-02	3.660E-07	3.752E-03	4.645E-05	1.609E-03	9.530E-04
9	1.916E-02	1.338E-09	4.114E-03	2.177E-06	1.952E-03	1.134E-03
11	1.921E-02	3.638E-12	4.220E-03	7.955E-08	2.117E-03	1.306E-03
13	1.923E-02	6.529E-14	4.255E-03	2.250E-09	2.178E-03	1.389E-03
15	1.924E-02	4.884E-14	4.271E-03	5.034E-11	2.203E-03	1.424E-03
21	1.926E-02	6.408E-14	4.289E-03	3.824E-14	2.223E-03	1.451E-03

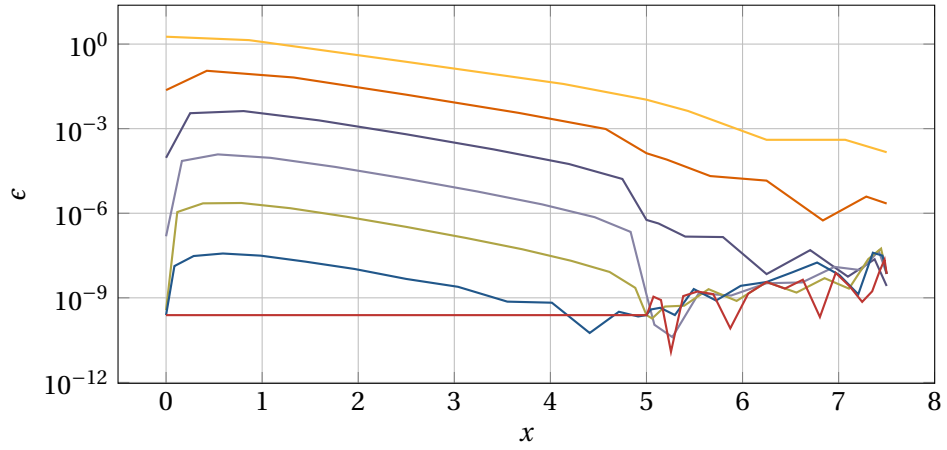

(a) P_1 approximation with $c = 0.1$.

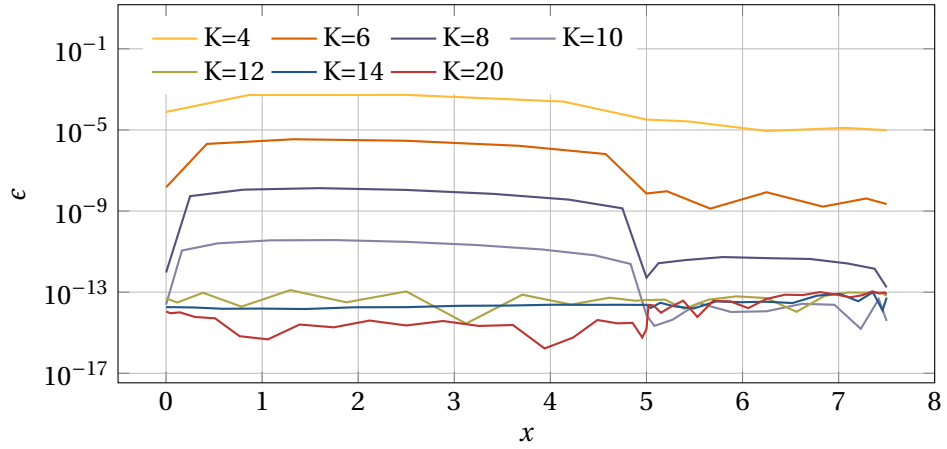

(b) P_1 approximation with $c = 0.9$.

Figure 2.6: Spatial relative errors $\epsilon(x_i)$ for the scalar flux of the periodic source problem, P_1 approximation.

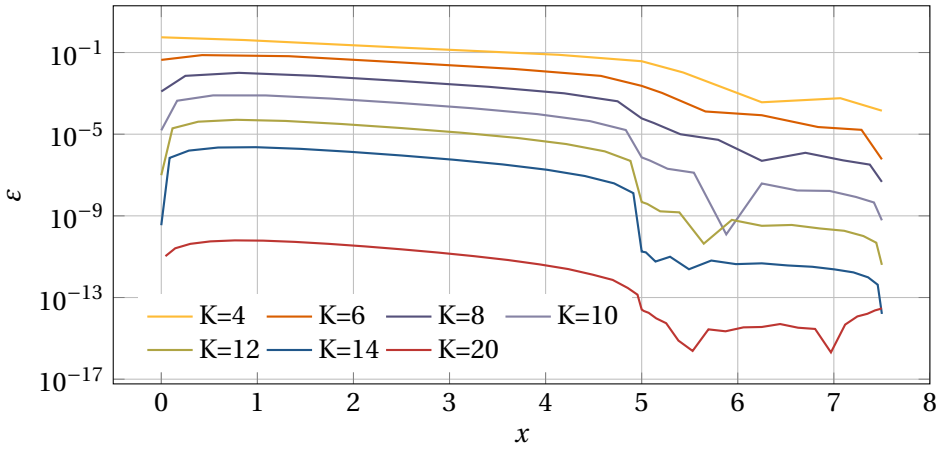

(a) P_3 approximation with $c = 0.1$.

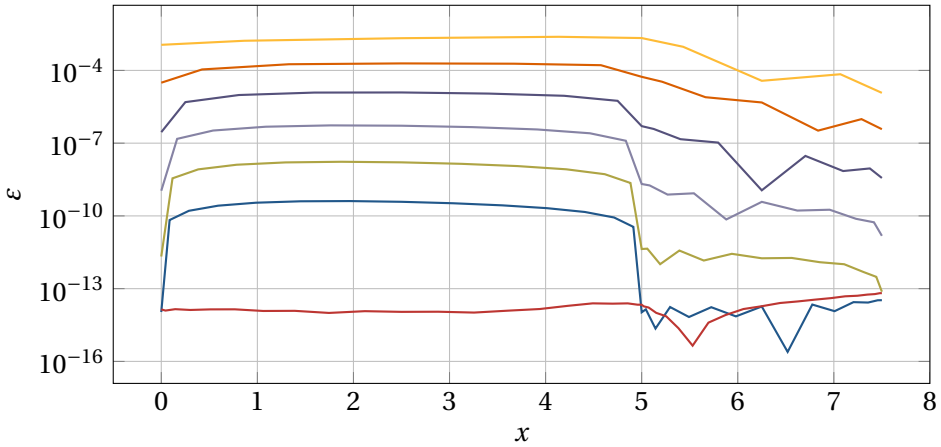

(b) P_3 approximation with $c = 0.9$.

Figure 2.7: Spatial relative errors for the periodic source problem, P_3 approximation.

values of c tend to slow down the convergence rate of the scheme, but this drawback is in common with all other combined angular/space discretizations since the mean free path of neutrons is numerically altered and, thus, the ability of a certain spatial mesh to correctly approximate the solution may be reduced. Moreover, as it is clear from the results, the high order polynomials and the automatic combined refinement of their order and the mesh size (endowed in the SEM structure) makes this aspect of less concern, becoming the angular discretization the weak point of the scheme.

In general, SEM outperforms low-order classical approximation schemes; its implementation is not shown explicitly in these pages, but can be inferred by the listings of the solver prepared to accomplish these studies: the scheme is close to a typical finite element solver, especially in this 1D case where, for both FEM and SEM, the pattern of the algebraic matrix can be easily foreseen and dedicated solution strategies are naturally implemented. This aspect is partially true also for higher dimensions, and this constitutes an advantage of SEM over FEM as it will be clear in what follows.

Concerning the applicability of this studies, they are basically numerical tests on idealized configurations aiming at checking and confirming a behavior more than giving practical results. Nonetheless, nowadays in industrial reactor analysis a number of calculation schemes still rely on one-dimensional analysis as in reflector calculations, fast shape reconstruction in transients and deep penetration problems for radiation protection. The SEM solver coded for this study could be used almost as it is in this framework.

2.2 On the way to local refinement: the Discontinuous Galerkin approach

In this part of the work the SEM approach is applied to the A_N approximation to multidimensional problems. Opposed to the developments that can be found in Barbarino [2010], the interfaces are treated with the Discontinuous Galerkin method (DG), which relaxes the grid continuity across the elements and allows, in perspective, a certain degree of local mesh refinement. This feature could be particularly relevant for the simulation of some advanced nuclear systems and for some instrumented assemblies in present light water reactors. Calculations on some benchmark cases are performed.

2.2.1 Discontinuous Galerkin approach

The main limitation deriving from the use of the Continuous Galerkin approach is the fact that all the elements of the domain are required to have the same number of degrees of freedom. In fact CG imposes the continuity of all the points of the trace of the solution on each interface; being the solution an interpolating function of nodal values, and being the basis the same, this immediately implies that the interface nodes must be coincident and carry the same value. The constraint on the same number of degrees of freedom in each mesh, regardless of its dimension, of the shape of the solution and of the behavior of the flux in that region, is a feature that limits the possibility to tailor the scheme to the physical problem and to optimize the computational effort.

The additional flexibility of the scheme allows the use of non-conformal grids and a free choice of the polynomial degree of the basis functions in each element. The final target should be to open the way to fully adaptive algorithms.

There are some techniques available to cope with such problems [Deville et al., 2002; Quarteroni, 2009]. One may cite the mortar patching, where particular sub-elements are created in order to "glue" several elements, or the overlapping Schwartz procedure, which are widespread in FEM applications and implemented in many codes.

In this work, the Discontinuous Galerkin method is introduced. The main difference stands in the fact that the function is no more compelled to be continuous on the interfaces; indeed, an integral relation joins the solution. Some details are given, in order to help in the interpretation of the results; for a complete derivation of the method and the associated properties one can refer to Rivière [2008] or Quarteroni [2009]. This approach, thanks to recent achievements in the consolidation of the knowledge of its convergence and stability, is a prominent candidate for next generation FEM industrial codes.

Some advantages of DG compared to CG approaches

A non-exhaustive list of advantages and disadvantages of the DG method compared to the CG approach previously used may be drawn from literature (especially from Rivière [2008]):

Hanging nodes In CG, sides touch sides and vertices touch only vertices. In DG, the vertex of an element may lie on the side of a neighboring element, thanks to the additional integral interface terms in the weak form.

Polynomial degree and basis functions It is relatively easy to implement a code where the polynomial degree of each element is chosen arbitrarily, or possibly with a refinement algorithm, and it is also possible to combine different basis functions or even different approximation schemes (SEM and FEM mixed grids, even with triangular elements).

Mass conservation It can be demonstrated that DG assures the conservation of the number of neutrons in each cell, property that is an appreciated feature of the Finite Volume Method, reason why all current nodal methods for full core and pin-by-pin analysis are based [Tomatis, 2010]. Continuous Galerkin can only guarantee a conservation in the entire calculation domain. Thus, higher accuracy in the computation of reaction rates is expected from DG.

Number of degrees of freedom For SEM tensorial grids the number of degrees of freedoms may be higher or lower than in the CG case. If the polynomial degree is the same in the two cases (and thus is the same in the whole grid), the interface unknowns superimpose spatially in the DG case, but their value do not. Thus, they are represented by two distinct nodes, and the algebraic set should have equations to describe them. So, in this case DG requires more computational effort. Anyway, if the polynomial degree is lowered in some elements, the balance may turn favorable.

Variational formulation of an elliptic problem in DG

Some basic concepts about the DG method are illustrated using the diffusion equation as elliptic model problem. The extension to A_N and other general second order differential transport models is straightforward and it is carried out in the following sections.

The DG approach accepts jumps of the function at the inner interface between elements. This is attained by adding some terms to the original variational form of the problem in equation (1.99). Let a general second-order model problem be

$$\begin{cases} -\nabla\left(D(\boldsymbol{r})\nabla\Phi\right)+\Sigma\Phi=f & \boldsymbol{r}\in\Omega, \\ \Phi=g_D & \boldsymbol{r}\in\Gamma^D, \\ D(\boldsymbol{r})\nabla\Phi\cdot\boldsymbol{n}=g_N & \boldsymbol{r}\in\Gamma^N. \end{cases} \tag{2.15}$$

The nomenclature has already been introduce in chapter 1. Dirichlet boundaries are consistently solved by the DG approach with the usual shift procedure [Quarteroni, 2009]; anyway they will not be considered in the following developments, nor in the solver implementation, because of their little interest in direct transport calculations, meaning an imposed flux on the boundary.

The weak form of the problem turns out to be

$$\int_\Omega \left(D\nabla\Phi\cdot\nabla v+\Sigma\Phi v\right)=\int_\Omega fv+\int_{\Gamma^N} v, \quad \forall v\in H^1(\Omega). \tag{2.16}$$

Function Φ, from now on, denotes the weak solution to problem (2.15), and its existence and uniqueness can be proven verifying that the weak problem satisfies the hypotheses of the Lax-Milgram theorem [Quarteroni, 2009; Rivière, 2008].

Restricting for simplicity to 2 dimensions, Ω is then subdivided into E quadrilateral elements Ω_e, globally forming the meshed domain Ω_E

$$\Omega=\bigcup_{e=1}^{E}\Omega^e, \tag{2.17}$$

which should be regular by construction[1]. The approximation space $\mathbb{V}$ is a broken Sobolev space rigorously defined by

$$\mathbb{V}\equiv H^s(\Omega_E)=\left\{v\in L^2(\Omega):\forall E\in\Omega_E, v|_E\in H^s(E)\right\}. \tag{2.18}$$

This choice do not pose constraints on the continuity of the functions across the elements, so they are let free to be discontinuous outside each element E.

[1] In FEM jargon, a regular mesh implies that, if h_E is the diameter of the element E and ρ_E is the maximum diameter of all circles inscribed in E, there exists a constant $\rho>0$ such that

$$\forall E\in\Omega_E, \quad \frac{h_E}{\rho_E}\leq\rho.$$

On the external boundary of Ω, say $\partial\Omega$, one assumes the existence of a set of non-overlapping curves $\Gamma_j^{(N)}$, $j = 1,\dots,N_N$ where Neumann or Robin boundary conditions apply. The union of all these curves (of course, in more dimensions they are surfaces) covers the whole external boundary, as:

$$\partial\Omega = \left(\bigcup_{j=1}^{N_N} \Gamma_j^{(N)}\right). \tag{2.19}$$

The set of all interior edges Γ_i of Ω_E is indicated by Γ_h, each of them endorsed with a unit normal vector $\boldsymbol{n}_i$. The orientation of such vector is not significant for the edges in Γ_h, while conventionally it always points outward for the boundary edges belonging to $\partial\Omega$.

If a function v belongs to the approximation space $\mathbb{V}$, considering that it is allowed to be discontinuous on each edge, in the simpler case[2] there are two traces of v on each interface Γ_i. Naming them $v^+_{\Gamma_i}$ and $v^-_{\Gamma_i}$, it is possible to define the *average* of v on Γ_i as

$$\{v\}_{\Gamma_i} = \frac{1}{2}v^+_{\Gamma_i} + \frac{1}{2}v^-_{\Gamma_i}, \tag{2.20a}$$

where the sign + or − is attributed to each section of v according to the orientation of the normal to Γ_i; similarly the jump is

$$[v]_{\Gamma_i} = v^+_{\Gamma_i} - v^-_{\Gamma_i}. \tag{2.20b}$$

On the boundary there is just one trace, but both the average and the jump are conventionally defined as

$$\{v\}_{\Gamma_i^{(N)}} = [v]_{\Gamma_i^{(N)}} = v^-_{\Gamma_i^{(D,N)}} \tag{2.20c}$$

in order to use a consistent notation for all edges.

Assuming now $s > 3/2$ in (2.18), it is possible to introduce the two bilinear forms $J_0^{\sigma_0,\beta_0}$ and $J_1^{\sigma_1,\beta_1}$ with values in $H^s(\Omega_E)\times H^s(\Omega_E)\to\mathbb{R}$ acting as penalty operators on the averages and jumps of both function v and derivatives:

$$J_0^{\sigma_0}(v,w) = \sum_{\Gamma_i\in\Gamma_h} \frac{\sigma_i^0}{|\Gamma_i|}\int_{\Gamma_i}[v][w], \tag{2.21a}$$

$$J_1^{\sigma_1}(v,w) = \sum_{\Gamma_i\in\Gamma_h} \frac{\sigma_i^1}{|\Gamma_i|}\int_{\Gamma_i}[D(\boldsymbol{r})\nabla v\cdot\boldsymbol{n}_i][D(\boldsymbol{r})\nabla w\cdot\boldsymbol{n}_i], \tag{2.21b}$$

where σ_i^0 and σ_i^1 are called penalty parameters, while $|\Gamma_i|$ stands for the length of side Γ_i.

The DG bilinear form $a_\epsilon : H^s(\Omega_E)\times H^s(\Omega_E)\to\mathbb{R}$:

$$a_\varepsilon(v,w) = \sum_{e=1}^{E}\left(\int_{\Omega_e} D(\boldsymbol{r})\nabla v\cdot\nabla w + \int_{\Omega_e}\Sigma v w\right) - \sum_{\Gamma_i\in\Gamma^h}\int_{\Gamma_i}\{D(\boldsymbol{r})\nabla v\cdot\boldsymbol{n}_i\}[w]$$
$$+\epsilon\sum_{\Gamma_i\in\Gamma_h}\int_{\Gamma_i}\{D(\boldsymbol{r})\nabla w\cdot\boldsymbol{n}_i\}[v] + J^{\sigma_i^1}(v,w) + J_1^{\sigma_i^1}(v,w) \tag{2.22}$$

[2] This is the case of conformal grids, without hanging nodes. In case of non conformal grids this argument can be extended.

The parity parameter ϵ may assume values -1,0 or $+1$. In the first case, a_ϵ is symmetric ans so will be the algebraic system obtained from its discretization. The linear form $L(v) := H^s(\Omega) \to \mathbb{R}$ is defined as:

$$L(v) = \int_\Omega f v + \sum_{\Gamma_i \in \Gamma^N} v g_N. \tag{2.23}$$

All the integrals in (2.22) and (2.23) make sense thanks to the Chauchy-Schwarz inequality and trace inequalities [Rivière, 2008; Quarteroni, 2009], provided $s > 3/2$ as already stated. Then, the general DG variational formulation for problem (2.15) is

$$\text{Find}\, \Phi \in \mathbb{V} := H^s(\Omega_E),\ s > 3/2 \ \text{ such that } \ \forall v \in \mathbb{V},\ a_\epsilon(\Phi, v) = L(v) \tag{2.24}$$

A DG-SEM scheme to solve A_N equations

A DG variational formulation can be easily derived using the original istropic model (1.55), the functionals (2.22) and (2.23) combined with proper boundary conditions. The derivative penalty term (2.21b) is typically considered of lower order with respect to (2.21a), then σ_i^1 is set to zero for any interface. After the choice of a suitable meshing Ω_E, one obtains:

$$\begin{aligned}
&\sum_{e=1}^{E} \int_{\Omega_e} \frac{\mu_\alpha^2}{\Sigma(\boldsymbol{r})} \nabla\varphi_\alpha(\boldsymbol{r}) \cdot \nabla\theta(\boldsymbol{r})\, \mathrm{d}\boldsymbol{r} - \sum_{i=1}^{N_N} \int_{\Gamma_i} \frac{\mu_\alpha^2}{\Sigma(\boldsymbol{r})} \theta(\boldsymbol{r}) \frac{\partial\varphi_\alpha(\boldsymbol{r})}{\partial \boldsymbol{n}}\, \mathrm{d}s + \sum_{e=1}^{E} \int_{\Omega_e} \Sigma(\boldsymbol{r})\varphi_\alpha(\boldsymbol{r})\theta(\boldsymbol{r})\, \mathrm{d}\boldsymbol{r} - \\
&\quad \sum_{\beta=1}^{N} w_\beta \sum_{e=1}^{E} \int_{\Omega_e} \Sigma_s(\boldsymbol{r})\varphi_\beta(\boldsymbol{r})\theta(\boldsymbol{r})\, \mathrm{d}\boldsymbol{r} - \sum_{j=1}^{N_h} \int_{\Gamma_j} \frac{\mu_\alpha^2}{\Sigma(\boldsymbol{r})} \{\nabla\varphi_\alpha(\boldsymbol{r}) \cdot \boldsymbol{n}_i|_{\Gamma_j}\} [\theta(\boldsymbol{r})|_{\Gamma_j}]\, \mathrm{d}s + \\
&\quad \epsilon \sum_{j=1}^{N_h} \int_{\Gamma_j} \frac{\mu_\alpha^2}{\Sigma(\boldsymbol{r})} \{\nabla\theta(\boldsymbol{r}) \cdot \boldsymbol{n}_i|_{\Gamma_j}\} [\varphi_\alpha(\boldsymbol{r})|_{\Gamma_j}]\, \mathrm{d}s + \sum_{j=1}^{N_h} \frac{\sigma_i^0}{|\Gamma_j|} \int_{\Gamma_j} [\varphi_\alpha(\boldsymbol{r})|_{\Gamma_j}] [\theta(\boldsymbol{r})|_{\Gamma_j}]\, \mathrm{d}s = \\
&\quad \sum_{e=1}^{E} \int_{\Omega_e} S(\boldsymbol{r})\theta(\boldsymbol{r})\, \mathrm{d}\boldsymbol{r} + \sum_{i=1}^{N_N} \int_{\Gamma_i} \theta(\boldsymbol{r}) g_i^{(N)}\, \mathrm{d}s, \qquad \forall \alpha = 1, 2, \ldots, N.
\end{aligned} \tag{2.25}$$

This is the form to be implemented in solvers, though the scheme already used for one and two-dimensional computations in chapter 1. In order to try and assemble a solver, the formula (2.25) has been further elaborated, in order to include the quadratures needed to evaluate each term. The next section deals with the algebraic details of this operation.

Implementation strategy

The main effort for the successful implementation of Eq. (2.25) clearly stands in the numerical approximation of (2.25) with its transformation into an associated linear system (to be properly stored and solved), once the basis has been defined.

Equation (2.25) defines each term of the matrix and of the right-hand-side of the system. Nonetheless, implementing each element as it is would waste much time in evaluating many terms which turn out to be null for the sparsity of the matrix, even introducing noise in case of cancellations. Moreover, space would be allocated also for null terms, reducing the amount of memory available for the solution algorithms, which are generally demanding in this sense, and further processing.

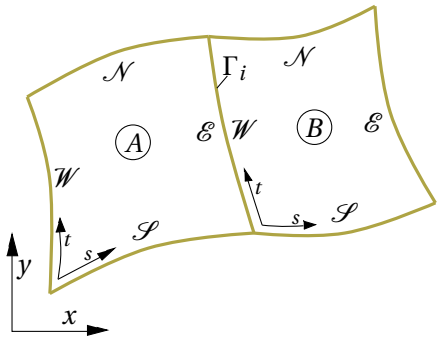

Figure 2.8: A schematic representaition of two adjacent elements A and B joined by the interface Γ_i, used in the derivation of the DG-SEM matrices.

It is recommended to elaborate the weak form and evaluate only the non vanishing terms, storing them in sparse form, for instance through the PETSc interface [Balay et al., 2013] used in this work. This practice is quite established in FEM, and it is even more required in SEM. Essentially, this is already done in the CG version [Barbarino, 2010] where the tensor product form of the SEM operators allow to build only the matrix blocks which are strictly needed; in addition, the quadrature formula is embedded into the reference operators.

In DG, the tensor form of the operators is lost, and with it goes the possibility to exploit some clever strategies for a fast assembly and numerical resolution of the system [Deville et al., 2002]. In what follows a strategy for the matrix construction is addressed: the DG weak form is fully developed using the SEM basis set and, again, the GLL formula for all quadratures[3], gaining an explicit representation of each single element of the matrix.

Inter-element terms The terms appearing in equation (2.25) are split into two categories. Setting ε and σ_i^0 to zero, one simply obtains the same expression used in CG in case of a single element problem with natural boundary conditions summed over all elements. Since the are no boundary adapted basis functions in the DG formulation, with their support strictly localized on a single element, the solution would be the union of single element solutions each one surrounded by an infinitesimally thin reflective wall. These terms then solve the problem using only the information about the element itself and neglecting any interaction with the adjacent ones.

The other contributions appearing in equation (2.25) are, according to the spatial dimensionality of the problem, line or surface integrals and include jumps and averages of both unknown and test functions.

Figure 2.8 For clarity, a simple example with two adjacent elements is introduced in Figure 2.8 and

[3] It is not compulsory to use the GLL formula also for the line quadratures on the edges. Using the same quadrature is advantageous when the grid is conformal, so there are not *hanging nodes*; in this case the nodal values on the trace corresponds to the boundary values of each node, thus no additional "service" nodes are needed. In case of adjacent edges with different lengths, the quadrature domain has to be scaled, and thus all nodes are evaluated by interpolation again: in this case the change of quadrature may be profitable, especially if the number of points to be interpolated is reduced.

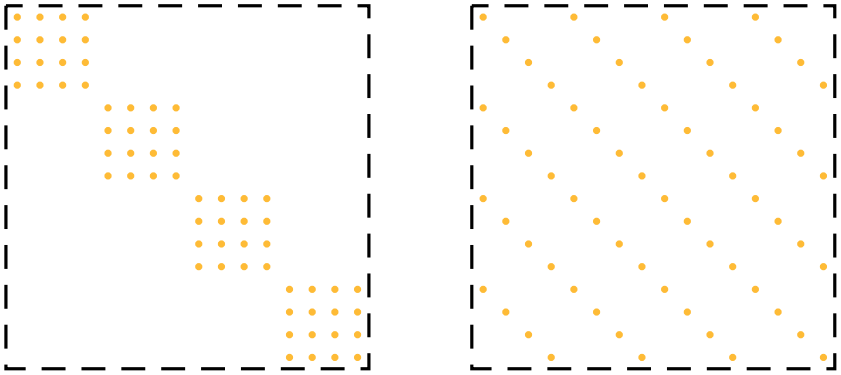

(a) Stiffness matrix (b) Mass matrix

Figure 2.9: Assembly of the algebraic matrix. Contribution of the inter-element terms associated to element A

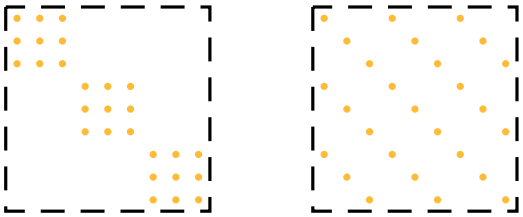

(a) Stiffness matrix (b) Mass matrix

Figure 2.10: Assembly of the algebraic matrix. Contribution of the inter-element terms associated to element A

will be used form now on. Matrices in Figures 2.9 and 2.10 are the stiffness and mass matrices coming out from the first part of the assembly in case element A is solved with SEM of order $K = 3$, while $K = 2$ holds for element B. *Figure 2.9* *Figure 2.10*

The first group of terms are treated exactly as it is done in CG case, defining reference stiffness and mass matrices, performing the integrals numerically and then going back to the physical element with the coordinate transformations (see section 1.2.3 and Barbarino [2010] for step-by-step instructions). As noted early, at the end of the process no direct stiffness summations is used, regardless of the presence of the superposition of the interfaces (and, even if nodes are superimposed, they are represented by different degrees of freedom in DG and in general they will be associated to different values of the solution). Each elemental matrix is then placed on the diagonal of the final assembly matrix, which will maintain this block structure even after the addition of the other DG terms. The right hand side follows the same rationale[4].

[4] In case of Dirichlet boundary conditions there would have been an additional term involving averages and jumps, requiring a special treatment. The outlined procedure could be easily adapted to include this term if needed.

Interface terms For all the other terms, it is necessary to expand both test and trial functions on the elemental basis and perform as many computations as possible on the reference element, following the idea of the general procedure outlined for the CG approach. The target is to find some matrix operators which will join the domains through the penalized discontinuous interface conditions; it will be evident that the terms concerning a single internal interface will populate with coefficients four blocks of the final matrix, two of them being on the block-diagonal. At the end of this section it will not seem possible to cast the coefficients found in the form of products of sub-matrices and vectors (at least without vectors of one non-null elements), nor this is the scope of the development. It will rather be found a set of handy specifications for the few lines and columns that are supposed to contain values, which is already of great interest for a sufficiently efficient implementation. All developments are in two dimensions, since this is the dimensionality of the problems which are managed by the companion DG-SEM solver written in the framework of the thesis.

For a generic interface Γ_i between the two elements A and B always of figure 2.8, the three terms of the weak form (2.25) not yet considered are:

$$T = -\int_{\Gamma_i} k\{\nabla\varphi\cdot\boldsymbol{n}_i\}\,[v] + \varepsilon\int_{\Gamma_i}\{k\nabla v\cdot\boldsymbol{n}_i\}\,[\varphi] + \frac{\sigma_i^0}{|\Gamma_i|}\int_{\Gamma_i}[\varphi]\,[v] \tag{2.26}$$

where k stands for μ_α^2/Σ and all α indexes and differentials are dropped for clarity.

Let it be $v(x,y)_A$ and $v(x,y)_B$ two generic basis functions belonging to the approximation spaces of element A and B respectively. Also, for clarity, the restriction of the solution to each element is indicated in the following by φ_A and φ_B; please remember that these two functions are both defined on the interface Γ_i at the same time with generally different values. Once the definitions of jumps and averages are substituted, the term T appears as the sum of four other terms in the 2D case, as:

$$T = m^{AA} + m^{BB} + m^{AB} + m^{BA}, \tag{2.27}$$

where, $\forall\, v_A, v_B$,

$$m^{AA} = -\frac{1}{2}\int_{\Gamma_i} k\nabla\varphi_A\cdot\boldsymbol{n}_i v_A + \frac{\varepsilon}{2}\int_{\Gamma_i} k\nabla v_A\cdot\boldsymbol{n}_i\varphi_A + \frac{\sigma_i^0}{|\Gamma_i|}\int_{\Gamma_i}\varphi_A v_A, \tag{2.28a}$$

$$m^{BB} = +\frac{1}{2}\int_{\Gamma_i} k\nabla\varphi_B\cdot\boldsymbol{n}_i v_B - \frac{\varepsilon}{2}\int_{\Gamma_i} k\nabla v_B\cdot\boldsymbol{n}_i\varphi_B + \frac{\sigma_i^0}{|\Gamma_i|}\int_{\Gamma_i}\varphi_B v_B, \tag{2.28b}$$

$$m^{AB} = -\frac{1}{2}\int_{\Gamma_i} k\nabla\varphi_B\cdot\boldsymbol{n}_i v_A - \frac{\varepsilon}{2}\int_{\Gamma_i} k\nabla v_A\cdot\boldsymbol{n}_i\varphi_B - \frac{\sigma_i^0}{|\Gamma_i|}\int_{\Gamma_i}\varphi_B v_A, \tag{2.28c}$$

$$m^{BA} = +\frac{1}{2}\int_{\Gamma_i} k\nabla\varphi_A\cdot\boldsymbol{n}_i v_B + \frac{\varepsilon}{2}\int_{\Gamma_i} k\nabla v_B\cdot\boldsymbol{n}_i\varphi_A - \frac{\sigma_i^0}{|\Gamma_i|}\int_{\Gamma_i}\varphi_A v_B. \tag{2.28d}$$

These terms represent the interactions between function and basis on the interface inside or across the elements. As they are tested against each basis function v_A and v_B, these terms bring four matrices $\mathbf{M}^{AA}$, $\mathbf{M}^{BB}$, $\mathbf{M}^{AB}$ and $\mathbf{M}^{BA}$; the number of rows and columns is

equal to the number of degrees of freedom in the first and the second element in superscript; regardless of the nature and the order, $\mathbf{M}^{AA}$ and $\mathbf{M}^{BB}$ are then always square matrices, representing the interaction of the values at the interface with the basis functions inside each element.

Up to this point the choice of the basis is not explicit, and the procedure will work also with FEM methods. As far as SEM is concerned, the basis functions used are always of tensor Lagrangian type

$$v_{ij}(x,y) = \chi_i(x)\chi_j(y), \tag{2.29}$$

where functions χ were already defined in section 1.2, equation (1.77) and they constitute also the basis for the expansion of the flux

$$\varphi(x,y) = \sum_{ij} \hat{\varphi}_{ij}\chi_i(x)\chi_j(y). \tag{2.30}$$

As for section 1.2, computations are preferably performed on a single reference element for each polynomial order K, whose coordinates are s and t and extend in the range $[-1,+1]$. Some other approaches for FEM elements, like Rivière [2008], tend at this point to calculate the value of the basis functions $\chi_i(x)$ and $\chi_j(y)$ at the interface, derive them where necessary, and then perform the integrals by means of quadrature formulas in order to transform them in linear combinations of the unknown coefficients $\hat{\varphi}_{ij}$. Indeed, for SEM typical Lagrange basis functions the re-construction and the derivation on curvilinear grids may be costly, due to the large number of degrees of freedom in each element. This difficulty is overcome in the development here presented.

Assume that the transformation of coordinates between the reference element s,t and the physical element $x(s,t)$ and $y(s,t)$ is known. The gradient of the unknown function φ in any point of the physical element can be written as

$$\nabla\varphi\big(x(s,t),y(s,t)\big) = \left(\frac{\partial\varphi}{\partial s}\frac{\partial s}{\partial x} + \frac{\partial\varphi}{\partial t}\frac{\partial t}{\partial x}, \frac{\partial\varphi}{\partial s}\frac{\partial s}{\partial y} + \frac{\partial\varphi}{\partial t}\frac{\partial t}{\partial y}\right), \tag{2.31}$$

which avoids the direct computation of derivatives in the physical space, passing through the coordinate transformation. Please note that the physical flux on the element, as well as each basis $v(x,y)$, can be easily mapped to the reference element with Lagrangian interpolators. In fact, the mapping procedure can be represented as a "shrinking" and "fitting" operation which deforms the domain in order to fit the reference square, and the overlying flux follows this transformation. The point values of the flux on corresponding coordinates are the same, but this is not true for the gradients, which have to be re-calculated. So, the expansion coefficients of the physical flux and those of the transformed ones are the same, the transformation is charged on the basis functions only. One assumes that the terms

$$\frac{\partial s}{\partial x}, \quad \frac{\partial t}{\partial x}, \quad \frac{\partial s}{\partial y}, \quad \frac{\partial t}{\partial y} \tag{2.32}$$

are known or easily evaluated from the transformation at least in the grid points of the reference domain. In this work, this is done by the inversion of the Jacobian of the transformation in each point of the grid (this operation is very cheap and can be performed also analytically in 2D).

The remaining terms, the derivatives of the flux with respect to the reference coordinate system, use the reference basis functions as follows:

$$\frac{\partial \varphi}{\partial s} = \frac{\partial}{\partial s} \sum_{ij} \hat{\varphi}_{ij} \chi_i(s) \chi_j(t) = \sum_{ij} \hat{\varphi}_{ij} \frac{\mathrm{d}\chi_i(s)}{\mathrm{d}s} \chi_j(t), \tag{2.33}$$

$$\frac{\partial \varphi}{\partial t} = \frac{\partial}{\partial t} \sum_{ij} \hat{\varphi}_{ij} \chi_i(s) \chi_j(t) = \sum_{ij} \hat{\varphi}_{ij} \chi_i(s) \frac{\mathrm{d}\chi_j(t)}{\mathrm{d}t}. \tag{2.34}$$

As far as the derivatives of the reference basis functions are concerned, they are available analytically on the nodes of the GLL grid through the derivation matrix in equation (1.81), but in general these points are not sufficient since the function is needed on the whole $[-1,+1]$ segment. Then, the available derivative values are interpolated using again the Lagrange functions, allowing to write:

$$\frac{\mathrm{d}\chi_\ell(\xi)}{\mathrm{d}\xi} = \sum_r D_{\ell r} \chi_r(\xi), \tag{2.35}$$

where $D_{\ell r} = \mathrm{d}\chi_\ell(\xi_r)/\mathrm{d}\xi$ is the derivation matrix.

Putting together all assumptions introduced so far, one is now able to calculate for instance the term

$$\int_{\Gamma_i} \nabla \varphi_A \cdot \boldsymbol{n}_i \, v_A. \tag{2.36}$$

appearing in the definition of m^{AA}. With reference to Figure 2.8, this integral is calculated on the $\mathscr{E}$ side of the A element, which corresponds also to the $\mathscr{W}$ side of B. Clearly, each side among $\mathscr{N}$, $\mathscr{S}$, $\mathscr{E}$ and $\mathscr{W}$ is the image of the corresponding side of the reference element with $t=+1$, $t=-1$, $s=+1$ and $s=-1$ respectively.

To solve the curvilinear integral, one needs the parametric $\boldsymbol{\gamma}_i(t)$ representation of the interface Γ_i. It can easily be determined using the transformation $s,t \to x,y$ of the element A by setting $s=+1$ or, equivalently, from B by setting $s=-1$. The parameter is then the coordinate t of the reference element. Then, the integral is transformed into a classical definite integral:

$$\int_{\Gamma_i} \nabla \varphi_A \cdot \boldsymbol{n}_i \, v_A = \int_{-1}^{+1} \left[\nabla \varphi_A \cdot \boldsymbol{n} \, v_A \right]_{\Gamma_i} (t) \left| \boldsymbol{\gamma}_i'(t) \right| \mathrm{d}t \tag{2.37}$$

The term $\rho(t) = \left|\boldsymbol{\gamma}_i'(t)\right|$ is easily obtained from the transformation. The argument of the integral is reformulated as

$$\begin{aligned} \nabla \varphi_A \cdot \boldsymbol{n} &= \frac{\partial \varphi_A}{\partial s} \left(\frac{\partial s}{\partial x} n_x(t) + \frac{\partial s}{\partial y} n_y(t) \right) + \frac{\partial \varphi_A}{\partial t} \left(\frac{\partial t}{\partial x} n_x(t) + \frac{\partial t}{\partial y} n_y(t) \right) \\ &= \frac{\partial \varphi_A}{\partial s} f(t) + \frac{\partial \varphi_A}{\partial t} g(t), \end{aligned} \tag{2.38}$$

where $f(t)$ and $g(t)$ are functions containing only geometrical known data. Substituting

the expansions and the derivatives

$$\int_{\Gamma_i} \nabla\varphi_A \cdot \boldsymbol{n}_i \, v_{n,m} = \int_{-1}^{+1} \rho(t) \Bigg[\Bigg(\sum_{ij} \hat{\varphi}_{ij} \sum_r D(r,i)\chi_j(t) f(t) + \sum_{ij} \hat{\varphi}_{ij} \chi_i(s) \sum_r D(r,j)\chi_r(t) \Bigg) \chi_n(s)\chi_m(t) \Bigg]_{s=+1} \mathrm{d}t \quad (2.39)$$

for all m, n in $1,\dots,K+1$. Each basis function $\chi_\ell(s=1)$ is non vanishing, by topology, if and only if $\ell = K+1$, where K is the order of the Lagrange polynomials (i.e. if it is the "last" function of the basis), being by definition

$$\chi_a(1) = \delta_{a,K+1}, \quad a = 1,\dots,K+1. \quad (2.40)$$

Moreover, the integral is solved numerically, using a Gaussian quadrature rule. Basically, the choice of this quadrature is free, but for the implementation the GLL formula is used. Then, if P is the order of the formula, and t_p, π_p for $p = 0,\dots,P$ are respectively its nodes and weights, one has:

$$\begin{aligned} \int_{\Gamma_i} \nabla\varphi_A \cdot \boldsymbol{n}_i \, v_{n,m} = {} & \sum_{ij} \hat{\varphi}_{ij} D_{K+1,i} \delta_{n,K+1} \sum_p \pi(t_p)\rho(t_p) f(t_p) \chi_j(t_p) \chi_\ell(t_p) \\ & + \sum_{ij} \hat{\varphi}_{ij} \delta_{i,K+1} \delta_{n,K+1} \sum_p \pi(t_p)\rho(t_p) g(t_p) \sum_r D_{kj} \chi_r(t_p) \chi_\ell(t_p), \quad \forall m,n. \end{aligned} \quad (2.41)$$

All contributions from the different m and n values are then considered at the same time. By defining the following vectors of quantities evaluated on the nodes of the quadrature grid

$$\boldsymbol{\pi} = \{\pi_p \,|\, \pi_p = \pi(t_p),\ p = 0,\dots,P\} \quad (2.42a)$$
$$\boldsymbol{\rho} = \{\rho_p \,|\, \rho_p = \rho(t_p),\ p = 0,\dots,P\} \quad (2.42b)$$
$$\boldsymbol{f} = \{f_p \,|\, f_p = f(t_p),\ p = 0,\dots,P\} \quad (2.42c)$$
$$\boldsymbol{g} = \{g_p \,|\, g_p = g(t_p),\ p = 0,\dots,P\} \quad (2.42d)$$

and the following matrices

$$\mathbf{X} = \{X_{ip} \,|\, X_{ip} = \chi_i(t_p),\ i = 1,\dots,K+1,\ p = 0,\dots,P\} \quad (2.43a)$$
$$\mathbf{C} = \sum_r D_{rj}\chi_r(t_p) = \mathbf{XD} \quad (2.43b)$$
$$\mathbf{E}^{AAA} = \mathbf{X}^T \operatorname{diag}[\boldsymbol{f}\boldsymbol{\pi}\boldsymbol{\rho}]\mathbf{X} \quad (2.43c)$$
$$\mathbf{F}^{AAA} = \mathbf{X}^T \operatorname{diag}[\boldsymbol{g}\boldsymbol{\pi}\boldsymbol{\rho}]\mathbf{C} \quad (2.43d)$$

and reordering, one can write the first contribution $\mathbf{M}^{AA,1}$ to the matrix $\mathbf{M}^{AA}$

$$M^{AA,1}_{n+m(K+1),i+j(K+1)} = \delta_{n,K+1}\left(D_{K+1,i}E^{AAA}_{mj} + \delta_{a,K+1}F^{AAA}_{mj}\right). \quad (2.44)$$

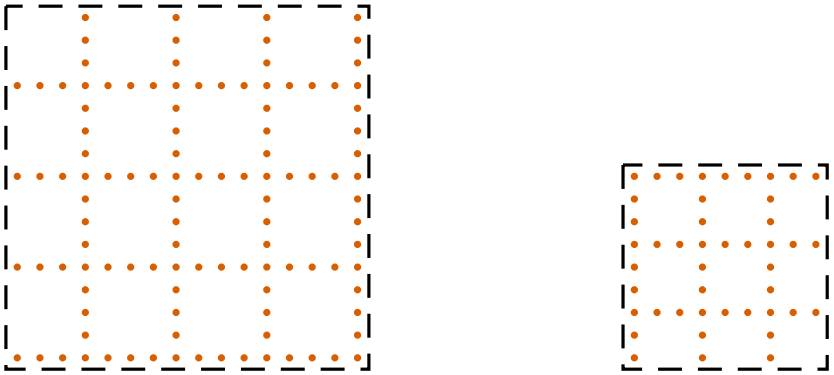

(a) $\mathbf{M}^{AA}$ (b) $\mathbf{M}^{BB}$

Figure 2.11: Matrices of inner interaction resulting from the disretization of (2.26).

Similarly, one can calculate the integral of the form

$$\int_e \varphi_A \nabla v_A \cdot \boldsymbol{n}, \tag{2.45}$$

which brings to the second contribution $\mathbf{M}^{AA,2}$

$$M^{AA,2}_{n+m(K+1),i+j(K+1)} = \delta_{i,K+1}\left(D_{K+1,n}E^{AAA}_{jm} + \delta_{n,K+1}F^{AAA}_{jm}\right), \tag{2.46}$$

and also the third contribution $\mathbf{M}^{AA,3}$, coming from the integral in the form

$$\int_e \varphi_A v_A, \tag{2.47}$$

which sums up the following elements

$$M^{AA,3}_{n+m(K+1),i+j(K+1)} = \delta_{n,K+1}\delta_{i,K+1}G^{AA}_{mi}, \tag{2.48}$$

where the matrix $\mathbf{G}^{AA}$ has the following definition:

$$\mathbf{G}^{AA} = \mathbf{X}^T \operatorname{diag}(\pi\rho)\mathbf{X}. \tag{2.49}$$

Because of the Kroenecker delta functions appearing in $\mathbf{M}^{AA,1}$,$\mathbf{M}^{AA,2}$ and $\mathbf{M}^{AA,3}$, one discovers that $\mathbf{M}^{AA}$ is not full, but has a fixed and easy sparsity pattern which may help its construction and its memory storage using dedicated libraries, because the programmer knows a priori which matrix elements are non-zero and where to place them. In particular, $\mathbf{M}^{AA,1}$ is nonzero only in $K+1$ rows in regular pattern, $\mathbf{M}^{AA,2}$ in $K+1$ columns and $\mathbf{M}^{AA,3}$ in the intersections of the first two matrices. Figure 2.11a shows the combined pattern.

Figure 2.11a

The procedure to assemble $\mathbf{M}^{BB}$ is easily derived from the one for $\mathbf{M}^{AA}$, where the interface is seen from element B, corresponding to an $s=-1$ side on the reference domain. So, in the curvilinear integral enter all functions restricted to $s=-1$ instead of $s=+1$ when mapped. The pattern of the matrix is analogous (a row and a column non vanishing every $K+1$ positions), symmetric with respect to the top-left corner, as shown in Figure 2.11b.

Figure 2.11b

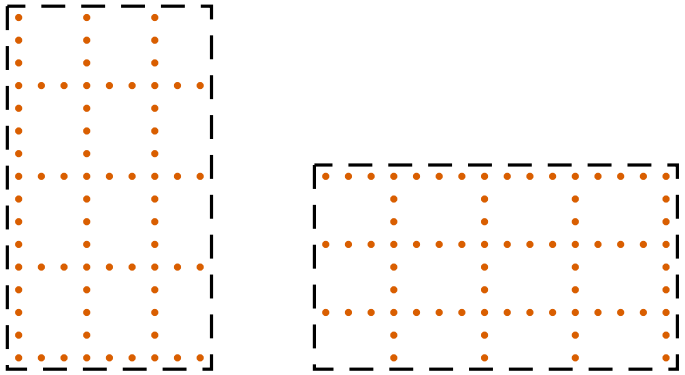

(a) $\mathbf{M}^{AB}$ (b) $\mathbf{M}^{BA}$

Figure 2.12: Matrices of cross-element interaction resulting from the disretization of Eq. (2.26).

In principle, also $\mathbf{M}^{AB}$ and $\mathbf{M}^{BA}$ are constructed in the same way, with mixed features. In the definitions of their generating integrals functions appear that are defined on different sides of the interface (but are, of course, both non vanishing exactly on e), which are represented in the reference domain by a $s = -1$ or $s = +1$ according to the fact that they belong to A or B. Another complication is given by the fact that different polynomial orders are used in the two elements, so the matrices are in general rectangular and one should consider different derivation matrices $\mathbf{D}_A$ and $\mathbf{D}_B$ for the unknowns and the test functions accordingly. Matrices $\mathbf{M}^{AB}$ and $\mathbf{M}^{BA}$ are represented in Figure 2.12. *Figure 2.12*

The pattern of the comprehensive algebraic matrix obtained at the end of this simple derivation is given in Figure 2.13. It is clear that it is sparse but completely predictable, as shown in the previous considerations. Sparse matrix storage algorithms coupled with appropriate solution routines are strongly advised for the solution of DG-SEM linear systems. *Figure 2.13*

Similar remarks apply to the case where the interface is not of type $\mathscr{E} - \mathscr{W}$. Provided that the axes "in contact" in the reference domain are oriented in the same way, one has simply to consider the correct parametrization for the border. For instance, for a $\mathscr{N} - \mathscr{S}$ case the functions defined on A are evaluated in $t = 1$, while in B for $t = -1$. The pattern of rows and columns change, since they collate each other for $\mathscr{N} - \mathscr{S}$ couplings, but their number is unchanged.

A slightly different approach is necessary if couplings are made between non opposing poles, like $\mathscr{E} - \mathscr{S}$: in this case one has to consider the correct parametrization and revert one of the axis. An example of this procedure has been implemented in the solver in a first phase of the development, but not retained in view of the properties of the transfinite interpolation technique shown in section 2.3.

Another example of DG-SEM matrix is presented in the next section, associated to one of the benchmark problems used.

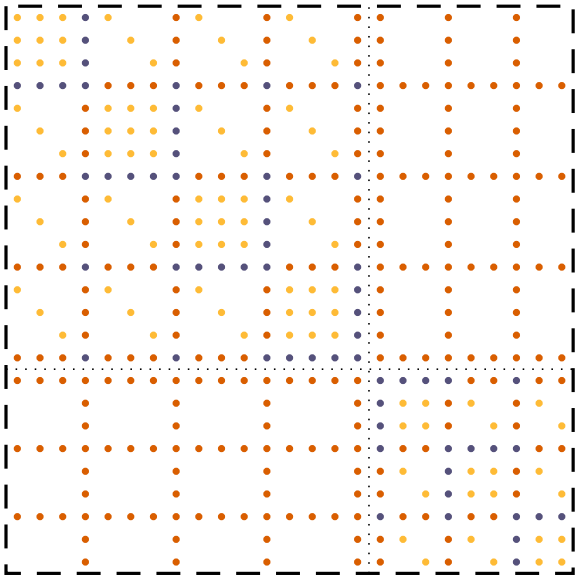

Figure 2.13: Complete matrix. The yellow dots belong to the tensor part of the weak operator. The orange dots are those issued from the discontinuous integral relations. The blue entries sees both contributions summing up.

2.2.2 Some results

The Natelson benchmark

A set of numerical results illustrates some of the advantages of the spectral element approach for a classical neutron transport problem, as originally proposed by Natelson [1971].
Figure 2.14 The calculation domain, shown in figure 2.14, is a 3×3 cm cell with a symmetry plane along one of the diagonals; an external unitary source is spread over $\mathscr{D}_1$, where also the isotropic
Table 2.8 scattering cross section differs from the value in the remaining of the cell (table 2.8). All the boundary conditions are assumed of the homogeneous Neumann type (which are natural in Galerkin schemes, so that one can avoid the introduction of boundary conditions while assembling the matrix). Results for approximations A_1, A_2 and A_3 are presented, while the domain is subdivided in four elements ($\mathscr{D}_1$, $\mathscr{D}_2^{(1)}$, $\mathscr{D}_2^{(2)}$ and $\mathscr{D}_2^{(3)}$).

Several authors have considered this problem, but it seems that none has ever provided an analytical reference solution. To perform some numerical assessments a very detailed SEM calculation has been retained as reference solution, using 28×28 degrees of freedom for each of the four quadrants in which the domain is decomposed. An analysis of the convergence trend suggests that the numerical error of the solver, due to the growing conditioning number of the matrix, is still kept under control by the algorithm.

For a first analysis, the same problem is solved using linear and quadratic finite elements on triangles, often referred as Courant elements P1 and P2 in finite element literature [Quarteroni, 2009]. All FEM calculations are performed with the FreeFem++ code [Pironneau et al., 2010]. The same problem is then solved with spectral elements of increasing order. The comparison between the two sets of solutions is performed for the

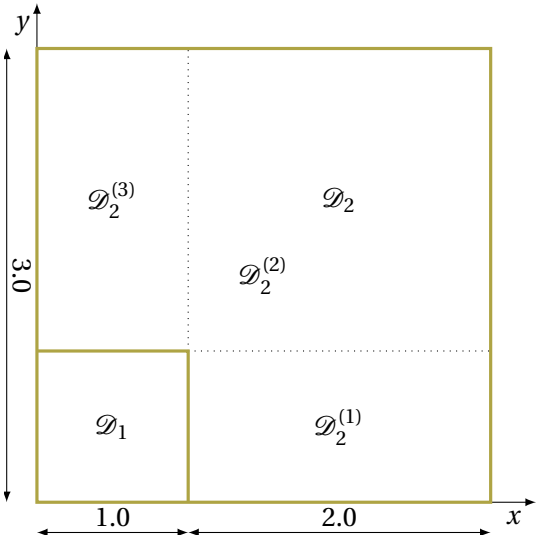

Figure 2.14: Geometry of the Natelson [1971] benchmark. Dimensions are in centimeters. The material region $\mathscr{D}_2$ has been subdivided into three computational elements $\mathscr{D}_2^{(1)}$,$\mathscr{D}_2^{(2)}$ and $\mathscr{D}_2^{(3)}$. Reflective boundary conditions are used.

Table 2.8: Material properties for the Natelson [1971] benchmark problem.

Region	Σ_t [cm^{-1}]	Σ_s [cm^{-1}]	Source strength [cm^{-3}s^{-1}]
$\mathscr{D}_1$	1.00	0.50	1.0
$\mathscr{D}_2$	1.00	0.25	0.0

same number of equations, corresponding to the nodes of the grid and roughly proportional to the computational burden.

The position of the unknowns for the two schemes is not the same, due to the completely different nature of the grid generation algorithm (Delaunay triangulation for FEM, tensor product of 1D GLL grids for SEM). Moreover, since the discontinuous SEM approach gives two values of the solution at the interfaces, point-wise evaluations of the error should be handled with special care, in particular to avoid interpolation processes as much as possible. Therefore, the error is evaluated on the central point of each quadrant, as it is uniquely defined and computed without interpolation at least for SEM if even values of K are used, on the middle point of one of the outer edges of the source region and on the integral mean values of the flux on the four subdomains, introducing anyway the quadrature error. This choice of indicators allows to describe in an accurate way the various error trends of the solution.

Figure 2.15 shows the non vanishing elements for the A_1 (diffusion model) case with $K = 3$, $K = 4$, $K = 6$ and $K = 5$ respectively for each cell. *Figure 2.15*

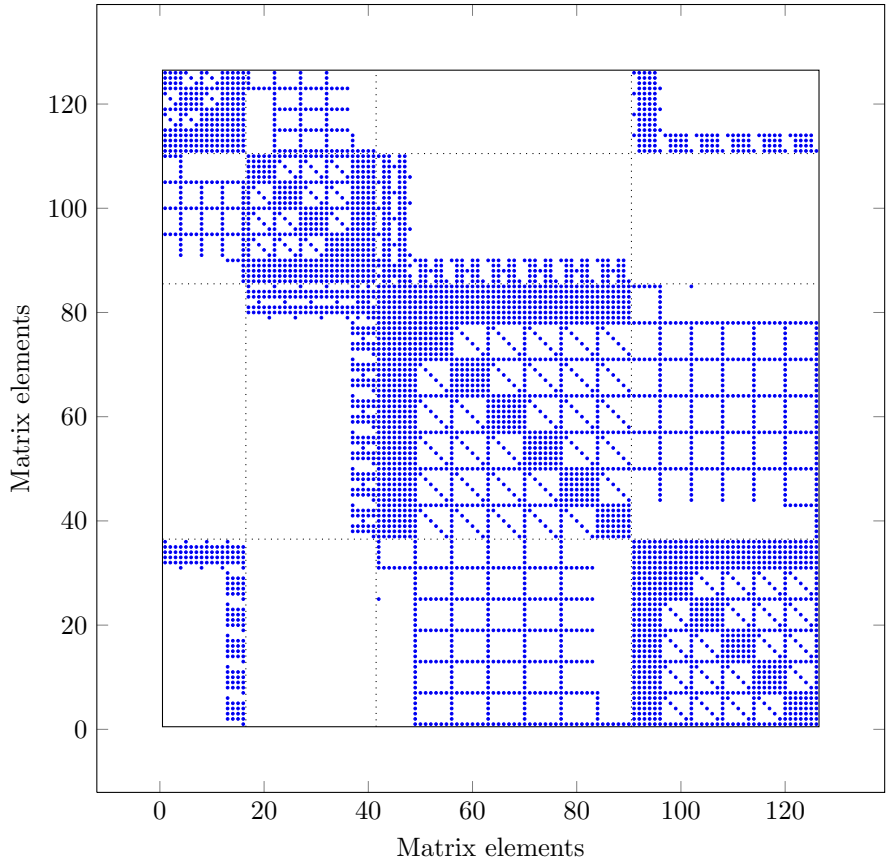

Figure 2.15: Example of sparsity pattern of a spectral element matrix operator with the discontinuous Galerkin approach. This case corresponds to an A_1 solution of the Natelson benchmark introduced in section 2.2.2.

Study of the convergence pattern To establish the feature of the convergence of the SEM and FEM numerical schemes, one can estimate how rapidly the digits of the solutions for the quantities indicated above reach stability, referring to the reference solution for SEM. For the FEM solution, the reference is obtained with a calculation using about 3500 equations, approximately corresponding to the number of points of the SEM reference calculation.

Some comparisons on the number of stable digits are illustrated in Figures 2.16 and 2.17. Both P1 and P2 finite elements are used, together with the SEM scheme. In all cases, the increased number of equations is achieved with a refinement of the grid adding the same number of degrees of freedom to each element $\mathscr{D}_i$. The number of stable digits reached by the SEM model is quite larger than for FEM for any number of unknowns. It is worth remarking that the upper limit of the number of unknowns adopted is due to the capability of the FEM solver. These results support our choice to adopt the SEM solution described above as reference for the following steps.

Figure 2.16
Figure 2.17

Comparison of FEM and SEM solutions to reference The relative error for the already mentioned quantities and functional of the solution is studied when the number of equations is progressively increased. Figure 2.18a shows the smooth trend of the error evaluated for the integral mean flux over the first quadrant $\mathscr{D}_1$. A similar graph is shown in figure 2.18b, referring to the solution at the midpoint of the outer edge of $\mathscr{D}_1$; even if the trends are less regular, the convergence speed is quite similar to the previous example.

Figure 2.18a
Figure 2.18b

An example to show the potential of adaptivity

The grid can be adapted to improve the performance of the numerical scheme, thus reducing the computational burden to reach a given approximation. A preliminary evaluation is presented to show the potentiality of an adaptive approach to enhance the performance of the SEM scheme.

A solution with 900 equations (15^2 equations for each of the four elements) is evaluated and assumed as reference for the subsequent calculations. The number of unknowns in the largest square is then progressively reduced (13^2, 11^2 and so on up to 3^2). In figure 2.19 the relative errors at each step are plotted as a function of the computational gain, expressed in terms of the relative reduction of the number of equations.

Figure 2.19

Benchmark IAEA-EIR2

In table 2.10 some results of the application of SEM to the benchmark problem IAEA-EIR2 (figure 2.20, material data and sources in table 2.9) are presented, together with some of the results available in literature. Namely, we have performed three calculations with FEM (Courant P2) with different values of the mesh size h and one with SEM. These results are compared with the Boundary Element Method and those obtained by the TWODANT code [Alcouffe et al., 1984] working with the discrete ordinates scheme. Except for the latter, all the numerical methods solve the A_2 model in the example. It has to be noted, however, that

Table 2.10
Figure 2.20
Table 2.9

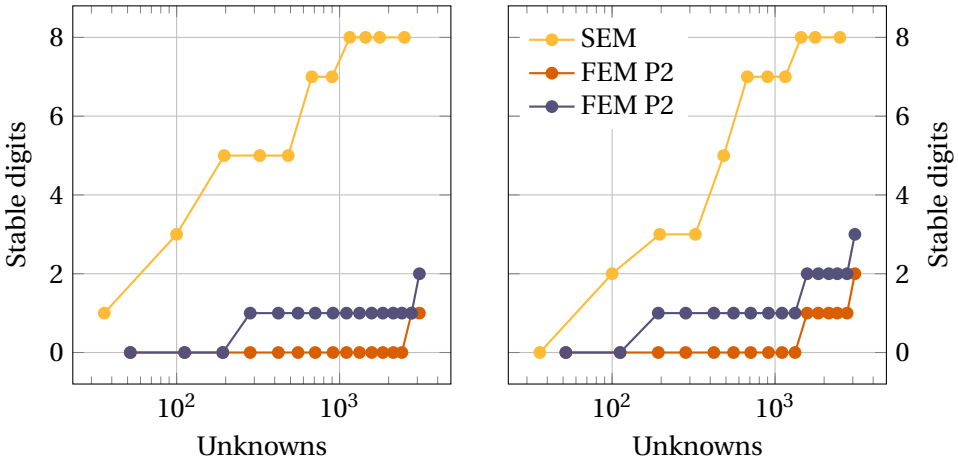

(a) Digits of the mean flux over $\mathscr{D}_1$, computed using the A_3 model.

(b) Digits of the mean flux over $\mathscr{D}_1$, computed using the A_2 model.

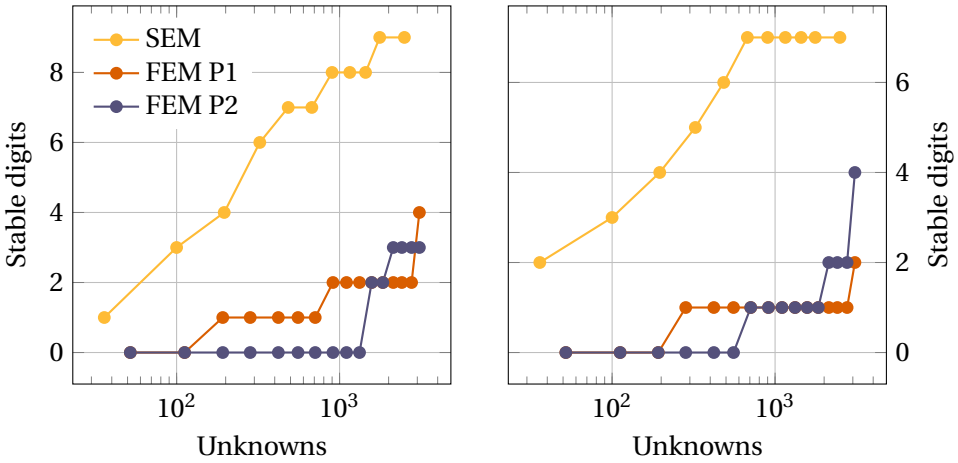

(c) Digits of the mean flux over $\mathscr{D}_2^{(1)}$, computed using the A_1 model.

(d) Digits of the mean flux over $\mathscr{D}_2^{(2)}$, computed using the A_1 model.

Figure 2.16: Number of stable digits of some functionals of the solution, using FEM P1 and P2 schemes and the spectral element method.

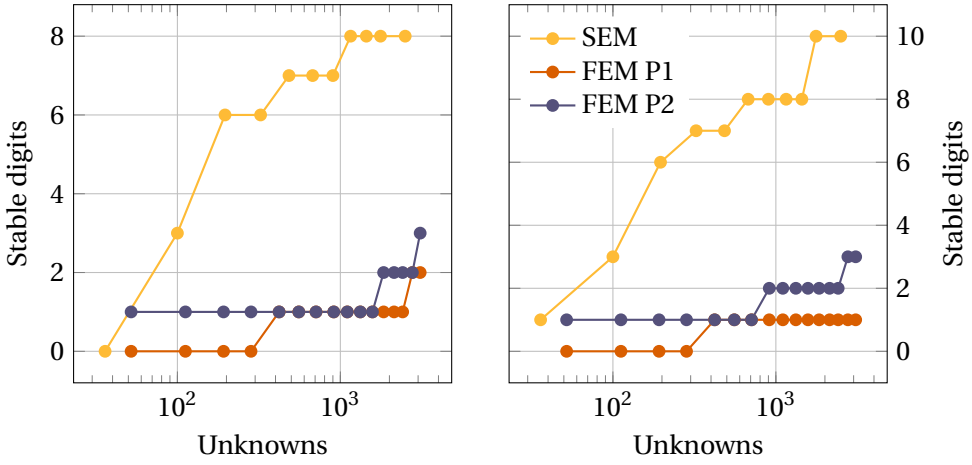

(a) Digits of the value of the flux in the center point of $\mathscr{D}_1$, computed using the A_1 model.

(b) Digits of the value of the flux in the midpoint of the outer edge of $\mathscr{D}_1$, computed using the A_1 model.

Figure 2.17: Number of stable digits of some functionals of the solution, using FEM P1 and P2 schemes and the spectral element method.

the comparison of the various A_2 calculations with the discrete ordinates has only an indicative value, owing to the intrinsic, and distinctive, approximation mechanism of the A_N method, while the approximation of the S_N method can be arbitrarily increased by letting N go to infinity. In this respect, the "pseudo-reference" SEM solution has been introduced to perform a comparison remaining inside the class of the A_N solution methods.

2.2.3 Comments on the DG approach

The original and typical formulation of the Spectral Elements Method carries some weaknesses concerning the grid specifications. The Continuous Galerkin approach, which is the classical reference framework for most Galerkin-type schemes, requires conformal grids. If, in FEM, this may not constitute a serious problem since the elements are typically "small" (compared to the characteristic dimensions of the domain), in SEM they tend to be far more

Table 2.9: Material properties for the IAEA EIR-2 benchmark problem [Khalil, 1985].

Region	Σ_t [cm^{-1}]	Σ_s [cm^{-1}]	Source strength [$cm^{-3}s^{-1}$]
$\mathscr{D}_1$	0.60	0.53	1.0
$\mathscr{D}_2$	0.48	0.20	0.0
$\mathscr{D}_3$	0.70	0.66	1.0
$\mathscr{D}_4$	0.65	0.50	0.0
$\mathscr{D}_5$	0.90	0.89	0.0

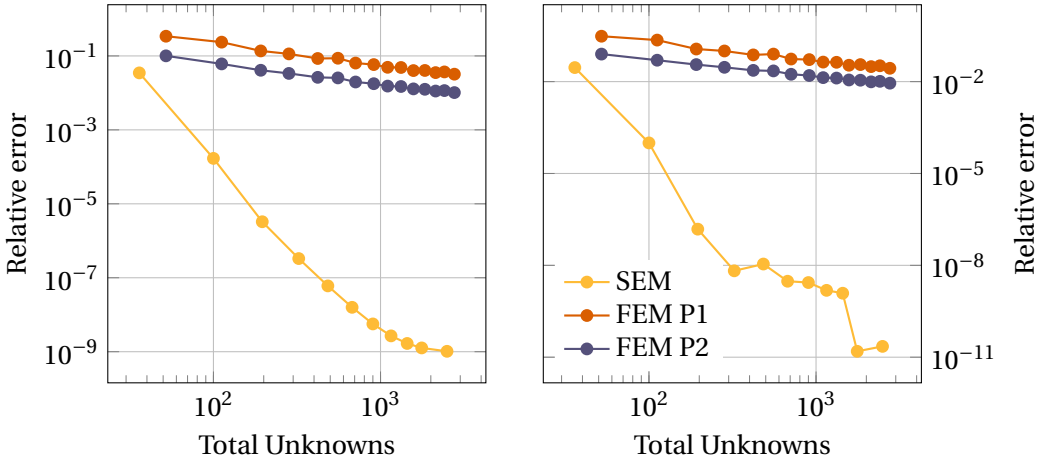

(a) Comparison in A_1 of the convergence rate of the solution versus the pseudo-reference for the mean flux in $\mathscr{D}_1$.

(b) Comparison in A_1 of the convergence rate of the solution versus the pseudo-reference for the the middle point of any outer edge of $\mathscr{D}_1$.

Figure 2.18: Convergence trends of the FEM and SEM solutions, compared to the reference SEM solution.

extended, since the gradients of the material characteristics and of the solution are optimally handled by the high polynomial degree.

The neutron flux in power and research reactors may show sufficiently steep gradients to require a local fine grid reconstruction. For instance, the presence of localized absorbers like gadolinized pins, self powered neutron detectors or shutdown rods distorts the flux shape with most of the effect in the spatial scale of the mean free path. On the other hand, localized reactivity insertions are known to provoke high isolated flux peaks: the procedures for safety evaluations require in this case a fine reconstruction of the power profile at a sub-assembly level in order to identify the most compromised pin and evaluate margins on it; currently, envelope statistical approaches are used, which could be substituted by

Table 2.10: Comparison of results for the IAEA-EIR2 benchmark. All values are in n/cm^2/s. BEM results are from Ciolini et al. [2002], TWODANT calculations from Khalil [1985]

	FEM $h = 1.0$ cm	FEM $h = 0.5$ cm	FEM $h = 0.3$ cm	SEM	BEM	TWODANT
$\overline{\Phi}_{\mathscr{D}_1}$	1.19987E+1	1.19705E+1	1.19623E+1	1.19459E+1	1.1973E+1	1.1960E+1
$\overline{\Phi}_{\mathscr{D}_2}$	6.01814E -1	5.70341E -1	5.60809E -1	5.43844E -1	5.3613E -1	5.3613E -1
$\overline{\Phi}_{\mathscr{D}_3}$	1.92649E+1	1.92215E+1	1.92051E+1	1.91766E+1	1.9222E+1	1.9202E+1
$\overline{\Phi}_{\mathscr{D}_4}$	9.09529E -1	8.71527E -1	8.59959E -1	8.38486E -1	8.2946E -1	8.3364E -1
$\overline{\Phi}_{\mathscr{D}_5}$	1.49461E+0	1.51175E+0	1.51697E+0	1.52707E+0	1.5318E+0	1.5263E+0

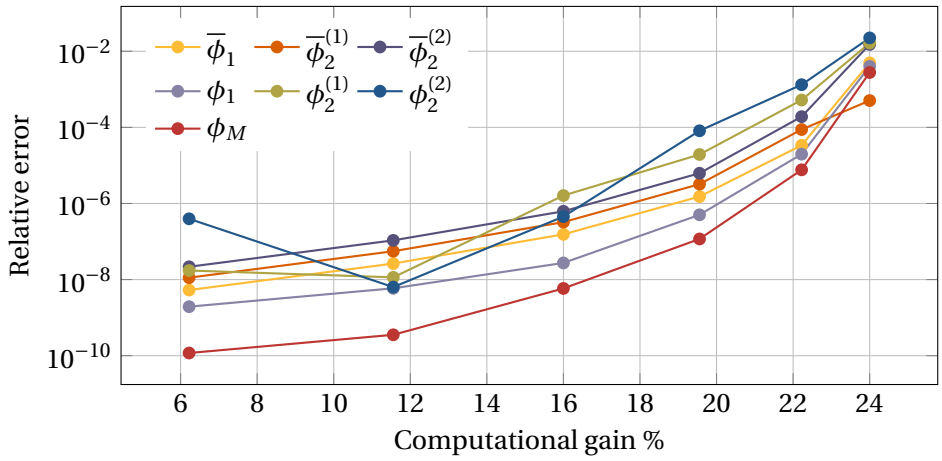

Figure 2.19: Behavior of the relative error of the quantities and solution functionals observed for an adaptive grid as a function of the computational gain. $\overline{\phi}_1, \overline{\phi}_2^{(1)}, \overline{\phi}_2^{(2)}$ and $\phi_1, \phi_2^{(1)}, \phi_2^{(2)}$ are respectively the mean and center-point scalar fluxes evaluated over $\mathscr{D}_1, \mathscr{D}_2^{(1)}, \mathscr{D}_2^{(2)}$. ϕ_M is the value of the scalar flux at the midpoint of the outer edge of $\mathscr{D}_1$.

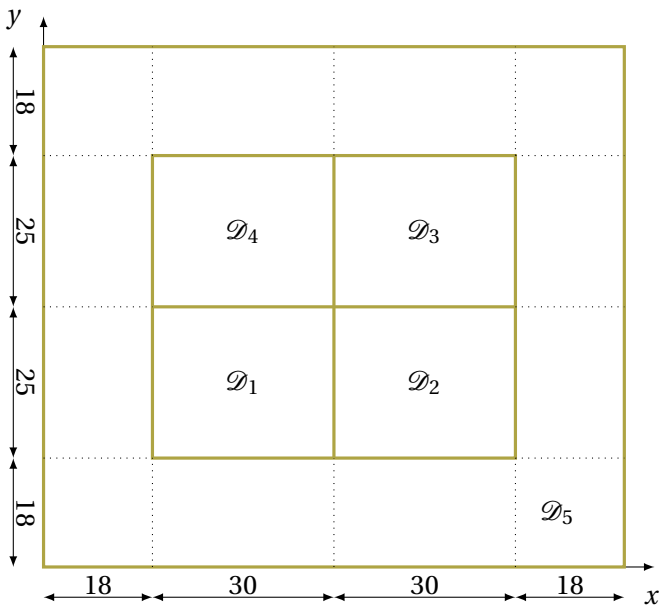

Figure 2.20: Geometry for the IAEA EIR-2 benchmark problem [Khalil, 1985]. Void boundary conditions are put on all four sides.

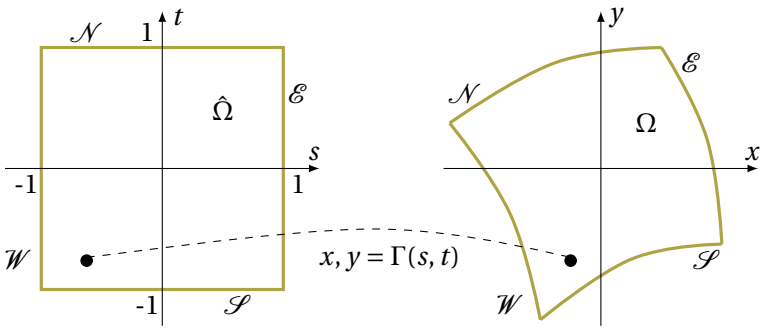

Figure 2.21: Deformation of a reference element

more accurate computations with localized grid refinement using SEM and DG in order to reduce incertitudes and allow lower provisions in the reactor design phase.

From the implementation point of view, the explicit block-matrix approach seems easily scalable to more complex domains; its memory consumption is low, because each block can be stored in memory in the final sparse matrix as soon as it is calculated and without cross terms, owing to the advantageous structure of the DG interface conditions acting solely on traces. Last, the conservation of the number of particles in each element is of great importance in nuclear engineering for the equivalence procedures, since it guarantees a high precision in the conservation of the reaction rates over which such calculation schemes are based. More details and results are presented in the next section, which adds to the DG-SEM scheme another feature to enhance even more its flexibility.

2.3 Domain deformation: Transfinite interpolation

2.3.1 Motivation

Up to this point, the SEM elements were considered rectangular, obtained by a scaling of a reference square with a different factor in each direction. General expressions for a rotated element were obtained by Barbarino [2010]. For certain computational domains, more grid flexibility is advisable. For instance, one may need to adapt the boundaries of each element to curved surfaces, and in doing so it could be advantageous to deform an element with the elimination of one side, reverting to the triangular shape which is a feature cleverly exploited by general FEM Courant schemes to assemble flexible grids.

In this section both problems are approached using transfinite interpolation and Radau polynomials, with reference to a specific exercise where these features are required at the same time.

2.3.2 Analytical deformation of a quadrangular mesh element

Assume a 2D reference domain $\hat{\Omega}(s,t) \in [-1,+1]^2$ as in Figure 2.21, which can be deformed by the transformation $\Gamma = x(s,t), y(s,t)$ into the domain $\Omega(x,y)$. Once Γ is obtained, it is

possible to calculate the Jacobian matrix and the metrics in all points, feeding the SEM scheme with the adjusted mass and stiffness matrices.

When the analytic expression for Γ is not easily recoverable, numerical methods exist, which are based on the solution of differential equations modelling pseudo-potentials allocating charges in equilibrium positions according to the interface nodes [Deville et al., 2002]. One of this methods has been successfully used by the author previously with SEM grids [Barbarino, 2010]; this method requires the solution of a partial differential equation on each internal point.

In these pages another approach is used, called transfinite interpolation. This method does not address the Γ transformation directly, but its Lagrangian interpolant obtained using only the parametric representation of the contours of the element. The accuracy of the method is improved by a clever choice of the interpolation basis, and typically brings handy expressions for the transformed coordinates, which can be treated analytically rather than numerically.

Transfinite interpolation basics

In order to introduce the grounds of the method, a mono-dimensional interpolation problem is first considered. Be $f(x)$ a suitable function defined in $[-1,+1]$; be $f^\star(x)$ its linear Lagrangian interpolation, obtained by applying to $f(x)$ the projection operator P_x as follows [Mund, 2011a]:

$$f^\star(x) = P_x f(x) = f(-1)\vartheta_1(x) + f(1)\vartheta_2(x), \tag{2.50}$$

where

$$\vartheta_1(x) = \frac{1-x}{2}, \quad \vartheta_2(x) = \frac{1+x}{2}.$$

The interpolation error may be represented as an operator Q_x acting on $f(x)$, being:

$$\varepsilon(x) = f(x) - f^\star(x) = (I - P_x) f(x) = Q_x f(x). \tag{2.51}$$

Standard textbooks report that the error associated to linear Lagrangian interpolation in 1D has an error which goes as the square of the mesh size, as:

$$||\varepsilon(x)|| = O(h^2). \tag{2.52}$$

Intuitively, the simplest extension to two or more dimensions implies the tensor product $P_\otimes$ of the two projectors P_x and P_y

$$\begin{aligned} f^\star(x,y) = P_\otimes f(x,y) = P_x P_y f(x,y) = f(-1,-1)\vartheta_1(x)\vartheta_1(y) + f(-1,1)\vartheta_1(x)\vartheta_2(y) \\ + f(1,-1)\vartheta_2(x)\vartheta_1(y) + f(1,1)\vartheta_2(x)\vartheta_2(y). \end{aligned} \tag{2.53}$$

The error operator $Q_\otimes$ associated to this projector is

$$Q_\otimes = I - P_\otimes = I - (I - Q_x)(I - Q_y) = Q_x + Q_y - Q_x Q_y = Q_x \oplus Q_y, \tag{2.54}$$

where $\oplus$ is the symbol for the boolean sum. By extension of equation (2.52), one observes that the error in this 2D case is of the same order of the 1D case, being

$$||\varepsilon_\otimes(x,y)|| = O(h_x^2) + O(h_y^2) \tag{2.55}$$

at the leading order. It can now be observed that reversing formally the roles of interpolation and error operators in equation (2.54), thanks to the fact that $Q+P=I$, the transfinite projection operator defined as

$$P_{\oplus} = P_x \oplus P_y = P_x + P_y - P_x P_y \tag{2.56}$$

has an associated error operator $Q_{\oplus} = Q_x Q_y$, and then the leading error magnitude is only

$$||\varepsilon_{\oplus}(x,y)|| = O(h_x^2 h_y^2), \tag{2.57}$$

considerably smaller than in the tensor case.

In addition to this proof, one may get a hint on the precision at which the original function is represented by each of the operators at the border of the domain. For instance, the interpolation of f, $f^{\star}(x,y)$, calculated in $x=-1$ is, according to equation (2.53):

$$f^{\star}(-1,y) = f(-1,-1)\vartheta_1(y) + f(-1,1)\vartheta_2(y), \tag{2.58}$$

and so the interpolator evaluated on the boundary is just a segment connecting the two values of f at the domain endpoints. Indeed, the expanded expression for the transfinite interpolation is

$$\begin{aligned} f^{\ddagger}(x,y) = {} & f(-1,y)\vartheta_1(x) + f(1,y)\vartheta_2(x) + f(x,-1)\vartheta_1(y) + f(x,1)\vartheta_2(y) \\ & - f(-1,-1)\vartheta_1(x)\vartheta_1(y) - f(-1,1)\vartheta_1(x)\vartheta_2(y) - f(1,-1)\vartheta_2(x)\vartheta_1(y) - f(1,1)\vartheta_2(x)\vartheta_2(y) \end{aligned} \tag{2.59}$$

which, evaluated in $x=1$ as before brings simply

$$f^{\ddagger}(-1,y) = f(-1,y), \tag{2.60}$$

meaning that, this time, the interpolant corresponds exactly to the values of the function at the boundaries (this rationale is valid for $x,y=\pm 1$ of course). Intuitively, if a better representation of the boundaries is available, one expects a better interpolation inside the domain, which is confirmed by equation (2.57).

Extension to three dimensions is quite straightforward. The transfinite operator is

$$P_{\oplus} = P_x \oplus P_y \oplus P_z = P_x + P_y + P_z - (P_x P_y + P_x P_y + P_y P_z) + P_x P_y P_z \tag{2.61}$$

and, given the associated error operator as $Q_x Q_y Q_z$, the norm of the interpolation error results $O(h_x^2 h_y^2 h_z^2)$. Again, the interpolation is exact on the six edges of the reference cube $[-1,1]^3$.

Use with coordinate transformation

The two-dimensional domain mapping problem consists in finding two functions $x(s,t)$ and $y(s,t)$ constituting the components of the transformation $\Gamma(s,t)$ between $\hat{\Omega}$ and Ω. Using the transfinite technique means rather looking for the boolean interpolated functions $x^{\ddagger}(s,t)$ and $y^{\ddagger}(s,t)$ of the transformation. It is clear from equation (2.59) that one needs to

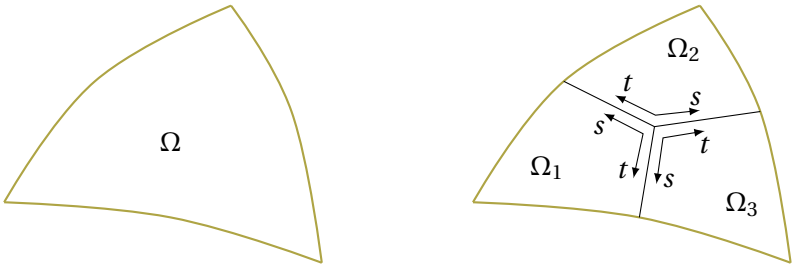

Figure 2.22: A triangular element split into three lozenges.

know the law $\{s,t\} \rightarrow \{x,y\}$ at least for each of the four sides $\mathscr{N}$, $\mathscr{S}$, $\mathscr{E}$, $\mathscr{W}$, which will be represented by the following loci:

$$\begin{aligned} \mathscr{N} &= [x^{\ddagger}(s,+1), y^{\ddagger}(s,+1)]^T, \\ \mathscr{E} &= [x^{\ddagger}(+1,t), y^{\ddagger}(+1,t)]^T, \\ \mathscr{S} &= [x^{\ddagger}(s,-1), y^{\ddagger}(s,-1)]^T, \\ \mathscr{W} &= [x^{\ddagger}(-1,t), y^{\ddagger}(-1,t)]^T. \end{aligned} \tag{2.62}$$

Assume that each side can be represented parametrically as

$$\mathscr{X}(\xi) = \left[x_{\mathscr{X}}(\xi), y_{\mathscr{X}}(\xi)\right]^T, \qquad \mathscr{X} \in \{\mathscr{N},\mathscr{S},\mathscr{E},\mathscr{W}\}, \tag{2.63}$$

where for all four cases ξ needs exactly the reference interval in $[-1,+1]$ to represent completely the corresponding side. One can impose that the free parameter appearing in equation (2.62) is equal to ξ, by virtue of the same domain $[-1,+1]$ and the fact that the second free parameter does not enter into the side definition, since it is equal to ± 1. In the end, the explicit expression of the transformation is

$$\begin{aligned} \Gamma^{\ddagger}(s,t) = [x^{\ddagger}(s,t), y^{\ddagger}(s,t)]^T &= \mathscr{W}(t)\vartheta_1(s) + \mathscr{E}(t)\vartheta_2(s) + \mathscr{S}(s)\vartheta_1(t) + \mathscr{N}(s)\vartheta_2(t) \\ &- \mathscr{W}(-1)\vartheta_1(s)\vartheta_1(t) - \mathscr{E}(-1)\vartheta_1(s)\vartheta_2(t) - \mathscr{W}(1)\vartheta_2(s)\vartheta_1(t) - \mathscr{E}(1)\vartheta_2(s)\vartheta_2(t). \end{aligned} \tag{2.64}$$

This transformation, though handy, has the important drawback of being non conformal, i.e. it does not conserve the angle between lines passing from $\hat{\Omega}$ to Ω [Ivanov and Trubetskov, 1995]. This requires particular care in a Continuous Galerkin framework, when imposing the continuity of currents in multi-region multi-media domains, since gradients must be calculated differently according to the side of each interface between two elements. In case of Discontinuous Galerkin, the mass conservation and the integral form of the interface conditions overcome this problem.

2.3.3 Trilateral elements

Sometimes, for symmetry reasons or to improve flexibility, it is necessary to include some triangular elements in the grid. The transfinite interpolation technique allows, in principle, to transform a side of the reference domain in a single point (x_0, y_0), simply setting the

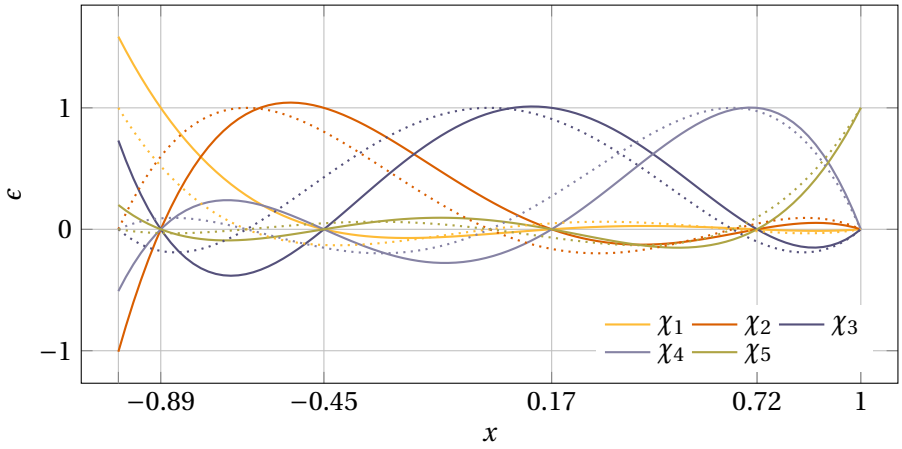

Figure 2.23: Radau basis in 1D, for $K = 4$ and including the $x = 1$ edge. Basis are simply specular if $x = -1$ is included in the set instead. With dotted lines, the same basis for the Lobatto case.

parametrization of the concerned $\mathscr{X}$ side artificially equal to $\Gamma_{\mathscr{X}}(\xi) = [x_0, y_0]$. Anyway the transformation is not invertible, because all the points on $\mathscr{X}$ are collapsed to the same coordinate in Ω; this implies a vanishing jacobian there, which prevents the evaluation of some of the integrals in the mass and stiffness matrices.

Two solutions have been identified, and successfully applied in this work. The first alternative consists of splitting each trilateral domain in three quadrilateral lozenges, deformed via the transfinite interpolation. This method, illustrated in Figure 2.22 has several disadvantages, for instance the presence of hanging nodes. The study of this alternative and its implementation have been performed, but they are not presented in this thesis.

Figure 2.22

The second solution identified changes the SEM interpolation basis in order to avoid the presence of nodes on the collapsed side.

As for the interpolator basis used classically in SEM methods, the new basis is constituted by Lagrange interpolators in the grid of the Gauss Radau quadrature formula. The nodes are defined in $(-1, +1]$ or $[-1, +1)$, and one extreme point is always excluded according to the formulation.

Radau nodes are the solutions of the polynomial equation

$$P_K(x) + P_{K+1}(x) = 0 \tag{2.65}$$

where P_K and P_{K+1} are the Legendre polynomials of order K and $K+1$ respectively. The nodes of the associated quadrature formula are obtained as

$$w_j = \begin{cases} \dfrac{2}{(K+1)^2}, & j = 1 \\ \dfrac{1}{(K+1)^2} \dfrac{1-\xi_j}{\left[P_K(\xi_j)\right]^2}, & 2 \le j \le K+1. \end{cases} \tag{2.66}$$

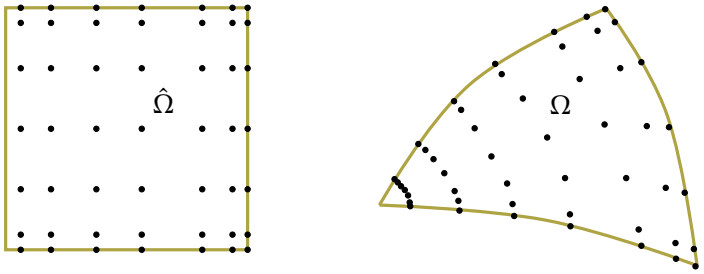

Figure 2.24: A triangular element treated with a change of basis

In two dimensions the interpolators are still tensor products of one-dimensional Lagrangian bases, and it is perfectly admissible to mix Radau and Lobatto polynomials in order to have nodes on the opposite side as before, in order to account for the interface values. Figure 2.24 is an example, where a Radau grid is used in the s direction of the reference element $\hat{\Omega}$, while a GLL grid is still used along t. The resulting spectral element lacks of degrees of freedom in one vertex, but this is beneficial because in all other points the Jacobian is strictly positive, and all matrices of the algebraic problem can be evaluated as before. As for the Lagrangian interpolators over the GLL grid, also in this case it is possible to get explicitly the value of the derivatives on the nodes of the Radau grid. Two differentiation matrices exist, according to the orientation of the grid. For the case where $\xi_1 > -1$, which implies that the last node is placed exactly in $+1$, the matrix is [Karniadakis and Sherwin, 2005]:

Figure 2.24

$$\mathbf{D}_{\text{Radau}} = \begin{cases} \dfrac{K(K+1)}{4}, & i = j = 1, \\ \dfrac{1}{2(1-\xi_i)}, & i = j > 1, \\ \dfrac{P_K(\xi_i)}{P_K(\xi_j)} \dfrac{1-\xi_j}{1-\xi_i} \dfrac{1}{\xi_i - \xi_j}, & \text{otherwise.} \end{cases} \tag{2.67}$$

The matrix corresponding to the other verse has a change in sign and all rows and columns are swapped, being:

$$\mathbf{D}_{\text{Radau}} = \begin{cases} -\dfrac{K(K+1)}{4}, & i = j = K+1, \\ -\dfrac{1}{2(1-\xi_{K+2-i})}, & i = j < K+1, \\ -\dfrac{P_K(\xi_{K+2-i})}{P_K(\xi_{K+2-j})} \dfrac{1-\xi_{K+2-j}}{1-\xi_{K+2-i}} \dfrac{1}{\xi_{K+2-i} - \xi_{K+2-j}}, & \text{otherwise.} \end{cases} \tag{2.68}$$

The matrix for the GLL grid has already been introduced in equation (1.81) and it is not changed.

2.3.4 The pin-cell problem

The techniques outlines in sections 2.3.2 and 2.3.3 are applied together to solve a lattice problem. The domain represents one eighth of a fuel cell, like the one depicted in Figure

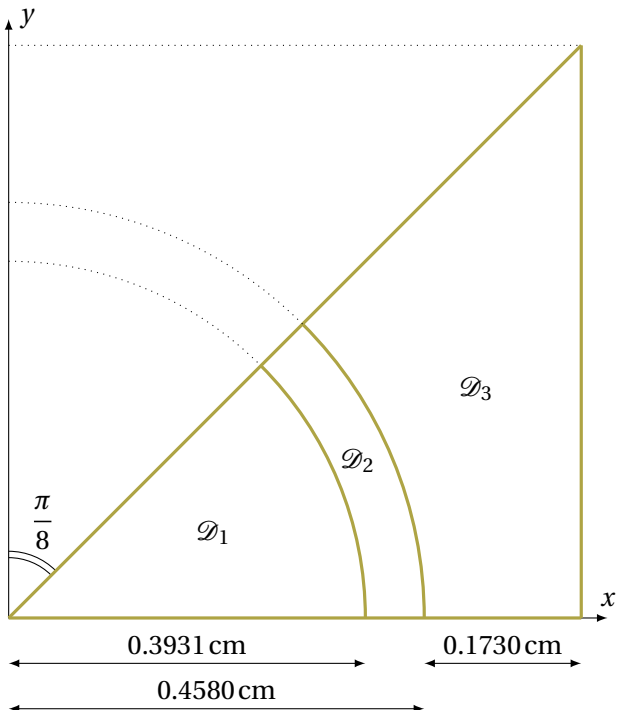

Figure 2.25: Domain for the Mosteller benchmark [Mosteller and Eisenhart, 1991], representing a typical lattice configuration.

Figure 2.25 2.25, comprising one or more concentrical fuel regions (for fine burnup analysis), the clad and the moderator. Reflection conditions are imposed on all sides, being a calculation which normally assumes no neutron leakage [Mosteller and Eisenhart, 1991].

For each cell type, the transformation is explicitly reported in the following paragraphs.

Figure 2.26b **Rings** With reference to Figure 2.26b, each hollow annular cell has four sides, whose parametric equations in t and s, with $-1 \leq t, s \leq +1$:

$$\mathscr{S}(s) = \begin{cases} x(s) = \dfrac{h}{2}(s+1) + r \\ y(s) = 0 \end{cases}, \qquad \mathscr{N}(s) = \begin{cases} x(s) = \dfrac{\sqrt{2}}{2}\left[\dfrac{h}{2}(s+1) + r\right] \\ y(s) = \dfrac{\sqrt{2}}{2}\left[\dfrac{h}{2}(s+1) + r\right] \end{cases},$$

$$\mathscr{E}(t) = \begin{cases} x(t) = (r+h)\cos\left[\dfrac{\pi}{8}(t+1)\right] \\ y(t) = (r+h)\sin\left[\dfrac{\pi}{8}(t+1)\right] \end{cases}, \qquad \mathscr{W}(t) = \begin{cases} x(t) = r\cos\left[\dfrac{\pi}{8}(t+1)\right] \\ y(t) = r\sin\left[\dfrac{\pi}{8}(t+1)\right] \end{cases}. \tag{2.69}$$

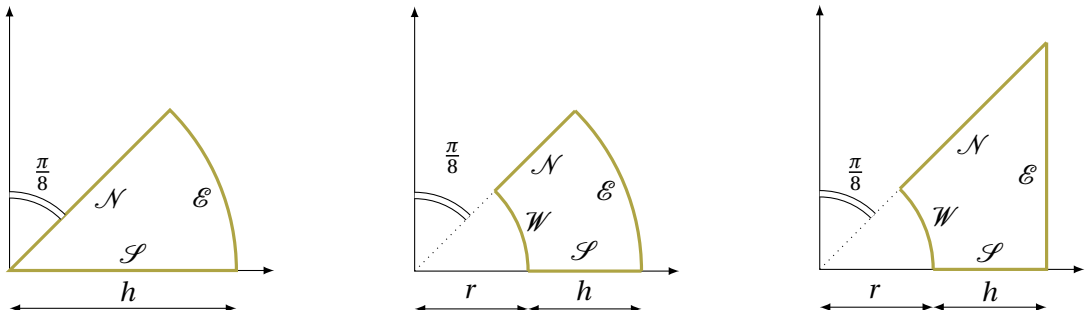

(a) Wedge (b) Ring (c) Moderator

Figure 2.26: Dimensions of the model cells

Introducing these definitions into equation (2.64), one has:

$$\Gamma(s,t) = \begin{cases} x(s,t) = \dfrac{1}{2}(h+2r+hs)\cos\left[\dfrac{\pi}{8}(1+t)\right], \\ y(s,t) = \dfrac{1}{2}(h+2r+hs)\sin\left[\dfrac{\pi}{8}(1+t)\right] \end{cases} \tag{2.70}$$

The transformation is invertible in any point, and so the associated jacobian is non vanishing everywhere.

Wedge By imposing a vanishing radius r to the previous relations, one obtains the mapping for the wedge (Figure 2.26a), representing the innermost fuel region. Thus, each side of the wedge can be parametrized as follows: *Figure 2.26a*

$$\mathscr{S}(s) = \begin{cases} x(s) = \dfrac{h}{2}(s+1) \\ y(s) = 0 \end{cases}, \qquad \mathscr{N}(s) = \begin{cases} x(s) = \dfrac{\sqrt{2}}{2}\left[\dfrac{h}{2}(s+1)\right] \\ y(s) = \dfrac{\sqrt{2}}{2}\left[\dfrac{h}{2}(s+1)\right] \end{cases},$$

$$\mathscr{E}(t) = \begin{cases} x(t) = h\cos\left(\dfrac{\pi}{8}(t+1)\right) \\ y(t) = h\sin\left(\dfrac{\pi}{8}(t+1)\right) \end{cases}, \qquad \mathscr{W}(t) = \begin{cases} x(t) = 0 \\ y(t) = 0 \end{cases}. \tag{2.71}$$

Please note the degenerate mapping which brings all points in $s = -1$ in $(0,0)$. The transfinite interpolation of the coordinate transformation is

$$\Gamma(s,t) = \begin{cases} x(s,t) = \dfrac{1}{2}h(s+1)\cos\left[\dfrac{\pi}{8}(1+t)\right], \\ y(s,t) = \dfrac{1}{2}h(s+1)\sin\left[\dfrac{\pi}{8}(1+t)\right] \end{cases} \tag{2.72}$$

which is non invertible for $x = 0$ and $y = 0$. Thus, it cannot be used if there are degrees of freedom placed in that point.

Moderator Finally, the moderator region can be represented by the area enclosed by these edges (Figure 2.26b):

Figure 2.26b

$$\mathscr{S}(s) = \begin{cases} x(s) = \dfrac{h}{2}(s+1) + r \\ y(s) = 0 \end{cases}, \qquad \mathscr{N}(s) = \begin{cases} x(s) = \dfrac{\sqrt{2}}{2}\left[\dfrac{h}{2}(s+1)\right] \\ y(s) = \dfrac{\sqrt{2}}{2}\left[\dfrac{h}{2}(s+1)\right] \end{cases},$$

$$\mathscr{E}(t) = \begin{cases} x(t) = r + h \\ y(t) = \dfrac{r+h}{2}(t+1) \end{cases}, \qquad \mathscr{W}(t) = \begin{cases} x(t) = r\cos\left[\dfrac{\pi}{8}(t+1)\right] \\ y(t) = r\sin\left[\dfrac{\pi}{8}(t+1)\right] \end{cases}. \tag{2.73}$$

The transformation from the reference domain takes the following form:

$$\Gamma(s,t) = \begin{cases} x(s,t) = \dfrac{1}{2}\left[(h+1)(1+s) - r(s-1)\cos\left(\dfrac{\pi}{8}(1+t)\right)\right], \\ y(s,t) = \dfrac{1}{4}\left[(h+r)(1+s)(1+t) - 2r(s-1)\sin\left(\dfrac{\pi}{8}(1+t)\right)\right]. \end{cases} \tag{2.74}$$

This transformation is invertible everywhere in the domain.

2.3.5 Results

A DG-SEM code with deformed elements has been implemented by the author using the MATLAB environment. The internal sparse matrix routines are used to optimize memory consumption. The solver has been specifically designed to cope with lattice problems in 8-th symmetry, like the Mosteller benchmark [Mosteller and Eisenhart, 1991] which has been already introduced. The code works in one group and source mode: its main aim is to demonstrate the convergence properties of the numerical scheme on the spatial resolution of the solution, rather than being a criticality solver. Nonetheless, its capabilities can be easily improved by adding the standard inner-outer iteration scheme or more involved protocols, as any other solver. The isotropic A_N model is fully implemented, allowing a certain degree of transport insight which is normally needed in these problems. The A_N set is solved with block iterations, one equation at a time, with a Gauss-Seidel scheme to update the pseudo-scattering terms in each solution and accelerate convergence.

Heterogeneous cylinder - comparison to diffusion

The first set of results refers to a simplified pin-clad configuration, where the presence of the moderator is neglected and reflective boundary conditions are enforced also on the curved boundary, i.e. at clad edge. The geometry (Figure 2.27) is adapted from the aforementioned Mosteller benchmark; even if the benchmark is quite idealized, the cross sections have been chosen to resemble the original values proposed by Mosteller for the original case(table 2.11). In particular, the benchmark as it is formulated has been calculated with the DRAGON code [Marleau et al., 2000] splitting the fuel region according to

Figure 2.27

Table 2.11

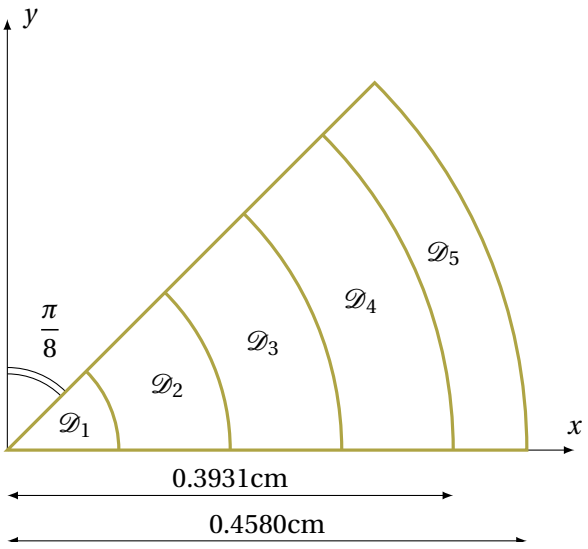

Figure 2.27: Domain for the bare pin benchmark. Dimensions are taken from the Mosteller benchmark. Regions $\mathscr{D}_1$ to $\mathscr{D}_4$ are all filled with the same fuel-like composition, and have the same extension along x (0.0983cm). Material properties may be found in table 2.11

the present case; the cross sections have been condensed to one energy group. Sources are arbitrary chosen with a step distribution trying to mimic a typical radial power distribution.

This first exercise is run only in diffusion (A_1) mode, in order to profit of the analytic solution which allows accurate evaluations on the convergence rate of DG-SEM. To compare with more classical approaches, FEM evaluations are also performed, using elements of Courant type [Quarteroni, 2009] P1 and P2 (triangular) using the code FreeFem++ [Pironneau et al., 2010].

The reaction rates for each cell is given in Figure 2.28, using the total number of degrees of freedom (N_{DOF}) as independent variable. This choice is made to compare SEM and FEM schemes considering the final size of the solution system and therefore the computational effort needed to solve it. All elements have the same polynomial order so, to recover the value of K, one may use the relation $6(K+1)^2 = N_{DOF}$, which is valid only for this domain. *Figure 2.28*

Table 2.11: Material properties for the heterogeneous source pin-clad benchmark problem.

Region	Σ_t [cm^{-1}]	Σ_s [cm^{-1}]	Source [$cm^{-3}s^{-1}$]
$\mathscr{D}_1$	4.0866E-01	3.6308E-01	1.5
$\mathscr{D}_2$	4.0866E-01	3.6308E-01	1.3
$\mathscr{D}_3$	4.0866E-01	3.6308E-01	1.0
$\mathscr{D}_4$	4.0866E-01	3.6308E-01	0.8
$\mathscr{D}_5$	2.4653E-01	2.4438E-01	0.0

Table 2.12: Material properties for the homogeneous source pin-cell benchmark problem.

Region	Σ_t [cm^{-1}]	Σ_s [cm^{-1}]	Source [$cm^{-3}s^{-1}$]
$\mathscr{D}_1$	7.2487E-01	7.0816E-01	1.0
$\mathscr{D}_2$	7.2487E-01	7.0816E-01	0.0
$\mathscr{D}_3$	7.2487E-01	7.0816E-01	0.0

The FEM grid is assembled using the FreeFEM++ embedded meshing tool, based on the Delunay algorithm for triangulation. Mesh size is uniform throughout the domain. The SEM scheme reaches quickly a level of error comparable to round-off, and its pattern is almost the same for any considered cell. On the contrary, the FEM schemes are much slower and the magnitude of the deviations varies considerably across the domain.

This fact is due to the local mass conservation principle, which is a distinctive feature available in DG and not in the CG of classical Courant FEM. The neutron balance is conserved in each cell, while for CG this statement is valid only looking at the ensemble of the cells forming the domain. For further confirmation, the error trend is calculated on the sum of the reaction rates of each cell (Figure 2.28f): while the FEM scheme shows the same trend as in each single cell, the values of the SEM trend are lower, indicating that the neutron balance is better conserved on a global scale than at the local one. This is of course a strong point in favor of the SEM approach for nuclear applications, since the main goal remains the computation of reaction rates in discrete portions of the system.

Figure 2.28f

Mosteller benchmark - homogeneous

Figure 2.25 The second set of results uses the geometry specified by Mosteller (Figure 2.25). There are only three elements, standing for the fuel, the clad and the moderator. The cross sections *Table 2.12* (Table 2.12) are again issued from a full homogenization of the original critical Mosteller benchmark on all three regions. The source in the fuel region reproduces the flux integrated values on each of the three cells, thus mimicking a realistic power profile for a lattice calculation. Anyway, since homogenization is concerned, the scope of this evaluation is again mainly to check the convergence of the method and, at the same time, the convergence of the A_N scheme to the transport solution, because in this case the asymptotic convergence is guaranteed by the equivalence to the integral form of the transport equation, as illustrated in chapter 1.

Figure 2.29 Figures 2.29 show the reaction rates of each of the cells $\mathscr{D}_1$, $\mathscr{D}_2$ and $\mathscr{D}_3$, followed by the *Figure 2.29d* total reaction rate $\mathscr{D}_1 + \mathscr{D}_2 + \mathscr{D}_3$ in Figure 2.29d. The model used is A_2.

The behavior of SEM, compared to FEM, is quite varying. Apart from very low-order schemes, where foreseeable oscillations are to be ascribed to the Lagrangian interpolation functions, the convergence trend is similar to the previous evaluations, with a fast convergence of SEM and a much slower trend for FEM. Anyway, the average value of the error in each cell changes; as far as SEM is concerned, it follows the density of degrees of freedom, being in the clad region the most remarkable accumulation of points in the radial direction.

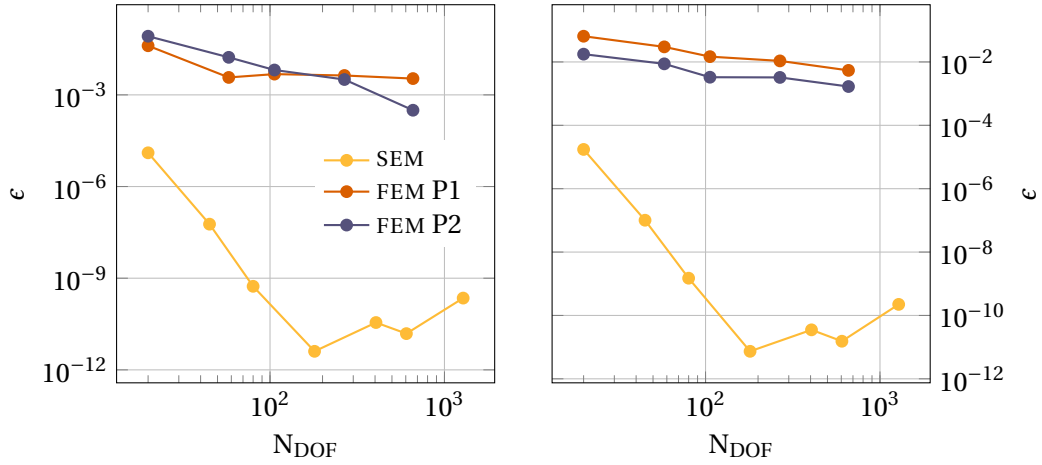

(a) Fuel (ring $\mathscr{D}_1$)

(b) Fuel (ring $\mathscr{D}_2$)

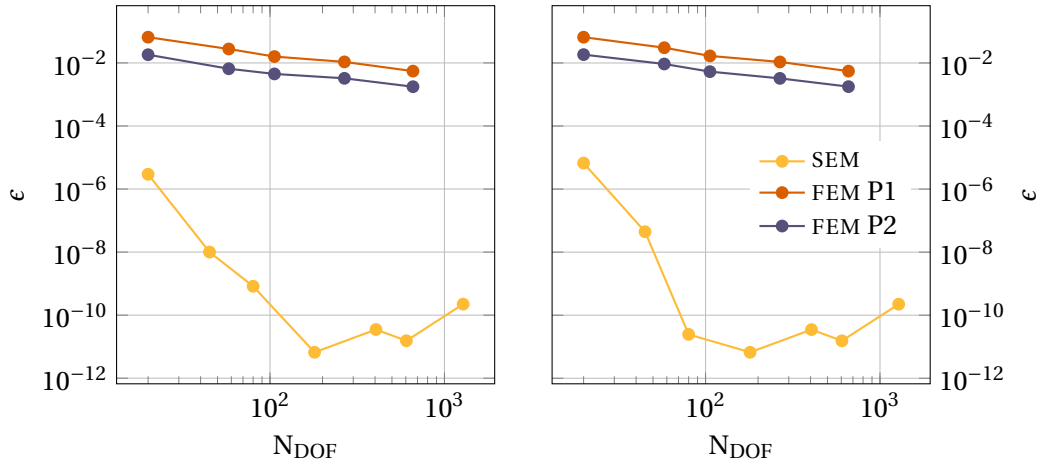

(c) Fuel (ring $\mathscr{D}_3$)

(d) Fuel (ring $\mathscr{D}_4$)

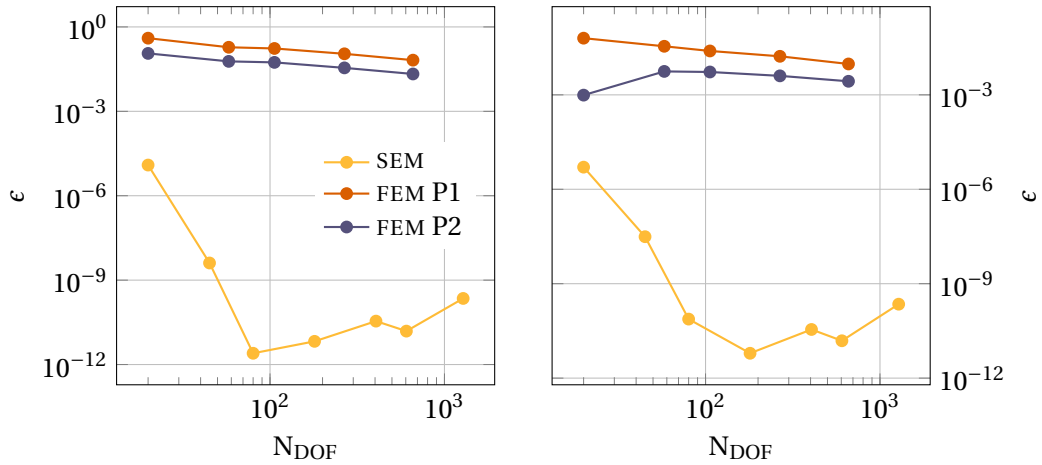

(e) Clad (ring $\mathscr{D}_5$)

(f) All the domain

Figure 2.28: Bare pin benchmark: reaction rates compared to diffusion, for each of the 5 cells in which the domain is subdivided

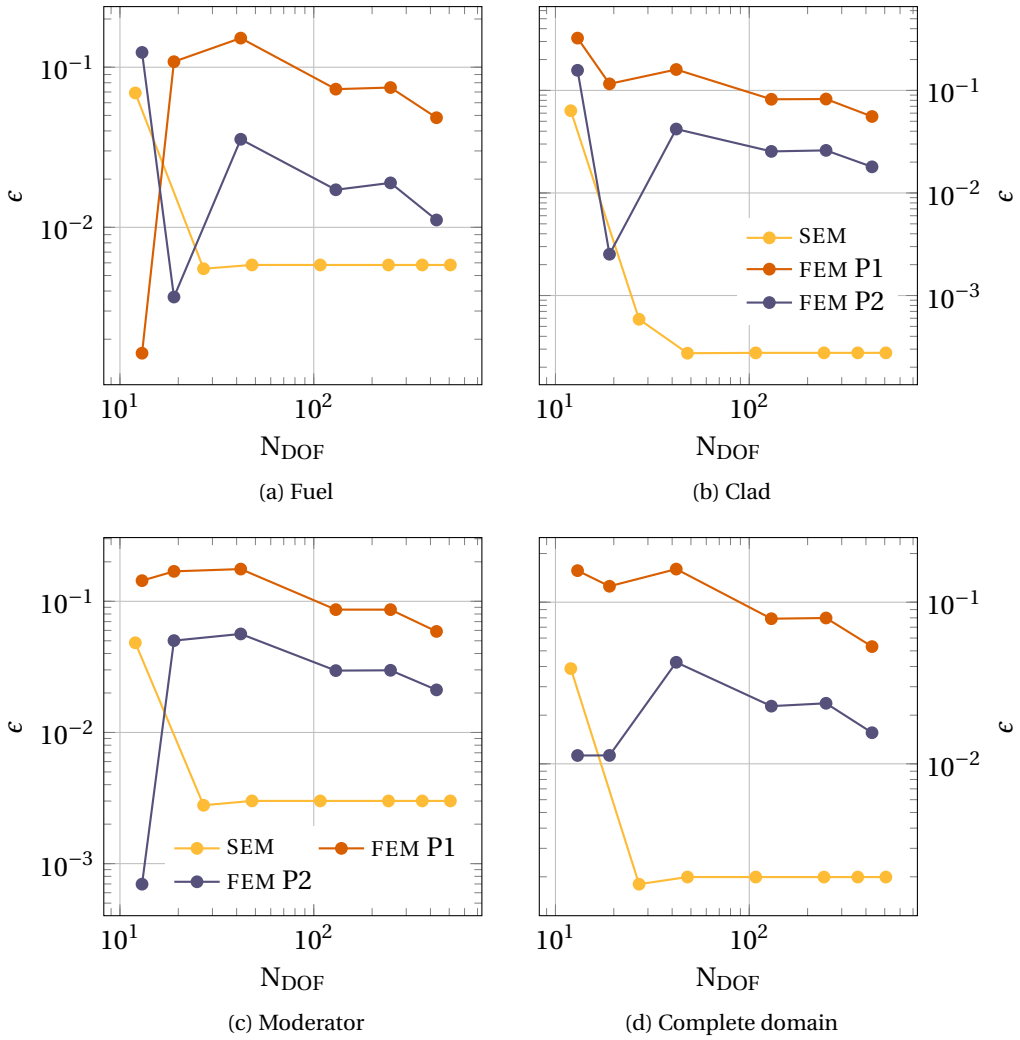

(a) Fuel (b) Clad

(c) Moderator (d) Complete domain

Figure 2.29: Homogeneous Mosteller benchmark: relative error of A_2 SEM and FEM schemes.

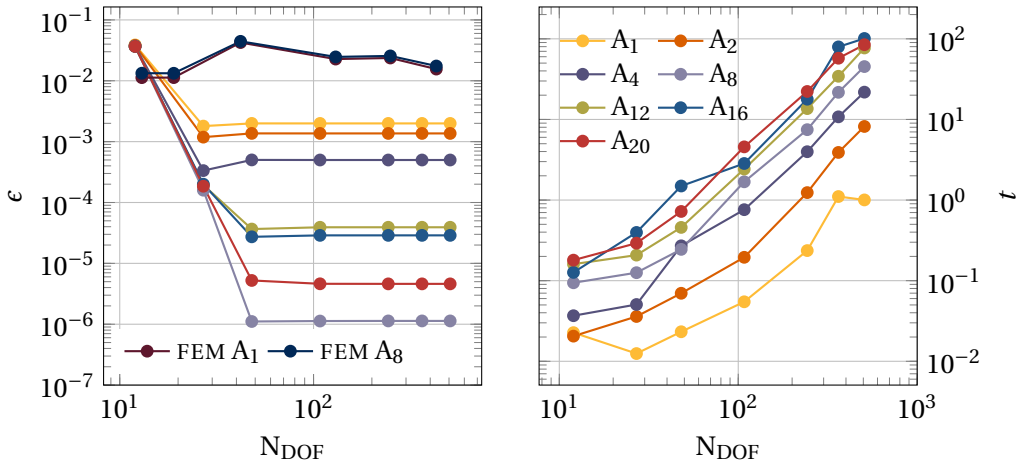

(a) Total reaction rate (b) Computational time

Figure 2.30: Homogeneous Mosteller benchmark: reaction rates and computational time, for various A_N orders. If not specified in the legend, values are for SEM computations.

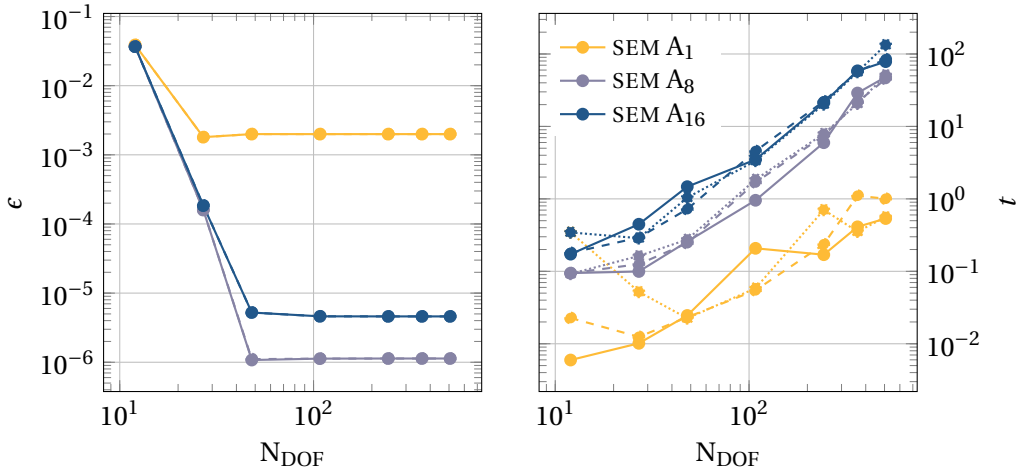

(a) Total reaction rate (b) Computational time

Figure 2.31: Mosteller homogeneous benchmark: parametric study on the total reaction rate and the computational time varying the DG penalty parameter σ. Values used are 1 (dotted lines), 5 (dashed lines) and 10 (solid lines).

Table 2.13: Material properties for the heterogeneous source pin-cell benchmark problem.

Region	Σ_t [cm^{-1}]	Σ_s [cm^{-1}]	Source [$cm^{-3}s^{-1}$]
$\mathscr{D}_1$	4.0866E-01	3.6308E-01	2.0
$\mathscr{D}_2$	2.4653E-01	2.4438E-01	0.0
$\mathscr{D}_3$	9.7874E-01	2.4438E-01	0.0

FEM does not show the same behavior because the triangular elements are not deformed too much, and thus its mesh remains homogeneous. The performances of SEM in the fuel region are not impressive, though quite satisfactory.

Figure 2.29d The total reaction rate is presented in Figure 2.29d. The total reaction rate is also given in *Figure 2.30a* Figure 2.30a, as a function of the order N. FEM schemes demonstrate low sensitivity to the model change, mainly due to the slow convergence which tends to shadow the improved accuracy of the model. On the other hand, the fast SEM convergence allows to appreciate the higher precision with increasing A_N order. It has to be noted that the DRAGON and FEM results are given with 6 significant digits, so the results in the 10^{-5}-10^{-6} range cannot be considered truly representative of the effective discrepancy between A_N and transport, which is demonstrated by theory.

Solution time has been measured, excluding the matrix preparation time in order to isolate the work done by the computing routines. As expected, it scales exponentially with the number of degrees of freedom, and almost linearly with the A_N order.

Finally, the role of the penalty parameter is investigated. The definition of the optimum parameter is still an open research question [Rivière, 2008]; for the scopes of this thesis, it is satisfactory to check if this parameter has a non-negligible effect on the reaction rates, identify a range, or a threshold value, for where it can be safely chosen, at least for this problem.

Calculations have been performed for all A_N orders from 1 to 20, for penalty parameters 1,5 and 10, which are values typically used in DG-FEM computations and are widely accepted by the community.

The influence of the penalty parameter on the total reaction rates is shown in Figure *Figure 2.31a* 2.31a, as well as for the computational time in Figure 2.31b. There does not seem to be any *Figure 2.31b* bias on the values of the reaction rates, meaning that the scheme remains consistent with the original weak formulation regardless of the penalty parameter. Not really significant differences on the computational times are imputable to the penalty.

Mosteller benchmark - heterogeneous

This last benchmark considers a heterogeneous pin-cell configuration. The original problem, as it was formulated by Mosteller has been solved with DRAGON using a 64 group library; single group condensed cross sections are then used to solve again a source problem with DRAGON, determining a reference solution. A unitary source imposed on the fuel region produces a flux distribution which is quite close to that obtained in the critical case.

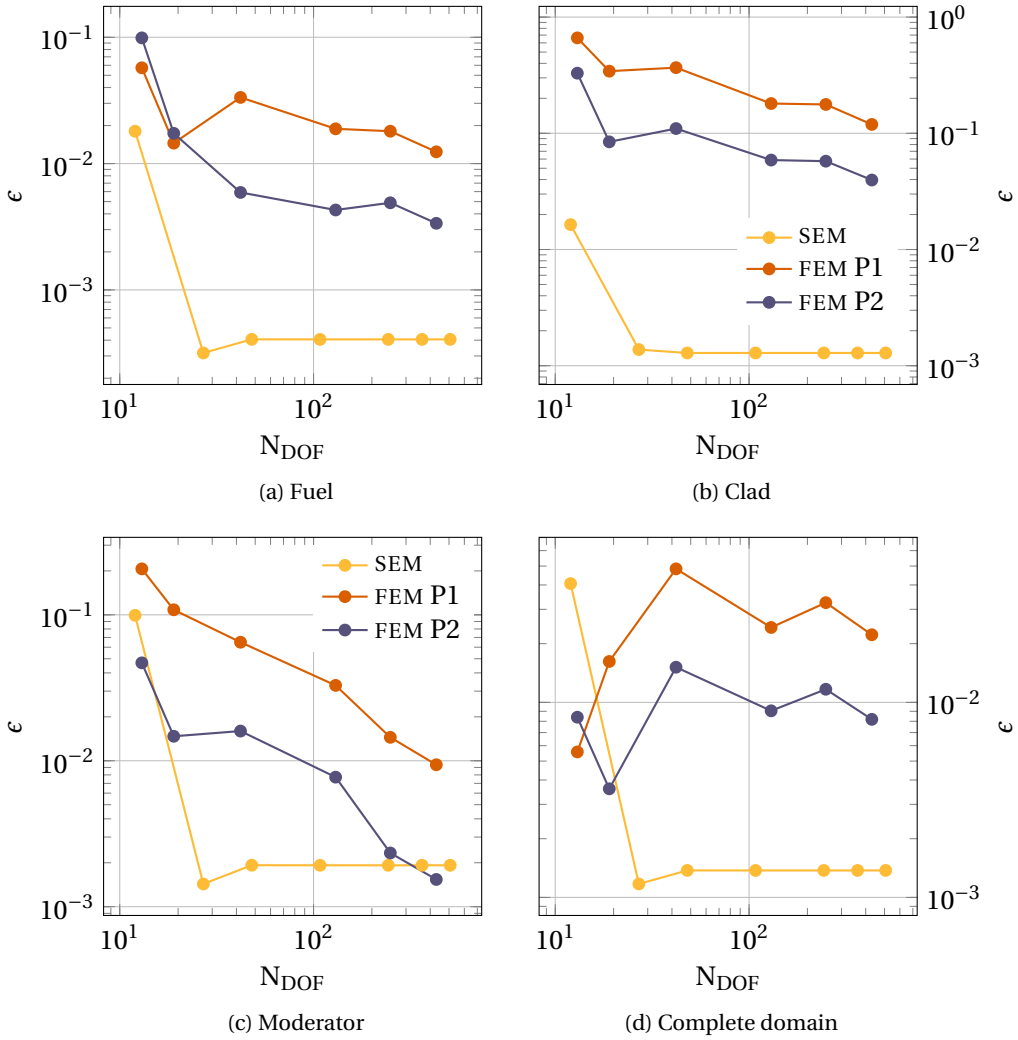

(a) Fuel

(b) Clad

(c) Moderator

(d) Complete domain

Figure 2.32: Relative error of A_2 SEM and FEM schemes compared to the reference analytic solution for the source-driven Mosteller benchmark.

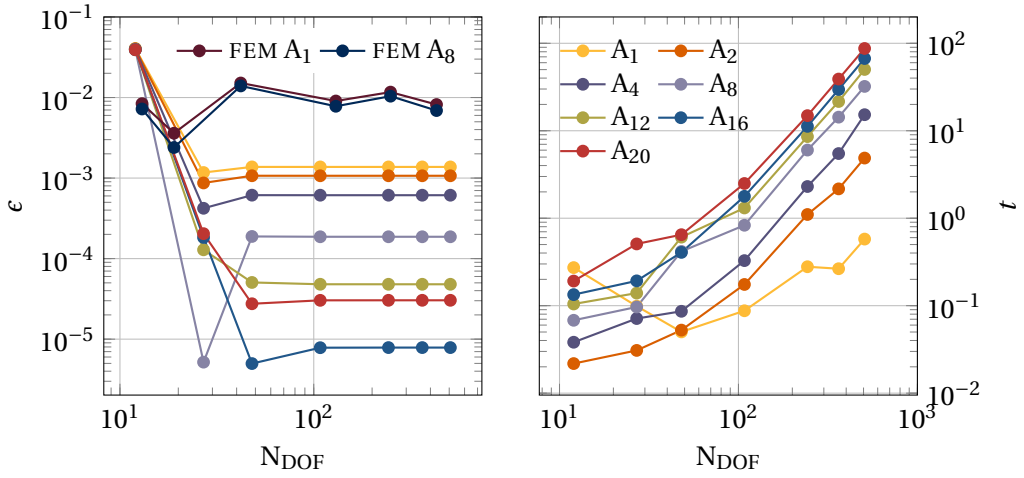

(a) Total reaction rates (b) Computational time

Figure 2.33: Heterogeneous Mosteller benchmark: reaction rates and computational time, for various A_N orders. If not specified in the legend, values are for SEM computations.

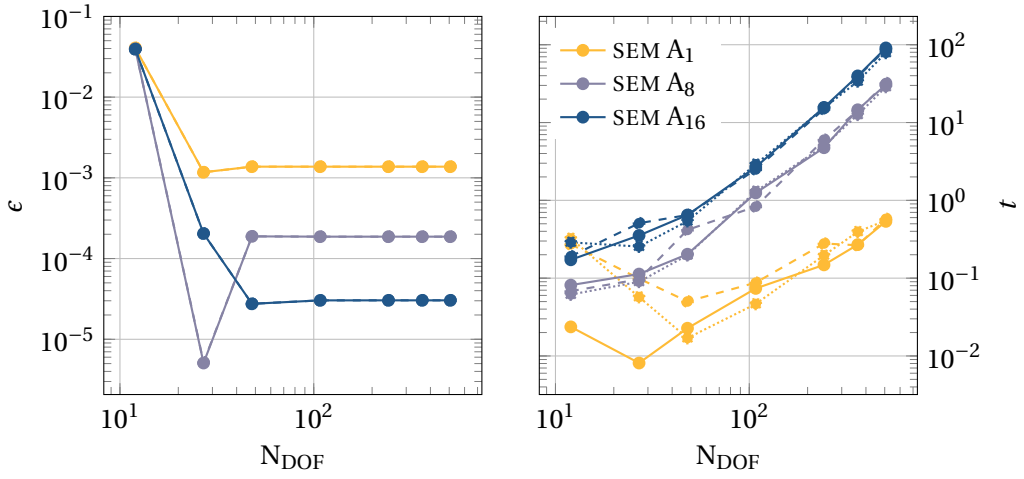

(a) Total reaction rate (b) Computational time

Figure 2.34: Mosteller heterogeneous benchmark: parametric study on the total reaction rate and the computational time varying the DG penalty parameter σ. Values used are 1 (dotted lines), 5 (dashed lines) and 10 (solid lines).

The same input parameters are used in the MATLAB DG-SEM code and in the FEM code (FreeFem++).

A set of results, similar to the ones obtained for the homogeneous case, are here presented.

Figure 2.32 shows the relative error of the reaction rates in each of the considered cells. *Figure 2.32*
The FEM calculations overlap the SEM ones in the moderator, where FEM seems to approach the correct solution while SEM seems to converge steadily on a biased value. Anyway, A_N (and A_2 even more) does not converge to the real transport solution, so the presence of a bias is expected. Moreover, the fact that the neutron balance is not respected in each cell may shift the FEM solution of some amount, which should anyway disappear with an infinitely refined grid. Since the source of the bias cannot be trivially isolated, one may look at the total reaction rate considering $\mathscr{D}_1 + \mathscr{D}_2 + \mathscr{D}_3$, Figure 2.32d, to eliminate at least *Figure 2.32d*
the problem of the conservation of neutrons. The results show a more natural convergence of the two schemes towards, possibly, the same solution, even if FEM schemes are slower compared to SEM that a common PC, like the one used for these evaluations, cannot cope with the huge algebraic systems required to achieve the same accuracy.

Furthermore, the effect of the A_N order is investigated and results are given in Figure 2.33a. The relative error compared to the DRAGON transport solution is evaluated for a *Figure 2.33a*
varying order K and reducing in parallel the length of the FEM average mesh, with an increasing transport detail. The SEM solution seems to reduce its margin versus the transport one as already observed in Figure 2.30a; the only difference seems to be a higher order of *Figure 2.30a*
the converged solution for A_{16}-A_{20} which, still considering the effect of the limited number of available digits, may suggest that the converged A_∞ solution and the real transport flux actually differ of a factor 10^{-5} on the total reaction rate.

Again, time scales almost linearly with the order N, suggesting that the spectral properties of the SEM-A_N operator, which is never assembled completely but solved iteratively, are not much altered by the change in order.

Finally, the effect of penalty is checked with the same motivation as before (Figures 2.34a *Figure 2.34a*
and 2.34b). Again, the numerical scheme shows a negligible sensitivity to the typical values *Figure 2.34b*
of penalty parameters used.

2.3.6 Comments on the transfinite interpolation approach

This section has introduced another efforts made to improve the flexibility of the SEM method for neutron transport problems. Compared to the classical approach [Barbarino, 2010], the DG-SEM one endowed with transfinite interpolation seems now adequate to cope with the involved geometries present in nuclear applications. The developments presented here are of help for the implementation, and the convergence properties analysed in simple one-dimensional benchmarks in section 2.1 are confirmed also for the the Mosteller exercise.

Nonetheless, such flexibility and precision has to cope with the limited definition of the second order transport models, which are the ones that may profit best of the SEM strategy. The DG-SEM approach reduces to very low levels the amount of spatial discretization error with limited computational cost, but the drawbacks of the A_N model are not touched, and

become now the weaker point of this approach, to be further investigated and mitigated. Anyway, at lattice level, results seem to show a quite limited amount of discrepancy, which may justify the use of this technique as it is.

3 Industrial core analysis with the A_N model

Due to the high number of full-core studies required for the design, licensing and operation phases of commercial nuclear reactors, time constrains are relevant on the formulation of the neutronic models and the solver architectures. Typically, only the diffusive approximation of the Boltzmann neutron transport equation is available in codes used for power nuclear installations.

This chapter deals with the implementation of the A_N model in legacy diffusion codes; its mathematical formulation is given in chapter 1, together with the hypotheses which allow its derivation.

The contents of the chapter are split into two parts. In section 3.1 the A_N method, in its isotropic form already introduced in equation (1.61), is implemented in some industrial core analysis tools and applied to representative clusters of assemblies (called *colorsets*) and to a full-core case.

The hypothesis on scattering isotropy is quite restricting for the industrial quality levels; nowadays very often at least the first moment of scattering is considered through a suitable adjustment of the diffusion parameters. In section 3.2, the anisotropic A_N model, already introduced in section 1.1.4 in the original form, is re-elaborated and three different algorithms are studied, taking into account the unfavorable mathematical structure of model (1.69) and the constraints of the code practice. Only one of the alternatives is implemented in a demonstrative solver, and some results are introduced for a 1D colorset.

Results are tailored to a feasibility analysis, but the real aim of the entire chapter is to highlight the many implementation issues: these aspects are predominant over modeling in the industrial framework, and the problems encountered may apply also to other schemes, like SP_N.

3.1 Isotropic A_N implementation

In industrial nuclear reactor simulation, the two-group diffusion model spatially discretized with a nodal approach has been used used for several decades. This configuration allows the implementation in very fast codes, but may suffer important limitations in the description of the power distribution: this physical model neglects completely the effect of the angular anisotropy of the neutron flux [Bell and Glasstone, 1970], with possible loss of accuracy.

The multi-level scheme presently in use, which starts from detailed transport calculations in given portions of the system to produce few-group cross section datasets for full-core analysis, is certainly very practical. Conservation of reaction rates achieved by spatial homogenization, energy condensation and proper flux factorization in coarse regions allows a great simplification in the treatment of strong localized transport effects [Bell and Glasstone, 1970; Zmijarevic et al., 2006]. When large volumes compared to the neutron mean free path are considered, and provided that pure particle absorption is not the dominant phenomenon, relevant transport effects may only arise at interfaces. However, the higher is the material heterogeneity the more they gain importance in the system, like for instance in complex UO_2 and MO_X fuel loading patterns.

As far as the accuracy of the model is concerned, there are generally different situations inside any nuclear system where local transport effects play a non-negligible role. At a lower spatial scale pin-by-pin calculations, where each fuel pin is homogenized to a single cell, are also highly affected by flux anisotropies, especially near the instrumentation and control rods. Possibly, the flux distribution may show steep variations, with unavoidable distortions of the flux isotropy postulated to accept the use of the diffusive approach.

In recent times, the SP_N method [Brantley and Larsen, 2000] has gained the attention of the industrial experts because it may constitute in the short term a valuable trade-off between implementation ease and angular detail resolved [Downar et al., 2004; Baudron and Lautard, 2007]. Among the various formulations available, the A_N formalism allows to arrange the SP_N model into a set of coupled second-order equations, which are handier to be solved with a cheap implementation effort; despite the different meaning of the coefficients, one formally obtains a set of equations of the same analytical nature of multi-group diffusion. The model has been introduced in section 1.1 and details can be found in Coppa and Ravetto [1982], Coppa and Ravetto [1981], Coppa et al. [1982] and Ciolini et al. [2002]. In principle, then, it is possible to treat this higher order transport approximation with any of the existing diffusion codes, even using the standard nodal approach for the space discretization.

In the SP_3, most neutronic codes currently in use solve the model by combining the equations in a way that two second-order diffusion-like equations remain, coupled only by the scattering term (see for instance Downar et al. [2004] for the PARCS code). The use of A_N is an effective strategy to increase the order of the transport approximation N with a consistent and straightforward procedure, nevertheless conserving the easiness to be embedded in production codes.

3.1.1 Nodal methods in reactor simulation

Cross section homogenization and condensation allow describing the nuclear core in a multi-region problem with a given set of constant data in each region, usually called node [Lawrence, 1986]. The number of nodes is instructed by computational time constraints and suggested by the geometrical regularity of the domain.

Larger volumes call generally for lower order transport operators, thus aiming only at asymptotic transport solutions. The standard technique to model water reactors employs quarters of fuel assemblies in diffusion theory; indeed, pin-by-pin calculations generally

need more accurate transport approximations or tailored diffusion entities to cope with finer meshes of the order of the neutron mean free path.

Considering meshes in a Cartesian reference frame, a typical scheme proceedes as follows. A first discretization is carried out by the finite volume technique [Ferziger and Peric, 2002]. Since analytical and semi-analytical solutions are known for linear second-order partial differential equations in the homogeneous medium, spectral synthesis methods are now extensively used to solve diffusion problems [Hébert, 2010; Tomatis, 2010]. Then, the problem is conveniently decoupled by the transverse integration procedure, which needs, however, some further approximations for the neutron leakage introducing additional non-linearity. The assumption of a quadratic leakage along the transverse directions of integration is usually accepted. Various flux expansions are accounted in literature, starting from polynomial bases to the kernel solutions of the associated homogeneous diffusion equation.

Full analytical multi-dimensional solutions are less common for specific numerical issues, but they are certainly of great interest [Melice, 1978; Fu and Cho, 2002].

3.1.2 Implementation and issues

Multigroup A_N operator in tensor form The isotropic multigroup A_N model has been introduced in (1.61), and it is repeated here for convenience:

$$\begin{cases} \dfrac{\mu_\alpha^2}{\Sigma_g}\nabla^2\varphi_{\alpha,g} - \Sigma_g\varphi_{\alpha,g} + \displaystyle\sum_{g'}^{G}\Sigma_{s,g'\to g}\Phi_g + \frac{1}{k}\chi_g\sum_{g'}^{G}\nu\Sigma_{f,g'}\Phi_{g'} = 0 \\ \Phi_g = \displaystyle\sum_{\beta=1}^{N} w_\beta\phi_{\beta,g}, \qquad \alpha = 1,\dots,N, \quad g = 1,\dots,G. \end{cases} \tag{3.1}$$

The notation can be simplified adopting a single index which counts all the possible combinations of g and α, obtaining a single equation set to be implemented in the standard procedures of the diffusion solver. This formalism is recovered by comparison to multigroup diffusion. In fact, the classical set of multi-group diffusion equations in compact matrix notation is:

$$\left[\mathbf{D}\nabla^2 - \mathbf{C} + \mathbf{T} + \frac{1}{k}\mathbf{F}\right]\boldsymbol{\Phi} = \mathbf{0}, \tag{3.2}$$

where

$$\begin{aligned} \mathbf{D} &= \left\{D_{gg'} = D_g\delta_{gg'}\right\}, \\ \mathbf{C} &= \left\{C_{gg'} = \Sigma_g\delta_{gg'}\right\}, \\ \mathbf{T} &= \left\{T_{gg'} = \Sigma_{s,g'\to g}\right\}, \\ \mathbf{F} &= \left\{F_{gg'} = \chi_g\nu\Sigma_{\mathrm{f},g'}\right\}, \\ \boldsymbol{\Phi} &= \left\{\Phi_g\right\}. \end{aligned}$$

By contrast, the A_N model writes:

$$\left[\mathbf{D}^\star\nabla^2 - \mathbf{C}^\star + \mathbf{T}\otimes\mathbf{U} + \frac{1}{k}\mathbf{F}\otimes\mathbf{U}\right]\boldsymbol{\varphi} = \mathbf{0}, \tag{3.3}$$

where

$$\mathbf{D}^\star := \left\{ D^\star_{\ell,\ell'} = \frac{\mu_\alpha}{\Sigma_g} \delta_{\ell,\ell'} \right\},$$
$$\mathbf{C}^\star := \left\{ C^\star_{\ell,\ell'} = \Sigma_g \delta_{\ell,\ell'} \right\},$$
$$\mathbf{U} := \left\{ U_{n,m} = w_m \right\},$$
$$\boldsymbol{\varphi} := \left\{ \varphi_\ell \right\},$$

with $g = 1,\dots,G$ and $m,n,\alpha = 1,\dots,N$ and using for the combined A_N-multigroup case the following ordering

$$\ell,\ell' = (g-1)N + \alpha; \tag{3.4}$$

the other definitions are unchanged. The ordering (3.4) preserves the diagonality of the diffusive and removal terms with respect to the operators found in (3.2).

Assembly discontinuity factors Nodal codes usually adopt the discontinuity factors defined according to the generalized perturbation theory [Lawrence, 1986]; these factors are calculated by the lattice codes for two of the three coordinate directions at least [Rechantin and Schenider, 2012]. The use of these factors is a compulsory complement to the homogenized cross section set which is obtained by the lattice model; they are typically used in conjunction with the diffusive hypothesis, but their applicability is not bounded to this specific flux description. Then, in principle it is certainly licit to use them with an A_N formalism, but it should be granted that the effect of the heterogenized fluxes and interface currents, the physical quantities on which discontinuity factors are defined, is conserved at least after the reconstruction.

If one considers two homogeneous adjacent regions A and B, the discontinuity condition [Lawrence, 1986]

$$f^{(A)}\Phi^{(A)} = f^{(B)}\Phi^{(B)} \tag{3.5}$$

may be A_N expanded as follows

$$f^{(A)} \sum_{\alpha=1}^{N} \varphi_\alpha^{(A)} = f^{(B)} \sum_{\alpha=1}^{N} \varphi_\alpha^{(B)} \tag{3.6}$$

Thanks to the linearity of the flux and current reconstruction relations (1.54) and imposing as interface conditions

$$f^{(A)}\varphi_\alpha^{(A)} = f^{(B)}\varphi_\alpha^{(B)} \tag{3.7}$$

for all $\alpha = 1,\dots,N$, one certainly satisfies (3.5) also with the discontinuity factors calculated for diffusion. A similar remark holds for currents, which obey to the the linear relation in equation (1.56).

Concerning the implementation of A_N, including the formalism of the discontinuity factors, with respect to the overall code structure, the modifications to be applied to a diffusion code are in principle restricted only to the flux solver and its cross section model; in particular the depletion, thermal feedback, dehomogenization modules as well as the homogenization and condensation schemes should be untouched by the introduction of the

A_N formalism. This feature is of great avail to core analysis in A_N theory on a large scale. Once cross sections are determined, no modifications in the main solving routines are necessary for steady-state problems; only extrapolation lengths may optionally be modified. Pre-processing of macroscopic cross sections and post-processing of pseudo-fluxes are the prominent required developments.

Issues concerning the implementation in legacy codes The implementation of second-order models requires diffusion codes working with general multi-group formalism [Barbarino and Tomatis, 2013a], and codes optimized for two groups might not suit the purpose [Downar et al., 2004; Larsen et al., 1996]; difficulties arise from specific optimizations and from the way the diffusive model is generally recast.

The first issue is related to the presence of certain routines, which are intended to be used rigidly with a specific formulation. These parts include in particular the accelerations and linear system solvers, which have to be modified or substituted with more general algorithms. The second issue is more severe: in order to reduce the flow of data through the solver and its memory footprint, often the classical two-group diffusion equation is recast in order to aggregate some parameters. For instance, a common approach represents the total and scattering cross sections through the absorption cross sections and arranging the up/down scattering terms in the removal cross section together with the homogenization spectrum [Dall'Osso and Ponce, 1998; Garland, 2005]; this model can be expressed in matrix form as:

$$-\nabla^2 \begin{bmatrix} D_1 & 0 \\ 0 & D_2 \end{bmatrix} \begin{pmatrix} \Phi_1 \\ \Phi_2 \end{pmatrix} + \begin{bmatrix} \Sigma_{a,1} & 0 \\ 0 & \Sigma_{a,2} \end{bmatrix} \begin{pmatrix} \Phi_1 \\ \Phi_2 \end{pmatrix} + \begin{bmatrix} -\Sigma_r & 0 \\ \Sigma_r & 0 \end{bmatrix} \begin{pmatrix} \Phi_1 \\ \Phi_2 \end{pmatrix} = \frac{1}{k} \begin{bmatrix} \nu\Sigma_{f,1} & \nu\Sigma_{f,2} \\ 0 & 0 \end{bmatrix} \begin{pmatrix} \Phi_1 \\ \Phi_2 \end{pmatrix} \tag{3.8}$$

As well, the set of optimized cross sections is provided by the lattice code of the calculation chain, and the reconfiguration of the output to retrieve full information on cross sections may not be promptly feasible for validation restrictions.

Another issue is related to the sign of the pseudo-fluxes. While physical fluxes are always positive, the pseudo-fluxes arising in A_N may in general change sign[1]. Both the finite volume approach and the nodal formalism should be insensible on the sign of the unknowns, but run-time control checks may have been added in order to stop execution with classical diffusion calculations. An extensive analysis of all ancillary routines is compulsory in order to identify these features and adapt them, or eventually inhibiting them without major consequences.

Finally, the derivation of A_N from the integral transport equation, presented in section 1.1.4, suggests that each pseudo-flux behaves like a virtual neutron population, thus endowed with a proper mean free path. While in diffusion theory the neutron mean free path scales as the inverse of the total cross section Σ, in A_N it goes as μ_α/Σ, as it is clear

[1] It can be demonstrated that only if the medium is homogeneous the sign is predictable, being always positive. In fact, in this particular case an equivalence with even parity S_N is proved, and in the latter case the unknowns are the sum of the physical fluxes on a couple of symmetrical directions [Coppa and Ravetto, 1981].

from (1.65). Being, by definition, $\mu_\alpha < 1$, the mean free path tends to reduce with growing values of N; pushing the order to high values, notwithstanding the general limitations of second-order approaches and the inefficacy of these models to increase the transport detail as explained in section 1.1.4, it may eventually reach very small values. This means, also, that the characteristic length of neutron motion reduces: the grid should be refined because steeper variations in the pseudo-fluxes appear and they should match the mesh size to be resolved. Grid refinement, though costly, is rarely possible on industrial code architectures, where the "quarter assembly" mesh size is a standard; often the mesh size is a trade-off arising from the coupling between the neutronic and thermal-hydraulic modules of the core analysis tool, and in this case there is no room for unbalanced grid refinement.

Some results after the implementation in the AREVA analysis tools A few A_N applications calculations by nodal diffusion codes demonstrate the practical feasibility of this approach. Results from a mono-dimensional diffusion solver are presented first, detailing the behavior of the neutron flux close to a representative node interface. Then, an AREVA industrial code is used to solve a UO_2/MO_X color-set problem and finally a realistic core configuration.

In the contest of this work, the A_N formulation is implemented in several existing codes, some of them being AREVA commercial codes used for reactor design and safety assessment. Due to the high degree of optimization achieved after almost 30 years of development, the codes are characterized by several peculiarities that are not usually found in more "general purpose" core analysis tools. Since the target of this section is to prove the feasibility of the A_N approach in an industrial framework, some interest has been placed on the investigation of these peculiarities and on the ways to handle them. Not all the details of the implementation are here reported, since they constitute sensitive industrial property.

The core analysis code is fed with a library of cross sections obtained by the lattice code, an AREVA customized version of the CEA code APOLLO2. In order to overcome the incompleteness of the cross section set, since the library contains only the cross sections specified in the model (3.8), some additional code modifications have been performed. When possible, the original APOLLO2 `hdf` output file has been read and the homogenized cross sections extracted, skipping the pre-processing actually responsible for producing the final library. This injection of raw cross sections into the core code is practical, but only suitable for small colorsets due to its low speed, and cannot be considered procedural.

Indeed, when a complete core is concerned, the library is retained and some assumptions are made. The diffusion coefficient D_g is retained, since it is obtained with a validated procedure [Rechantin and Schenider, 2012] from a single-assembly homogenization in critical conditions. A guess of the transport cross section $\Sigma_{\mathrm{tr},g} = \Sigma_g - \Sigma_{\mathrm{s},g,1}$ is derived assuming

$$D_g = \frac{1}{3\Sigma_{\mathrm{tr},g}}, \quad g = 1,2; \tag{3.9}$$

in absence of any other clue on the Σ_g value, parameter κ is introduced, which allows to estimate the group total cross section as $\Sigma_g = (1+\kappa)\Sigma_{\mathrm{tr},g}$, adding and removing some

scattering to the physics of the material. The in-group scattering cross section follows as $\Sigma_{s,g,0} = \Sigma_g - \Sigma_{a,g}$, being the absorption cross section always available in diffusion libraries. The parameter κ is here unknown, and it is let varying on a wide range. Even if this escamotage does not allows precise evaluations on a single reactor state point, nonetheless this procedure builds several cross section sets describing comprehensive operating conditions, which is acceptable for the scope of this work. Moreover, the removal cross section $\Sigma_{r,g}$ is used as the down-scattering term, and no up-scattering is explicitly considered, even though its amount is consistently included in the removal formalism[2]. Furthermore, to comply with the standard treatment of anisotropy in diffusion codes, the $1/\Sigma_g$ in the leakage term of each A_N equation has been substituted by $1/\Sigma_{tr,g}$: in this way the approximation adopted in diffusion is transferred to all A_N equations and to the interface currents in exactly the same way; thus only approximated, this treatment is straightforward to implement and does not affect negatively the scheme accuracy. Section 3.2.1 will introduce more involved algorithms studied to consider anisotropy in a fully consistent fashion.

All these considerations lead to implement the following A_N multigroup set of equations:

$$\begin{cases} \dfrac{\mu_\alpha^2}{\Sigma_{tr,1}}\nabla^2\varphi_{\alpha,1} - \Sigma_1\varphi_{\alpha,1} \\ \qquad + \left(\Sigma_{s,1,0} - \Sigma_r + \dfrac{1}{k}\nu\Sigma_{f,1}\right)\displaystyle\sum_{\beta=1}^{N} w_\beta\varphi_{\beta,1} + \frac{1}{k}\nu\Sigma_{f,2}\sum_{\beta=1}^{N} w_\beta\varphi_{\beta,2} = 0, \\ \dfrac{\mu_\alpha^2}{\Sigma_{tr,2}}\nabla^2\varphi_{\alpha,2} - \Sigma_2\varphi_{\alpha,2} + \Sigma_r\displaystyle\sum_{\beta=1}^{N} w_\beta\varphi_{\beta,1} + \Sigma_{s,2,0}\sum_{\beta=1}^{N} w_\beta\varphi_{\beta,2} = 0, \\ \Phi_g = \displaystyle\sum_{\alpha=1}^{N} w_\alpha\varphi_{\alpha,g} \end{cases} \tag{3.10}$$

for $\alpha = 1,\dots,N$ and $g = 1,\dots,G$.

3.1.3 Results

The 1D interface problem

The A_N methodology has been implemented in a multi-group 1D diffusion solver. In order to have a transport reference, an S_N solver is also used, with the same machine precision (single) but a different numerical scheme, since it adopts the diamond difference sweeping algorithm [Lewis and Miller, 1993]

The 1D solver has been originally prepared by Dr. Tomatis and adapted by the author, and reproduces accurately the coarse mesh algorithm of finite volumes and polynomial nodal method used in industrial codes in more dimensions, with the only absence of the transverse leakage model.

The computational domain is composed of two layers of different homogeneous materials. Each block is 10.75 cm thick and is subdivided into 40 elementary cells to get rid of any spatial discretization error. Both the nodal code and the S_N algorithm use the same

[2] $\Sigma_r = \Sigma_{s,1\to2} - \Sigma_{s,2\to1}\Phi_1/\Phi_2$, where Φ_1 and Φ_2 are the fast and thermal scalar fluxes in homogenization conditions [Rechantin and Schenider, 2012].

Table 3.1: Input data for the 1D interface problem.

	MO_X layer		*UO_2 layer*	
	Group 1	Group 2	Group 1	Group 2
$\Sigma_{t,g}$	5.24895×10^{-1}	1.57348	5.31150×10^{-1}	1.30058
$\Sigma_{s,0,g\to1}$	4.97321×10^{-1}	4.73917×10^{-3}	5.04664×10^{-1}	2.03884×10^{-3}
$\Sigma_{s,0,g\to2}$	1.08826×10^{-2}	1.23734	1.62955×10^{-2}	1.19134
χ_g	1.0	0.0	1.0	0.0
$\nu\Sigma_{f,g}$	1.43654×10^{-2}	5.05968×10^{-1}	7.15848×10^{-3}	1.41284×10^{-1}
F_g	9.91226×10^{-1}	1.24472	9.94868×10^{-1}	1.01536

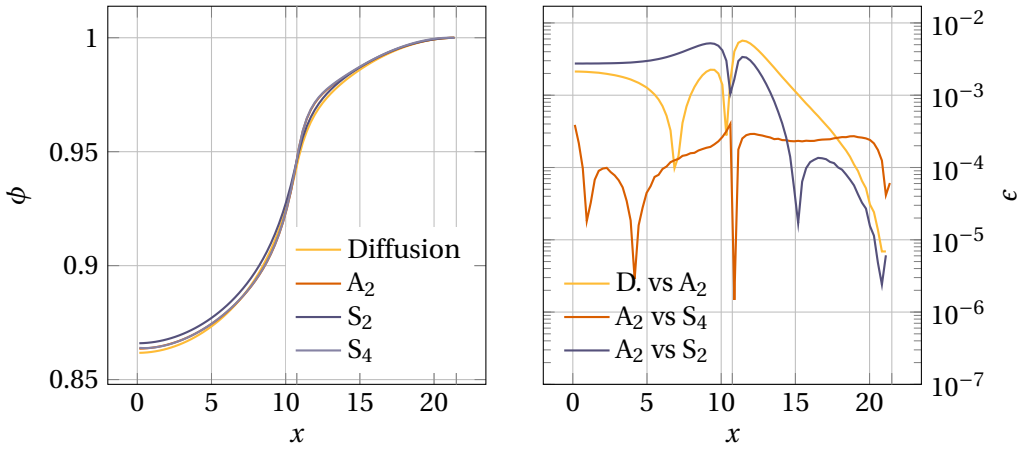

(a) Flux (b) Error

Figure 3.1: Profiles of the fast flux.

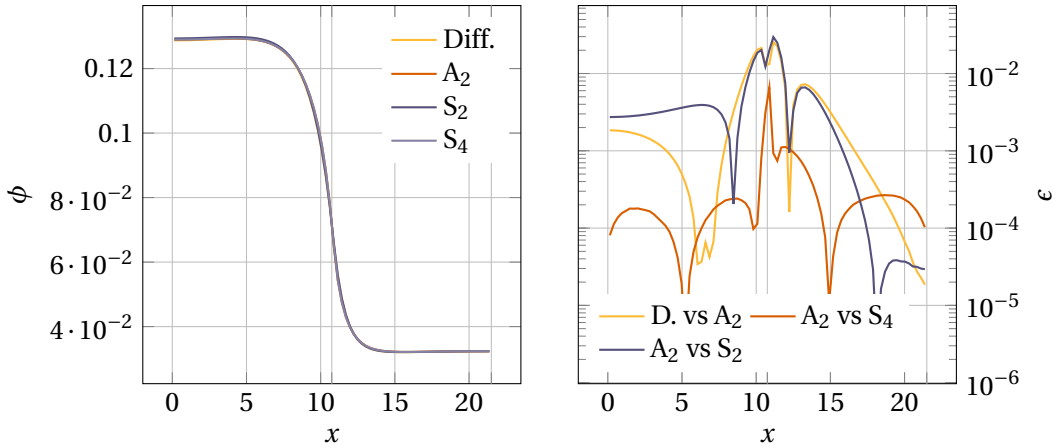

(a) Flux (b) Error

Figure 3.2: Thermal flux profile Φ_2.

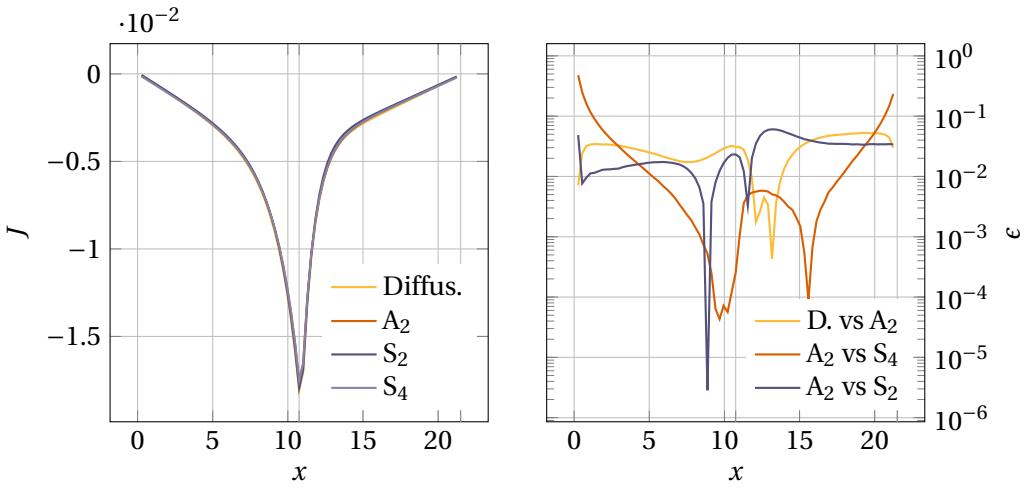

(a) Flux (b) Error

Figure 3.3: Fast net current profile $\boldsymbol{J}_1$.

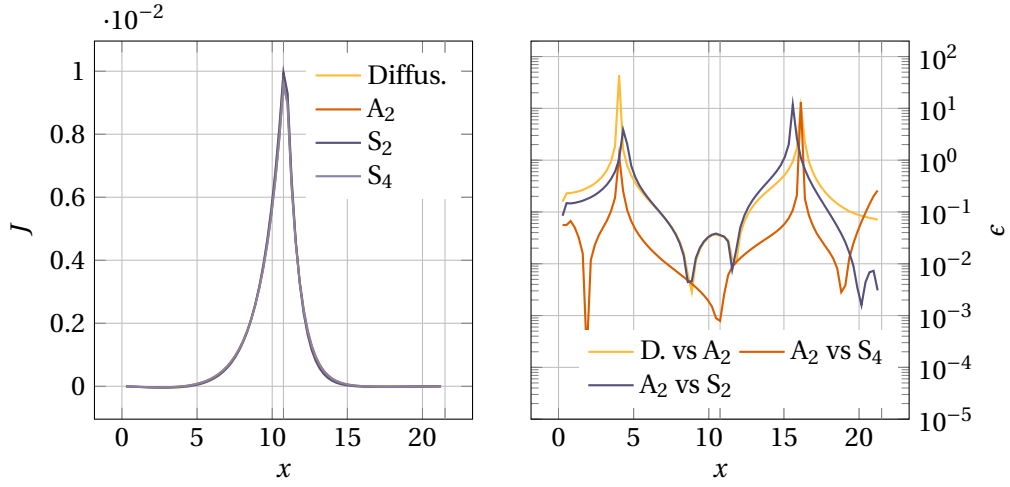

(a) Flux (b) Error

Figure 3.4: Thermal net current profile $\boldsymbol{J}_2$.

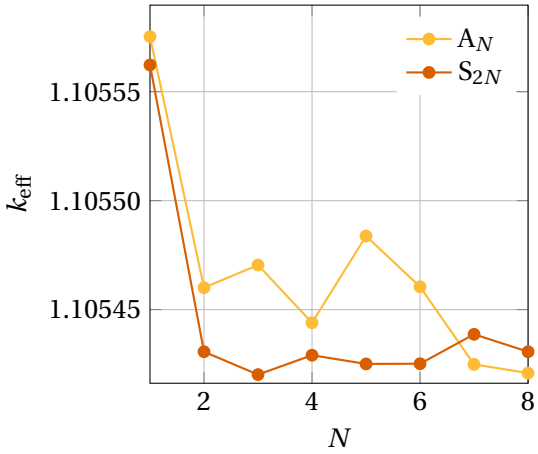

Figure 3.5: Multiplication constant k_{eff}.

grid. The two-group cross sections have been obtained by homogenization from two reference assemblies, one filled with uranium dioxide fuel (UO_2), and the other with mixed uranium-plutonium oxides (MO_X). Cross sections have been produced by the APOLLO2-A code in single assembly conditions (see Table 3.1). The diffusion coefficient is here simply defined as $D_g = 1/(3\Sigma_{t,g})$.

Table 3.1

Figures from 3.1 to 3.5 summarize some of the results achieved. It should be noted that the following numerical tests are for verification purposes only, and are not to be intended as a physical validation of the model, which is already partly attained in chapter 1 and in numerous works in literature regarding the fully equivalent SP_N model.

Figure 3.1

Figure 3.1 shows the fast flux profile using different transport approximations. Close to the interface between the materials the discrepancy between the fast flux calculated with the nodal diffusion calculation and the one from the nodal A_2 option is slightly above the percentage point, and tends to worsen towards the boundaries. A similar consideration holds comparing S_2 and A_2 while the pattern changes because of the numerical algorithms, which are completely different in nature. A small distinction is noticed between A_2 and S_4: for the equivalence on moments of A_N, SP_{2N-1}, P_{2N-1} and S_{2N} in planar geometry, the two fluxes should overlap, but the numerical schemes and the single precision adopted unavoidably insert an offset.

Figure 3.2

Figure 3.2 shows the same quantities introduced in Figure 3.1, referring to the thermal flux. Towards the interface using A_2 instead of diffusion implies about 5% of difference, which is reducing below 1% near the reflective boundaries.

Figure 3.3
Figure 3.4

Figures 3.3 and 3.4 show the net neutron current of fast and thermalized neutrons, respectively. It is clear that both the group currents approach rapidly the machine precision close to the boundaries; for this reason, the relative error is to be disregarded therein. The relative deviation of the interface current calculated with diffusion and A_2 is about 5% in the two cases. Basically, the same difference is observed when comparing A_2 to S_2. As already stated for the flux, the accuracy of the nodal A_2 and S_4 is largely comparable.

Figure 3.5

Last, Figure 3.5 plots the multiplication constant as a function of N for both models A_N

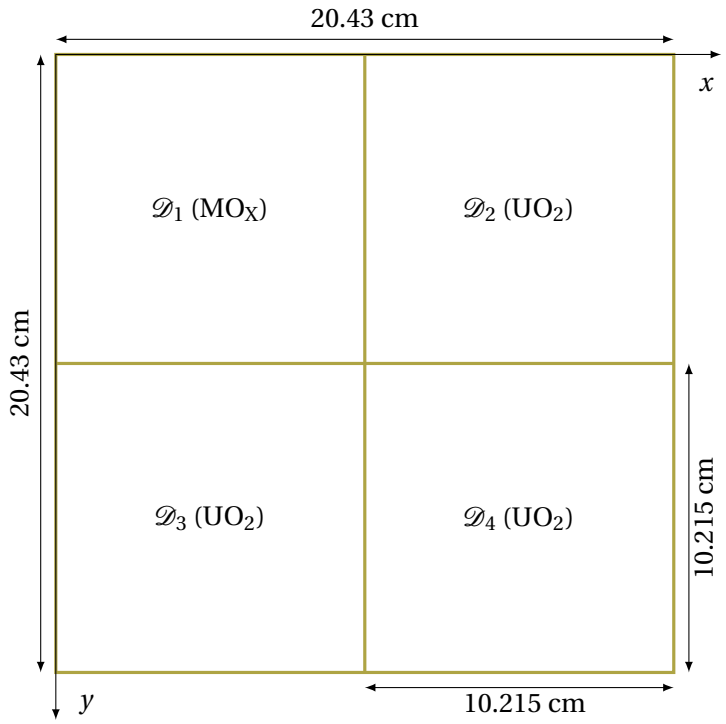

Figure 3.6: Domain of the colorset problem.

and S_{2N}. The S_{2N} results are much more stable increasing the number of directions. Both trends have a sharp peak in the lowest order approximation, which corresponds to the diffusion equation. The A_N results tend to oscillate, slightly overestimating the value of k_{eff}, eventually converging towards the S_{2N} result. Nonetheless, A_2 is able to catch the reduction of the k_{eff} which is neglected by diffusion.

The 2D colorset example

Similarly to the one-dimensional case, the A_N method has been successfully implemented in an industrial version of a three dimensional nodal code, which is developed to perform full-core calculations for design and safety studies in AREVA NP, and is also used for 2D validation studies on portions of fuel assemblies.

The colorset problem is composed of four neighboring quarters of assemblies, considered as axially infinite (see Figure 3.6). Cross section datasets have been produced by APOLLO2-A (see Table 3.2). Homogenized cross sections in the real environment conditions would yield more accurate results for validation purposes. Nevertheless, the input cross sections come from homogenization with reflective conditions for each single assembly, in compliance with the standard procedure in core analysis[3].

Figure 3.6 *Table 3.2*

Table 3.3 collects the main results. The reference solution is here provided by the lattice

Table 3.3

[3] Assembly discontinuity factors are unitary along the z direction

Table 3.2: Input data for the colorset interface problem.

	MOX ass. 1	*UOX ass. 2-3*	*UOX ass. 4*
Group 1			
$\Sigma_{t,g}$	5.3085370×10^{-1}	5.3346366×10^{-1}	5.3346336×10^{-1}
$\Sigma_{s,0,g\to1}$	5.0378040×10^{-1}	5.0692120×10^{-1}	5.0692016×10^{-1}
$\Sigma_{s,0,g\to2}$	1.3187183×10^{-2}	1.6795540×10^{-2}	1.6795665×10^{-2}
χ_g	1.0	1.0	1.0
$\nu\Sigma_{f,g}$	9.9567280×10^{-3}	7.4732252×10^{-3}	7.4732490×10^{-3}
$F_{g,x}$	9.8905790×10^{-1}	9.9372095×10^{-1}	9.9371410×10^{-1}
$F_{g,y}$	9.8905790×10^{-1}	9.9371730×10^{-1}	9.9371410×10^{-1}
$F_{g,z}$	1.0	1.0	1.0
Group 2			
$\Sigma_{t,g}$	1.4964706×10^{0}	1.3164625×10^{0}	1.3164611×10^{0}
$\Sigma_{s,0,g\to1}$	3.6090766×10^{-3}	1.7578889×10^{-3}	1.7578837×10^{-3}
$\Sigma_{s,0,g\to2}$	1.2561710×10^{0}	1.2192476×10^{0}	1.2192501×10^{0}
χ_g	0.0	0.0	0.0
$\nu\Sigma_{f,g}$	3.7379852×10^{-1}	1.5534373×10^{-1}	1.5534236×10^{-1}
$F_{g,x}$	1.3471475×10^{0}	1.0657552×10^{0}	1.0657581×10^{0}
$F_{g,y}$	1.3471475×10^{0}	1.0657319×10^{0}	1.0657581×10^{0}
$F_{g,z}$	1.0	1.0	1.0

APOLLO2-A calculation on the entire colorset.

The solver in A_N mode is in perfect accordance with the standard diffusive solution, demonstrating the correct implementation. Both seems having the same bias if compared to the reference APOLLO2-A solution, due to the environment effects of the cross sections. Even if much of the impact of transport is not visible due to the large mesh size compared to neutron mean free path, it is possible to appreciate some improvement in the MO_X fueled assembly. The error on the reactivity of the diffusion and of A_N is of the same order.

A three-dimensional configuration

The following calculations reproduce the neutron flux in a commercial reactor of the French operating fleet (900 MWe PWR, first cycle). The mesh of the quarter assembly calculation shows 18 planes of 884 nodes each (cell dimensions are about $10 \times 10 \times 20$ cm), where the bottom and the top planes host the axial reflector, a virtual homogenized region which accounts for the top and bottom nozzles of the assemblies, plus some structural material. The boundary conditions are of void type on all external surfaces. The first evaluations refer to homogeneous cross sections in the whole reactor, to move then to real configurations at hot full power (pressure 155 bar, average core burnup 14 GWd/t after an all-rods-out depletion, end of cycle). Comparisons against diffusion are limited to A_2, since higher orders do not provide significant additional contributions [Barbarino and Tomatis, 2013b]. The

Table 3.3: Some results for the colorset problem.

	MOX ass. 1		*UOX ass. 2-3*		*UOX ass. 4*		*Colorset*	
	$\frac{\Phi_1}{\Phi_2}$	$\varepsilon_{\text{AP2A}}$	$\frac{\Phi_1}{\Phi_2}$	$\varepsilon_{\text{AP2A}}$	$\frac{\Phi_1}{\Phi_2}$	$\varepsilon_{\text{AP2A}}$	k_{eff}	$\varepsilon_{\text{AP2A}}$
Diffusion	16.086	4.38%	6.051	1.41%	5.825	0.83%	1.26501	0.22%
A_2	16.013	3.91%	6.066	1.17%	5.819	0.95%	1.26676	0.36%
A_3	16.014	3.92%	6.066	1.17%	5.819	0.95%	1.26676	0.36%
APOLLO2-A	15.411	-	6.137	-	5.874	-	1.2622666	-

thermal feedback on cross sections is not taken into account since the focus is on the effect of second-order transport on the scalar flux.

Homogeneous reactor This set of results concerns a homogeneous reactor, where the cross sections are the same in each node of the mesh. This ideal framework, in conjunction with the optical dimension of the domain compared to the neutron mean free path, removes heterogeneities and interface phenomena, endowing the central part of the reactor with an infinite medium behavior. Here, the difference between transport and diffusion approximations vanishes, thereby allowing the required verification of the scheme.

Figure 3.7a shows the computed scalar flux in the thermal group for values of κ between −90% and +90%. The negative side of the range represents a set of configurations where scattering tend to become less and less important as a neutron interaction mechanism, accentuating transport effects; on the other hand, the amount of scattering grows in the positive range of κ, indicating a marked diffusive setting. For each value of κ the cell relative error compared to A_1 is given, condensed in a box plot representation[4]. A similar behavior is noticed for the fast flux with differences of the same order of magnitude. Figure 3.7c, which presents the same evaluations from the point of view of the intranodal currents in each coordinate direction, is characterized by an analogous behavior with a slightly higher average error. Again, a similar argument holds for the fast currents.

Figure 3.7a

Figure 3.7c

As anticipated, for such optically large system there is no difference between diffusion and transport. Diffusion gives already an adequate description of the neutron fluxes and currents, which are not expected to be substantially modified by any higher order transport scheme. This is perfectly confirmed by the calculations which show, regardless of the amount of scattering, basically a flat behavior in the distribution of the errors.

The baseline deviation, around 1%, is due to the different extrapolation lengths used to model the behavior of the neutrons at the external boundaries of the system. As a proof, Figures 3.7b and 3.7d show the distribution of the errors on a representative plane (the

Figure 3.7b

Figure 3.7d

[4]The convention adopted is: the lower edge of the box represent the 25$^{\text{th}}$ percentile, the top edge stands for the 75$^{\text{th}}$ percentile, the central line is the median. Whiskers extend from the lowest datum still within 1.5 times the inter-quartile range (IQR, the length of the box) of the lower quartile, and the highest datum still within 1.5 IQR of the upper quartile. Outliers are indicated with crosses. If the distribution is of normal type, the outliers are those points exceeding ± 2.698 times the standard deviation around the median [McGill et al., 1978].

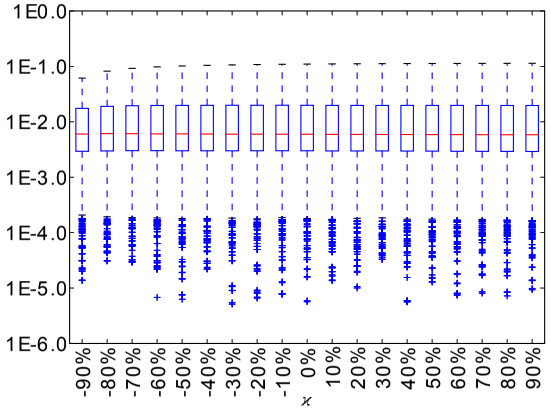

(a) Distribution of the relative deviation for thermal scalar flux compared to A_1 model (diffusion).

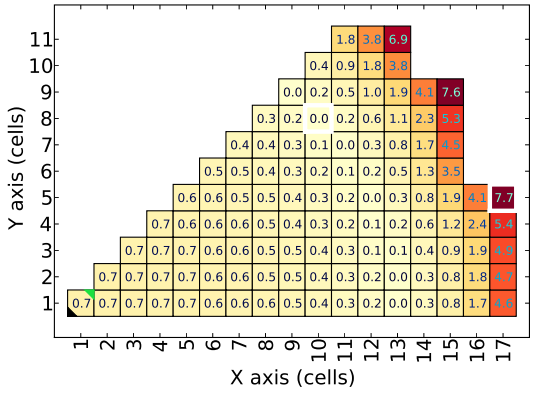

(b) Fast flux in the 9^{th} plane, where the maximum is localized for both A_1 (diffusion) and A_2.

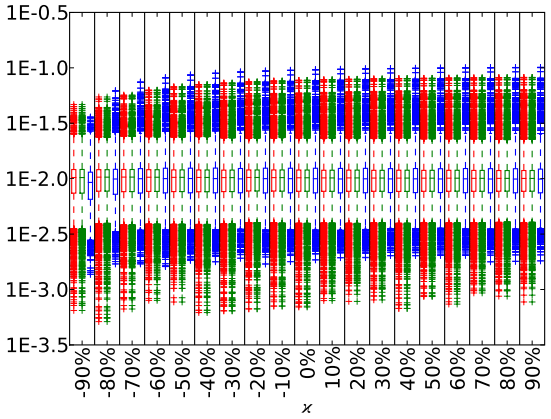

(c) Distribution of the relative deviation for thermal interface currents compared to A_1 model (diffusion).

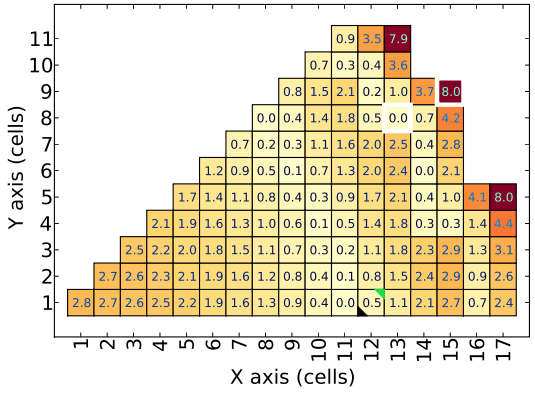

(d) Relative deviation (%) on the thermal flux in the 9^{th} plane, where the maximum is localized for both A_1 (diffusion) and A_2.

Figure 3.7: Homogeneous reactor calculations with A_1 and A_2 models.

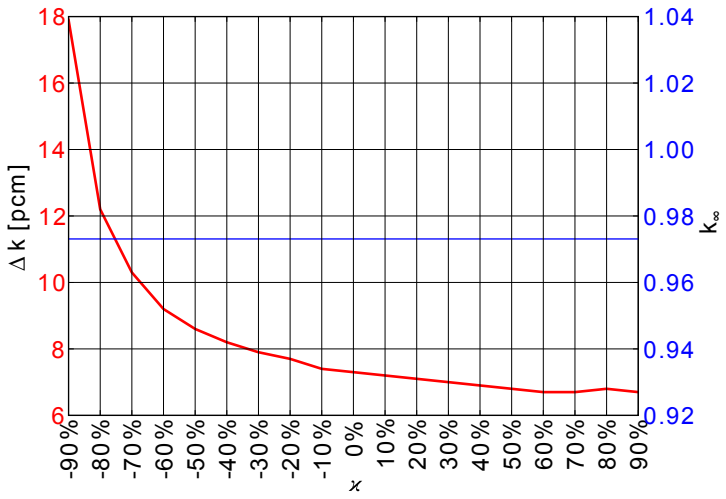

Figure 3.8: Homogeneous reactor: effective multiplication factor relative deviation, compared to A_1.

central one, where the maximum flux can be found for both diffusion and A_N). The black triangle identifies the cell where A_2 has its maximum, the white one is for A_1. The white boxes mark the cells of maximum and minimum percent deviation with respect to the values of this plane only. The error is not negligible on the outer layer of the reactor only. The resulting multiplication factor is plotted in Figure 3.8, the differences calculated are definitely negligible and only due to the leakage close to the boundary.

Figure 3.8

Heterogeneous reactor The heterogeneous reactor allows to highlight and isolate the effects of second-order transport on the flux solution. Assembly discontinuity factors are used for currents on each radial plane, as delivered by the lattice code[5].

Figure 3.9a shows the relative deviation of the thermal scalar flux in A_2 approximation, compared to diffusion. Similar distributions of the error are noticed in all modeled conditions, with a shift to higher values for increasingly transportistic settings (when κ decreases below zero). On the other side, more scatterizing situations present a stabilization to an asymptotic value. As far as the latter configurations are concerned, the residual errors are due to interface effects and the modeling of the void boundary conditions (Figure 3.9b). As predicted, the higher order of the A_N model has limited efficacy if the transport mechanism is dominated by scattering, even if heterogeneities are present. Anyway, the correction is far more evident when transport effect are expected to dominate. An analogous situation is valid for the currents: Figure 3.9c represents the error on the thermal ones, and similar values are observed in the fast group.

Figure 3.9a

Figure 3.9b

Figure 3.9c

The value of k_{eff} (Figure 3.10) is affected about one order of magnitude more than in the

Figure 3.10

[5] At present, also in diffusion simulations for industrial use the axial discontinuity factors are typically not modeled.

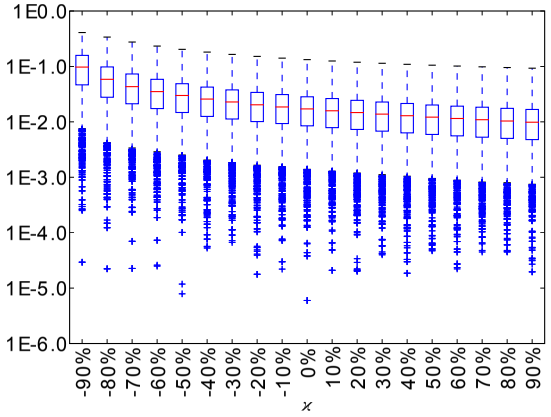

(a) Distribution of the relative deviation for thermal scalar flux compared to the A_1 model (diffusion).

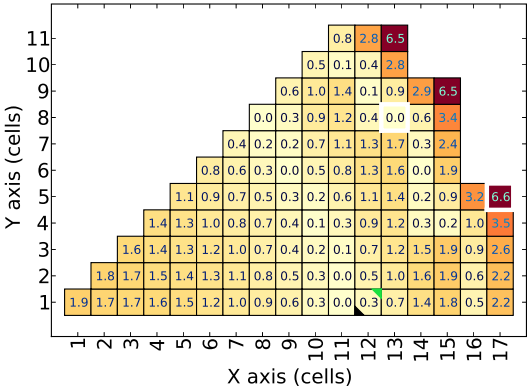

(b) Relative deviation (%) on the thermal flux between A_2 with $\kappa = +90\%$ and diffusion.

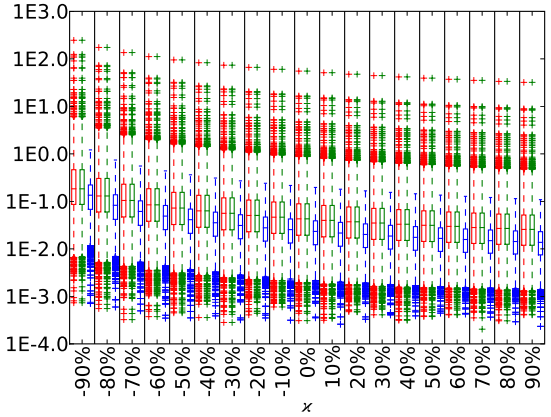

(c) Distribution of the relative deviation for thermal interface currents compared to A_1 model (diffusion).

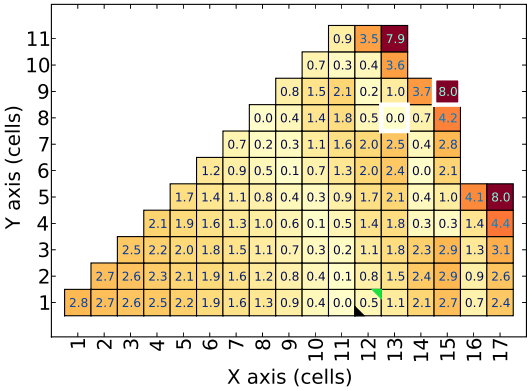

(d) Relative deviation (%) on the thermal flux in the 9^{th} plane, where the maximum is localized for both A_1 (diffusion) and A_2.

Figure 3.9: Heterogeneous reactor calculations with A_1 and A_2 models.

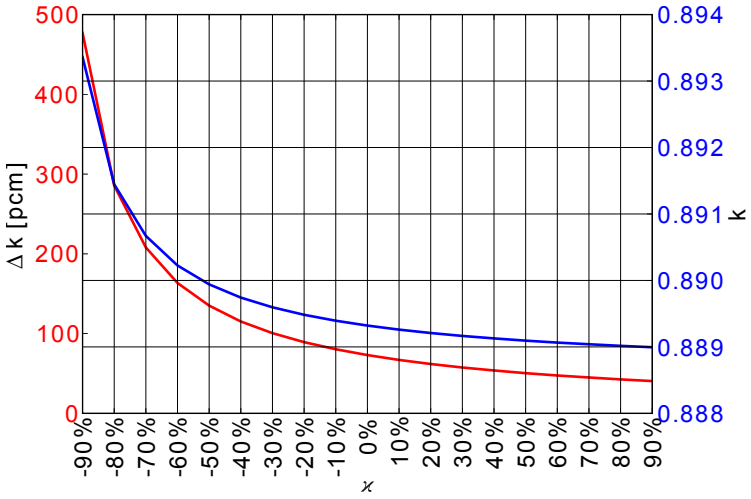

Figure 3.10: Realistic reactor: effective multiplication factor relative deviation, compared to A_1.

previous case, notwithstanding that the variations are below 1% also in the extremes of the range of κ.

3.1.4 Conclusions

The A_N transport model allows great flexibility for the implementation of second-order models, like the SP_N transport into ordinary core simulators. In fact, provided a sufficiently flexible diffusive solver, few code changes are required to retrieve A_N solutions, with an acceptable increase in computational time. Anyway, the implementation is not straightforward as it may appear looking solely at the model equations, mainly for the lack of availability of some cross sections in the full-core libraries; the modification of the solver innermost data structure is often extremely complex, especially when a high level of optimization is present and unavoidable for performance reasons.

The definition of a proper diffusion coefficient issued by cross section homogenization is not necessary with the A_N formulation. Furthermore, the A_N allows to use again assembly discontinuity factors, contrary to other second-order transport models, for which their proper utilization is still debated.

Tests on a standard PWR core shows corrections of about 1-2 % on flux peaks caused by A_N, with a few hundreds pcm changes on the neutron multiplication factor. It is important to notice that most of the correction comes already from lower orders A_N, and this turns as beneficial for the global computational performance.

3.2 Anisotropic A_N implementation

In chapter 1, section 1.1, the anisotropic A_N model has been briefly introduced. The model shares the second-order differential operator in space with the isotropic one, but the diagonality of the matrix cannot, apparently, be easily recovered. Anyway, anisotropy to the first order at least is nowadays a requirement for any industrial grade reactor analysis, and an explicit treatment is foreseen.

Demonstrated the feasibility of the implementation of the isotropic A_N into diffusion codes, the task of this section is to focus on the anisotrpic model to elaborate some strategies for its implementation. The constraints with respect to the previous analysis are the same: limited coding effort, limited verification, robustness, non-regression of the model on the results where it is not needed.

Three possible algorithm are discussed. Only the last option is finally retained for the implementation, because it seems to necessitate of minor code changes in the solver driving routines.

3.2.1 Perturbative solution

First, a perturbative approach is presented. The underlying physical assumption is that anisotropy introduces a small perturbation to the isotropic solution. This assumption requires some insight into the configuration to be analyzed to be justified. Mathematically, one assumes that the parameter ζ:

$$\zeta = \frac{\Sigma_{s,1}}{\Sigma_{\mathrm{tr}}} \tag{3.11}$$

can be considered small with respect to the leading order of the other terms. Then, the solution is assumed as a power expansion in ζ. The truncation at a certain order P yields:

$$\varphi_\alpha = \sum_{p=0}^{P} \varphi_\alpha^{(p)} \zeta^p + 0(\zeta^{P+1}). \tag{3.12}$$

The larger the perturbation parameter ζ, the higher the perturbation order P is expected in order to reproduce accurate solutions. For eigenvalue problems, both components of the fundamental eigenpair should be expanded like the flux. This procedure requires also complex expansions of the other eigenvectors and detailed knowledge of the eigenspectrum [Rellich, 1954], which would prevent its application for practical uses. Hence, considering that the power method and its derivates show subsequent source problems, for which a single expansion of (3.12) is sufficient, it is easier to solve different successive perturbation problems. This derivation avoids the expansions of the multiplication factor k and other unknowns.

Once the developed flux is inserted into the original formulation, one can gather the power terms in ζ. In order to satisfy the equality, perturbation theory requires that each term is vanishing. Thus, a set of $P+1$ problems has to be solved, the first being

$$\frac{\mu_\alpha^2}{w_\alpha \Sigma_{\mathrm{t}}} \nabla^2 \varphi_\alpha^{(0)} + \frac{\Sigma_{\mathrm{t}}}{w_\alpha} \varphi_\alpha^{(0)} = \left(\Sigma_{s,0} + \frac{1}{k} \nu \Sigma_f \right) \Phi, \tag{3.13a}$$

and the others are

$$\frac{\mu_\alpha^2}{w_\alpha \Sigma_t}\nabla^2\varphi_\alpha^{(p)} + \frac{\Sigma_t}{w_\alpha}\varphi_\alpha^{(p)} = -\left[3\frac{\zeta}{\Sigma_t}\mu_\alpha^2\mu_\beta^2\right]\nabla^2\varphi_\alpha^{(p-1)}, \tag{3.13b}$$

for $p = 1,\ldots,P$. The last equation is

$$\left(3\frac{\zeta}{\Sigma_t}\mu_\alpha^2\mu_\beta^2\right)\nabla^2\varphi_\alpha^{(P)} = 0, \tag{3.13c}$$

which is also providing a suitable error criterion for the P perturbation approximation. Equations (3.13) hold for $\alpha = 1,\ldots,N$.

The scattering and fission sources are entered only into the 0th-order problem, yielding the starting isotropic solution. The problems are solved in chain at the level of the inner iterations, where neutron production is fixed, coming from the previous outer iteration.

This option requires main code changes at the level of inner iterations.

3.2.2 Leakage iterations

The second option regains iterative methods with the supplementary divergence of the current considered as known term at each iteration step. This implies the resolution of successive source problems. As well, eigenvalue problems are also treated as sequences of source problems by the power method or by other derived versions.

Different implementation schemes can be adopted, because code modifications are necessarily requested at the level of inner iterations. Many schemes for inner iterations are available in literature and in codes used in industry, and they follow from very specific methodologies too. The most common methodologies are coarse mesh finite volumes (CMFV), nodal expansion (NEM), response matrix (RM), finite elements (FE) and boundary element methods (BEM). The first three techniques are currently employed in AREVA full-core codes. Moreover, it is important to note that the nodal expansion method follows different implementation in the core codes of the SCIENCE code suite, the CASMO/NEMO US code suite as well as in the core codes ARTEMIS (ARCADIA code suite) and PRISM (CASCADE code suite) [Dall'Osso and Ponce, 1998; Hobson, 2008].

The application of nodal expansion methods which recomputes several estimates of currents at the node surfaces, suggests source updates in the same existing iterations to contain the computational charge. However, other possible nested iteration levels may show different approximations and numerical formulas for the currents, requiring careful and formal consistency check.

An optimal implementation scheme in case of one of the AREVA codes is detailed in the following. This code couples a coarse mesh finite volume method yielding average nodal fluxes and a nodal expansion method to compute corrections for the currents at node surfaces. Because of this coupling, the algorithm needs code modifications in the corresponding sections. Finite volumes uses finite differences for currents, whereas the nodal scheme uses analytical function expansions.

Another iteration level for the leakage term is built on both inner schemes, where the anisotropic term is inserted into the external source. Being a constant over the cell, it appears only in the 0-th order moment weighted equations. If it were not constant, additional terms should be included in other equations, without additional complications for the solver since they would be still known terms.

Since the numerical scheme solves the diffusion equation using a finite volume approach, the anisotropic source term appears always integrated into the cell volume. Then, the Gauss theorem over the node volume yields

$$\int_V \mathrm{d}\boldsymbol{r}\mu_\alpha^2\zeta\sum_{\beta=1}^{N}\mu_\beta^2\nabla\varphi_{\beta,g} = \sum_{\beta=1}^{N}\mu_\alpha^2\mu_\beta^2\zeta\cdot \left[\left(\nabla\varphi_{\beta,g}\big|_{x^+} - \nabla\varphi_{\beta,g}\big|_{x^-}\right) + \left(\nabla\varphi_{\beta,g}\big|_{y^+} - \nabla\varphi_{\beta,g}\big|_{y^-}\right) + \left(\nabla\varphi_{\beta,g}\big|_{z^+} - \nabla\varphi_{\beta,g}\big|_{z^-}\right)\right], \quad (3.14)$$

where the the subscripts $x^+, x^-, y^+, y^-, z^+, z^-$ stand for the coordinates of the faces of the hexahedral finite volumes in each Cartesian direction. Gradients are discretized by centered finite differences to feed the pure diffusive solver

$$\nabla\varphi(x_{i+1/2}) = 2\frac{\varphi(x_{i+1}) - \varphi(x_i)}{\Delta_{i+1} + \Delta_{i-1}}, \quad (3.15)$$

as usually done throughout the finite volume scheme.

The gradients are evaluated in two different ways in the implementation, according to the available data. While calculating the anisotropic source to feed the pure diffusive solver, the values of the nodal flux are used with centered finite differences. In order to estimate the gradients, interpolation is adopted. For a cell surrounded by other active cells, it is possible to use the centered scheme

$$\nabla\varphi(x_i) = \left(\varphi(x_{i+1}) - \varphi(x_{i-1})\right)\frac{2}{\Delta_{i+1} + \Delta_{i-1}} \quad (3.16)$$

At the boundaries such centered scheme is not possible. It is possible to estimate the gradient, with the same accuracy, by fitting a parabola on three continguos values of the function φ (the three values of the first or last cells in a certain direction), and then evaluate the gradient of the parabolic shape at the boundaries.

At boundaries, a parabolic interpolation fit is chosen to keep the same second-order truncation error. Three continguos values of the flux are selected backwards, and on the left boundary x_∂^- in one dimension it comes out that

$$\nabla\varphi(x_\partial^-) = \frac{(a-1)\,\varphi(x_0) + \varphi(x_1) - a\,\varphi(x_2)}{x_1 - x_0 - a}, \text{ with } a = \frac{x_1^2 - x_0^2}{x_2^2 - x_0^2}. \quad (3.17)$$

For the right boundary x_∂^+ with I cells, the formula becomes

$$\nabla\varphi(x_\partial^+) = \frac{(b-1)\,\varphi(x_I) + \varphi(x_{I-1}) - b\,\varphi(x_{I-2})}{l_1 - l_0 - b}, \text{ with } b = \frac{l_1^2 - l_0^2}{l_2^2 - l_0^2} \quad (3.18)$$

and $l_0 = x_\partial^+ - x_I$, $l_1 = x_\partial^+ - x_{I-1}$, $l_2 = x_\partial^+ - x_{I-2}$.

On the other hand, the nodal expansion routine provides already the currents through the combination of same analytical functions used for the flux, making the leakage iterations easier to implement.

So far, the scheme has been successfully implemented in a 1D multigroup diffusion solver; the absence of the transverse leakage does not prevent the testing purposes. Anyway, the amount of modifications still remains sizeable.

3.2.3 Diagonalization

It has been demonstrated that the original A_N formulation can be obtained from the SP_{2N-1} transport approximation by diagonalization of the differential operator acting on the even flux moments. This leads to another set of second-order differential equations coupled only by possible terms of scattering anisotropy.

A further approach could be the application of an additional diagonalization on the new anisotropy differential operator, trying to recover again the diagonal form of the streaming term. This entails determining a suitable basis change valid throughout the whole domain. In other words, one would like to join the leakage into a unique term which shows again the ensued diagonal form.

In order to simplify the derivation, the original notation used in literature is adopted, i.e. the unknowns appearing in Eq. (1.69) are all divided by the corresponding weights, as $\varphi_\alpha \leftarrow \varphi_\alpha / w_\alpha$; thus, in a one group model, is

$$\frac{1}{\Sigma}\mathbf{A}\nabla^2\boldsymbol{\varphi} - \Sigma\mathbf{I}\boldsymbol{\varphi} + \left(\Sigma_{s,0} + \frac{1}{k}\nu\Sigma_f\right)\mathbf{B}\boldsymbol{\varphi} + 3\frac{1}{\Sigma}\zeta\mathbf{A}\mathbf{C}\nabla^2\boldsymbol{\varphi} = \mathbf{0}, \tag{3.19}$$

where, using[6] $\boldsymbol{w} = [w_\beta, \beta = 1,\dots,N]$, $\boldsymbol{\mu}_2 = [\mu_\alpha^2, \alpha = 1,\dots,N]$, $\boldsymbol{\rho} = \boldsymbol{\mu}_2 \circ \boldsymbol{w}$ and $\mathbf{1}_N$ as unit column vector of dimension N, it is

$$\mathbf{A} = \mathrm{diag}(\boldsymbol{\mu}_2), \qquad \mathbf{B} = \mathbf{1}_N \times \boldsymbol{w}^T, \qquad \mathbf{C} = \mathbf{1}_N \times \boldsymbol{\rho}^T$$

Extension to multigroup systems is straightforward and will be given afterwards.

Matrix $\mathbf{A}^{-1}$ has on the main diagonal the reciprocal of the elements in $\mathbf{A}$. Equation (3.19) is left-multiplied by $\mathbf{A}^{-1}$, then the operator acting on the laplacian of the moments is diagonalized; in order to accomplish this task one has to look for the eigenpairs of the operator $[\mathbf{I} + 3\zeta\mathbf{C}]$, thus solving the following problem

$$(\mathbf{I}_{N\times N} + 3\zeta\mathbf{C})\,\boldsymbol{\xi}_i = \lambda_i\boldsymbol{\xi}_i, \tag{3.20a}$$

which holds for $i = 1,2,\dots,N$ or, in matrix form:

$$(\mathbf{I}_{N\times N} + 3\zeta\mathbf{C}) = \mathbf{E}\Lambda\mathbf{E}^{-1}, \tag{3.20b}$$

where the eigenvalues λ_i are collected on the diagonal of Λ, and the columns of $\mathbf{E}$ are the corresponding eigenvectors $\boldsymbol{\xi}_i$. Therefore $\mathbf{E}$ becomes a change-of-basis matrix, and so it

[6] being $\circ$ the symbol indicating the Hadamard product, $(\boldsymbol{a}\circ\boldsymbol{b})_i = a_i \cdot b_i$.

is always invertible. Moving to the right hand side the first term of the summation of Eq. (3.20a), one has

$$3\zeta\epsilon_i \mathbf{1}_N = (\lambda_i - 1)\,\boldsymbol{\xi}_i, \qquad \text{with} \quad \epsilon_i = \sum_\beta \mu_\beta^2 w_\beta \xi_{i,\beta}. \tag{3.21}$$

By virtue of the arbitrariness of the eigenvector normalization, the first possible solution is $\boldsymbol{\xi}_1 = \mathbf{1}_N$, yielding $\epsilon_1 = \sum_\beta \mu_\beta^2 w_\beta = 1/3$ and finally $\lambda_1 = 1+\zeta$. The remaining eigenvectors follow from $\epsilon_i = 0$, for $1 < i \leq N$, with corresponding unitary eigenvalues, and arbitrary components.

In order to determine a closed form also for $\mathbf{E}^{-1}$, it is worth noticing that problem (3.20b) can be manipulated to obtain

$$(\mathbf{I}_{N\times N} + 3\zeta \boldsymbol{C})^T (\mathbf{E}^{-1})^T = \left(\mathbf{I}_{N\times N} + 3\zeta \boldsymbol{\rho} \times \mathbf{1}_N\right) = \left(\mathbf{E}^{-1}\right)^T \Lambda, \tag{3.22}$$

and so the elements of $\mathbf{E}^{-1}$, needed for all subsequent calculations, can be obtained again with the solution of this eigenproblem. This implies that the first eigenvector is equal to $\boldsymbol{\rho}$, whereas the only constraint is that the sum of all components must vanish for the remaining ones.

After diagonalization, the unknown pseudo-fluxes will be decomposed on the new basis as

$$\boldsymbol{\varphi} = \mathbf{E}\boldsymbol{\psi}. \tag{3.23}$$

Note that no material information is needed for $\mathbf{E}$, and thus the decomposition is unique everywhere in the computational domain. Hence, no modification is demanded for boundary conditions and assembly discontinuity factors, if any. Eq. (3.19) is then left-multiplied by the inverse of $\mathbf{E}$, obtaining

$$\frac{1}{\Sigma}\Lambda\nabla^2\boldsymbol{\psi} - \Sigma_t \Upsilon \boldsymbol{\psi} + \left(\Sigma_{s,0} + \frac{1}{k}\nu\Sigma_f\right)\Theta\boldsymbol{\psi} = \mathbf{0}, \tag{3.24}$$

where

$$\Upsilon = \mathbf{E}^{-1}\mathbf{A}^{-1}\mathbf{E}, \qquad \Theta = \mathbf{E}^{-1}\mathbf{A}^{-1}\mathbf{B}\mathbf{E}.$$

Still in order to retrieve a standard form for diffusion codes, the removal operator should be diagonal. Then, one can use $\Gamma = \mathrm{diag}(\Upsilon)$, shifting the remaining part of the operator to the scattering term, which has already a full pattern.

Then, the final form of the model is

$$\frac{1}{\Sigma}\Lambda\nabla^2\boldsymbol{\psi} - \Sigma\Gamma\boldsymbol{\psi} + \left[\Sigma_s\Theta + \Sigma\left(\Gamma - \Upsilon\right)\right]\boldsymbol{\psi} + \frac{1}{k}\nu\Sigma_f\Theta\boldsymbol{\psi} = 0 \tag{3.25}$$

The scalar flux is easily obtained using the change of basis matrix:

$$\Phi = \boldsymbol{w}^T \cdot \boldsymbol{\varphi} = \left(\boldsymbol{w}^T \cdot \mathbf{E}\right)\boldsymbol{\psi} \tag{3.26}$$

Finally, in a multigroup approach each equation is expanded in pseudo-fluxes. Then, one has to solve a set of G matrix equations in the form, for $g = 1, \ldots, G$:

$$\frac{1}{\Sigma}\Lambda_{\mathbf{g}}\nabla^2\psi_g - \Sigma_g\Gamma\psi_g + \left[\Sigma_{s,0,g\to g}\Theta + \Sigma_g(\Gamma - \Upsilon)\right]\psi_g + \sum_{\substack{g'=1 \\ g'\neq g}}^{G}\Sigma_{s,0,g'\to g}\psi_{g'} + \frac{1}{k}\chi_g\sum_{g'=1}^{G}\nu\Sigma_{\mathrm{f},g'}\Theta\psi_{g'} = \mathbf{0}. \quad (3.27)$$

Change of basis options

Only the first eigenvector of the eigenproblem at equations (3.20) is well-defined, and there are different options for the remaining ones, still ensuring the condition $\epsilon_i = 0$ (see equation (3.21)).

The first option uses the properties of the Gauss-Legendre quadrature, which can integrate exactly polynomials in the segment $[-1, 1]$ up to the order $(4N-1)$, where N is provided by the given A_N approximation. The parity of even monomials yields

$$\int_0^1 \mu^m d\mu = \frac{1}{m+1} = \sum_{i=1}^{N} w_i\mu_i^m, \quad m < 4N-1, \quad (3.28)$$

thus suggesting the following definition for $\boldsymbol{\xi}_j$ $(j > 1)$:

$$\xi_{i,j} = \mu_i^{j-1} - \frac{3}{j+2}, \quad i = 1, \ldots, N. \quad (3.29)$$

Vandermonde matrices arise in the determination of the components of the inverse matrix $\mathbf{E}^{-1}$, whose inversion can be carried by means of Lagrange polynomials.

Another definition for $\mathbf{E}$ is simply derived from the conditions of the vanishing weighted sum, $\epsilon_i = 0$:

$$\xi_{i,j} = \begin{cases} 1, & \text{if } i \neq j \\ -\dfrac{\sum_{\beta\neq j}\mu_\beta^2 w_\beta}{\mu_i^2 w_i}, & \text{otherwise.} \end{cases} \quad (3.30)$$

In this case, the matrix $\mathbf{E}^{-1}$ is numerically determined.

Other options are provided by standard numerical routines, which solve directly the main eigenproblem.

3.2.4 Numerical results

In this section some numerical results are introduced, obtained by the formal diagonalization method. The other two methods, still valid on a theoretical point of view, can be implemented in standard diffusion codes applying significant modifications to the source code, and the economicity of this operation (considering also verification and validation) is questionable due to the development of an ad-hoc solution.

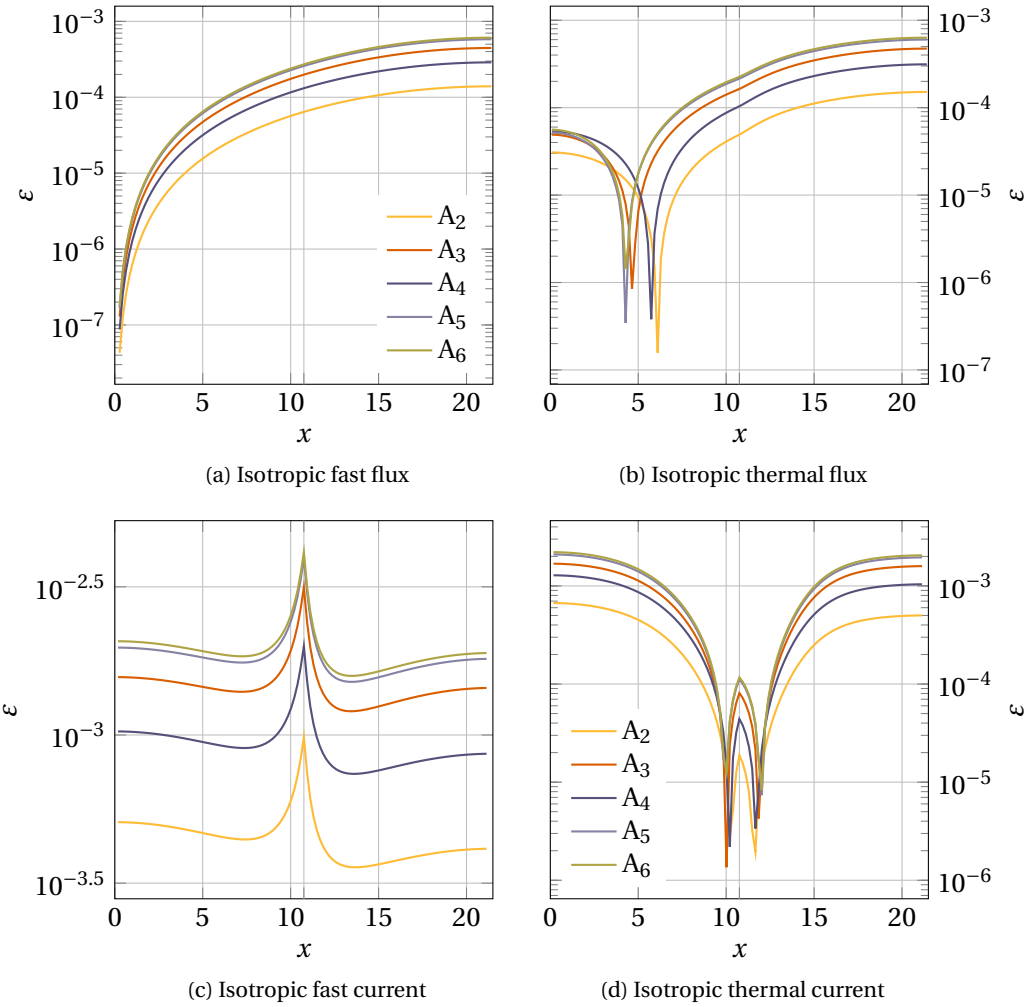

(a) Isotropic fast flux

(b) Isotropic thermal flux

(c) Isotropic fast current

(d) Isotropic thermal current

Figure 3.11: Verification of the formal diagonalization operators: anisotropic cases compared to the one calculated with the original isotropic A_N formulation.

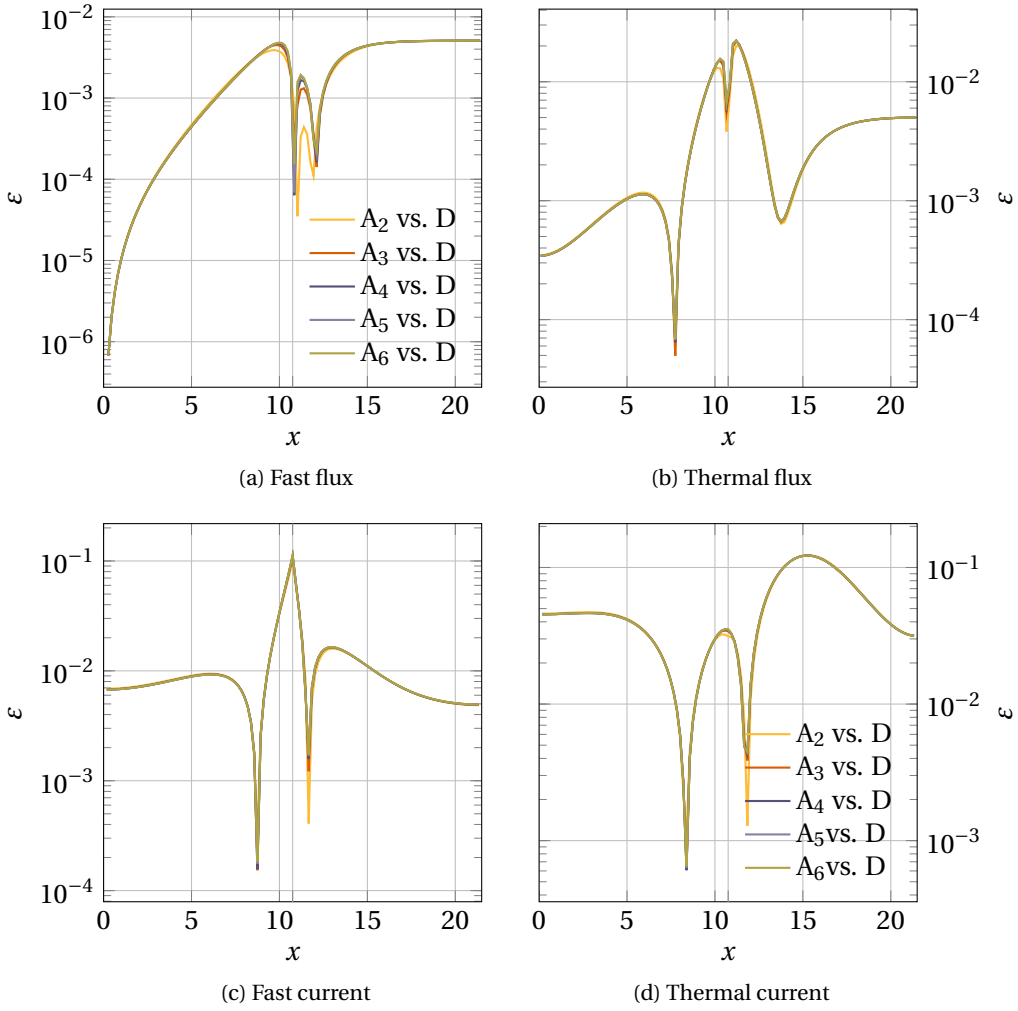

(a) Fast flux

(b) Thermal flux

(c) Fast current

(d) Thermal current

Figure 3.12: Anisotropic calculation using the formal diagonalization: comparison between diffusion and higher order approximations.

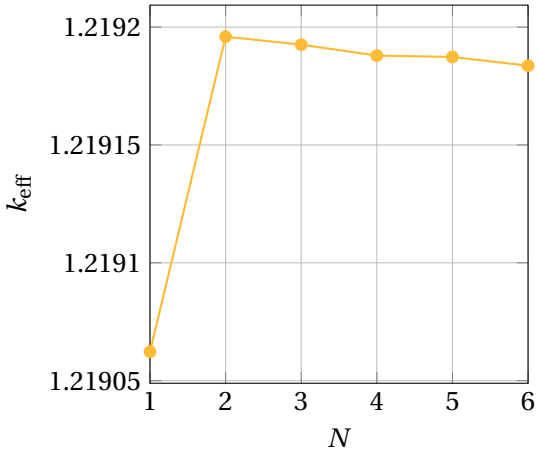

Figure 3.13: Anisotropic calculation using the formal diagonalization: multiplication factor as a function of the order of the transport approximation.

A 1D multi-group solver for multi-region problem has been developed in the SciLab programming language. The solver is based on a simple finite difference approach using regular equi-spaced grids. Both the isotropic A_N mode (adopting the standard definitions of the operators) and the anisotropic version are available in the code, implemented in a preprocessing module acting only on the macroscopic cross sections: thus, the two modes use the very same computational routines. The material specifications for the model problem
Table 3.4 are reported in Table 3.4, and are representative of a simple colorset involving two adjacent MO_X and UO_2 assemblies. Reflector conditions are applied at boundaries, as well. Both half assembly lengths are of 10.752 cm.

A first batch of tests aims at verifying the definition of the operators resulting from the formal diagonalization procedure. The problem is considered isotropic ($\Sigma_{\text{tr},g} = \Sigma_{\text{t},g}$), and is solved using both the original A_N operators (3.1) and the new ones (3.27).

From a merely mathematical point of view, the formal diagonalization process does not have any influence on the accuracy of the transport model, since it is just a change of the basis by which the solution is represented. However, numerical issues related to the mag-

Table 3.4: Input data for the 1D interface problem. All cross sections are in cm^{-1}.

	MO_X layer		*UO_2 layer*	
	Group 1	Group 2	Group 1	Group 2
Σ_g	5.327840×10^{-1}	1.314048×10^{0}	5.3334587×10^{-1}	1.502423
$\Sigma_{\text{tr},g}$	2.968346×10^{-1}	9.877822×10^{-1}	2.982115×10^{-1}	1.1436665×10^{0}
$\Sigma_{\text{s},0,g\to1}$	5.065018×10^{-1}	1.8083068×10^{-3}	5.056410×10^{-1}	3.2951059×10^{-3}
$\Sigma_{\text{s},0,g\to2}$	1.6562084×10^{-2}	1.217201×10^{0}	1.3668350×10^{-2}	1.263938×10^{0}
χ_g	1.0	0.0	1.0	0.0
$\nu\Sigma_{\text{f},g}$	7.4499152×10^{-3}	1.546263×10^{-1}	1.0006606×10^{-2}	3.714562×10^{-1}

nitude of the new coefficients of the equations can arise, questioning the use of the single real precision in computation or requiring more attention for the definition of the basis change matrix **E**.

Figures 3.11a and 3.11b show the percentage relative difference ϵ between the computed scalar flux functions, for both fast and thermal groups, varying the order of the A_N approximation. For the A_1 case, no results are shown since the two bases are identical, thus all quantities coincide. For the other orders $N > 1$, it appears a clear shift in the corresponding solutions, whose magnitude depends on the order N of the approximation in a non regular manner. The original functions are normalized to one on their maximum, and this is the motivation for the odd spatial distribution of the error. Anyway, this deviation never goes as high as 0.1%, negligible for any practical application. As far as the currents are concerned (Figures 3.11c and 3.11d), the argument is basically the same. Again, the maximum difference in the values stands below 1%. *Figure 3.11a* *Figure 3.11b* *Figure 3.11c* *Figure 3.11d*

A second batch of tests focuses on the difference between the results, including the anisotropy effect, using various A_N approximations up to $N = 6$, compared to the diffusive case (A_1). The relative difference ϵ is computed as much as the fast and thermal fluxes (Figures 3.12a and 3.12b) and currents (Figures. 3.12c and 3.12d). *Figure 3.12a* *Figure 3.12b* *Figure 3.12c* *Figure 3.12d*

All A_N approximations have basically the same performance in the test; the errors are hardly distinguishable even at the lowest order A_2. Discrepancies compared to diffusion theory are localized around the interface (occurring at 10.7 cm), and though in this case the anisotropy effect do not play a major role, the thermal flux is corrected by about 5% , and the correction on currents approaches 10%.

Figure 3.13 shows how the k_{eff} is affected by the additional moments of the angular flux considered in the solution. Much of the effect is observed passing from diffusion (A_1) to A_2, the rest being almost vanishing corrections. *Figure 3.13*

3.2.5 Remarks

There are some numerical issues related to the use of the formal diagonalization, which could affect the stability of the algorithm and its applicability to reactor codes. These problems come from the topology of the base chosen for the formal diagonalization, and are not present in the original A_N isotropic formulation. In particular, for a problem modeled with G groups and adopting N equations, one has that G pseudo-fluxes have magnitude much higher than the others (see Figure 3.14 for an example with $G = 2$ and $N = 3$, and they have all the same sign). The other psudo-fluxes have much smaller values, changing sign inside the calculation domain (Figure 3.14b provide a magnification of Figure 3.14a for the minor pseudo-fluxes around the interface). Moreover, Figure 3.14b shows that the minor unknowns develop non negligible steeps around the interface, and this fact could break, for instance, the nodal approach if the spatial mesh size or the nodal functional expansion are not able to resolve correctly the peculiar shape of these functions. *Figure 3.14*

Further investigations are necessary to search for a robust methodology to cope with these patterns and mitigate their impact on the accuracy of the model.

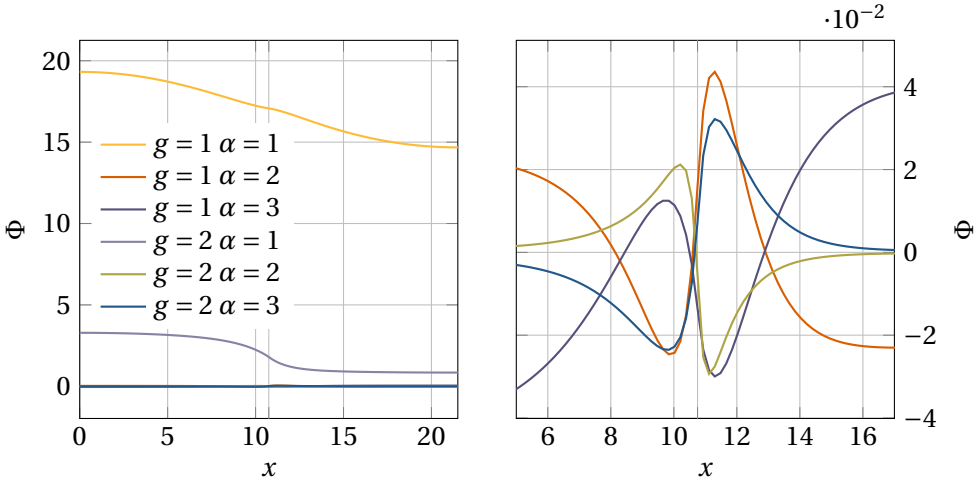

(a) Fluxes

(b) Magnification of the characteristic anisotropic components close to the interface.

Figure 3.14: Pseudofluxes for the A_3 calculation with anisotropy and two energy groups

3.2.6 Conclusion

This work presents three options to take into account the linearly anisotropic scattering into the A_N neutron transport model. The first solution attempt recurs to perturbation theory, the second to an additional leakage iteration within diffusion solvers and the third introduces a formal diagonalization procedure on the A_N system equations. The main requirement of this work is using common neutron diffusion solvers with very minor modifications in the source code.

The first attempt is only formally discussed, whereas the others have been implemented in a 1D code and numerically verified. Since the option of leakage iteration requests code changes in the solvers, the diagonalization procedure has been initially selected for the final implementation in core simulators.

Unfortunately, the diagonalization procedure yields stiff problems to resolve, with the new unknowns differing of some orders in magnitude. This occurs with any change of variables, outlined in the given procedure. Indeed, this reveals the perturbative nature of the problem, that adds small corrections to the global solution obtained without anisotropic scattering. This stiffness may cause single real precision algorithms to fail, especially in situations close to the infinite medium, and also demand for more restrictive error criteria in iterative schemes. Furthermore, the corrective components can show steep behaviors, requiring finer meshes close to material discontinuities. Eventually, the diagonalization technique can fit mostly finite difference solvers on fine meshes, like for instance in pin-by-pin problems, rather than commercial nodal solvers.

A careful analysis about the feasibility of the perturbative approach, together with a possible reformulation of the technique still to get minor code modification, is proposed as future development.

4 Studies on ray effects in S_N discretized problems

The numerical solution of the linear transport model with a deterministic approach, widely adopted in the description of the neutron population behavior in the nuclear engineering discipline, is based on the discretization of the phase-space variables [Lewis and Miller, 1993]; the resulting set of linear equations for the unknowns is then solved with appropriate algorithms. The discretization schemes, especially when the angular variable is concerned, can introduce modifications in the physical features of the transport phenomenon, producing a wide range of distortions usually called ray effects [Lathorp, 1968; Duderstadt and Martin, 1979]. The ray effect phenomenon strongly affects the numerical solution of transport problems in various different situations; it is therefore important to identify and evaluate such effects in order to correctly interpret the results of numerical simulations and to facilitate the development of ray effect mitigation schemes [Lathorp, 1971; Miller and Reed, 1977; Morel et al., 2003]

Ray effects are a well known issue in multi-dimensional transport in a steady-state situation; the mathematical reason for ray effects is found in the lack of rotational symmetry of the discretized transport streaming operator [Morel et al., 2003]. Only P_N methods exhibit such property, but typically they are not able to provide sufficiently accurate solutions to those problems affected by ray effects under the S_N framework [Larsen and Morel, 2010]; this is due to the fact that the angular flux in these situations has a strong anisotropic behavior, which is not easily taken into account by the global nature of the spherical harmonics.

Moreover, the distortion of the physical propagation phenomenon can also be experienced in 1D when the time-dependence is considered. The time-ray effect can be particularly relevant when the propagation of high energy particles is considered [Dulla and Ravetto, 2004; Dulla et al., 2006; Zerr and Baker, 2011], thus requiring a high-order approximation of the transport operator to reduce the impact of such distortions.

This chapter aims at a thorough characterization of how the transport phenomena is distorted when introducing the discretization of the variables involved, with a specific focus on the angle and time variables that are responsible for the appearance of ray effects.

To obtain this objective, simplified configurations are chosen, allowing a direct analytical approach. The transport problem in two-dimensional plane geometry is approached at first by means of integral transforms. The analysis of the transport kernel in the Fourier transformed space is performed, allowing to provide a quantitative evaluation of the distortion that can be expected through a properly defined index depending on the physical

characteristics of the system under consideration. The analysis of the bidimensional problem is also carried out in the direct space, obtaining an analytical solution to a source problem in the absence of scattering and proposing a definition of the aforementioned ray effect indicator suitable for this analysis. The study performed for the $x-y$ geometry is then used as a guideline in order to investigate the problem of the time-ray effect in one-dimensional slab configurations. The Fourier-trasformed transport kernel is studied, properly defining the ray effect indicator for this model. The analysis in the direct space includes the comparison of the adoption of different quadrature schemes for the angular integration and a critical discussion on the use of alternative discretization approaches that might be beneficial for the reduction of the time-ray effect. Another important objective of the present work is to gain a deep physical insight on the ray effect phenomenon, considering the various configurations that may lead to the appearance of such artifacts. It is finally worth remarking that this approach to clarifying the physics of ray effects through a combination of classical analysis and simple numerics may also have some pedagogical value.

The extent of this work, originally conceived for the 2012 ANS Summer Meeting [Barbarino et al., 2012] and then extended for the ICTT23 [Barbarino et al., 2013a], is still of course introductory; the novelty of the topic obliges to proceed by limited but consolidated steps. Further studies, with the support of simulations on realistic configurations, are imperative to assess the effective capabilities of the indicators.

4.1 Static transport problems in two dimensions

4.1.1 Transport model in $x-y$ flat-land in the Fourier-transformed space

The appearance of ray effects is the typical consequence of the discretization of the angular variable in a multi-dimensional transport problem and steady-state condition, due to the directional collimation of the propagation of particles associated with a fine set of discrete directions.

The objective of the present analysis is to identify a technique for the quantitative evaluation of this effect; therefore, the model to be studied is simplified neglecting the energy dependence and the attention is focused on the interaction of the spatial and angular variables. Moreover, a two-dimensional $x-y$ geometry is chosen, assuming that particles are propagating on the $x-y$ plane only (i.e., a flat-land approximation, as defined in section 1.1.1), since the ray effect features can be easily characterized also in this simplified case compared to those visible in a 3D geometry. The transport model considered then takes the form:

$$\cos\theta\frac{\partial}{\partial x}\phi(x,y,\theta)+\sin\theta\frac{\partial}{\partial y}\phi(x,y,\theta)+\Sigma\phi(x,y,\theta)=\frac{c\Sigma}{2\pi}\Phi(x,y)+\frac{S(x,y)}{2\pi}, \tag{4.1}$$

where the scalar flux $\Phi(x,y)$ is defined by

$$\Phi(x,y)=\int_0^{2\pi}\phi(x,y,\theta)\,d\theta.$$

and c is the number of secondaries per collision. The scattering phenomenon and the external source are assumed to be isotropic. A homogeneous infinite system is considered, in order to apply the Fourier transform [Case et al., 1953] to both spatial variables:

$$\begin{aligned} &i\omega_x \cos\theta \tilde{\phi}(\omega_x,\omega_y,\theta) + i\omega_y \sin\theta \tilde{\phi}(\omega_x,\omega_y,\theta) + \Sigma\tilde{\phi}(\omega_x,\omega_y,\theta) \\ &\qquad = \frac{c\Sigma}{2\pi}\tilde{\Phi}(\omega_x,\omega_y) + \frac{\tilde{S}(\omega_x,\omega_y)}{2\pi}. \end{aligned} \tag{4.2}$$

The analysis of the problem in the Fourier transformed space allows an explicit formulation of the exact transport operator, that will be then compared to the approximated form obtained when introducing the angular discretization.

Expression (4.2) can be rearranged to make explicit the angular flux:

$$\tilde{\phi}(\omega_x,\omega_y,\theta) = \frac{1}{2\pi}\left[\frac{1}{i\omega_x\cos\theta + i\omega_y\sin\theta + \Sigma}\right]\left(c\Sigma\Phi(\omega_x,\omega_y) + \tilde{S}(\omega_x,\omega_y)\right) \tag{4.3}$$

and, integrating over the angle θ, an expression connecting the scalar flux and the external source is obtained:

$$\tilde{\Phi}(\omega_x,\omega_y) = \frac{1}{2\pi}\left[\int_0^{2\pi}\frac{\mathrm{d}\theta}{i\omega_x\cos\theta + i\omega_y\sin\theta + \Sigma}\right]\left(c\Sigma\Phi(\omega_x,\omega_y) + \tilde{S}(\omega_x,\omega_y)\right). \tag{4.4}$$

Rearranging terms, it is possible to explicitly obtain the functional relation between the scalar flux and the external source:

$$\tilde{\Phi}(\omega_x,\omega_y) = \frac{\Gamma(\omega_x,\omega_y)}{1 - c\Sigma\Gamma(\omega_x,\omega_y)}\tilde{S}(\omega_x,\omega_y) \quad = G(\omega_x,\omega_y)\tilde{S}(\omega_x,\omega_y), \tag{4.5}$$

where

$$\Gamma(\omega_x,\omega_y) = \frac{1}{2\pi}\int_0^{2\pi}\frac{\mathrm{d}\theta}{i\omega_x\cos\theta + i\omega_y\sin\theta + \Sigma} = \frac{1}{\sqrt{\Sigma^2+\omega_x^2+\omega_y^2}} = \frac{1}{\sqrt{\Sigma^2+\rho^2}}. \tag{4.6}$$

Function G plays the role of a transfer function, since it produces the resulting total flux when applied to any source. Symbol ρ indicates the distance from the center of the coordinate system in the transformed space. The transfer function G allows to identify the key characteristics of the transport model: if one assumes a localized δ source in the center of the coordinates, the transfer function represents directly the scalar flux response, and it depends on the distance ρ from the source position; as expected, a perfect circular symmetry is shown, owing to the angular isotropy of the source. An example of the pattern of the transfer function obtained is given in Fig. 4.1a. *Figure 4.1a*

The angular discretization is introduced into the model by substituting the analytical integration of equation (4.4) with a suitable quadrature, as prescribed by the discrete ordinate approximation scheme:

$$\tilde{\Phi}(\omega_x,\omega_y) = \frac{1}{2\pi}\left[\sum_{n=1}^{2N}\frac{w_n}{i\omega_x\cos\theta_n + i\omega_y\sin\theta_n + \Sigma}\right]\left(c\Sigma\Phi(\omega_x,\omega_y) + \tilde{S}(\omega_x,\omega_y)\right). \tag{4.7}$$

Table 4.1: Maximum value of the ray effect indicator for the $x-y$ case with different values of c.

$c\rightarrow$	0	0.2	0.4	0.6	0.8	0.95
S_2	0.4477	0.4000	0.3394	0.2610	0.1550	0.0457
S_4	0.2251	0.1900	0.1508	0.1069	0.0571	0.0150
S_6	0.1502	0.1245	0.0969	0.0671	0.0349	0.0090
S_8	0.1127	0.0926	0.0713	0.0489	0.0252	0.0064

The relation between flux and source can be given the same form as in equation (4.5) also in this case, with a different definition for the Γ function, namely:

$$\Gamma_{S_N}(\omega_x,\omega_y)=\frac{1}{2\pi}\sum_{n}^{2N}\frac{w_\alpha}{\Sigma+i\cos\left(\theta_n-\tan^{-1}\left(\omega_x/\omega_y\right)\right)\rho}. \tag{4.8}$$

The total number of directions considered is defined in accordance to the S_N formalism adopted in 1D slab geometry for the μ variable, in order to preserve the rotational symmetry, e.g. S_2 has one direction per quadrant and S_4 has two directions per quadrant. The discrete-ordinate transport kernel shows an explicit dependence on the two transformed coordinates ω_x and ω_y, resulting in the loss of the rotational symmetry previously observed.

Figure 4.1b *Figure 4.1c* *Figure 4.1d* Figures 4.1b, 4.1c and 4.1d represent the modulus of the complex kernel G of the discretized transfer functions for S_2, S_4 and S_8 cases, respectively. The discrete directions can be easily identified and, as expected, the distortion is reduced when a larger number of ordinates is adopted. The scattering phenomenon also affects the appearance of ray effects, attenuating the magnitude of the discrete artifacts when the number of secondaries per collision c is increased. *Figure 4.2* Figure 4.2 provides the same set of results as Figure 4.1 with a larger value of c, to graphically show the reduction of the ray effect.

The graphical isoline representation of the kernels provides a practical approach for the quantitative estimation of the magnitude of ray effect phenomenon. If the exact transfer function is superimposed to the discrete one, it is possible to measure the maximum distance between the isolines allowing a direct quantification of the amount of distortion introduced by the angular discretization. Obviously, this difference depends on the isoline considered and hence on the value of ρ associated with it. *Figure 4.3a* In Figure 4.3a an example of how the ray effect indicator I_{RE} is identified is reported. *Figure 4.3b* Figure 4.3b shows the resulting curves obtained for different angular approximations; their maximal values can be used as a quantifier for the relevance of ray effect in a certain configuration. *Table 4.1* Table 4.1 summarizes the values of such maxima obtained for different angular approximations and number of secondaries per collision, showing that this indicator models correctly the dumping effect of scattering on the ray effect.

4.1.2 Problem in $x-y$ in the direct space

The analysis of the simplified $x-y$ transport problem treated in the previous section was shown to be readily amenable using Fourier transforms, and moreover a measure for the

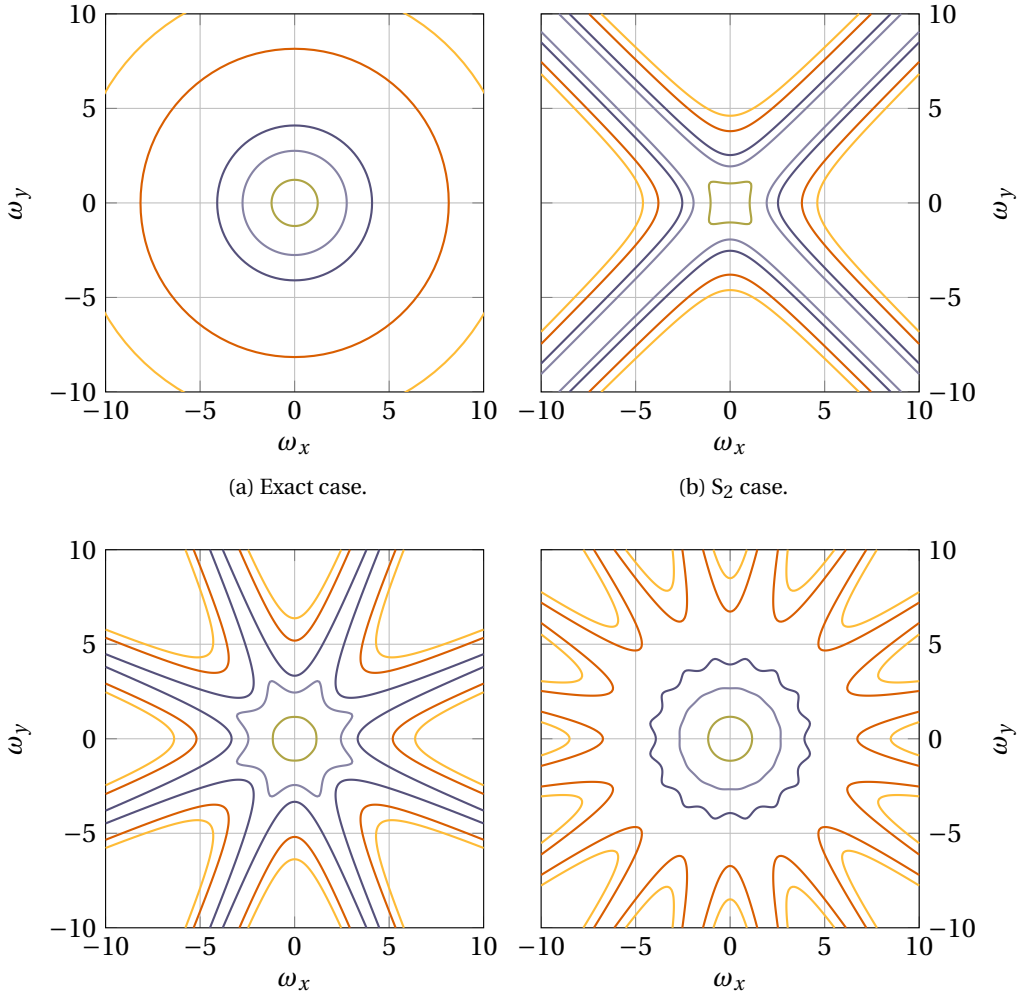

(a) Exact case.

(b) S_2 case.

(c) S_4 case.

(d) S_8 case.

Figure 4.1: Contour plot of the exact transport kernel (top left), compared to the discretized versions obtained adopting different numbers of discrete ordinates. Material data: $\Sigma = 1$ cm^{-1}; $c = 0.2$. Isolines plotted for values 0.6, 0.3, 0.2, 0.1 and 0.07, starting from the center.

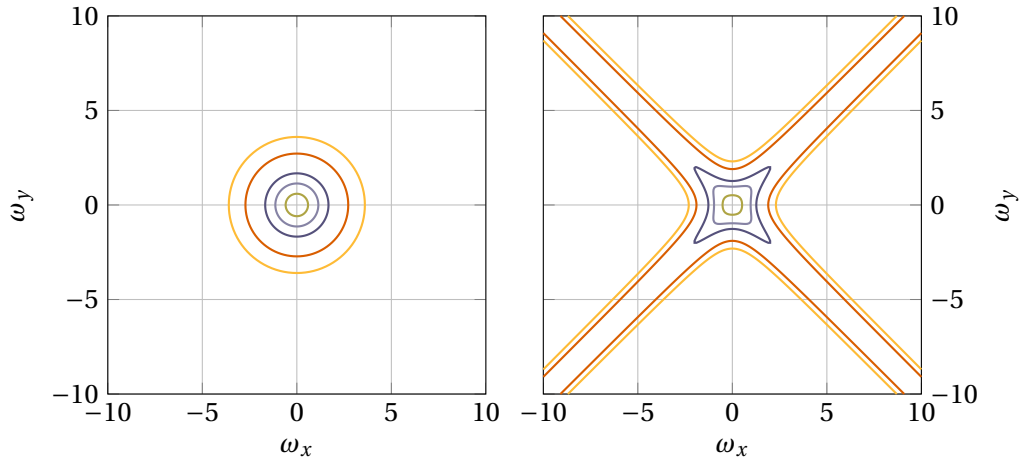

(a) Exact case.

(b) S_2 case.

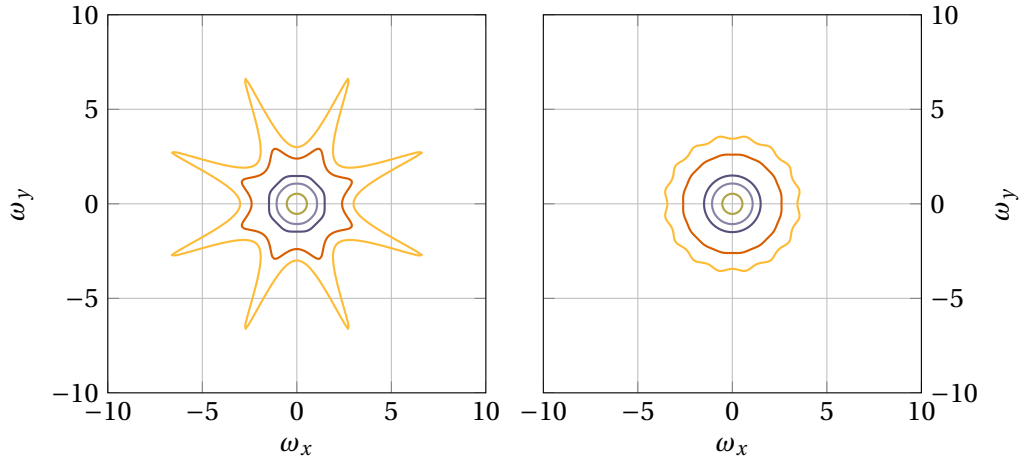

(c) S_4 case.

(d) S_8 case.

Figure 4.2: Contour plot of the modulus exact transport kernel (top left), compared to the discretized versions obtained adopting different numbers of discrete ordinates. $\Sigma = 1\ \mathrm{cm}^{-1}$, $c = 0.8$. Isolines plotted for values 0.6, 0.3, 0.2, 0.1 and 0.07 starting from the center. The maximum of the functions is normalized to one.

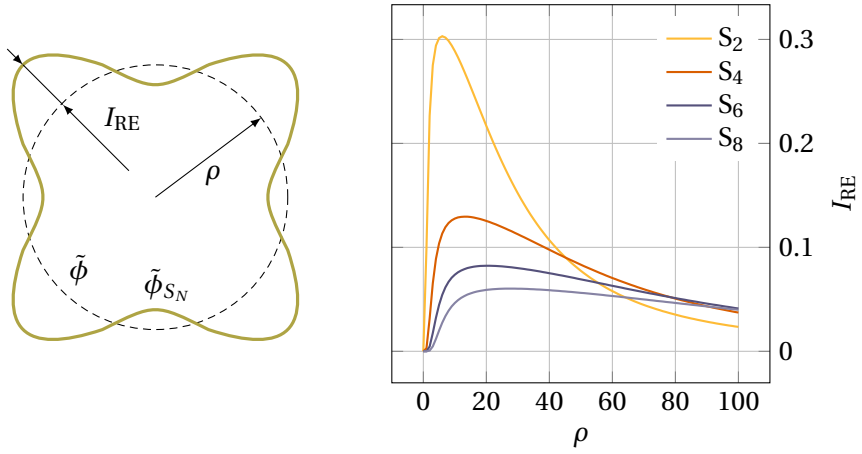

(a) Identification of I_{RE}.

(b) $x-y$ case.

Figure 4.3: Ray effect indicator I_{RE} ($\Sigma = 1$ cm^{-1}, $c = 0.5$).

ray effect phenomenon was apparent in this framework. However, the information obtained may easily turn out to be difficult to interpret, and its connection to the features of the problem in the physical space is lost. On the other hand, the analysis of the transport phenomenon in the physical space requires the introduction of important simplifications in the source terms.

In this section, the characterization of a transport problem is carried out in bidimensional $x-y$ geometry by analytical means, in order to identify a suitable ray effect indicator with the same philosophy adopted in the Fourier transformed space. To do so, a homogeneous medium in the absence of scattering is considered, which permits the analytical representation of the solution for the flux and, at the same time, it is the most challenging configuration for the appearance of the ray effect. The domain considered is a square with an edge of 2 m.f.p., with no volume sources, and an incoming isotropic flux ϕ_0 on one portion $[0; y_0]$ of the vertical edge, where $y_0 = 1$ m.f.p for simplicity. A vacuum boundary condition is assumed on the rest of the sides. The transport model considered is again flatland-like, with no loss of significance of the results. It is possible to show [Barbarino et al., 2013a] that the angular flux is non-zero in all the spatial points of the domain, and it takes the form:

$$\phi(x,y,\theta) = \begin{cases} \phi_0 \exp\left[-\dfrac{\Sigma}{\cos\theta}x\right] & \alpha_1 \le \theta \le \alpha_0 \\ 0 & \text{otherwise,} \end{cases} \tag{4.9}$$

where

$$\alpha_1 = \tan^{-1}\frac{y-y_0}{x}, \quad \alpha_0 = \tan^{-1}\frac{y}{x}.$$

The scalar flux can then be retrieved as:

$$\Phi(x,y) = \int_{\alpha_1}^{\alpha_0} \phi(x,y,\theta)\,\mathrm{d}\theta. \tag{4.10}$$

The integral (4.10) does not seem solvable in terms of elementary functions, so a reference solution is obtained by performing the integration numerically to a high degree of accu-
Figure 4.4a racy. The resulting spatial distribution of the scalar flux is depicted in Figure 4.4a. The same physical problem is then solved adopting a discrete ordinates S_N approach: a reduced number of ordinates is assumed and a quadrature formula is used to evaluate the
Figure 4.4b integral. In Figures 4.4b, 4.4c and 4.4d the results obtained assuming 2, 4 and 8 equally
Figure 4.4c spaced and weighted directions on the $x-y$ plane are reported. Directions may also be
Figure 4.4d identified adopting a Gauss-Legendre quadrature on the interval $[0;2\pi]$.

In order to quantify the amount of ray effect in this case and in analogous $x-y$ configurations, a simple, practical scheme is set up. Consider the solution for the scalar flux restricted along a generic straight line γ crossing the domain, denoted by the symbol f_γ. If the solution is exact, intuitively from equation (4.9) one could imagine that the function obtained would be quite well represented by an expansion in terms of few exponentials:

$$f_\gamma(\xi) \approx h_\gamma^{(M)}(\xi) = \sum_{m=1}^{M} a_m e^{m\xi}, \tag{4.11}$$

where ξ is the characteristic coordinate along the designated line γ. In other words, the value of M needed to reduce the error-norm $\|f_\gamma - h_\gamma\|$ below a certain small threshold should be small, having possibly excluded the areas close to the source.

On the other hand, the more the solution is biased by ray artifacts (in the form of steep gradients, localized peaks and discontinuities), the more f_γ should be difficult to be represented by the expansion (4.11) with few terms.

Following this intuition, a simple indicator is defined which theoretically should be able to classify the solutions according to the amount of spatial ray effect without knowing the exact solution, but only its mathematical nature.

In order to obtain a reference, the procedure is first applied to the exact solution, using a set of 100 equally spaced lines parallel to the x axis and other 100 equally spaced parallel to y. For each of the 200 restrictions of the flux, f_γ, the corresponding approximated function h_γ is calculated adopting a least squares algorithm. The discrepancy between the two functions is evaluated as the root of the mean squared error. The values falling in the rectangle $(x,y) \in \{(0,0)\times(0.1,1.1)\}$ are neglected, in order to attenuate the strong gradients induced by the boundary source. All the obtained values are averaged arithmetically, obtaining a global indicator for the whole domain. The procedure shows for this case that an exponential expansion with $M=4$ represents well enough the solution, with the indicator in the order of 10^{-2}.

The same procedure is repeated on the S_N solutions introduced earlier, using Gauss-Legendre quadratures of increasing order, as well as equally spaced and weighted directions. These two approaches to the angular treatment are associated with an exact solution for the spatial dependence (as inequation (4.9)) at first; then, the effect of the spatial discretization is considered assuming a spatial mesh $\Delta x = \Delta y = 0.1$ m.f.p. and a standard diamond difference scheme.

Figure 4.5 The resulting values of the ray effect indicator for all cases are summarized in Figure 4.5. As mentioned earlier, the "exact" curve represents the difference of the exact solution as

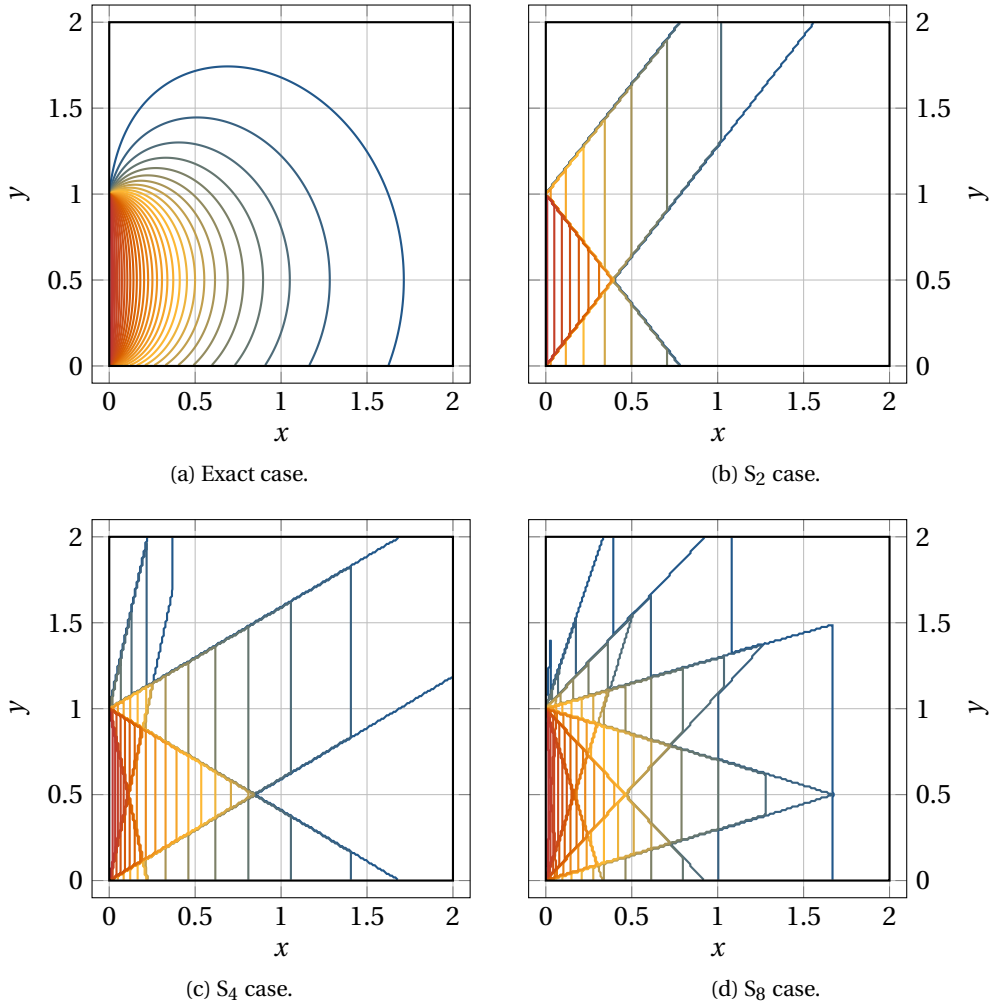

(a) Exact case.

(b) S_2 case.

(c) S_4 case.

(d) S_8 case.

Figure 4.4: Contour plot of the solution of the $x-y$ problem in the absence of scattering. Comparison of discrete ordinates with the exact solution.

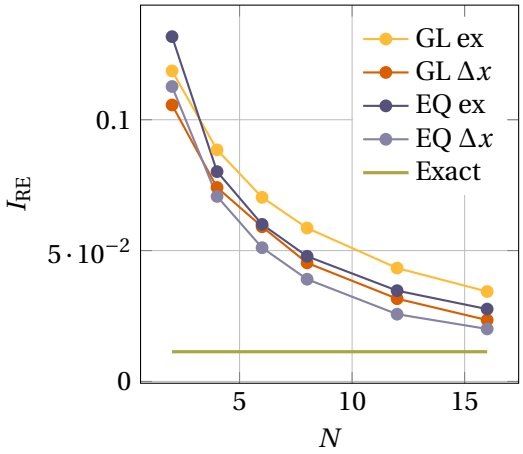

Figure 4.5: Ray effect indicator based on the use of a four-term exponential expansion, compared to the reference (Exact) and angular discretized solutions of the $x-y$ transport problem. Results are provided for Gauss-Legendre nodes and weights in association to an exact representation (GL ex) and discretized solution (GL Δx) of the spatial operator. The same evaluations are performed adopting equally spaced angular nodes (EQ ex and EQ Δx).

compared to the four-term exponential representation, and it is therefore constant, while the indicator calculated on the discretized solution is, as expected, higher. The beneficial effect of the increase in the number of discrete ordinates is reflected in the decrease of the indicator, while the choice of the quadrature set and the introduction of the spatial discretization has a less relevant influence. Additionally, it may be observed that the spatially discretized solutions are associated to a slightly smaller ray effect indicator as defined above. This can be justified by the spatial discretization scheme that, imposing a local balance of the flux on the bi-dimensional mesh, may smooth the sharp gradient of the angular discretized solution and therefore reduce the ray effects.

The proposed definition of a ray effect indicator based on the understanding of the mathematical nature of the solution has proven to be rather effective for the evaluation of the numerical artifacts in the bi-dimensional case under analysis. The extension of such method to a general case, including the effect of scattering and the heterogeneity of the medium, is not straightforward and would require additional studies, foreseen for future works.

4.2 Time dependent problems

4.2.1 Problems in $x-t$ in the transformed space

The transport model in one-dimensional slab geometry is not affected by ray effect phenomena in steady-state conditions. However, distortions of the propagation of particles associated to the discretization of the angular variable can be observed also in 1D when time-dependence is also considered. These phenomena are usually called time-ray effects [Dulla et al., 2006]; they can be easily understood from a physical point of view if one con-

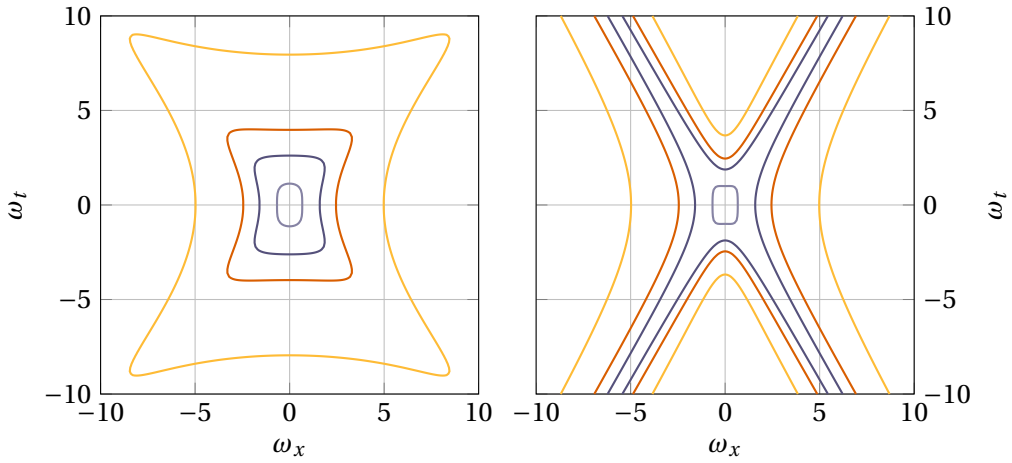

(a) Exact case.

(b) S_2 case.

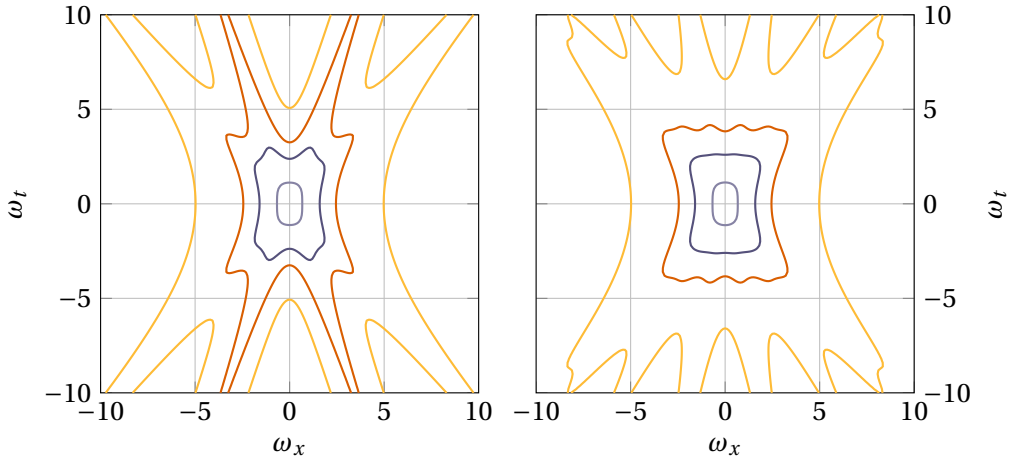

(c) S_4 case.

(d) S_8 case.

Figure 4.6: Contour lines of the modulus of the Fourier-transformed transport kernel for the $x-t$ problem (top left), compared to the discretized versions obtained adopting different numbers of discrete ordinates ($\Sigma = 1cm^{-1}$, $c = 0.5$, $v = 1cm/s$). Isolines, from the center, correspond to values 0.6, 0.3, 0.2 and 0.1.

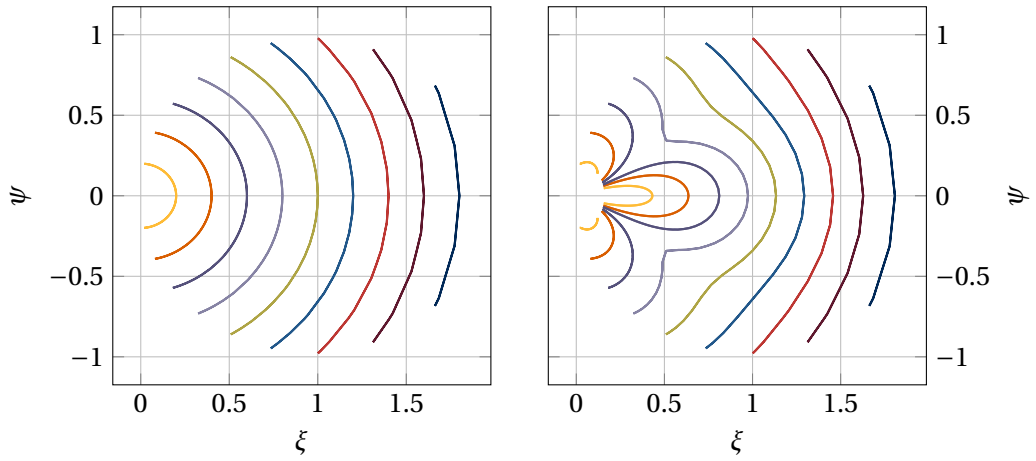

(a) Exact case.

(b) S_2 case.

(c) S_4 case.

(d) S_8 case.

Figure 4.7: Contour lines of the modulus of Fourier-transformed transport kernel for the $x-t$ model, where the coordinates of the frequency space are conveniently mapped $\{\omega_x, \omega_t\} \mapsto \{\xi, \psi\}$ to recover the circular pattern of the exact solution. Isolines, from the left, go from 0.1 to 0.9 with increments of 0.1.

siders that particles moving along a specific direction in the set of the discrete ordinates can reach some specific points in free flight only at a certain specific time, determined by the particle velocity.

The general transport problem experiencing time ray effects can be written in the form:

$$\frac{1}{\mathrm{v}}\frac{\partial}{\partial t}\phi(x,\mu,t)+\mu\frac{\partial}{\partial x}\phi(x,\mu,t)+\Sigma\phi(x,\mu,t)=\frac{c\Sigma}{2}\Phi(x,t)+\frac{S(x,t)}{2}, \tag{4.12}$$

where, again, the energy dependence is neglected in order to focus on the interaction among angle, space and time. The system is considered to be infinite and homogeneous, and the mathematical form of the present model is analogous to the previous $x-y$ case, allowing the application of the Fourier transforms to obtain the solution. Equation (4.12) when transformed in both space and time reads:

$$\left(i\frac{\omega_t}{\mathrm{v}}+i\mu\omega_x+\Sigma\right)\tilde{\phi}(\omega_x,\omega_t,\mu)=\frac{c\Sigma}{2}\tilde{\Phi}(\omega_x,\omega_t)+\frac{\tilde{S}(\omega_x,\omega_t)}{2}, \tag{4.13}$$

which can be solved to obtain the transformed scalar flux:

$$\tilde{\Phi}(\omega_x,\omega_t)=\frac{1}{2}\int_1^1 \mathrm{d}\mu\frac{1}{i\frac{\omega_t}{\mathrm{v}}+i\mu\omega_x+\Sigma}\left(c\Sigma\tilde{\Phi}(\omega_x,\omega_t)+\tilde{S}(\omega_x,\omega_t)\right), \tag{4.14}$$

or, explicitly:

$$\tilde{\Phi}(\omega_x,\omega_t)=\frac{\Lambda(\omega_x,\omega_t)}{1-c\Sigma\Lambda(\omega_x,\omega_t)}\tilde{S}(\omega_x,\omega_t) \quad =H(\omega_x,\omega_t)\tilde{S}(\omega_x,\omega_t), \tag{4.15}$$

where in this case

$$\Lambda(\omega_x,\omega_t)=\frac{1}{2i\omega_x}\log\left[\frac{i\omega_t+\Sigma\mathrm{v}+i\mathrm{v}\omega_x}{i\omega_t+\Sigma\mathrm{v}-i\mathrm{v}\omega_x}\right].$$

Although the mathematical nature of the $x-y$ and $x-t$ problem is similar, the corresponding kernel in the transformed space shows different features. In particular, it can be easily observed from formula (4.2.1) that the kernel depends on both the transformed coordinates separately, and not only on their vector modulus, therefore no circular symmetry can be expected in this case. This is made clear by the direct observation of the modulus of the transfer function in Figure 4.6a, which for the time-dependent case shows a different symmetry in the transformed space with respect to Figure 4.1a. However, the appearance of ray effects can be observed in the transport kernel also in this case; the integral over μ in (4.14) is now substituted by a quadrature formula, leading to a different definition for the function Λ:

Figure 4.6a

$$\Lambda_{S_N}(\omega_x,\omega_t)=\frac{1}{2}\sum_{n=1}^{N}\left[\frac{w_n}{i\frac{\omega_t}{\mathrm{v}}+i\mu\omega_x+\Sigma}\right], \tag{4.16}$$

and the resulting transport kernel is plotted in Figs. 4.6b, 4.6c and 4.6d for different angular approximations. Again, it is possible to identify the distortions associated with the discrete directions.

Figure 4.6b
Figure 4.6c
Figure 4.6d

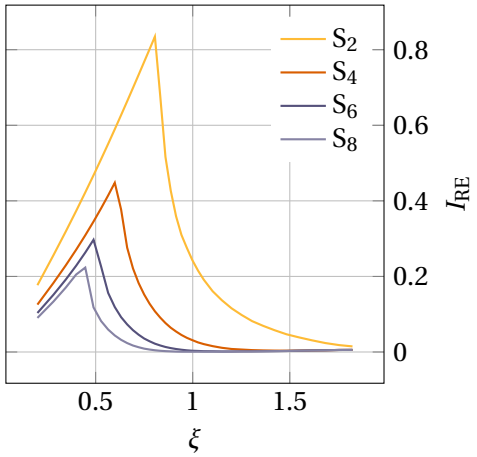

Figure 4.8: Ray effect indicator I_{RE} (Σ=1 cm^{-1}, c=0.5, v=1 m/s) in the $x-t$ case.

The relevance of ray effect in $x-t$ configurations can be seen more clearly by performing a suitable change of coordinates $\{\omega_x,\omega_t\} \mapsto \{\xi,\psi\}$, in order to recover a circular symmetry for the exact transport kernel, as shown in Figure 4.7a. The coordinate transformation amounts to writing explicitly the real and imaginary parts of the complex function $H(\omega_x,\omega_t)$ in formula (4.15) as $\xi + i\psi$, so that the modulus of the exact transfer function shows a circular symmetry. When the same mapping procedure is applied to the S_N discretized transfer functions, the appearance of a distortion in the particle propagation is clearly visible, as can be observed in Figure 4.7.

Figure 4.7

The representation of the $x-t$ transport kernels in the transformed space with respect to the new coordinates ξ and ψ allows the introduction of the ray effect indicator I_{RE} as in the previous case. The distortion in the isolines is measured like Figure 4.3a and the resulting values as function of ξ are reported in Figure 4.8. It is observed a pattern similar to the $x-y$ case, with the presence of a maximum, and the attenuation of the distortion when a larger number of directions is adopted is confirmed.

Figure 4.8

4.2.2 Effect of the improvement of the angular description

At this point, it may be of interest to investigate the possibility to adopt a different approach for the angular treatment in the time-dependent problem considered above, with the aim of mitigating or smoothing the time-ray effect phenomena. Till now the mathematical similarities of the $x-y$ and $x-t$ problems have been exploited; hence, the methods that have been adopted in the literature for the reduction of ray effects in multi-dimensional steady-state transport problems are first considered.

The appearance of ray effects in multi-dimensional transport is due to the physical distortion in the streaming of particles, forced to propagate along specific directions. The reduction of such distortion can be attained operating on the number of ordinates adopted, also making use of localized refinement of the angular mesh, but still retaining an S_N-like formalism of the problem [Longoni and Haghighat, 2002]. Other approaches are based on

the use of different basis functions for the representation of the angular dependence, such as wavelets [Buchan et al., 2008] and finite elements [Briggs et al., 1975; Coppa et al., 1990; Drumm et al., 2013]. The attention is focused on this second class of techniques, trying to understand whether the application of finite elements to the angular variable μ in the $x-t$ transport problem can be beneficial for the reduction of time-ray effects.

Finite element methods of different flavors have been applied to linear transport problems. A large deal of work has focused on the standard FEM approach, where the bidimensional Ω angular domain to be discretized is subdivided in triangular meshes and the classic "tent" trial functions are introduced into the model equation to minimize the residual *à la Galerkin* [Martin et al., 1981; Drumm et al., 2013]. Other developments have been performed introducing basis functions on the angle with a global support [Coppa et al., 1990; Coppa and Ravetto, 1995], therefore allowing a description of the angular behavior of the flux with a larger number of degrees of freedom. In the $x-t$ transport model under analysis, such approaches can be seen as a generic representation of the angular flux in the form:

$$\varphi(x,\mu,t) = \sum_{k=1}^{K} U_k(\mu) g_k(x,t), \tag{4.17}$$

where the functions U_k may be defined across two discretization meshes, as in standard FEM, or on the whole μ domain, as it is done for the spatial treatment with the spectral element method. Once the expansion (4.17) is introduced into the model (4.12), the integrals of the equation, weighted by the same functions U_k, over μ provide a set of linear equations for the expansion coefficients g_k. This process has been applied in Coppa et al. [1990] to $x-y$ flat-land transport, leading to a set of equations recast in matrix form. The same can be done here, leading to an expression written in compact form as:

$$\frac{1}{\mathrm{v}}\hat{A}\frac{\partial \boldsymbol{X}}{\partial t} + \hat{B}\frac{\partial \boldsymbol{X}}{\partial x} + \Sigma\hat{A}\boldsymbol{X} = \frac{c\Sigma}{2}\hat{C}\boldsymbol{X} + \frac{\boldsymbol{S}}{2} \tag{4.18}$$

where the unknown column vector $\boldsymbol{X}$ contains all the functions g_k, and the other terms in the equation are defined as follows:

$$\hat{A} = \{a_{ij}\}, \qquad a_{ij} = \int_{-1}^{1} \mathrm{d}\mu U_i(\mu) U_j(\mu), \tag{4.19}$$

$$\hat{B} = \{b_{ij}\}, \qquad b_{ij} = \int_{-1}^{1} \mathrm{d}\mu\mu U_i(\mu) U_j(\mu), \tag{4.20}$$

$$\hat{C} = \{c_{ij}\}, \qquad c_{ij} = \int_{-1}^{1} \mathrm{d}\mu' U_i(\mu') \int_{-1}^{1} \mathrm{d}\mu U_j(\mu), \tag{4.21}$$

$$\boldsymbol{S} = \left[S\int_{-1}^{1} \mathrm{d}\mu U_1(\mu), \quad S\int_{-1}^{1} \mathrm{d}\mu U_2(\mu), \quad \ldots, \quad S\int_{-1}^{1} \mathrm{d}\mu U_K(\mu) \right]^t. \tag{4.22}$$

The procedure makes then use of the solution of the generalized eigenvalue problem for the matrices $\hat{A}$ and $\hat{B}$:

$$\hat{A}\boldsymbol{V}_\alpha = \lambda_\alpha \hat{B}\boldsymbol{V}_\alpha, \qquad \alpha = 1,2,\ldots,K, \tag{4.23}$$

that can be written alternatively as:

$$\begin{aligned} \hat{A}\boldsymbol{V}_\alpha &= \nu_\alpha \boldsymbol{n}_\alpha, \\ \hat{B}\boldsymbol{V}_\alpha &= \eta_\alpha \boldsymbol{n}_\alpha, \\ \lambda_\alpha &= \nu_\alpha / \eta_\alpha. \end{aligned} \tag{4.24}$$

The unknown vector $\boldsymbol{X}$ is projected on the basis vectors $\boldsymbol{V}_\alpha$ and the orthogonality with respect to the vectors $\boldsymbol{n}_\alpha$ allows to diagonalize the first two terms of equation (4.18). The resulting system of equations is decoupled for what concerns the two differential terms. When the process is applied to bi-dimensional steady-state transport, the diagonalization process also modifies the collision term in the balance equation maintaining its coupling, resulting in an increased collision and scattering contribution with a beneficial smoothing of the ray effect.

On the contrary, when the diagonalization process is applied to the $x-t$ model in matrix form, equation (4.18), the collision term on the left-hand-side of the equation is also diagonalized, since the same matrix $\hat{A}$ appears in both the time derivative and collision terms. As a consequence, no additional collisionality is introduced by the process, and a standard S_N-like formulation of the problem is obtained, with a possible different definition of the quadrature set, as obtained by the diagonalization of matrix $\hat{B}$. This fact is due to the different form of the matrix equation obtained in the $x-t$ case, equation (4.18), with respect to the steady-state problem treated in Coppa et al. [1990]: in this latter case, all the coefficient matrices appearing in the equation are distinct, and the diagonalization process for the matrices associated with the differential part of the problem results in an additional coupling in the rest of the equation, that can be physically interpreted as increased collisions and scattering.

The mathematical sketch of the application of a generic collocation method, as in (4.17), and the consequent verification of the uselessness of such procedure, can be given a more general explanation.

The starting point of the methods introduced before, the expansion of the flux in terms of a set of function of the variable μ, aims at the characterization of the angular dependence of the neutron population with a large number of degrees of freedom. This can be obtained by adopting linear "tent" functions on a fine discretization of the μ domain as in FEM, or by the adoption of polynomial functions of μ on the whole interval, as it is done in spectral element methods.

We should also remember that also the P_N method, applied to the $x-t$ transport model, works with the same philosophy, assuming a polynomial form of the N-th order for the angular dependence of the angular flux. Moreover, the time-dependent P_N model in 1D slab is equivalent to the corresponding S_{N+1} model, having properly defined the discrete ordinates and integration weights, together with the boundary conditions, in the representation of the scalar flux. Therefore, the time-ray effect experienced with S_N models in $x-t$ transport is the same effect that can be observed when approaching the problem with the P_N formalism and, by extension, it will be observed in any collocation method as finite elements and spectral elements. The only difference that any of these methods can introduce is in the definition of the directions and weights for the quadrature integral.

In conclusion, we can state that the features of the time ray-effect in time-dependent 1D transport cannot be reduced by the application of a different numerical scheme for the angle as it has been done successfully with finite elements in multi-dimensional problems. To this aim, more innovative and complex approaches need to be identified.

4.2.3 Problem $x-t$ in direct space without scattering

In the previous sections the problem of time-ray effects has been addressed, firstly studying the characteristics of the transport operator in the Fourier transformed space, and then discussing the possibility to reduce such distortions by a suitable change of the discretization scheme for the angle.

Since one of the main conclusions of the previous section is that different discretization schemes are performing no better than S_N, the attention is now focused on the analysis of the same problem in the direct time-space domain, providing analytical results and comparing the performance of different quadrature sets for the S_N scheme.

All the problems considered are source-driven, and the medium is homogeneous and purely absorbing. These hypotheses allow an analytical solution for the angular and scalar flux, to be used as reference against the results obtained when the integral over the angle is substituted by quadrature in S_N.

The transport equation providing the angular flux ϕ in an infinite slab of homogeneous absorbing material is:

$$\frac{1}{\mathrm{v}}\frac{\partial\phi(x,\mu,t)}{\partial t}+\mu\frac{\partial\phi(x,\mu,t)}{\partial x}+\Sigma\phi(x,\mu,t)=Q(x,\mu,t). \tag{4.25}$$

The Green function of the problem is evaluated at first, introducing into the model (4.25) a delta source in space, angle and time:

$$Q_{\mathrm{G}}(x,\mu,t;x',\mu')=\delta(x-x')\delta(\mu-\mu')\delta(t). \tag{4.26}$$

The time dependence is handled by application of the Laplace transform, reducing (4.25) to an ordinary differential equation in x, whose solution is the Green function of the problem:

$$\tilde{\phi}_{\mathrm{G}}\left(x-x',\mu-\mu',s\right)=\frac{\delta(\mu-\mu')}{|\mu|}\exp\left[-\frac{1}{\mu}\left(\Sigma+\frac{s}{\mathrm{v}}\right)\left(x-x'\right)\right]\cdot\vartheta\left[\mathrm{sgn}(\mu')\left(x-x'\right)\right], \tag{4.27}$$

where ϑ denotes the Heaviside function. Obviously, the solution (4.27) depends parametrically on the transformed variable s. The Green function in the physical time domain can be obtained performing the inverse transform:

$$\phi_{\mathrm{G}}\left(x-x',\mu-\mu',t\right)=\mathscr{L}^{-1}_{s\to t}\left(\tilde{\phi}_{\mathrm{G}}\left(x-x',\mu-\mu',s\right)\right), \tag{4.28}$$

and the subsequent convolution with any generic source yields the solution to the transport model for the angular and scalar flux:

$$\phi(x,\mu,t)=\int_{-\infty}^{+\infty}\mathrm{d}x'\int_{-1}^{+1}\mathrm{d}\mu'\int_{0}^{t}\mathrm{d}t'Q(x',t',\mu')\phi_{\mathrm{G}}\left(x-x',\mu-\mu',t-t'\right) \tag{4.29}$$

$$\Phi(x,t)=\int_{-1}^{1}\mathrm{d}\mu\phi(x,\mu,t). \tag{4.30}$$

Equations (4.30), if written down explicitly, provides the exact solution to the transport problem and can be considered as a reference. The angular discretization can be introduced through a quadrature evaluations of the integrals over μ in equations (4.30), yielding the S_N-like solution to be compared to the reference.

In the following, the flux responses to some source distributions are explicitly calculated and compared to S_N results.

Analytical solution to some benchmark problems

Isotropic pulsed point source The first source considered emits a pulse of particles isotropically at $x = 0$, therefore the source reads as:

$$Q_1(x,\mu,t) = \frac{1}{2}\delta(x)\delta(t) \quad \rightarrow \quad \tilde{Q}_1(x,\mu,s) = \frac{1}{2}\delta(x). \tag{4.31}$$

The scalar flux in this simple case can be evaluated in the Laplace transformed space as:

$$\tilde{\Phi}_1(x,s) = \frac{1}{2}\int_{-1}^{+1} \mathrm{d}\mu \int_{-\infty}^{+\infty} \mathrm{d}x' \int_{-1}^{+1} \mathrm{d}\mu' \tilde{\phi}_G(x-x',\mu-\mu',s)\delta(x') = \frac{1}{2}\mathrm{E}_1\left[\left(\Sigma + \frac{s}{\mathrm{v}}\right)|x|\right], \tag{4.32}$$

where E_1 is the exponential integral function, defined as:

$$\mathrm{E}_1\left[\left(\Sigma + \frac{s}{v}\right)|x|\right] = \int_0^1 \frac{\mathrm{d}\mu}{\mu} \exp\left[-\frac{\left(\Sigma + \frac{s}{\mathrm{v}}\right)|x|}{\mu}\right]. \tag{4.33}$$

The inverse transform of (4.32) can be expressed analytically, giving the final result:

$$\Phi_1(x,t) = \frac{1}{2}\vartheta\left[t - \frac{|x|}{\mathrm{v}}\right]\frac{\exp\left[-\Sigma \mathrm{v} t\right]}{t}. \tag{4.34}$$

This solution will be used in the following as the Green function for a more general case of an isotropic pulsed source with a general spatial distribution.

Isotropic pulsed Gaussian source The second source considered has a Gaussian spatial distribution, centered at $x = m$ with standard deviation σ:

$$Q_2(x,\mu,t) = \frac{1}{2}\frac{1}{\sqrt{2\pi\sigma^2}}\exp\left(-\frac{(x-m)^2}{2\sigma^2}\right)\delta(t). \tag{4.35}$$

The flux response to source Q_2 is obtained directly by a convolution product of the source with the appropriate Green function for this problem, Eq. (4.34), giving the result:

$$\Phi_2(x,t) = \frac{1}{4}\frac{e^{-\Sigma \mathrm{v} t}}{t}\left[\mathrm{erf}\left(\frac{x-m+\mathrm{v}t}{\sqrt{2\sigma^2}}\right) - \mathrm{erf}\left(\frac{x-m-\mathrm{v}t}{\sqrt{2\sigma^2}}\right)\right]. \tag{4.36}$$

Collimated pulsed Gaussian source The case here considered is based on the previous source Q_2, introducing a collimation along the direction μ_0 for the particles emitted:

$$Q_3(x,\mu,t) = \frac{1}{\sqrt{2\pi\sigma^2}} \exp\left(-\frac{(x-m)^2}{2\sigma^2}\right) \delta(t)\delta(\mu-\mu_0). \tag{4.37}$$

The corresponding flux is obtained performing the convolution product reported in formula (4.30), giving as a result:

$$\Phi_3(x,t) = \frac{\mathrm{v}}{\sqrt{2\pi\sigma^2}} \exp\left(-\mathrm{v}\Sigma t\right) \exp\left(-\frac{(x-m-\mathrm{v}\mu_0 t)^2}{2\sigma^2}\right). \tag{4.38}$$

Pulsed Gaussian source with finite angle polarization This last configuration can be seen as a variation of the previous case, useful for the following discussion on how to treat anisotropic source with an S_N scheme. The angular dependence of the source is here given in the form of a gate function as:

$$Q_4(x,\mu,t) = \frac{1}{2}\frac{1}{\sqrt{2\pi\sigma^2}} \exp\left(-\frac{(x-m)^2}{2\sigma^2}\right) \delta(t) \left[\vartheta\left(\mu-a\right) - \vartheta\left(\mu-b\right)\right], \tag{4.39}$$

where a and b are such that $-1 \leq a < b \leq 1$ and represent the limits for the region where the angular dependence is constant and non-zero. The convolution of this source with the Green function (4.28) gives the following expression for the scalar flux:

$$\Phi_4(x,t) = \frac{1}{4}\frac{\exp\left(-\Sigma\mathrm{v}t\right)}{t} \left[\mathrm{erf}\left(\frac{x-m-\mathrm{v}at}{\sigma\sqrt{2}}\right) - \mathrm{erf}\left(\frac{x-m-\mathrm{v}bt}{\sigma\sqrt{2}}\right)\right]. \tag{4.40}$$

S_N solution and comparison of different quadrature schemes

The solutions evaluated in the previous section can be used as reference to be compared to the approximate results that can be obtained when adopting an S_N scheme for the angular treatment. This can be done evaluating the integrals over μ by a quadrature rule, thus allowing to identify the effect of the discrete ordinates without the superposition of any other discretization scheme for the other phase-space variables.

The interest is focused on the possible effects associated with the choice of directions and weights. Therefore, several quadrature schemes are applied [Abramowitz and Stegun, 1972], in order to evaluate how the S_N approximate solution is modified by the different choices of directions and weights.

The Gauss-Jacobi quadrature provides a general definition valid for most schemes:

$$\int_{-1}^{+1} f(\mu)(1-\mu)^{\alpha}(1+\mu)^{\beta}\,\mathrm{d}\mu = \sum_{n=1}^{N} w_n f(\mu_n), \tag{4.41}$$

where α and β are two real numbers and are both strictly larger than -1. Different situations can be identified:

- $\alpha = \beta$: Gegenbauer quadrature (GB);

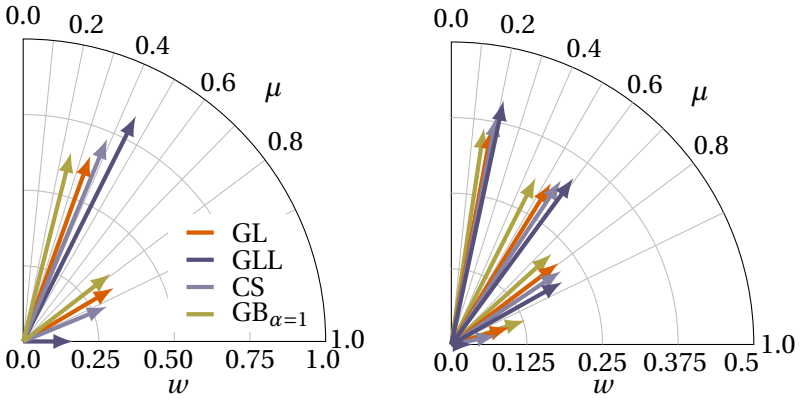

(a) Directions adopted in S_4.

(b) Directions adopted in S_8.

Figure 4.9: Schematics of the quadrature rules adopted. The length of the arrows is representative of the corresponding weight.

- $\alpha = \beta = -0.5$: Chebyshev quadrature (CS);
- $\alpha = \beta = 0$: Gauss-Legendre quadrature (GL).

A fourth quadrature set, which cannot be directly obtained from (4.41) as GB and CS, is the Gauss-Lobatto-Legendre formula: it has a unit weight function, as with Gauss-Legendre, and both integration endpoints belong to the set of nodes.

The presence of the weight function $(1-\mu)^\alpha(1+\mu)^\beta$ in the integral to be approximated represents a limitation for the application of the quadrature in a general case. The problem can be circumvented by an elaboration of the integral to be performed, thus modifying the weights that will be adopted in the quadrature:

$$\begin{aligned}\int_{-1}^{+1} f(\mu)\,\mathrm{d}\mu &= \int_{-1}^{+1} (1-\mu)^\alpha(\mu+1)^\beta \frac{f(\mu)}{(1-\mu)^\alpha(1+\mu)^\beta} \\ &\approx \sum_{n=1}^{N} w_n \frac{f(\mu_n)}{(1-\mu_n)^\alpha(1+\mu_n)^\beta} \\ &\approx \sum_{n=1}^{N} w'_n f(\mu_n).\end{aligned} \tag{4.42}$$

The corrected weights w'_n can be easily evaluated and do not require the knowledge of the function to be integrated. Interestingly, when the adjustment (4.42) of the weights is performed assuming α and β values both approaching -1, a set of directions and weights is obtained that has its limit in those of the Gauss-Lobatto-Legendre quadrature.

Figure 4.9 Figure 4.9 gives a graphical representation of the directions assumed for each quadrature scheme, where the length of the arrows is proportional to the corresponding weight.

The various quadrature sets introduced are now applied for the evaluation of the scalar fluxes in response to the different sources described above. In the following the generic

symbol w_i is adopted to denote the weights, bearing in mind the required modification (4.42) for the use of various quadrature schemes.

Isotropic pulsed point source In this case, the scalar flux $\Phi_1^\star$ is obtained starting from the Laplace-transformed expression (4.32), substituting the integral over μ with the quadrature:

$$\begin{aligned}\Phi_1^\star(x,t) &= \frac{1}{2}\mathscr{L}_{s\to t}^{-1}\left\{\mathrm{E}_1\left[\left(\Sigma+\frac{s}{\mathrm{v}}\right)|x|\right]\right\}\\ &= \frac{1}{2}\mathscr{L}_{s\to t}^{-1}\left\{\sum_{i=1}^{N/2}\frac{w_i}{\mu_i}\exp\left[-\frac{\left(\Sigma+\frac{s}{\mathrm{v}}\right)|x|}{\mu_i}\right]\right\},\end{aligned} \tag{4.43}$$

where the sum is limited to the positive values of μ to be consistent with the integral (4.33).

Since the inverse transform operator is linear, it is possible to move it inside the sum: the inverse transform of each exponential term gives a Dirac delta function in the direct space, namely:

$$\begin{aligned}\Phi_1^\star(x,t) &= \frac{1}{2}\sum_{i=1}^{N/2}\frac{w_i}{\mu_i}\mathscr{L}_{s\to t}^{-1}\left\{\exp\left[-\frac{\left(\Sigma+\frac{s}{\mathrm{v}}\right)|x|}{\mu_i}\right]\right\}\\ &= \frac{1}{2}\sum_{i=1}^{N/2}\frac{w_i}{\mu_i}\exp\left(-\frac{\Sigma|x|}{\mu_i}\right)\delta\left(t-\frac{|x|}{\mathrm{v}\mu_i}\right).\end{aligned} \tag{4.44}$$

Expression (4.44) clearly states that neutrons are propagated only along specific collimated directions, identified by the ordinates where the delta functions are centered, thus distorting the physics of the propagation as represented by the reference solution (4.34).

Isotropic pulsed Gaussian source The approximate solution just evaluated, (4.44), is now used as Green function to obtain the scalar flux associated with the source Q_2:

$$\begin{aligned}\Phi_2^\star(x,t) = \frac{\mathrm{v}}{2\sqrt{2\pi\sigma^2}}\exp(-\Sigma\mathrm{v}t)\times\\ \sum_{i=1}^{N/2}w_i\left[\exp\left(-\frac{(x-m-\mathrm{v}\mu_i t)^2}{2\sigma^2}\right)+\exp\left(-\frac{(x-m+\mathrm{v}\mu_i t)^2}{2\sigma^2}\right)\right]\end{aligned} \tag{4.45}$$

The analytical solution (4.36) is compared to the different S_N discretized forms that can be obtained adopting different quadrature sets in Figures 4.10 and 4.11 for a source symmetrically located with respect to $x = 0$. The solutions for the positive half-domain at different time instants are reported, since the solution is even. The different localization of the maxima in the S_N fluxes is due to the different directions adopted, while their height reflects the weights associated with such directions. As expected, the choice of a different quadrature scheme is not providing an attenuation of the ray effects phenomenon. However, the different direction choice is affecting the localization of the artifacts and their amplitude is directly related to the associated weight that ensures the conservation of particles.

Figure 4.10
Figure 4.11

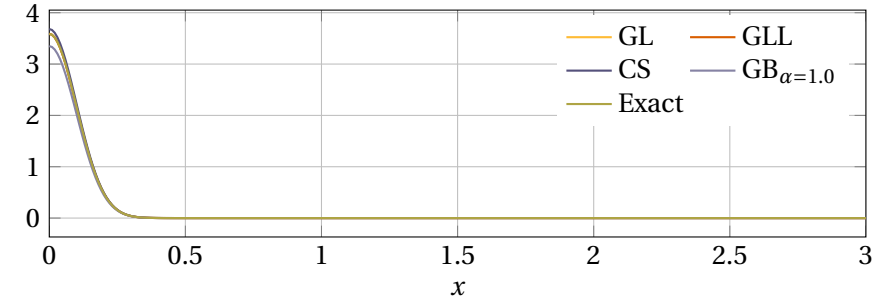

(a) $t = 0.001$

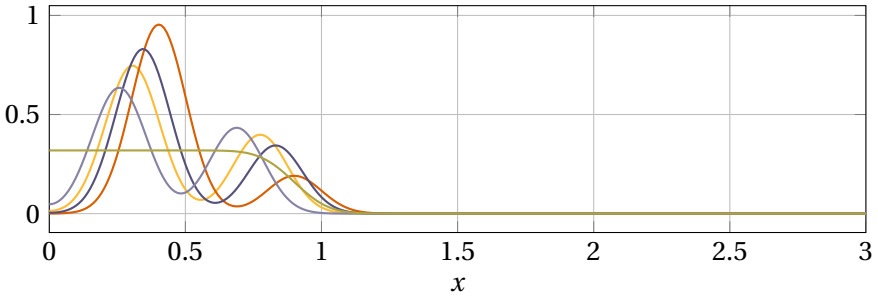

(b) $t = 1$

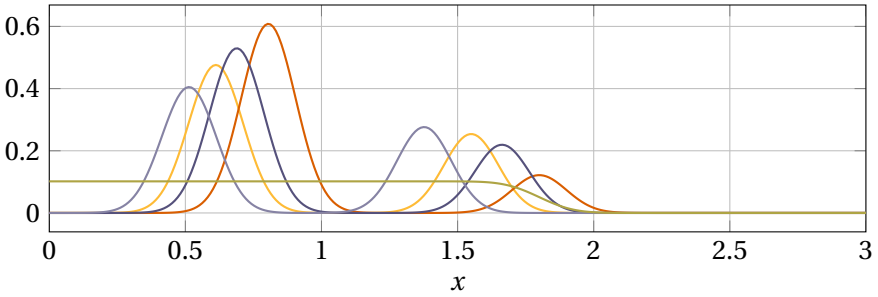

(c) $t = 2$

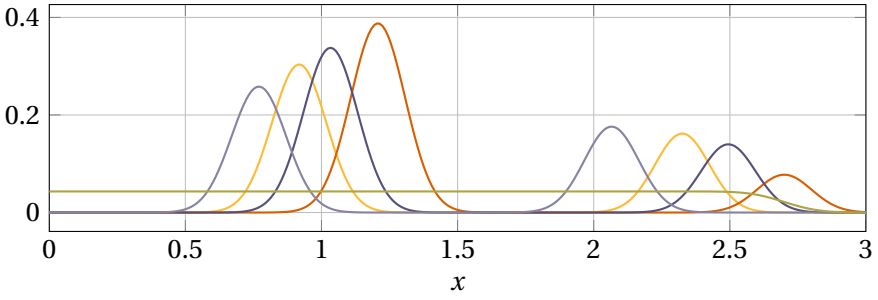

(d) $t = 3$

Figure 4.10: Flux response to an isotropic pulsed Gaussian source ($m = 0$ cm, $\sigma = 0.1$ cm), solved with exact transport and S_4 ($\Sigma = 0.5$ cm,v = 0.9 cm/s).

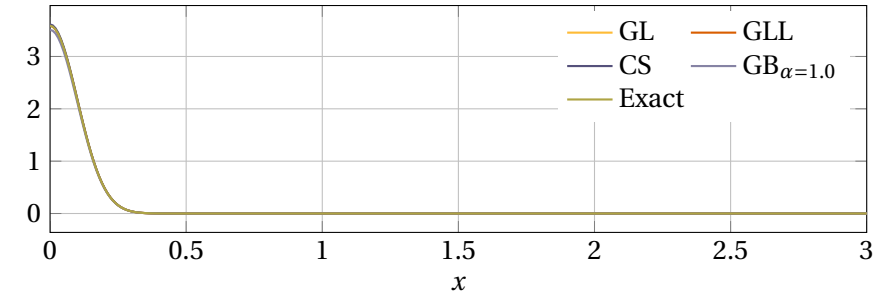

(a) $t = 0.001$

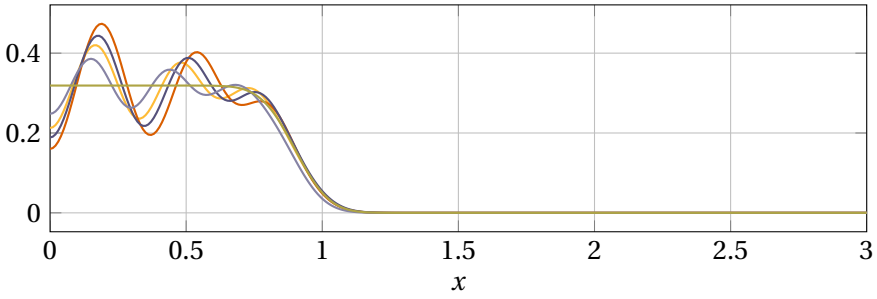

(b) $t = 1$

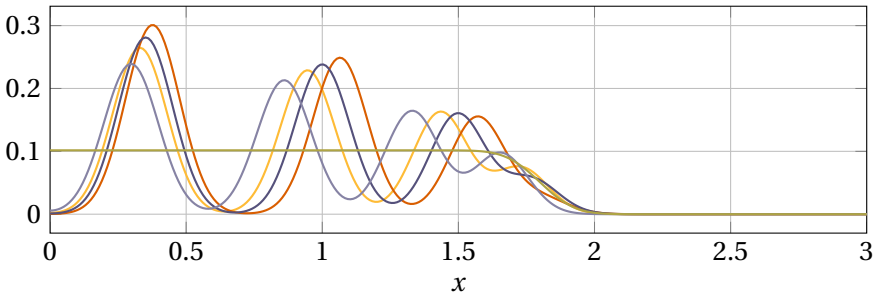

(c) $t = 2$

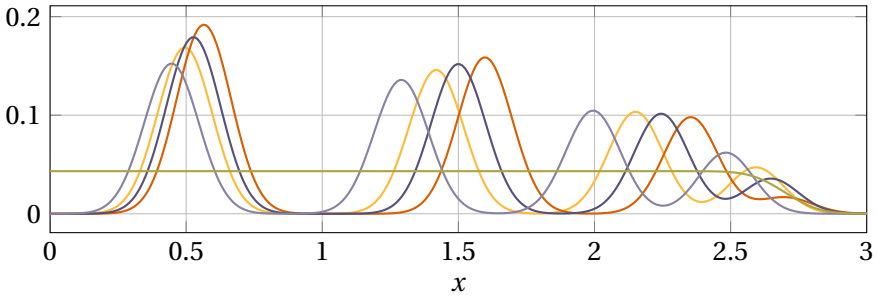

(d) $t = 3$

Figure 4.11: Flux response to an isotropic pulsed Gaussian source ($m = 0$ cm, $\sigma = 0.1$ cm), solved with exact transport and S_8 ($\Sigma = 0.5$ cm^{-1}, v = 0.9 cm/s).

Collimated pulsed Gaussian source The S_N solution for this collimated source takes the form:

$$\Phi_3^\star = \frac{\mathrm{v}}{\sqrt{2\pi\sigma^2}} \exp\left(-\Sigma \mathrm{v} t\right) \sum_{i=1}^{N/2} w_i \exp\left(-\frac{\left(x - m - \mu_0 \mathrm{v} t\right)^2}{2\sigma^2}\right) \delta(\mu_i - \mu_0). \tag{4.46}$$

Is is important to notice that the discretized solution for such a strongly collimated source can provide a null result, if the direction of propagation is not part of the discrete directions adopted. This extreme situation is representative of the problems that can be encountered when treating strongly anisotropic phenomena with a discrete ordinate approach. A more general case of an anisotropic source emission and some additional discussion on this subject are presented in the following.

Pulsed Gaussian source with finite angle polarization Finally, using Q_4 one obtains the following discretized solution to the transport model (4.25):

$$\Phi_4^\star(x,t) = \frac{\mathrm{v}}{2\sigma\sqrt{2\pi}} \exp\left(-\Sigma \mathrm{v} t\right) \sum_{i=1}^{N/2} w_i \exp\left(\frac{(x - m - \mathrm{v}\mu_i t)^2}{2\sigma^2}\right) \left[\vartheta\left(\mu_i - a\right) - \vartheta\left(\mu_i - b\right)\right] \tag{4.47}$$

The nature of this solution depends on the relative position of the gate with respect to the discrete ordinates available in the set chosen. If none of the directions is included between a and b, the discretized solution vanishes for any $t > 0$. In the other cases, the solution depends solely on the number of discrete ordinates seen by the gate function, but the exact values a and b will have no influence on the solution. This also implies that the exact number of particles emitted by the source is never correctly taken into account, since only a few discrete contributions of the source are considered by the scheme. The response function obtained is over or under-estimating the correct solution in a quite unpredictable way, with foreseeable increased loss of accuracy if a small number of directions is adopted. In such a case, it might be advisable to adopt a non conventional quadrature scheme with respect to the standard Gauss-Legendre set, for the purpose of following more closely the direction propagation of the collimated particles.

The problem of the lack of particle conservation can be overcome in this particular case with a calibration of the quadrature scheme. Since the angular behavior $s(\mu)$ of the neutron source is known at $t = 0$, it is plausible to think that its integral over $[-1, +1]$ can be evaluated analytically or with a sufficient accuracy with another method which does not pose the same resolution problem of a Gaussian schemes. Then, the following equality can be imposed, appropriately modifying the weights:

$$\sum_{n=1}^{N} w_n^\star s(\mu_n) = \int_{-1}^{+1} s(\mu)\, \mathrm{d}\mu, \tag{4.48}$$

where $w_n^\star$ are the rescaled weights to preserve the source strength. In our case equation (4.48) reads as:

$$\sum_{a<\mu_n<b} w_n^\star s(\mu_n) = \int_a^b \mathrm{d}\mu = b - a. \tag{4.49}$$

Since the angular distribution of the particles does not change during the propagation due to the absence of scattering, it can be assumed that the rescaled quadrature is able to account correctly for all particles. However, it is clear that such adjustment is not working when scattering is taken into account.

The formula adopted to rescale the weights and properly preserve particles in the collimated source problem is:

$$w_n^\star = w_n \frac{\int_{-1}^{+1} s(\mu)\,\mathrm{d}\mu}{\sum_{m=1}^{N} w_m s(\mu_m)}. \tag{4.50}$$

In other words the weights are all corrected proportionally to the ratio between the expected result of the quadrature and the actual one.

Figures 4.12 and 4.13 show the discretized scalar fluxes associated with source Q_4 with two different μ intervals, adopting the standard weights and the rescaled ones to preserve particles. The gate functions is chosen in the first case ($0.05 < \mu < 0.21$) in order to include the same number of discrete ordinates for each scheme (Figure 4.12). Results presented in Figure 4.13 are for an interval over μ that includes the second most forward-peaked Gegenbauer direction (namely $0.05 < \mu < 0.50$), the other quadrature schemes still including only one direction.

Figure 4.12
Figure 4.13

The comparison of Figures 4.12 and 4.13 concerning the GL, GLL and CS results shows that, when the original set of weights w_n is adopted, the same results in the two configurations are obtained. This is due to the fact that the same ordinates are considered and therefore the exact limits of the collimation interval $[a;b]$ play no role. When the weights are then rescaled some differences in the two cases are observed, since both are preserving the total number of emitted particles. The use of the Gegenbauer quadrature produces different results in this comparison, since the number of ordinates involved is changed. However, all these results show a different localization and height of the flux peaks, due to the different directions and weights, but time-ray effects are, as expected, unavoidably present in all solutions. However, the choice of the Gegenbauer quadrature may be considered more suitable for the problem at hand, since it allows to describe more properly the most forward-peaked part of the source.

4.3 Conclusions

The physical distortions and numerical effects associated with the discretization of the angular variable in linear transport problems, usually called ray effects, have been analyzed and characterized in multidimensional configurations in steady-state, as well as in time-dependent problems in 1D slab geometry. The analysis of the transport kernel in the Fourier-transformed space has allowed to identify and measure the role of the ray artifact appearing in $x-y$ geometry and $x-t$ problems. This approach has allowed the definition of a proper ray effect indicator, depending on the angular discretization adopted and on the physical characteristics of the medium. The analysis of the ray effect phenomenon has also been performed in the direct space, assuming a purely absorbing medium that allows

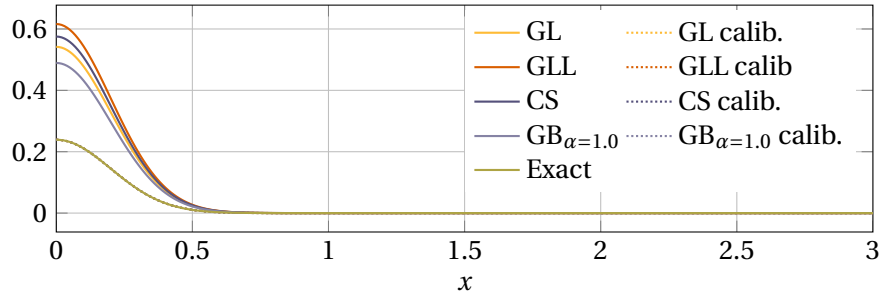

(a) $t = 0.001$

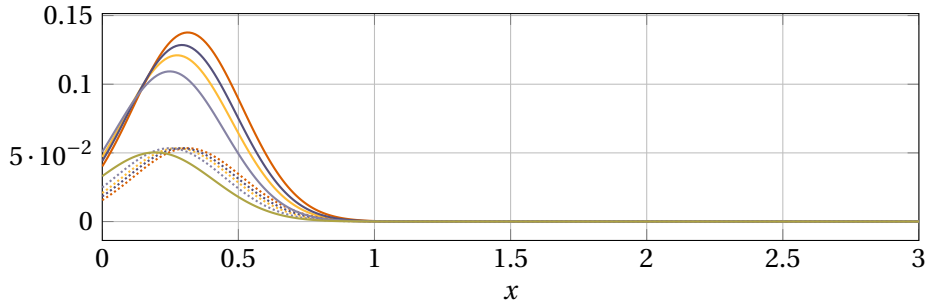

(b) $t = 1$

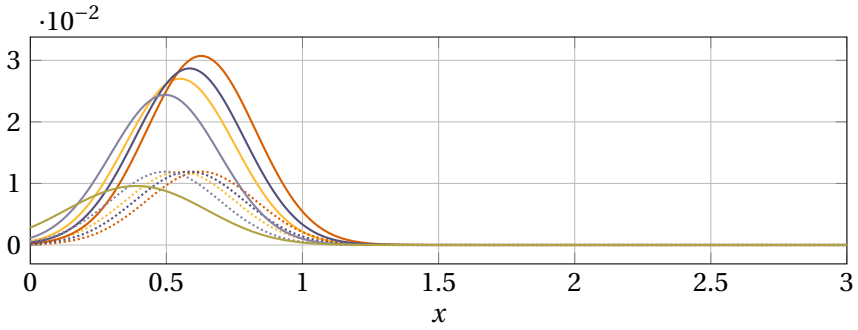

(c) $t = 2$

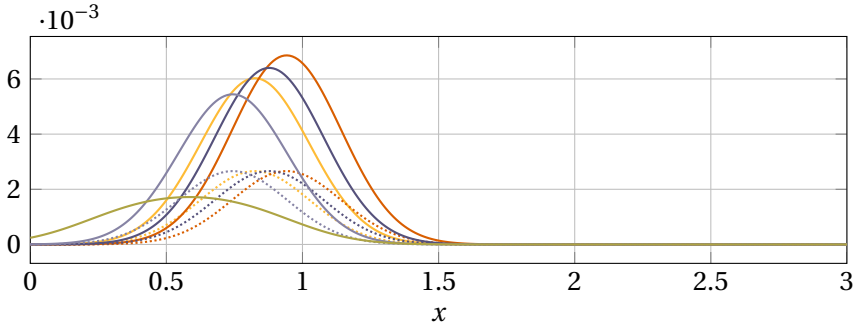

(d) $t = 3$

Figure 4.12: Flux response to a pulsed Gaussian source ($m = 0$ cm, $\sigma = 0.2$ cm), collimated in the interval $0.05 < \mu < 0.21$, solved with exact transport and S_8, adopting different angular schemes ($\Sigma = 1.0$ cm^{-1}, $v = 1.5$ cm/s).

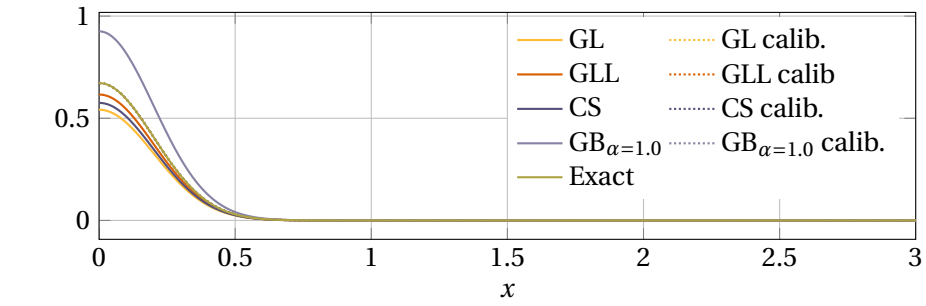

(a) $t = 0.001$

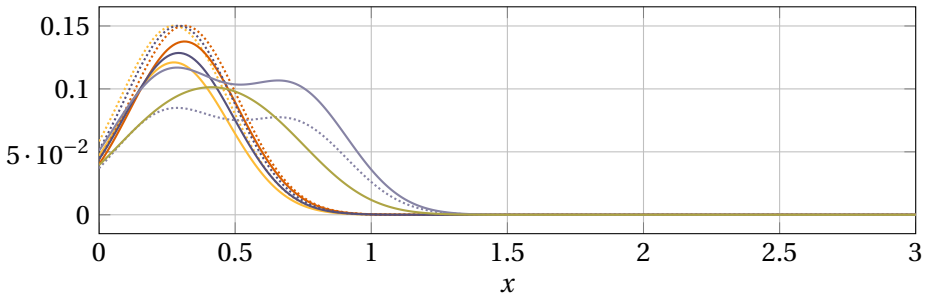

(b) $t = 1$

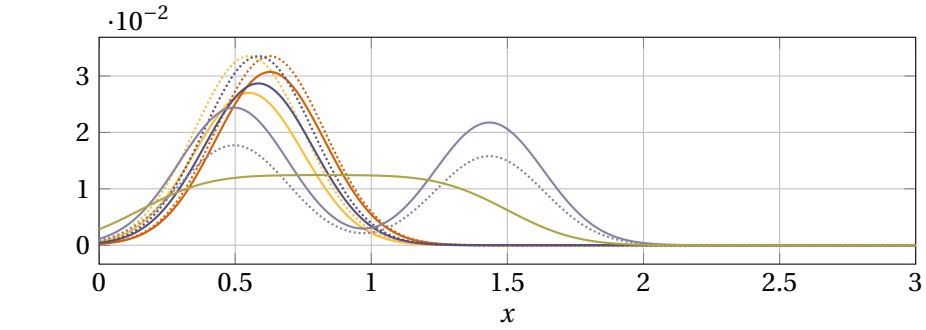

(c) $t = 2$

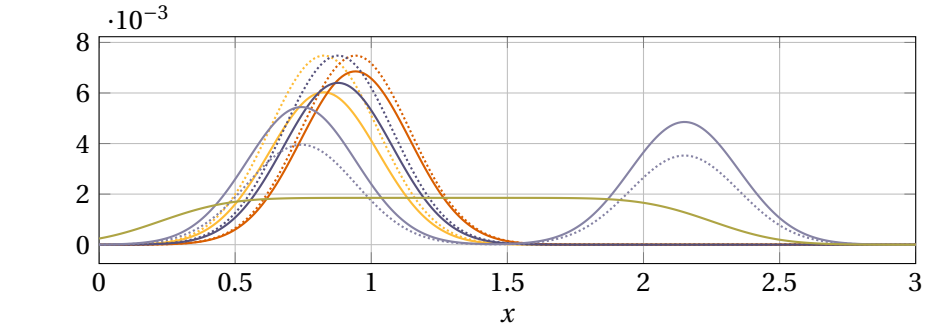

(d) $t = 3$

Figure 4.13: Flux response to a pulsed Gaussian source ($m = 0$ cm, $\sigma = 0.2$ cm), collimated in the interval $0.05 < \mu < 0.50$, solved with exact transport and S_8, adopting different angular schemes ($\Sigma = 1.0$ cm^{-1}, $v = 1.5$ cm/s).

an analytical solution for the transport equation. A definition of the ray effect indicator has been proposed also in this case, based on the understanding of the mathematical nature of the transport solution, with similar performances to the configurations observed in the Fourier analysis. The definition of the ray effect indicator in the direct space for this simplified problem provides a starting point for the definition of proper indicators to be applied in more realistic configurations. The peculiarities of the time-dependent problem in 1D slab, characterized by the appearance of time-ray effects, have been discussed in order to provide a more complete understanding of the phenomenon. The possibility of the adoption of different discretization approaches for the reduction of ray artifacts has been examined, starting from the typical approaches used in multi-dimensional transport and discussing the physico-mathematical reasons that prevent these alternative schemes from being successful in the reduction of time-ray effect. The modification in the numerical solution introduced by the adoption of different quadrature sets has been studied, clarifying how the choice of a different quadrature scheme is in principle not able to attenuate the ray effects, but could provide more significant results when strongly anisotropic problems are considered.

Conclusions and proposals for future developments

The studies on ray effects conclude the thesis.

As it is stated in the introduction, this work explores some topics in the field of neutron transport for core calculations.

Concerning the application of the Spectral Element method in neutronics, the analysis is focused on the possibility to couple effectively the numerical method, which addresses only the space part of the model, with angular discretizations in typical calculation domains. Even if a full-core tool is not available at the end of this thesis, its main "building blocks" are discussed.

Section 2.1 has addressed the convergence properties of the SEM applied to some standard transport models. In particular, the spherical harmonics and discrete ordinate formulations have been considered. This characterization should help in understanding the combined effect of the discretization in space and angle, highlighting that using SEM one gets a coupling depending on the scattering ratio: this parameter tends to slow down the convergence rate of the scheme. The drawback is in common with all other combined angular/space discretizations since it alters the mean free path of neutrons and, thus, the ability of a certain spatial mesh to correctly resolve the flux gradients. By the way, as it is clear from the results, the high-order polynomials and the automatic combined refinement of order and mesh size, endowed in the SEM structure, reduces this concern. It is observed that the high convergence rates demonstrated by SEM on general second-order models are confirmed when applied to neutron transport, constituting an advantage compared to the classical discretization techniques used so far for these applications. In general, SEM outperforms low-order classical approximation schemes and do not add, in principle, much complexity to the implementation: even if most of the coding effort is not treated in the thesis, the scheme is close to a typical Finite Element solver, especially in this 1D case where, for both FEM and SEM, the pattern of the algebraic matrix can be easily foreseen and dedicated solution strategies are naturally implemented. Moreover, SEM keeps a predictable pattern also in higher dimensions, which is a clear advantage for memory optimization.

Sections 2.2 and 2.3 try to reduce the drawbacks of the original SEM grid specifications. The classical reference for variational methods like SEM and FEM is typically the Galerkin approach, and it requires essentially conformal grids: the mesh edges always end on a node and the interface degrees of freedom are superimposed to the ones of the nearby element. If the elements are "small", grid flexibility may be recovered by refinement. In SEM, the mesh size is typically "large" compared to the characteristic dimensions of the domain, due to the high number of internal degrees of freedom. While this feature focuses on the optimal handling of gradients by the polynomial degree of the expansion basis rather than

to the mesh radius, it may pose problems in adapting the grid to some involved features that may appear on common computational domains. Nonetheless, the neutron flux in power and research reactors may show sufficiently steep gradients to require a further local fine reconstruction. For instance, the presence of localized absorbers like burnable poison pins, self neutron power detectors and shut-down rods distort the flux shape with most of the effect in the spatial scale of the mean free path. Or, there are situations where the procedures for safety evaluations require a fine reconstruction of the power profile at a sub-assembly level, like in presence of localized reactivity insertions: at the moment, mainly envelope approaches are used, adding costly provisions to the results.

These problems could be overcome by a different treatment of mesh interfaces, moving from the Continuous to the much more flexible Discontinuous Galerkin approach, as illustrated by means of some examples in section 2.2.

From the implementation point of view, the explicit block-matrix approach developed in the context of this work for DG-SEM seems easily scalable to more complex domains, and it is preferable to the automatic algorithms which are proposed for FEM schemes; its memory consumption is low, because each block can be stored in the final sparse matrix as soon as it is calculated, without cross-terms due to the advantageous structure of the DG interface conditions. Last, the conservation of the number of particles in each element is of great importance in nuclear engineering for the equivalence procedures, since it guarantees a high precision in the conservation of the reaction rates over which such calculation schemes are based. Discontinuous Galerkin, opposed to classical Continuous Galerkin, guarantees it by means of its formulation; this feature alone, whose efficacy is proven in several convergence tests targeted on the reaction rates, justifies the use of this method for any reactor physics calculation using SEM.

Finally, the Cartesian flavor of the grids used so far is removed by the transfinite interpolation in section 2.3, a robust and accurate technique of mesh deformation which ha been tightly integrated into the SEM formalism and kept at an analytical level to reduce the number of machine operations. With this last block, DG-SEM seems now adequate to cope with the involved geometries present in nuclear applications, when compared to the original approach. The developments presented are of help for the implementation, and the convergence properties analyzed for simple one-dimensional benchmarks are confirmed also for the case of the bi-dimensional Mosteller test.

From the point of view of the global accuracy of the results, such flexibility is now able to cope excellently with the space discretization errors; nonetheless, the focus should move now on the accuracy of second-order transport models, which turns out to be the the weak point of the global approach. The DG-SEM approach reduces to very low levels, even machine round-off, the amount of spatial discretization error with limited computational cost, but the limitations of the A_N model are penalizing in those situations where transport effects are very strong, to be further investigated and mitigated. Anyway, looking at the numerical tests carried out in section 2.3 and compared with fine DRAGON solutions, even at pin level the discrepancies, though evident, seem acceptable on an engineering basis.

Solvers could be integrated in transport code packages, but some further development is mandatory before proceeding in this research topic. Even if not strictly necessary for many analyses, the extension to three dimensions would provide interesting results on the

assessment of the SEM features in realistic three-dimensional problems. Formally, this task could be fulfilled as an extension of the procedures already applied in the two-dimensional studies; anyway, there are some challenges concerning the implementation which do not appear completely in this work. First, memory consumption increases rapidly with the addition of one more dimension: in this sense, dedicated sparse matrix routines have already been used in the solvers (PETSc for the Fortran codes and the MATLAB embedded ones in the other cases), and they have a direct effect on the size of the domains that were used for the examples provided in the text. For A_N and multi-group calculations the presence of nested iteration loops compels to store the matrices for each equation, and this strategy limits the extension of the final system. Smarter algorithms are to be studied in order to reduce the number of elements stored and quickly build on-the-fly the remaining ones. Moreover, grid handling should be improved, for the presence of surfaces and edges and the relative orientation problems. They were only partially encountered and addressed for the transfinite solver. Then, the conditioning number should be properly controlled with a suitable preconditioning scheme. No exact recipes are available at the moment for SEM schemes, but much research is on this topic as reported in the cited references. Finally, a proper development environment should be used to replace the Fortran language. The procedural style of the Fortran code practice has been deprecated since several years in the field of variational methods, since the complexity which arises from large codes can be treated only if a object oriented language is used, and in a proper way, and the price of a reduced execution speed is largely balanced by the easier maintenance. Examples of such codes in the nuclear field are still not very common, but the Fortran heavy limitations are already starting to show up and the switch will be soon inevitable.

The A_N transport model, if its use is somehow questionable in problems with a small scale compared to the neutron mean free path, is an optimal trade-off for core calculations where the hypotheses stated in section 1.1 assure a sufficient consistency with respect to the original transport model.

In general, second-order transport models like SP_N or A_N have gained attention in the last years because they seem handy to implement into ordinary core simulators, eventually as modules. In fact, provided a sufficiently flexible diffusive solver, relatively few code changes are needed to obtain an A_N solution, with an acceptable increase in computational time. The definition of a proper diffusion coefficient issued from cross section homogenization is not necessary with the A_N formulation, in principle. Furthermore, A_N allows to use again assembly discontinuity factors as they are defined in diffusion, opposed to other second-order transport models for which their proper use is still debated. Tests on periodic lattices of realistic fuel assemblies (colorsets) and a standard PWR core show corrections of about 1-2% on flux peaks caused by A_N, with a few hundreds pcm changes on the neutron multiplication factor. It is important to note that most of the corrections come from lower orders A_N, and this turns beneficial for the global computational performance.

Considering linearly anisotropic scattering into the A_N neutron transport model destroys, looking at the original formulation, the diffusion-like structure of the isotropic A_N model. With the imperative constraint of solving this model again with diffusive solvers, the equations are reformulated and three algorithms are outlined in section 3.2. The first attempt recurs to perturbation theory, the second to an additional leakage iteration within

diffusion solvers and the third introduces a formal diagonalization procedure on the A_N system equations.

The first attempt is only formally discussed not because of its efficacy, but for the complexity of the implementation in pre-existing diffusion codes, whereas the others have been implemented in a 1D code and numerically verified. Since the option of leakage iteration requires code changes in the solvers, the diagonalization procedure has been initially selected for the final implementation in core simulators. Unfortunately, the diagonalization procedure yields stiff problems, with the new unknowns differing of some orders in magnitude. This seems to occur regardless of the choice of the projection basis for diagonalization, notwithstanding the freedom in the choice of its parameters. Indeed, this confirms the perturbative nature of the problem, that adds small corrections to the global solution obtained without anisotropic scattering. This stiffness may cause single real precision algorithms to fail, especially in situations close to the infinite medium, and also demand for more restrictive error criteria in iterative schemes. Furthermore, the corrective components can show steep behaviors, requiring finer meshes close to material discontinuities. Mesh adaption, unfortunately, is seldom a feature of standard solvers, where mesh size is optimized taking into account only the available data, the speed and the coupling with thermal-hydraulic codes. Eventually, the diagonalization technique can fit mostly finite difference solvers on fine meshes, like for instance in pin-by-pin problems, rather than commercial nodal solvers.

The last chapter focuses on the physical distortions and numerical effects associated to the discretization of the angular variable in linear transport problems, usually called ray effects, that are analyzed and characterized in multi-dimensional configurations in steady-state as well as in time dependent problems.

The analysis of the transport kernel in the Fourier transformed space has allowed to identify and measure the role of the ray artefacts appearing in $x-y$ geometry and $x-t$ problems. This approach has allowed the definition of a proper ray effect indicator, depending on the angular discretization adopted and on the physical characteristics of the medium. The analysis of the ray effect phenomenon has also been performed in the direct space, assuming a purely absorbing medium that allows an analytical solution for the transport equation. A definition of the ray effect indicator has been proposed also in this case, with similar performances to the configurations observed in the Fourier analysis. The peculiarities of the time-dependent problem in a 1D slab, characterized by the appearance of time-ray effects, have been discussed. The possibility of the adoption of different discretization approaches for the reduction of ray artefacts has been examined, and the modification in the numerical solution introduced by the adoption of different quadrature sets have been studied.

Future work may include the development of suitable ray effect indicators applicable in more general configurations. The indicators in the transformed space are easily defined, but this tool shifts the result in a mathematical framework where its interpretation is difficult. The acquisition of a greater insight in the transfer function is certainly of interest for the future; in a shorter perspective, the recognition of typical ray effect patterns seems more viable. The indicators defined in the direct space try and formalize the process of visual recognition of the characteristic features of a biased propagation; in this sense, in the

field of image processing there exist algorithm capable of advanced edge recognition and multi-dimensional Fourier filtering: their possible application on ray-affected flux maps could provide interesting results in their quality assessment. Moreover, it is clear that the addition of discrete ordinates to the schemes used in $x-t$ problems is only palliative; more effective corrections to the S_N scheme are still to be found and studied.

Bibliography

E. A. Abbott. *Flatland: A Romance of Many Dimensions*. Seely & Co., 1884.

M. Abramowitz and I. A. Stegun, editors. *Handbook of Mathematical Functions (with Formulas, Graphs, and Mathematical Tables)*. Dover, 1972.

R. Alcouffe, F. J. Brinkley, D. Marr, and R. O'Dell. *User's guide for TWODANT: a code package for two-dimensional, diffusion-accelerated, neutral particle transport*. Los Alamos National Laboratory, rev. 1 edition, October 1984.

S. Balay, J. Brown, K. Buschelman, V. Eijkhout, W. Gropp, D. Kaushik, M. Knepley, L. Curfman McInnes, B. Smith, and H. Zhang. *PETSc Users Manual*. Mathematics and Computer Science Division, Argonne National Laboratory, 2013. URL www.mcs.anl.gov/petsc/petsc-current/docs/manual.pdf.

A. Barbarino and D. Tomatis. The A_N neutron transport by nodal diffusion. In *Proceedings of the International Conference on Mathematics and Computations, M&C 2013*, Sun Valley, Idaho, USA, May 2013a.

A. Barbarino, S. Dulla, A. K. Prinja, and P. Ravetto. Evaluation of ray effects in linear transport problems. In *23rd International Conference on Transport Theory*, Santa Fe, NM, USA, September 2013a.

A. Barbarino. The Spectral Element approach for the solution of neutron transport problems. Master thesis, Politecnico di Torino, November 2010.

A. Barbarino and D. Tomatis. A_N core analysis. In *Proceeding of the Joint International Conference on Supercomputing in Nuclear Applications and Monte Carlo 2013 (SNA + MC 2013)*, Paris, October 2013b.

A. Barbarino, S. Dulla, P. Ravetto, and E. H. Mund. The Spectral Element approach for the solution of neutron transport problems. In *International Conference on Mathematics and Computational Methods Applied to Nuclear Science and Engineering, M&C 2011*, page 15, Rio de Janeiro, Brazil, May 2011.

A. Barbarino, S. Dulla, and P. Ravetto. On the evaluation of ray effects in multidimensional and time-dependent transport problems. *Transactions of the American Nuclear Society*, 106:369–371, 2012.

A. Barbarino, S. Dulla, and P. Ravetto. Integral neutron transport and new computational methods: A review. In C. Constanda, B. E. Bodmann, and H. F. de Campos Velho, editors, *Integral Methods in Science and Engineering - Progress in Numerical and Analytical Techniques*, chapter 2, pages 41–56. Springer New York, 2013b.

A. Barbarino, S. Dulla, P. Ravetto, and E. H. Mund. The spectral element method for static neutron transport in A_n approximation. *Annals of Nuclear Energy*, 53:372–380, 2013c.

A. Barbarino, S. Dulla, E. Mund, and P. Ravetto. Assessment of the performance of the spectral element method applied to neutron transport problems. *Annals of Nuclear Energy*, 65:190–198, March 2014.

A. Baudron and J. Lautard. MINOS: a simplified P_N solver for core calculation. *Nuclear Science and Engineering*, 155(2):250–263, 2007.

G. Bell and S. Glasstone. *Nuclear Reactor Theory*. Van Nostrand Reinhold, New York, 1970.

P. Brantley and E. Larsen. Simplified P_3 approximation. *Nuclear Science and Engineering*, 134(1):1–21, 2000.

L. L. Briggs, W. F. J. Miller, and E. E. Lewis. Ray-effect mitigation in discrete ordinate-like angular finite element approximation in neutron transport. *Nuclear Science and Engineering*, 57:205–217, 1975.

A. G. Buchan, M. D. Pain, C. C. Eaton, R. P. Smedley-Stevenson, and A. J. H. Goddard. Self-adaptive spherical wavelets for angular discretizations of the boltzmann transport equations. *Nuclear Science and Engineering*, 158:244–263, 2008.

C. Canuto, M. Y. Hussaini, A. Quarteroni, and T. A. Zang. *Spectral Methods - Fundamentals in Single Domains*. Scientific Computations. Springer Berlin Heidelberg, 2006.

C. Canuto, M. Y. Hussaini, A. Quarteroni, and T. A. Zang. *Spectral Methods - Evolution to Complex Geometries and Applications to Fluid Dynamics*. Scientific Computing. Springer Berlin Heidelberg, 2007.

K. M. Case, F. De Hoffmann, and G. Placzek. *Introduction to the Theory of Neutron Diffusion*. Los Alamos Scientific Laboratory, Los Alamos, 1953.

K. M. Case and P. F. Zweifel. *Linear Transport Theory*. Addison-Wesley, Reading, MA, 1967.

R. Ciolini, G. G. M. Coppa, B. Montagnini, and P. Ravetto. Simplified P_N and A_N methods in neutron transport. *Progress in Nuclear Energy*, 40(2):237 – 264, 2002. ISSN 0149-1970.

G. Coppa and Ravetto. An approximate method to study the one-velocity neutron integral transport equation. *Annals of Nuclear Energy*, 9:169–174, 1982.

G. Coppa and P. Ravetto. Su un nuovo metodo approssimato per lo studio della soluzione della equazione del trasporto per i neutroni. Rapporto interno PT IN-FR 121, Politecnico di Torino, April 1981.

G. G. M. Coppa, P. Ravetto, and M. Sumini. The A_N method and the spherical harmonics approximation in neutron transpor theory. *Annals of Nuclear Energy*, 9:169–174, 1982.

G. G. M. Coppa, G. Lapenta, and P. Ravetto. Angular finite-element techniques in neutron transport. *Annals of Nuclear Energy*, 17:363–378, 1990.

G. G. M. Coppa, V. Giusti, B. Montagnini, and P. Ravetto. On the relation between spherical harmonics and simplified spherical harmonics methods. *Transport Theory and Statistical Physics*, 39:164–191, 2011.

G. Coppa and P. Ravetto. Quasi-singular angular finite element methods in neutron transport problems. *Transport Theory and Statistical Physics*, 24:155–172, 1995.

A. Dall'Osso and M. Ponce. *SMART: Manuel d'Utilisation, EPDN DC 0098*. Framatome ANP, Paris, France, 1998.

M. O. Deville, E. Mund, and A. Patera. Iterative solution of isoparametric spectral element equations by low order finite-element preconditioning. *Journal of Computational and Applied Mathematics*, 20:189–197, 1987.

M. O. Deville, P. F. Fischer, and E. H. Mund. *High-Order Methods for Incompressible Fluid Flow*. Cambridge University Press, Cambridge, 2002.

T. Downar, D. Lee, Y. Xu, and T. Kozlowski. *PARCS v2.6: U.S. NRC Core Neutronics Simulator*. School of Nuclear Engineering, Purdue University, IN, US, 2004.

C. Drumm, W. Fan, and S. Pautz. Phase-space finite elements in a least-squares solution of the transport equation. In *Proceedings of the International Conference M&C 2013*, Sun Valley, ID, USA, May 2013.

J. J. Duderstadt and W. R. Martin. *Transport Theory*. Wiley, 1979.

S. Dulla, B. Ganapol, and P. Ravetto. Space asymptotic methods for the study of neutron propagation. *Annals of Nuclear Energy*, 33:932–940, 2006.

S. Dulla and P. Ravetto. Analytical stechniques discrete ordinate time dependent transport problems. *Transactions of the American Nuclear Society*, 90:278–280, 2004.

S. Dulla, A. Barbarino, A. K. Prinja, and P. Ravetto. Evaluation of ray effects in linear transport problems. *Transport Theory and Statistical Physics*, 2014. (in press).

J. Ferziger and M. Peric. *Computational Methods for Fluid Dynamics*. Springer-Verlag Berlin, 2002.

X. Fu and N. Cho. Nonlinear analytic and semi-analytic nodal methods for multigroup neutron diffusion calculations. *Journal of Nuclear Science and Technology*, 39(10):1015–1025, 2002.

B. D. Ganapol. *Analytical Benchmarks for Nuclear Engineering Applications, Case Studies in Neutron Transport Theory*. OECD-NEA, Paris, 2008.

B. Garland. Reactor Physics: Multigroup Diffusion. http://www.nuceng.ca/ep4d3, 2005.

E. M. Gelbard. Application of the spherical harmonics method to reactor problems. Technical Report WAPD-BT-20, Bettis Atomic Power Laboratory, Pittsburgh, 1960.

A. Hébert. *Applied Reactor Physics*. Presses internationales Polytechnique, 2009.

A. Hébert. The search for superconverge in spherical harmonics approximations. *Nuclear Science and Engineeing*, 154:134, 2006.

A. Hébert. Multigroup neutron transport and diffusion computations. In D. G. Cacuci, editor, *Handbook of Nuclear Engineering*, volume II, pages 751–911. Springer, New York, 2010.

G. Hobson. *ARTEMIS Methodology Manual*. AREVA NP, Erlangen, Germany, 2008. CONV08_0064, Internal Publication.

V. Ivanov and M. Trubetskov. *Handbook of conformal mapping with computer-aided visualization*. Boca Raton CRC, 1995.

G. E. Karniadakis and S. Sherwin. *Spectral/hp Element Methods for Computational Fluid Dynamics*. Numerical Mathematics and Scientific Computation. Oxford Science Publications, 2005.

H. Khalil. A Nodal Diffusion Technique for Synthetic Acceleration of Nodal S_n calculations. *Nuclear Science and Engineering*, 90:263–280, 1985.

E. W. Larsen and J. E. Morel. Advances in discrete-ordinates methodology. In Y. Azmy and E. Sartori, editors, *Nuclear Computational Science: A Century in Review*, chapter 1, pages 1–81. Springer, 2010.

E. Larsen, J. Morel, and J. McGhee. Asymptotic derivation of the multigroup p1 and simplified pn equations with anisotropic scattering. *Nuclear Science and Engineering*, 123(3): 328–342, 1996.

K. D. Lathorp. Ray effects in discrete ordinates equations. *Nuclear Science and Engineeing*, 32:357–369, 1968.

K. D. Lathorp. Remedies for ray effects. *Nuclear Science and Engineering*, 45:225–268, 1971.

R. D. Lawrence. Progress in nodal methods for the solution of the neutron diffusion and transport equations. *Progress in Nuclear Energy*, 17(3):271–301, 1986. ISSN 0149-1970.

E. E. Lewis. Second-order neutron transport methods. In Y. Azmy and E. Sartori, editors, *Nuclear Computational Science: A Century in Review*, chapter 2, pages 85–105. Springer, 2010.

E. E. Lewis and W. F. Miller. *Computational Methods of Neutron Transport*. American Nuclear Society, La Grange Park, 1993.

G. Longoni and A. Haghighat. Development and application of the regional angular refinement technique and its applications to non-conventional problems. In *Proceedings of the International Conference PHYSOR 2002*, Seoul, Republic of Korea, October 7-10 2002.

G. Marleau, A. Hébert, and R. Roy. *A User Guide for DRAGON*. École Polytechnique de Montréal, Québec, 2000. Version DRAGON_000331 Release 3.04.

W. R. Martin, L. Yehnert, C. E. Lorence, and J. J. Duderstadt. Phase-space finite element methods applied to the first-order form of the transport equation. *Annals of Nuclear Energy*, 8:633–649, 1981.

R. McGill, J. W. Tukey, and W. A. Larsen. Variations of box plots. *The American Statistician*, 32:12–16, 1978.

R. V. Meghreblian and D. K. Holmes. *Reactor Analysis*. McGraw-Hill, New York, 1960.

M. Melice. A nodal-modal coarse-mesh method for solving the two group diffusion equation. Technical Report KNSM/69/GDC (NEACRP-L-228), ELECTROBEL, Belgium, November 1978.

W. F. Miller and W. H. Reed. Ray effect mitigation methods for two-dimensional neutron transport theory. *Nuclear Science and Engineering*, 62:391–411, 1977.

J. E. Morel, T. A. Wareing, R. B. Lowrie, and D. K. Parsons. Analysis of ray-effect mitigation techniques. *Nuclear Science and Engineering*, 144:1–22, 2003.

R. D. Mosteller and L. D. Eisenhart. Benchmark Calculations for the Doppler Coefficient of Reactivity. *Nuclear Science and Engineering*, 107:265–271, 1991.

E. Mund. A primer on transfinite interpolation in multi-dimensional cartesian geometry. Private communication, September 2011a.

E. Mund. Spectral element solutions for the P_N neutron transport equations. *Computers & Fluids*, 43(1):102 – 106, 2011b. ISSN 0045-7930. special issue dedicated to Prof. Michel Deville.

N. Natelson. Variational derivation of discrete ordinate-like approximations. *Nuclear Science and Engineering*, 43:131–134, 1971.

A. Patera. A spectral element method for fluid dynamics: Laminar flow in a channel expansion. *Journal of Computational Physics*, 54:468–488, 1984.

O. Pironneau, F. Hecht, A. Le Hyaric, and J. Morice. *FreeFem++ Manual*. Université Pierre et Marie Curie - Laboratoire Jacques-Louis Lions, 2010.

G. C. Pomraning. Asymptotic and variational derivations of the simplified P_N equations. *Annals of Nuclear Energy*, 20(9):623 – 637, 1993. ISSN 0306-4549.

A. K. Prinja and E. W. Larsen. General principles of neutron transport. In D. G. Cacuci, editor, *Handbook of Nuclear Engineering*, volume I, pages 427–542. Springer, New York, 2010.

A. Quarteroni. *Numerical Models for Differential Problems*. MS&A. Springer, 2009.

C. Rechantin and M. Schenider. *APOLLO2-A User's Manual Version 1.20.0*. AREVA NP, Paris, France, 2012. CONV12_0004/PEPDF12_0016, Internal Publication.

F. Rellich. Perturbation theory of eigenvalue problems. Technical Report IMM-NYU 212, New York University, 1954.

B. Rivière. *Discontinuous Galerkin Methods for Solving Elliptic and Parabolic Equations: theory and implementation*. Society for Industrial and Applied Mathemathics, Philadelphia, 2008.

Y. Saad and M. H. Schultz. GMRES: A generalized minimal residual algorithm for solving nonsymmetric linear systems. *SIAM J. Sci. Stat. Comput.*, 7(3):856–869, July 1986.

D. M. Silva, E. J. Lydia, M. R. Guida, J. H. Zani, H. Alves Filho, R. C. Barros, and H. Alves Filho. Analytical methods for computational modeling of fixed-source slab-geometry discrete ordinates transport problems: Response matrix and hybrid s_n. *Progress in Nuclear Energy (New Series)*, 1:1–15, 2013.

D. Tomatis. *The Migration Mode Method*. PhD thesis, Politecnico di Torino, 2010.

V. S. Vladimirov. Mathematical problems in the one-velocity theory of particle transport. Technical report, Atomic Energy of Canada Ltd., Ontario, Canada, 1961. translated: V. A. Steklov Mathematical Institute.

J. Warsa, J. Densmore, A. Prinja, and J. Morel. Manufactured solutions in the thick diffusion limit. *Nuclear Science and Engineering*, 166(1):36–47, September 2010.

R. J. Zerr and R. S. Baker. On the matter of time-dependent ray effects. *Transactions of the American Nuclear Society*, 105:438–439, 2011.

T. Zmijarevic, E. Masiello, and R. Sanchez. Flux reconstruction methods for assembly calculations in the code APOLLO2. In *Proceedings of the International Conference on Reactor Physics PHYSOR 2006, Vancouver, BC, Canada*, September 10–14 2006.

Acknowledgments

This work has been made possible by several people, that I want here to mention and thank sincerely.

First, I would like to acknowledge AREVA NP SaS, the enterprise that has materially sustained my activity during the three years. I really appreciated the AREVA efforts to support scientific research leaving me, at the same time, a high level of freedom in the management of the topics and in the developments, which is an attitude not to be taken for granted when industry and academia meet.

Among the AREVA staff that I have met, my highest gratitude goes to Daniele Tomatis. He has closely followed my activity during the year and a half that I have passed in Paris; even if his professional activity as research engineer in the Codes and Methods Development department has a tight schedule, he was always available to answer promptly my questions and to take part into the developments, which otherwise would have been limited due to my limited familiarity with the codes. I would like to express him my wishes for its career and his professional satisfaction.

I would like to thank also Aldo Dall'Osso, cornerstone of the code expertise, whose advice has often helped me and Daniele in getting out of the issues we have encountered during the implementation of the A_N method. Many thanks also to Emanuele Martinolli and Anthony Barbier, my line managers of the PEPDDF section, for their availability and their attitude towards me. Moreover, I would like to acknowledge Rossella Baldoni and Gabriele Grassi for their role in bridging AREVA and the Politecnico di Torino in the starting phase; in case of Rossella, also in helping me understanding the differences between French and Italian humor...

I have really appreciated my colleagues of the PEPDDF and PEPDVF sections. They were almost all my little French world, and thanks to their experiences I have understood interesting aspects of their culture.

Paris is notably a beautiful but rainy city; anyway, where there are a few Italians you can feel the Mediterranean heat. I had the chance to meet a lot of very pleasant Italian colleagues, and I have passed a very good time with them. I would like to give thanks to Emanuele Autino in particular, who deserves absolutely a special mention: without his kind hospitality my first month in France would have been far more complicated than it actually was.

Moving a little east, I am indebted to Prof. Ernest Mund, senior professor of the Free University of Brussels; he is the initiator of the Spectral Element approach to neutron transport problems and has kindly shared with me many of his intuitions, which are now contained in this work. In addition, I would like to give credit to Prof. Anjil Prinja and Prof. Barry Ganapol for their support.

In Turin, I would like to thank Sandra Dulla and Piero Ravetto. I am perfectly aware that

putting the thesis advisers in the acknowledgments is against the conventions and may sound sycophant. The scientific contribution to this work has been in line with their level of professionalism, but I feel that their impact has gone far beyond their academic role. In fact, they have really disclosed me their experience as researchers, contributing to open my views.

And, finally, my gratitude and best wishes for a brilliant future go to my colleagues in Turin, for their sympathy, their company and their empathy. When I ask myself if I miss something of my little Italian world, they are the only item in the list.

These three years have been the hardest in my life. Three years of work, travels, challenges, achievements, disappointments, loneliness. Nonetheless, the spark of optimism embedded in my personality induces me to interpret this time as a real investment for my future, in a globally positive sense.

For the moment, I have decided to leave research and to concentrate myself on a more "engineering" career among the ranks of AREVA NP. I am presently an associated professional devoted to core transient and accident analysis for several AREVA important international projects. This is not a surrender, nor an escape from research. (Re)Searching is one of my strongest attitudes and the most evident effect of this PhD is its renovated vigor. Simply, my target has become wider than a single scientific topic.

> Tho' much is taken, much abides; and tho'
> We are not now that strength which in old days
> Moved earth and heaven, that which we are, we are;
> One equal temper of heroic hearts,
> Made weak by time and fate, but strong in will
> To strive, to seek, to find, and not to yield.
>
> — Alfred Tennyson, *Ulysses*